Barium Sulphate Formation Kinetics and Inhibition at Surfaces

Eleftheria Mavredaki

Submitted in accordance with the requirements for the degree of
Doctor of Philosophy

The University of Leeds
School of Mechanical Engineering

August, 2009

The candidate confirms that the work submitted is his/her own and that appropriate credit has been given where reference has been made to the work of others.

Acknowledgements

I would like to thank my supervisor Professor Anne Neville for guiding this study with her knowledge and experience. Mostly I want to thank her for showing trust on this work.

I am thankful to Marian Millar from Heriot Watt University for helping in committing the Atomic Force Microscope, also Zhong Zhong for his help on the *in-situ* SXRD measurements, Tao Chen, Xiaojun Lai and Aurelie Martinod for the long conversations on Synchrotron X-Ray Diffraction data issues. I want to thank the people from Heriot Watt University; Ken Sorbie, Eric McKay, Lorraine Boak, Oscar Vasquez and Mike Singleton and the Flow Assurance Scale Control team, for constructive conversations, nice scale meetings and finance support of this study.

Many thanks to Coserg group and to the scale team for the good team atmosphere. Many appreciations to: Graham Jakeman, Ron Cellier, Graham Blyth and Ted Allwood for technical contributions on this work.

At last I would like to thank:

- my friends; Aggeliki, Rena, Aurelie, Anda, Bertram, Violette, Rob, Efi, Eirini, Dora, Billy, Sotiris, Eirini K., Argirw, Eva, Yiannis, Wendy, Thimbaut, Rock, John, Simon, Abinesh, Rupesh, Natalia, Ali, Katerina, Irune and Stratos for the times we have been through, also my family for staying close during all my studies, Katerina and Tom for always being open hearted and my Andreas for showing me only good aspects of life.

Abstract

This study refers to experimental work and analysis of the barium sulphate deposition onto surfaces. In the oil field the formation of barium sulphate is a major flow assurance issue. The build up of the $BaSO_4$ inorganic scale on surfaces and facilities is undesirable as it causes increased function, reduction in production and other flow assurance issues. To date the overwhelming amount of research has been on the bulk precipitation of barite and little attention has been paid to deposition onto surfaces. This study shows an integrated approach to access the formation kinetics of barite at surfaces.

Both the formation kinetics and the crystallography of the deposited barite are explored under examined conditions intended to imitate in some part the off-shore environment. In addition the effect of chemical additives performing as inhibitors of the barite growth is kept as a main concern of this study. Understanding the behavior of the inhibitors and their retardation mechanisms can further target the improvement of inhibition and overall antiscaling techniques.

The thesis work has demonstrated that the surface growth kinetics of barite is largely different to bulk kinetics and interesting phenomena occur at surfaces especially when inhibitors are used. There are complex interactions of the inhibitor with the scale and both growth kinetics and crystal morphology are affected with threshold concentrations. The input of the inhibition mechanisms is discussed.

Table of contents

Acknowledgements ii

Abstract iii

Table of contents iv

Table of figures viii

Tables xv

List of Publications xvii

Nomenclature xviii

CHAPTER 1 Introduction 1

1.1 Oil through the ages 1

1.2 Scale 4

1.3 Scale treatment 5

1.4 Objectives 7

1.5 Thesis layout 8

CHAPTER 2 Theory and literature review on scale formation and inhibition; The case of barium sulphate 10

2.1 Introduction 10

2.2 Precipitation stages 12

2.2.1 Nucleation 12

2.2.1.1 Primary nucleation 13

2.2.1.2 Secondary nucleation 15

2.3 Induction time and calculation of thermodynamic quantities 17

2.4 Crystal growth 19

2.4.1 Surface energy theories 19

2.4.2 Adsorption layer theories 20

2.4.3 Dislocation theory 22

2.5 Adhesion 23

2.5.1 Description of the adhesion phenomenon 23

2.5.2 Adhesion forces 23

2.5.3 Methods for measuring adhesion 25

2.6 Barium Sulphate 27

2.6.1 Chemical properties of $BaSO_4$ 27

2.6.2 Crystallography of $BaSO_4$ 29

2.6.2.1 Introduction 29

2.6.2.2 Miller Indices 31
2.6.2.3 Periodic Bond Chains theory (PBC) 34

2.7 Factors affecting nucleation and crystal growth of $BaSO_4$ **35**
2.7.1 Supersaturation Ratio 35
2.7.2 Solubility 38
2.7.3 Temperature & Pressure 38
2.7.4 pH 39
2.7.5 Divalent Cations 39
2.7.6 Stoichiometry of lattice ions in solutions 40
2.7.7 Inhibitors structure and concentration 41

2.8 Applied techniques for scale surface studies **42**
2.8.1 Stopped flow technique 42
2.8.2 Rotating cylinder electrode 43
2.8.3 Thickness Shear Mode Resonator 43
2.8.4 Quartz Crystal Microbalance 44
2.8.5 Atomic force applications 45
2.8.6 X-ray diffraction applications 46

2.9 Dissolution **48**

2.10 Inhibition **50**
2.10.1 Introduction 50
2.10.2 Inhibition efficiency 51
2.10.3 Inhibitor families 52
2.10.4 Barium sulphate inhibitor performance in bulk solutions 54

2.11 Inhibition Mechanisms **62**
2.11.1 Threshold effect 63
2.11.2 Crystal distortion 63
2.11.3 Dispersancy and stabilization 64

2.12 Synopsis of the literature review **64**

CHAPTER 3 Development of the experimental techniques 65

3.1 Introduction **65**

3.2 Chemical Reagents **65**

3.3 Scale Inhibitors **66**

3.4 Quartz Crystal Microbalance **67**
3.4.1 Introduction 67
3.4.2 Quartz crystal microbalance apparatus 67
3.4.3 Quartz crystal microbalance principles 68
3.4.4 Quartz crystal microbalance measurements in liquid environment 70
3.4.5 Quartz Crystals 72
3.4.6 Static Tests with Quartz Crystal Microbalance for $BaSO_4$ Deposition 74

3.5 Atomic Force Microscope **75**
3.5.1 Introduction 75
3.5.2 AFM instrumentation 76
3.5.3 AFM principle 79
3.5.4 AFM adjustments and analysis of the AFM topography maps 81

3.6 Synchrotron X - ray diffraction **82**
3.6.1 Introduction 82
3.6.2 Principles of X-ray diffraction 82

3.6.3 Powder X-Ray Diffraction 84
3.6.4 SXRD set up 85

3.7 Metal Substrates 88

3.8 Techniques for bulk scale measurements 89
3.8.1 Inductive coupled plasma atomic emission spectroscopy for barium ions detection ... 89
3.8.2 Measuring the turbidity 90

CHAPTER 4 Initial stages of barium sulphate formation kinetics on a metallic surface in the presence and absence of inhibitors 92

4.1 Introduction 92

4.2 Experimental details 92

4.3 Barium sulphate measurements on the surface 94
4.3.1 Technique's challenges 94
4.3.2 $BaSO_4$ formation kinetics from mixture A 95
4.3.3 $BaSO_4$ precipitation kinetics from mixture B 98
4.3.3.1 Uninhibited formation of barite 99
4.3.3.2 Inhibited formation of $BaSO_4$ - Effect of PPCA 102
4.3.3.3 Inhibited formation of $BaSO_4$ - Effect of DETPMP 108
4.3.4 $BaSO_4$ formation kinetics from mixture C 114
4.3.4.1 Uninhibited formation of barite 115
4.3.4.2 Inhibited formation of barite 118

4.4 Barium sulphate measurements in the bulk phase 126
4.4.1 Experimental details 126
4.4.2 Uninhibited $BaSO_4$ precipitation measurements 127
4.4.3 Inhibited $BaSO_4$ precipitation measurements 129
4.4.3.1 PPCA effect 129
4.4.3.2 DETPMP effect 131

CHAPTER 5 *In-situ* X-ray diffraction for $BaSO_4$ formation in uninhibited and inhibited conditions 133

5.1 Introduction 133

5.2 Experimental details 134
5.2.1 *In-situ* SXRD set up 134
5.2.2 Experimental Overview 134

5.3 In-situ SXRD measurements 136
5.3.1 *In-situ* SXRD analysis remarks 136
5.3.2 Uninhibited $BaSO_4$ formation precipitating from mixture C 139
5.3.3 The effect of PPCA on the formed barite precipitated at high supersaturation ratio conditions 143
5.3.3.1 Inhibition at 95 °C 143
5.3.4 Inhibition at 57°C 147
5.3.5 The effect of DETPMP on the formed barite precipitated at high supersaturation index conditions 150
5.3.5.1 Inhibition at 95 °C 150
5.3.5.2 Inhibition at 57 °C 153
5.3.6 Incorporation of Sr^{2+} into the barite lattice 155
5.3.6.2 (111) plane of celestine barian 156
5.3.6.3 (212) and (031) planes of celestine barian 157

5.3.7 Uninhibited $BaSO_4$ formation precipitating from mixture B 158

CHAPTER 6 Discussion 161

6.1 Introduction 161

6.2 Kinetics 162
6.2.1 Growth rate of $BaSO_4$ 162
6.2.1.1 Uninhibited tests 162
6.2.1.2 Linear growth of $BaSO_4$ 168
6.2.2 Quantification of barite scale formed at different growth rates 171
6.2.3 Comparison of the bulk and surface kinetics 174
6.2.3.1 Uninhibited case 174
6.2.3.2 Inhibited cases for mixture B 176
6.2.3.3 Inhibited cases for mixture C 178
6.2.4 Supersaturation index 179

6.3 Mechanisms 181
6.3.1 Formation mechanism of $BaSO_4$ at low supersaturation index 182
6.3.2 Formation mechanism of $BaSO_4$ at medium and high supersaturation indices 183

6.4 Inhibition 186
6.4.1 Characteristics of the adherent $BaSO_4$ morphologies 186
6.4.2 Functional groups of inhibitors 192
6.4.3 Identification of $BaSO_4$ crystal faces with *in-situ* SXRD 193
6.4.4 Characterization of $BaSO_4$ crystal faces based on PBC theory 197
6.4.5 Establishment of an effective inhibition on barium sulphate 199

6.5 Practical considerations 200
6.5.1 Growth trends 201
6.5.2 Inhibitor efficiency 201
6.5.3 Presence of foreign ions 204
6.5.4 Crystallography of the adhered $BaSO_4$ 206

CHAPTER 7 CONCLUSIONS 207

7.1 Introduction 207

7.2 $BaSO_4$ formation kinetics on surface 207

7.3 Inhibition of $BaSO_4$ 208

7.4 Crystallography of $BaSO_4$ 209

CHAPTER 8 FUTURE WORK 211

8.1 Introduction 211

8.2 Refinement of barite structures in the absence and presence of inhibitors 211

8.3 Inhibitors 212

8.4 Kinetics and modelling 213

8.5 Effect of divalent cations 213

REFERENCES 214

Table of figures

Figure 1.1: Diagram of the three main industrial problems [3] 3
Figure 1.2: Scale formation in pipe 4
Figure 2.1: Free energy diagram of nucleation 13
Figure 2.2: Kinetic stages involved in precipitation [21] 15
Figure 2.3: Growth of crystal faces (a) maintenance of the crystal faces and (b) overlapping [37] 20
Figure 2.4: Crystal growth schematic diagram [37] 21
Figure 2.5: Diagram of the screw dislocation mechanism 22
Figure 2.6: Barium sulphate mineral [54] 27
Figure 2.7: IR spectra of $BaSO_4$ [61] 29
Figure 2.8: Unit cell of barite 31
Figure 2.9: Intercept of planes on the crystallographic axes 32
Figure 2.10: The (210) and (001) lattice plane of $BaSO_4$ 33
Figure 2.11: The appearance of the (002) and (211) lattice planes of barite [68] 33
Figure 2.12: Diagram of F, S & K crystal faces [37] 35
Figure 2.13: Solubility supersaturation zones for $BaSO_4$ [8] 37
Figure 2.14: DTPA structure structure 49
Figure 2.15: EDTA (ethylenediaminetetraacetic acid) structure 50
Figure 2.16: PPAA structure 54
Figure 2.17: Poly-phoshinocarboxylix acid (PPCA) structure 55
Figure 2.18: PMA-PVS structure 56
Figure 2.19: PAA-PVS structure 56
Figure 2.20: PBTC -2-Phosphonobutane-1, 2, 4-tricarboxylic acid structure 57
Figure 2.21: ATMP -Amino tri (methylene-phosphonic) acid structure 57
Figure 2.22: DETPMP-Diethylenetriamine penta methylenephosphonic acid structure 58
Figure 2.23: Mellitic acid structure 59
Figure 2.24: Polyepoxysuccinic acid structure 60

Figure 2.25: Agaric acid structure....60
Figure 2.26: Polymaleic acid structure....61
Figure 2.28: Three main inhibition mechanisms [111]....63
Figure 3.1: Complete QCM set up (QCM200 Digital Controller, QCM25 Crystal Oscillator,....68
Figure 3.2: Crystal holder components....68
Figure 3.3: Amplitude and acceleration decay at the quartz – liquid interface [142]71
Figure 3.4: Assignment of axes to a quartz crystal [140]....72
Figure 3.5: AT-cut angle....73
Figure 3.6: BT-cut angle....73
Figure 3.7: Diagram of the AFM equipment [150]....77
Figure 3.8: Sample translator [150]....77
Figure 3.9: AFM explorer [150]....78
Figure 3.10: Diagram of the scanning process in non-contact operation [150]....79
Figure 3.11: Diagram of the Van Der Vaals forces distance between the tip and the sample....80
Figure 3.12: Diffraction of X-rays by a crystal [152]....83
Figure 3.13: Debye Rings of barite formed at 95°C....84
Figure 3.14: Schematic representation of powder X-Ray Diffraction....85
Figure 3.15: Diagram of the SXRD set up....86
Figure 3.16: SXRD pattern of dominant barite surfaces formed at 95°C....88
Figure 4.1: QCM measurements for mixture A....96
Figure 4.2: (a) Adhered $BaSO_4$ on quartz crystal & (b) different scanned area of the crystal....96
Figure 4.3: AFM image of the $BaSO_4$ rhombohedral structures (a) 50.25 x 50.25 μm scanning range (b) 20.1 x 20.1 μm scanning range....97
Figure 4.4: The (210), (001) and (011) crystal faces of the formed barite....97
Figure 4.5: QCM measurements for mixture B....99
Figure 4.6: Deposited $BaSO_4$ on the quartz crystal at supersaturation index= 2.64 100
Figure 4.7: AFM images of barite crystals at scanning range 50 x 50 μm....101

Figure 4.8: (a) AFM image of barite and (b) Diagram of typical barite crystal [163] 101
Figure 4.9: QCM measurements of barium sulphate after treatment with 1 ppm PPCA.....102
Figure 4.10: Barite crystals after treatment with 1 ppm PPCA (a) first scanned area of the surface & (b) second scanned area of the surface.....103
Figure 4.11: Barite morphologies under the treatment of 1 ppm PPCA.....103
Figure 4.12: QCM measurements of barium sulphate after treatment with 4 ppm PPCA.....104
Figure 4.13: Barite morphologies after treatment with 4 ppm PPCA (a) first scanned area of the surface & (b) second scanned area.....105
Figure 4.14: AFM images of the inhibited barite crystals at (a) 20.1 x 20.1μm & (b) 11.31 x 11.31 μm 105
Figure 4.15: QCM measurements of barium sulphate after treatment with 10 ppm PPCA.....106
Figure 4.16: AFM images of barite morphologies after treatment with 10 ppm PPCA (a) first scanned area of the surface & (b) second scanned area.....107
Figure 4.17: AFM images of inhibited barium sulphate crystals at (a) 20.05 x 20.05 μm & 107
Figure 4.18: Standard deviation of PPCA effect on formed barium sulphate 108
Figure 4.19: QCM measurements of barium sulphate after treatment with 1 ppm DETPMP.....109
Figure 4.20: Formed barite scale after treatment with 1 ppm DETPMP 109
Figure 4.21: AFM image of barite morphology (50x50 μm).....110
Figure 4.22: QCM measurements of barium sulphate after treatment with 4 ppm DETPMP.....110
Figure 4.23: The effect of 4 ppm DETPMP on barite structures (a) big size barite crystals & (b) small size crystals 111
Figure 4.24: Star like and needle shaped barite structures at (a) 50 x 50 μm & (b) 20 x 20 μm 112

Figure 4.25: QCM measurements of barium sulphate after treatment with 10 ppm DETPMP....112
Figure 4.26: Barite morphologies under treatment of 10 ppm DETPMP (a) first scanned area of the substrate & (b) second scanned area....113
Figure 4.27: AFM scanning (a) 50.75 x 50.75 μm and (b) 10 x 10 μm....113
Figure 4.28: Standard deviations for DETPMP effect on the deposited $BaSO_4$....114
Figure 4.29: QCM measurements for mixture C....116
Figure 4.30: Barite morphologies at high supersaturation index (SI=4.32)....116
Figure 4.31: AFM images of deposited $BaSO_4$ at scanning rates (a) 50 x 50 μm & (b) 20.07 x 20.07 μm....117
Figure 4.32: Barite crystal grown along the [120]....117
Figure 4.33: QCM measurements of barium sulphate after treatment with 1 ppm PPCA....118
Figure 4.34: Formed barite under 1ppm PPCA treatment (a) scanning range 100 x 100 μm (b) scanning range 50.5 x 50.5 μm....119
Figure 4.35: (a) Formation of barite growth steps (b) [010] and [120] growth directions of barite morphologies....119
Figure 4.36: QCM measurements of barium sulphate after treatment with 2 ppm PPCA....120
Figure 4.37: Barite morphologies after treatment with 2 ppm PPCA....120
Figure 4.38: AFM images (a) scanning range 49.8 x 49.8 μm (b) 20.17 x 20.17 μm....121
Figure 4.39: QCM measurements of barium sulphate after treatment with 4 ppm PPCA....121
Figure 4.40: $BaSO_4$ formations after treatment with 4 ppm PPCA (a) First scanned area (b) different scanned area....122
Figure 4.41: (a) Barite structures (b) Pyramidal structure of barium sulphate with absent growth steps....123
Figure 4.42: QCM measurements of barium sulphate after treatment with 10 ppm PPCA....123
Figure 4.43: $BaSO_4$ formations under the treatment of 10 ppm PPCA....124

Figure 4.44: AFM image of formed scale type (a) 50.25 x 50.25 μm (b) 21.36 x 21.36 μm 124
Figure 4.45: Standard deviations of PPCA effect on barite precipitating from mixture C 125
Figure 4.46: Turbidity measurements for mixture A 128
Figure 4.47: Comparison of the turbidity for the three mixtures 128
Figure 4.48 : Turbidity measurements of mixture B for 1 hour – treatment with PPCA 130
Figure 4.49: Turbidity measurements of mixture C- Treatment with PPCA 131
Figure 4.50: Turbidity measurements of mixture B – Treatment with DETPMP ...132
Figure 5.1: SXRD pattern showing the stable peaks 137
Figure 5.2: SXRD plot of uninhibited $BaSO_4$ formation at 95°C 139
Figure 5.3: SXRD plot of uninhibited $BaSO_4$ formation at 57°C 141
Figure 5.4: Debye rings of formed barite on surface at (a) 95°C and (b) 57°C 142
Figure 5.5: Effect of 1ppm PPCA at 95°C 143
Figure 5.6: Effect of 4 ppm PPCA at 95°C 144
Figure 5.7: Effect of 10 ppm PPCA at 95°C 145
Figure 5.8: SXRD pattern of $BaSO_4$ after treatment with 10 ppm PPCA 146
Figure 5.9: Overview of PPCA effect on dominant barite planes at 95°C 147
Figure 5.10: Effect of 4 ppm PPCA on the dominant barite planes at 57°C 148
Figure 5.11: Effect of 10ppm PPCA on the dominant barite planes at 57°C 149
Figure 5.12: Overview of the PPCA effect on dominant barite planes at 57°C 149
Figure 5.13: Effect of 10ppm DETPMP on dominant barite planes at 95°C 151
Figure 5.14: SXRD pattern of barite planes after treatment with 10 ppm DETPMP at 95°C 151
Figure 5.15: Effect of 20 ppm DETPMP on dominant barite planes at 95°C 152
Figure 5.16: Overview of DETPMP effect on dominant barite planes at 95°C 153
Figure 5.17: Effect of 10 ppm DETPMP on dominant barite planes at 57°C 154
Figure 5.18: Effect of 20 ppm DETPMP on dominant barite planes at 57°C 154
Figure 5.19: Overview of DETPMP effect on dominant barite planes at 57°C 155

Figure 5.20: Effect of inhibitors on (111) crystal face of celestine barian at 95°C .156
Figure 5.21: Effect of inhibitors on (111) crystal face of celestine barian at 57°C .157
Figure 5.22: SXRD pattern for barite precipitating from mixture B at 95°C 159
Figure 6.1: Deposition of $BaSO_4$ on quartz crystal at three different supersaturation indices 163
Figure 6.2: Initial stage of $BaSO_4$ deposition after precipitating from mixture A...164
Figure 6.3: Initial stage of $BaSO_4$ deposition after precipitating from mixture B ...165
Figure 6.4: Initial stage of $BaSO_4$ deposition after precipitating from mixture C ...165
Figure 6.5: Approach of the induction time of barium sulphate on the surface for mixture B 167
Figure 6.6: Surface and Bulk measurements for the three different brines (a) overview of all the kinetics and (b) focusing on the lower scale measurements.....175
Figure 6.7: Comparison of bulk and surface measurements for mixture B after treatment with PPCA 176
Figure 6.8: Comparison of bulk and surface measurements for mixture B after treatment with DETPMP.....177
Figure 6.9: Comparison of bulk and surface measurements for mixture C after treatment with PPCA 178
Figure 6.10: Plot of induction time versus supersaturation index.....179
Figure 6.11: Effect of supersaturation index on induction period for $BaSO_4$ nucleation.....180
Figure 6.12: The logarithm of supersaturation index versus induction time 181
Figure 6.13: $BaSO_4$ formation under spiral growth mechanism (a) experimental morphologies and (b) simulations of rhombohedral structures [64].....182
Figure 6.14: Spiral mechanism at screw dislocation [104] 183
Figure 6.15: $BaSO_4$ particles precipitating from mixture B.....184
Figure 6.16: Two dimensional nuclei of barium sulphate formed at medium SI 184
Figure 6.17: Deposited barite from mixture C 185
Figure 6.18: Two dimensional nucleation in the [120] direction.....186

Figure 6.19: Diagram of the Z height of formed barite versus distance in the absence of inhibitor 187
Figure 6.20: Diagram of the Z height of the formed barite versus distance in the presence of 10 ppm PPCA 187
Figure 6.21: Round shaped barite particles after treatment with (a) 1 ppm PPCA (b) 4 ppm PPCA (c) 10 ppm PPCA.....189
Figure 6.22: Effect of DETPMP on barium sulphate particles at concentrations (a) 1ppm (b) 4 ppm.....190
Figure 6.23: (a) Presence of growth steps, (b) Absence of growth steps and (c) Appearance of less intense steps.....191
Figure 6.24: Diagram of $BaSO_4$ main crystal faces [163] 195
Figure 6.25: Step height of (210) barite crystal face versus SI.....198

Tables

Table 2.1: Scale removal treatments [17] 11
Table 2.2: Chemical properties of $BaSO_4$ [55] 27
Table 2.3: The seven crystal systems [37] 30
Table 2.4: Crystal faces found in barite minerals 34
Table 3.1: Inorganic salts of the brines 65
Table 3.2: Composition of the Stainless Steel Cell 89
Table 4.1: Summary of the experimental session 93
Table 4.2: Composition of mixture A 95
Table 4.3: Composition of mixture B 98
Table 4.4: Composition of mixture C 115
Table 4.5: Overview of the turbidity measurements 127
Table 4.6 : ICP measurements 130
Table 5.1: Experimental overview of the *in-situ* X-ray diffraction measurements.. 135
Table 5.2: Summary of the final intensities for (212) & (031) crystal faces of Celestine barian 158
Table 6.1: Fitted equation on the experimental data during of barite deposition the first two minutes 166
Table 6.2: Fitted equation on the experimental data during linear stage of the barite deposition in the presence of inhibitors 169
Table 6.3: Slope of the linear growth of $BaSO_4$ 170
Table 6.4: Equations fitted on data recorded during the first 0.5 minutes of barite deposition 172
Table 6.5: Evaluation of the $BaSO_4$ mass formed at different growth rates 173
Table 6.6: Induction time of the bulk phase 180
Table 6.7: Characteristics of barite morphologies 188
Table 6.8: $BaSO_4$ crystal faces at 95°C 194
Table 6.9: $BaSO_4$ crystal faces at 57°C 196
Table 6.10: Inhibitors efficiency at medium supersaturation index (SI=2.64) 202
Table 6.11: Inhibitors efficiency at high supersaturation index (SI=4.32) 203

Table 6.12: Summary of the *in-situ* SXRD experimental duration.....205

List of Publications

- Eleftheria Mavredaki, Anne Neville, Ken S. Sorbie (2008), *Study of $BaSO_4$ Formation Kinetics and Inhibition Effect of Polyphosphino-Carboxylic Acid (PPCA) on Barite Formation with Synchrotron X-Ray Diffraction (SXRD)*, SPE 114039, Aberdeen

- Eleftheria Mavredaki, Anne Neville, Ken S. Sorbie (2009), *Using Synchrotron X-Ray Diffraction (SXRD) for studying the $BaSO_4$ formation kinetics and the effect of inhibitors on barite formation,* Proceedings of American Institute of Physics, International Conference on Neutron and X-ray Scattering, Kuala Lumpur

Nomenclature

R^*: radius of critical nuclei

J_n: nucleation rate (cm^{-3} s^{-1})

ΔG_{cr}: free energy change for the critical cluster size formation (J $mole^{-1}$)

A: frequency constant (cm^{-3} s^{-1})

k: Boltzmann constant

T: absolute temperature (K)

σ: interfacial tension (J m^{-2})

β: shape factor

V_m: molecular volume (cm^2 $mole^{-1}$)

f: correction factor

R: gas constant (8.314 J $mole^{-1}K^{-1}$)

SI: supersaturation index

$t_{induction}$: induction time (s)

E_a: activation energy (J mol^{-1})

B: slope of the plot $logt_{induction}$ and $1/(SI)^2$

N_A: Avogadro number ($6.02214179 \times 10^{23}$ mol)

W_{121}: work of the adhesion (N m^{-1})

F(z)/A: integral of the force per unit area between the surfaces in the medium

γ_{12}: interfacial tension (J)

SI: supersaturation index

a: ion activity

K_{sp}: solubility product (M^2)

ΔH^-_{lat}: lattice enthalpy (kJ/mol)

$\Delta H^-_{hyd.}$ hydration enthalpy (kJ/mol)

Δf: measured frequency shift (Hz)

f_o: resonance frequency (Hz)

Δm: the mass change (μg)

A: effective area of the electrode (m^2)

μ_q: shear modulus of the quartz (2.947×10^{11} g cm^{-1} s^{-2})

d_q: quartz density (2.648 g cm^{-3})

f_0: frequency of oscillation of unloaded crystal (Hz)

ρ_L: density of liquid in contact with the electrode assess (g cm^{-3})

η_L: viscosity of the liquid in contact with the electrode (g cm^{-1} s^{-1})

A_0: maximum vibration amplitude

δ: penetration depth = $(n_L/\pi f_0 \rho_L)^{1/2}$

n: interger number

λ: wavelength (nm)

2a: distance (nm)

d: distance between atomic planes

θ: angle of incidence of the x-ray beam and the atomic planes (°)

k_c: rate constant for crystallization (l^2 mol^{-1} min^{-1} m^{-2})

s: function of number of active growth sites on the added seed crystals

m: concentration of barium sulphate at time t (M)

m_0: concentration of barium sulphate at equilibrium (M)

CHAPTER 1 Introduction

1.1 Oil through the ages

The history of oil illustrates the world history. The actual age of the oil recovered today is 300 million years when the earth was totally covered by plants. The initial references to oil from the human kind are known from Herodotus scripts at 450 BC, where the presence of oil pits near Babylon was reported.

This type of fossil fuel has been kept in different layers of the earth and its initially slow consumption by people started in order to cover basic needs like the street lighting. The amount of energy than can be released when oil is burned was until then unknown. To common knowledge the first oil drilling took place in China in 347 AD, where the oil was extracted by bamboo pipes and the depth of the drilling approached 800 feet. One of the first wells that produced oil which was further marketed was drilled near Marietta in Ohio, in 1814. The real purpose of the drilling was extraction of salt water, hence at that point the drilling of oil was considered as useless and undesirable as often the well was spoiled by the oil [1]. Yet even unexpectedly that was the start of the upcoming revolutionary changes in the global scene making the transition from agricultural to industrial life real.

Nowadays oil is one of the consumables that guides the global economy, thus its political and social impact is dominant. Almost all the aspects of the daily human life are related to the use and consumption of the oil. In order to satisfy the need for oil, the extraction of oil has been kept constant by the oil industry for the last decades.

The most common production mechanism for oil recovery involves consumption and production of high amounts of water. The oil production is characterized by

three recovery phases which are the primary, secondary and tertiary or enhanced oil recovery [2].

During the primary recovery the natural pressure of the reservoir drives oil into the wellbore. Then artificial lift techniques such as pumps bring the oil to the surface. The oil production during the primary recovery is very low (around 10% of the total production).

The secondary recovery consists of the main area of concern. This stage involves injection of water or gas which drives the oil into the wellbore. In case of simultaneous production of natural gas with the oil, the gas is re-injected in order to maintain reservoir pressure. The secondary recovery oil production path produces high amounts of water characterized by high temperature, high salinity and high substance in organic compounds. The water must be treated before its reinjection into the reservoir and further use or disposal into the sea.

The tertiary or enhanced oil recovery involves actions that take place after the secondary recovery in order for production to be increased. Changes in temperature or pressure and/or addition of gases, chemicals, microbes, heat, or even the addition of energy, such as the stimulation of the oil through vibration energy can cause production enhancement. The challenge during the enhanced oil recovery is to recover the oil which is located in difficult to access regions and in the pores where it is held by capillary pressure.

The consumption of high amounts of supersaturated water results in promotion of the three problems that characterize both the oil industry and the desalination plants. The diagram in Figure 1.1 shows the three dimensions of the problem.

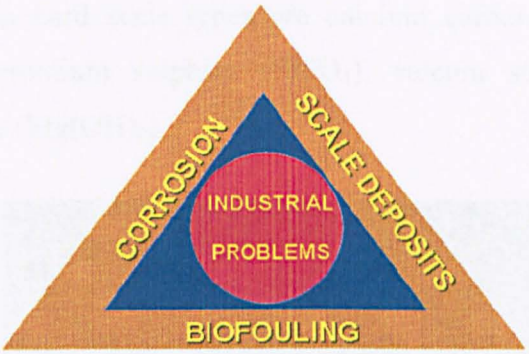

Figure 1.1: Diagram of the three main industrial problems [3]

Corrosion is one of the most well known industrial problems and it occurs in the parts of the industrial equipment where the metal of the surfaces reacts with the water and the oxygen [4]. The corrosion phenomena are favoured in the areas where scale deposit has already occurred. Under deposit corrosion the metallic surfaces start to oxidize until they are completely damaged.

Biofouling occurs due to the presence of microorganisms in the fresh injected water or in the flowing air of the system [5]. The biofouling development is favoured by the conditions of the system like the presence of organic compounds which are treated as nutrients by the microorganisms. Biofouling enhancement results in problems in the flow rate of the brines and in ineffective heat exchange.

Scale precipitation, like corrosion and biofouling can cause major operational problems and it occurs when the seawater is injected into the reservoir and is being mixed with the formation water. The hard inorganic salts form due to the chemical incompatibility of the reservoir formation water and the injected seawater [6]. Usually the same seawater is used in many injection circles during the secondary oil recovery, so it becomes highly supersaturated in ions subsequently the formation of inorganic scale is further promoted.

The most common hard scale types are calcium carbonate ($CaCO_3$), barium sulphate ($BaSO_4$), strontium sulphate ($SrSO_4$), calcum sulphate ($CaSO_4$) and magnesium hydroxide ($Mg(OH)_2$).

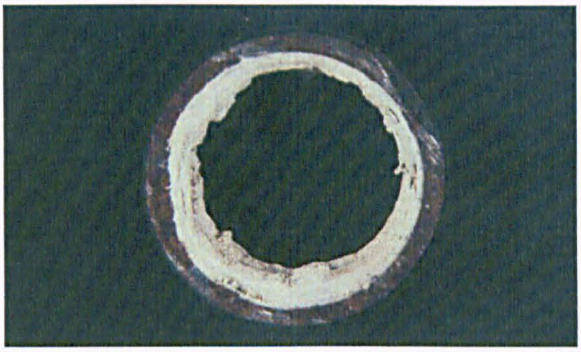

Figure 1.2: Scale formation in pipe

Many problems in the oil fields are due to high concentration of sulphates in the water. It is worth noting that the concentration of sulphates in the Gulf seawater in Saudi Arabia approaches the value of 4,450 mg/l [7]. In addition the produced waters from Arabian Gulf oil fields contain excessive concentrations of divalent cations (barium, calcium and strontium). Thus any injection of seawater without selective removal of sulphates would lead to substantial sulphate scale formation mainly in the forms of barium sulphate ($BaSO_4$) calcium sulphate ($CaSO_4$) and strontium sulphate ($SrSO_4$).

1.2 Scale

In this study the main focus is the formation of scale as a deposit at the surface of components. The deposition of the inorganic salts that compose the adherent scale may occur wherever mixing of incompatible brines takes place. Thus the potential parts of the oil plant where scale builds up are [8]:

1. At the surface water injection facility
2. In the injection well
3. Downhole in the reservoir

4. At the connection of a branched zone
5. At the manifold of a producing zone
6. At topside facilities
7. At disposal wells

The extent of mixing, the amount of the deposited scale, the impact on flow and also the difficulty or effectiveness of the inhibition or removal may be different for each of these parts mentioned above.

Even for cases where reverse osmosis membranes are used, problems due to scale formation occur. The only difference is that inorganic scale is formed on the reverse osmosis membranes when these technologies are applied to surface, ground and water sea sources. The formation of high amounts of scale decrease the permeability of the reverse osmosis membrane [8]. This results in higher feed pressure in order to maintain the productivity and recovery and hence an increase in differential pressure across the membrane occurs.

The formation of scale is critical problem for the performance and the life duration of a well. Extensive formation of scale results in shutting down the oil plant until the equipment is repaired or replaced. This procedure is costly for an oil company since the amounts of money for the new equipment are high and most important the company is temporarily out of the production.

1.3 Scale treatment

The oil fields are treated as separate cases since the quality of the injected water varies according to geographical position of the oil plant. Different composition of the injected waters results in different treatment of the oil field. Generally the given oil field economical value represents the value of the injected water. In the cases of 'ill-planned' water injection operations, the economical value usually is a liability [9]. This is due to the costly scale remedial workovers, the high environmental

impact and health hazard, the reduction in the productivity index, the deferred oil production and the permanent formation damage, which results in ultimate well shutdown. An accurate estimation of the global cost for these 'ill-planned' water injection systems gives a price of $50 billion per year [9]. On the contrary in the case of 'well-planned' water injection systems the recovery is always better. The formation damages, the remedial workovers and the environmental impact are minimal. This type of water injection systems generates additional revenue rather than cost.

The use of antiscalants has been promoted for the last decades as the most effective treatment to the constant rising scale problems. The number of scale inhibitor families used so far is high as the need for tracking the most effective chemical additive becomes bigger. However many of the known inhibitors contain elements like phosphorus and nitrogen [10,11] which make them hazardous. Thus the effort now is turned on (i) identifying the minimum effective concentrations of inhibitors and (ii) using benign and environmentally friendly compounds [12]. By identifying the minimum inhibition concentration, the proper treatment of an oil field is ensured and the danger of mistreating or overtreating the well by using the wrong amount of antiscalant is avoided. As far as the treatments with environmentally friendly inhibitors, they are domain of active research. Most antiscalants have been reported to promote biofouling. This is due to their designed biodegradability in order to result in more environmentally favourable concentrate disposal [8]. However the new developed antiscalants although being biodegradable do not give rise to biofouling. The OSPAR commission has adopted the protocols on methods of testing the chemicals used in the off-shore industry [13]. According to the protocols the eco-toxicological characteristics of the substance should not meet 2 of the 3 following criteria:

- Biodegradation $< 60\%$ in 28 days
- Bioaccumulation potential (or log Pow) ≥ 3

- Toxicity level of lethal concentration (LC_{50}) or effect concentration (EC_{50}) < 10 mg/l

Furthermore full OSPAR data sets on the algae, crustacean and fish or sediment reworker tests are required.

1.4 Objectives

This study is dealing with the formation of barium sulphate ($BaSO_4$) also known as barite in supersaturated brine. Barite is used in many daily applications as pigments in paints, fillers, in coatings and as radiocontrast agent for X-Ray imaging [14]. However for the oil industry it brings major operational problems due to its spontaneous precipitation and deposition on surfaces. Barium sulphate is only slightly soluble thus its removal with mechanical and chemical methods is hard. Probing into the barite formation processes on a surface is a challenge as has been shown in past work.

The specific objectives of this study are to:

- Follow the kinetics of barium sulphate formation on a surface during the initial stages. So far barium sulphate studies have taken place focusing mostly on the bulk phase although scaling as a problem is directly linked to the formations of inorganic salts on surfaces. Thus the results presented in this thesis are referring to the formation of barite on metallic surfaces. The main objective of this study is to determine the kinetic processes during the early stages of precipitation and deposition on a surface as they consist crucial stage for the following growth of the barite scale.

- Determine the mechanisms by which the barite scale forms and grows on the surface under different supersaturation index conditions. It is known that

different supersaturation index levels result in different $BaSO_4$ growth mechanism. Hence three supersaturation index levels have been examined in order to examine the supersaturation index effect on the formation of barite.

- Investigate the effect of two inhibitors on the formation kinetics of barium sulphate. Once scale is encountered beyond the ability of any type of chemical treatment in a given field, mechanical drilling or reaming is the remedial measure regardless of the scale types. Since the best way to avoid sulphate scale is to prevent it from forming, the interpretation of the inhibitors effect on barite formation is a key point.

- Determine the crystallographic nature of barium sulphate in the presence and absence of the inhibitors. Probing into the crystallography of the formed scale on a surface is dominant for understanding; (i) which lattice planes of $BaSO_4$ are pronounced during the growth process (ii) what is the inhibitors effect on these pronounced crystal faces of barium sulphate and (iii) identify the mechanisms of the inhibitors.

1.5 Thesis layout

In this chapter an introduction to the scale field is given and further the objectives of this study are presented.

In Chapter 2, a constructive review on the scale formation processes and on the inhibition as scale removal treatment is presented. The focus is turned on the case of barium sulphate scale type.

Chapter 3 refers to the techniques and materials that were used for this study. The experimental set ups and the methodologies are described in detail.

In Chapter 4 the results received regarding the kinetics of barium sulphate formed in the presence or absence of inhibitors with Quartz Crystal Microbalance are presented. Also the topography of the adherent barite deposits is presented, as it was recorded with the Atomic Force Microscope.

Chapter 5 is dedicated to the data recorded during the *in-situ* X-ray diffraction measurements. The formation of $BaSO_4$ was followed *in-situ* under uninhibited and inhibited conditions, at high temperatures.

Discussion on the results presented in the two previous chapters and how these results contribute to the understanding of this goal is given in Chapter 6.

Chapter 7 and Chapter 8 are referring to the conclusions of this study and the recommended future work.

CHAPTER 2 Theory and literature review on scale formation and inhibition; The case of barium sulphate

2.1 Introduction

Scale is defined as the formed layer of inorganic salt built up on a solid surface. The most common sulphate inorganic salts are barium sulphate ($BaSO_4$), strontium sulphate ($SrSO_4$) and calcium sulphate ($CaSO_4$). The simultaneous co-precipitation of two, and less often three sulphate minerals occurs when the formation water is mixed with the injected seawater in the reservoir [15].

Another problematic scale type in the oil industry and in water desalination plants is calcium carbonate ($CaCO_3$). The formation of calcium carbonate is inevitable when HCO_3^- is present in the reservoir. Inorganic salts containing iron, and more specifically iron carbonate ($FeCO_3$), iron sulphides (FeS, FeS_2) and iron oxides ($Fe(OH)_2$, Fe_2O_3, Fe_3O_4) are also well known scale types forming at the oil industry surfaces.

The scale deposits adhere on the surfaces of the producing well tubing and on parts of water handling equipment. The mineral scale builds up in time and leads to problems in reservoirs, pumps, valves and topside facilities [15]. Moreover the deposition/adhesion takes place in heat transfer equipment such as boilers and heat exchangers. Thus a decrease in the performance of the heat exchanger as well as reduction in flow rates occurs [16]. The increase of the deposits in time leads to inevitable damage of the equipment parts. As a consequence, suspension of oil operations is necessary for the recovery or replacement of damaged parts. In the oil field these interruptions are accompanied by extremely high costs.

Table 2.1 presents the way these scale types are formed, also if the inorganic salts are soluble in acid or not and the removal treatments which are being applied in industry despite the cost effect and the environmental impact.

Table 2.1: Scale removal treatments [17]

Type of inorganic scale	Formation	Solubility in Acid	Treatment
$BaSO_4$	Mixing of formation water (Ba^{2+}) source with injected seawater (SO_4^{2-})	NO	Na_4EDTA High-pH chelating treatment
$SrSO_4$	Mixing of formation water (Sr^{2+}) source with injected seawater (SO_4^{2-})	NO	Na_4EDTA High-pH chelating treatment
$CaCO_3$	Presence of Ca^{2+} and bicarbonate in produced water	YES	HCl (5-15%) Organic acids Na_2EDTA (up to 9%)
$CaSO_4$	Mixing of formation water (Ca^{2+}) source with injected seawater (SO_4^{2-})	NO	Na_4EDTA 'gyp converter'
$FeSO_4$	Corrosion Reactions	YES	HCl (15%) Na_2EDTA
FeS	Corrosion Reactions	Depends on the formed type	HCl (15%)
Iron Oxides	Corrosion Reactions	YES	HCl

The removal treatments that are being applied for the different forming scale types are based on the use of high amounts of inhibited hydrochloric acid (HCl) and

more commonly on the addition of organic acids. Also ethylenediaminetetraacetic disodium or tetrasodium salts (Na_2SO_4 – Na_4SO_4) perform as chelators. The cost of these treatments is high and more important the environmental impact is even higher. The most effective approach of preventing scale formation seems to be the treatment of the water with chemical scale inhibitors [18]. Inhibition of mineral scale formation is characterized by low cost compared to other removal approaches and it is also the most effective method [19]. In order for the inhibition to be successful, the complexity of the scaling system needs to be fully understood.

Thus for complete investigation of the scaling system processes, it is necessary for all the aspects of the system to be considered. First the precipitation that occurs in the bulk phase of the system must be studied followed by the deposition of the scale on the surface [20]. The stages of the surface deposition process during the scale formation are; (1) nucleation of the crystals, (2) growth of the crystals at the surface site and finally (3) adhesion of crystals.

2.2 Precipitation stages

2.2.1 Nucleation

After the mixing of formation water and seawater, the supersaturated formed solution is characterized by a number of minute solid bodies, embryos and nuclei or seeds. This stage is known as bold nucleation and it occurs before the development of crystals in the solution. Nucleation may occur spontaneously or it may be induced artificially and is characterized as primary or secondary [21].

2.2.1.1 Primary nucleation

Primary nucleation is distinguished into homogenous and heterogeneous nucleation. Homogeneous nucleation occurs when nuclei of the solute are formed in perfectly clean solutions in the absence of foreign surfaces [22]. Homogeneous nucleation is dominant at high supersaturation ratio and it describes the spontaneous formation of critical nuclei within the supersaturated solution [8].

The formed critical nuclei with radius R* continuously grow in the supersaturated environment as the total free energy decreases (Figure 2.1). During homogeneous nucleation the precipitate formations are not adherent on the surface [23].

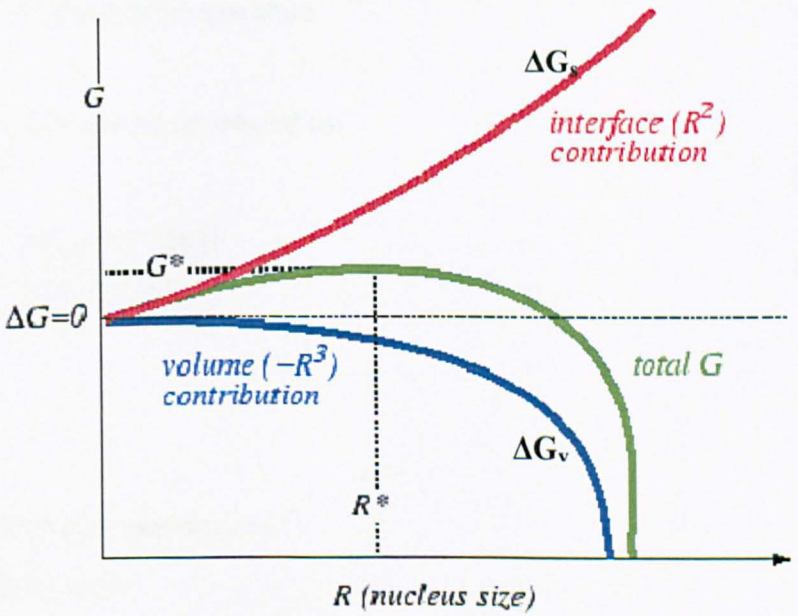

Figure 2.1: Free energy diagram of nucleation

Heterogeneous nucleation is principally an extension of homogeneous nucleation. This type of nucleation occurs when certain solid bodies extraneous to the system, promote phase transformations, particularly condensation and crystallization [22]. At the presence of suitable, foreign bodies or surfaces, nucleation can be induced at

degrees of supersaturation ratio lower than those required for homogeneous nucleation.

Two important parameters which characterize the nucleation process are (i) the free energy change and (ii) the rate of nuclei formation. The nucleation rate J_n according to Arrhenius is given by the following equation [24]:

$$J_n = A \exp\left[-\frac{\Delta G_{cr}}{kT}\right] \qquad \textbf{Equation 2.1}$$

Where ΔG_{cr}: free energy change for the critical cluster size formation

A: constant

k: Boltzmann constant

T: absolute temperature

Equation 2.1 can also be expressed as:

$$J_n = A \exp\left\{-\frac{\beta V_m^2 \sigma^3 N_A f(\theta)}{(RT^3)(2.3SI)^2}\right\} \qquad \textbf{Equation 2.2}$$

Where:

σ: interfacial tension (J m^{-2})

β: shape factor

V_m: molecular volume (cm^3 $mole^{-1}$)

f: correction factor

R: gas constant (8.314 J $mole^{-1}$ K^{-1})

T: absolute temperature (K)

SI: supersaturation index

For homogeneous nucleation the correction factor f(ϑ) (Equation 2.2) is equal to 1 and for heterogeneous nucleation is less than 1 [25]. The variations in the values of f(ϑ) confirm that the crystallization on surfaces or in the presence of impurities requires less interfacial area.

2.2.1.2 Secondary nucleation

Secondary nucleation is the other dominant mechanism of nucleation and its main characteristic is the increasing nucleation rate (Figure 2.2) [26]. Due to the small particles sizes the secondary processes can be very fast and can occur even at the early stages of particle formation in competition with the primary processes [27]. Secondary nucleation usually occurs in the presence of crystals of the material being crystallized. Depending on the processes that take place, secondary nucleation occurs through aggregation or Ostwald ripening phenomenon.

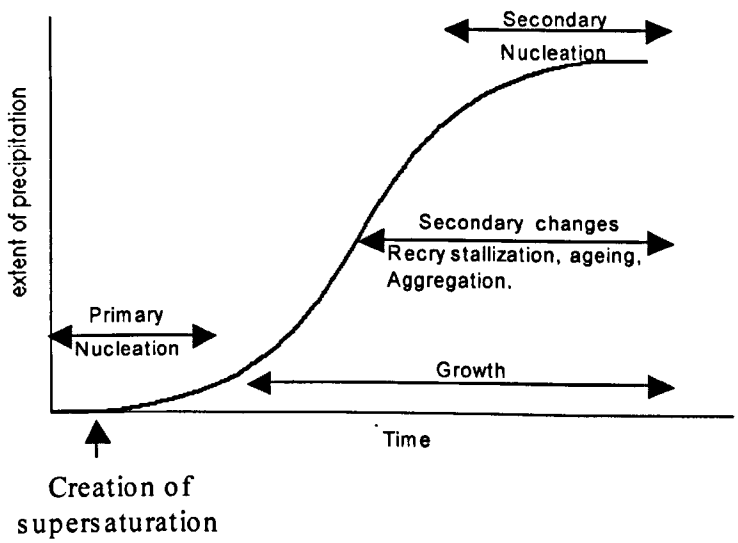

Figure 2.2: Kinetic stages involved in precipitation [21]

During aggregation formations the already existing crystals induce the formation of new crystals by shedding crystal dust from the surface or by a crystal fragmentation following a collision [28]. This type of nucleation involves the dislodgment of nuclei from the parent crystal at supersaturation index levels at which primary, heterogeneous nucleation would not occur.

Ostwald ripening phenomenon consist another solvent-mediated recrystallization process, which depends on the presence of a favourable difference in interface energy as driving force. Due to this phenomenon an increase in the characteristic size of the scale of a multiphase microstructure occurs within the time [29]. Ostwald ripening as phenomenon is important in many solidification and heat treating processes as it influences the size scale and the properties of the processed material. Driving force of the ripening process is the reduction of the excess free energy associated with interfaces in a multiphase system. During the Ostwald ripening stage, the Gibbs – Thomson effect becomes significant [30]. What actually happens is dissolution of smaller clusters as they become thermodynamically unstable followed by transfer of their mass to larger clusters, which manage to grow.

For $BaSO_4$ precipitation, the secondary nucleation has been previously identified [27]. It was determined that the nucleation and the molecular growth of barium sulphate were followed by secondary processes such as aggregation. Ordered aggregation was responsible for the porous internal structure, whereas molecular growth was responsible for the regular surface. Evidence of the characteristic aggregation during the secondary stage of $BaSO_4$ nucleation, was the formation of particles consisting of nanocrystallites. At the end of the precipitation these formations were turned into perfectly monocrystalline. The formation of barium sulphate aggregations has been confirmed by Schwarzer *et al.* who further used the aggregation kinetics for simulations [31]. The developed model was tested positively for different values of ionic strength, size of the primary particles as well as different pH values.

2.3 Induction time and calculation of thermodynamic quantities

The induction time is defined as the time elapsed between the creation of supersaturation and the first appearance of the new crystal solid phase, ideally nuclei with critical cluster size dimensions [8]. According to Söhnel and Mullin the induction time can not be experimentally measured as it is not possible to detect the formation of critical nuclei [32]. In order to perform successful measurements the examined nuclei must grow until they reach a detectable size.

Induction time is usually determined by measuring the variations in the turbidity of the solution [33,34]. Tantayakom *et al.* determined the turbidity at pre-established intervals and the measurements provided details about the early stages of the spontaneous precipitation [19]. The main concern was to examine the performances of the inhibitors in a function of time through these turbidity measurements. When effective inhibitors were present an increase in the induction time (t_{ind}) was expected. The aim is to prolong the induction time, so then the heat transfer resistance remains small and the nucleation takes place at localized sites.

Calculations of induction time offer the basis for estimation of two characteristic thermodynamic quantities [35]. Dependence of $t_{ind.}$ on the temperature (Equation 2.3) allows evaluation of the activation energy for nucleation. The activation energy for barium sulphate nucleation is given by Equation 2.4 [26]. Furthermore dependence of $t_{ind.}$ on the supersaturation index allows the determination of the interfacial tension between the crystal and the aqueous solution (Equation 2.5). Calculating the interfacial tension of a solid phase within the solution is difficult whether the calculations are based on theoretical predictions or experimental data. Using the induction time for determination of the interfacial tension value is the most reliable way.

For $BaSO_4$ scale precipitation, the estimated value of interfacial tension was 79 mJ m^{-2} in 1 M NaCl solution (25°C) and the activation energy value was equal to 41 kJ/mol [25]. The equations that lead to calculations of the above mentioned quantities are the following:

Induction time:

$$\log(t_{induction}) = A + \frac{B}{T^3(\log\sigma)^2} \qquad \textbf{Equation 2.3}$$

Where A is constant and B the slope of the plot ($\log t_{ind}$ and $1/(SI)^2$).

Activation energy:

$$\log\left(\frac{1}{t_{induction}}\right) = A_1 - \frac{E_a}{2.3RT} \qquad \textbf{Equation 2.4}$$

Where A_1 is constant.

The interfacial tension is calculated through Equation 2.5 and all the parameters are known from the Equation 2.2.

Interfacial tension:

$$B = \frac{\beta\sigma^3 V_m^2 N_A f}{(2.3RT)^3} \qquad \textbf{Equation 2.5}$$

The induction time of barium sulphate precipitation has been determined with a stopped flow technique under a high supersaturation ratio [36]. The Durrum stopped flow mixing apparatus was used and measurements of the intensity of the beam light, which passes through the mixing chamber took place. These measurements resulted in calculations of the induction time in the range of 5 miliseconds to 30 seconds. As the initial concentration of barium sulphate was decreased, the number of the nuclei and respectively the induction time was also decreased.

The determination of the induction time allowed the calculation of the interfacial tension of the formed barite. The interfacial tension of barium sulphate was calculated according to the theory of Nielsen and Söhnel and was found equal to 83 mJ/m^2, when the growth unit of barite was equal to 25.9 cm^3/mol.

2.4 Crystal growth

Crystal growth as a process is based on the formation of particles larger than the critical size in the supersaturated solution. During this stage of the precipitation the particles grow into crystals of visible size. The growth process actually starts when the transport of solute to the crystal solution interface takes place [37]. Afterwards the adsorption of the solute at the surface and the incorporation of the crystals constituents into the lattice are the main stages of the process. The crystal growth theories are divided in (a) surface energy theories (b) adsorption layer theories and (c) screw dislocation theory. All of these theories although they are strongly established do not take into account the actual surface structure and the attachment energies on specific surface sites [38].

2.4.1 Surface energy theories

The beginning of the surface energy theories was made by Gibbs in 1878, when he suggested that the total free energy of a crystal in equilibrium with its surroundings at constant temperature and pressure would be a minimum for a given volume [37]. If the crystal grows due to favorable supersaturation conditions then it should be developed into an equilibrium shape. Hence the lattice planes should emerge in a manner that the total free energy is kept to a minimum for a given volume. In 1901 Wulff further suggested that the crystal faces would grow at rates

proportional to their respective surface energies hence the equilibrium shape of the crystal is preserved [39]. This suggestion was proved 50 years later by Herring.

Experimentally this theory seems to be incomplete as in many cases it has been proved that the crystals do not maintain the geometric similarity during the growth. What actually happens is that the small faces which grow faster compared to the rest faces gradually disappear (overlapping mode) as shown in Figure 2.3.

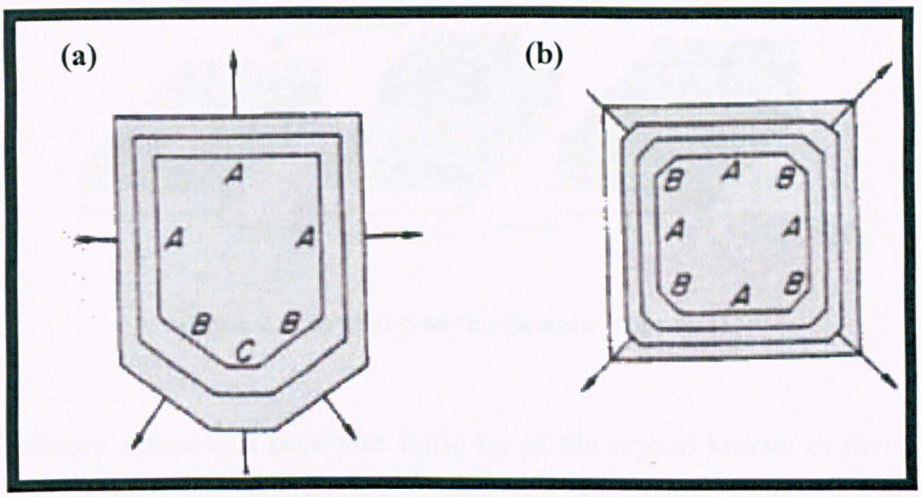

Figure 2.3: Growth of crystal faces (a) maintenance of the crystal faces and (b) overlapping [37]

2.4.2 Adsorption layer theories

According to this growth mechanism established by Volmer and Gibbs the initial stage of crystallization is based on a surface diffusion process. The crystallizing substances approach the crystal face but they are not directly integrated into the lattice. The molecules which have the trend to be adsorbed are held at fixed lattice points [28]. Transfers of the adsorbed molecules to the next lattice points can be obtained in time as transfer of the molecules across the whole surface. Thermodynamically these substances lose one degree of freedom and are free to migrate over the crystal surface. In time these crystallizing units compose an

adsorbed layer at the interface resulting in equilibrium between this new formed layer and the bulk solution.

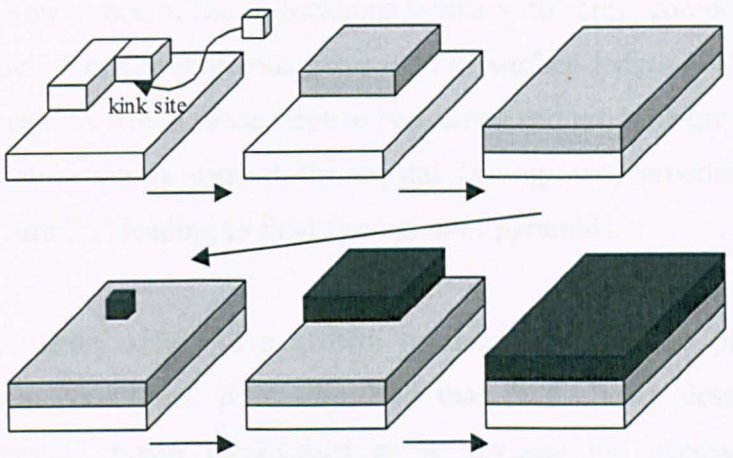

Figure 2.4: Crystal growth schematic diagram [37]

This theory refers to a step-wise build up of the crystal known as the birth and spread model [40]. As presented in Figure 2.4 the growth units are most easily incorporated into the crystal at a kink. As the kink moves along the step with further mergence of other growth units, the advancement of the molecular steps occurs

In order for a new layer to further commence on the already formed face, there must be an 'active' crystallization centre which is going to promote the growth process. According to the theory a monolayer island nucleus otherwise called two-dimensional nucleus, is created and plays the role of the active centre for the surface nucleation. The two-dimensional nucleation occurs on the pre-existing surface at high local supersaturation ratio.

2.4.3 Dislocation theory

In 1951 Burton, Cabrera and Frank contributed significantly to the crystal growth theories with the BCF theory, named with respect to their names. The BCF theory refers to the emergence of the dislocations points with screw components at crystal surfaces, which acts as continuous generators of surface ledges [41]. Most crystals contain dislocations which cause steps to be formed and promote growth. As soon as the screw dislocation is formed the crystal face grows perpetually as a spiral staircase (Figure 2.5) leading to final formation of pyramids.

The BCF theory refers to a growth mechanism that takes place under low supersaturation conditions. It is suggested that BCF theory describes the most dominant crystal growth mechanism as it obviates the necessity for surface nucleation.

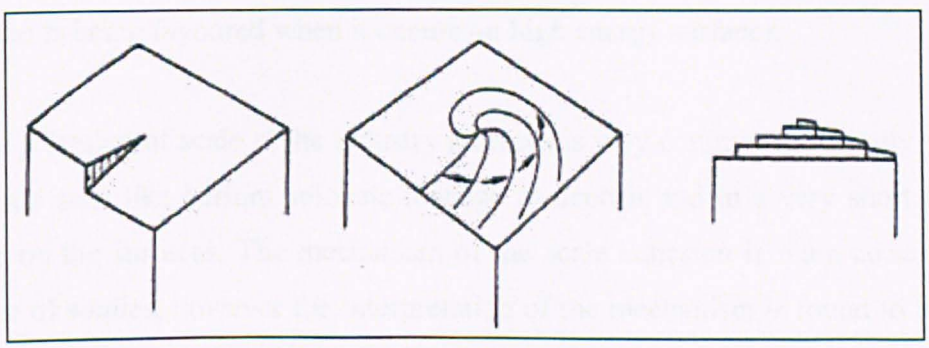

Figure 2.5: Diagram of the screw dislocation mechanism

Concerning the curvature of the developed spiral is determined by the critical radius for a two dimensional nucleus under the present supersaturation conditions of the medium where the crystal is growing. For barium sulphate the microtopographic features of the nuclei and the spiral on the barite (001) face indicate strong structural control of the growth process [38].

2.5 Adhesion

2.5.1 Description of the adhesion phenomenon

Adhesion describes the phenomenon or the state where two bodies are stuck together in relatively straightforward way [42]. The adhesion between nominally flat surfaces is strongly influenced by the roughness of the surface [43]. Hence adhesion phenomena can not be described correctly if the nature of the surface is ignored.

When adhesion occurs, the surface chemistry and the physical phenomena determine the interactions with the fluid or solid phases. For complete understanding of adsorption and further of adhesion in a specific system, is it necessary to determine the surface energetic heterogeneity, the crystal chemistry of the adsorbent and the physicochemistry of surfactants in aqueous solutions [44]. As expected, adhesion is being favoured when it occurs on high energy surfaces.

The adhesion of scale at the industry surfaces is very common. Sparingly soluble inorganic salts like barium sulphate manage to deposit and in a very short time to adhere on the surfaces. The mechanism of the scale adhesion is main concern of a number of studies, however the interpretation of the mechanism is found to be quite complicated as the phenomenon of the adhesion itself.

2.5.2 Adhesion forces

Most studies agree that the forces which are responsible for the adhesion phenomena in a liquid-solid interface are the Van Der Waals forces, Dispersion forces also known as London forces and Polar forces (Interactions dipole - dipole, interactions dipole-molecule). These types of forces consist the non electrostatic forces that result in adhesion. Concerning the electrostatic forces their presence is

essential for adhesion to occur. The DLVO theory explains the importance of the electrostatic forces.

The DLVO theory was developed in the 1940's [45]. For better understanding of the DVLO theory distinction between the lyophobic (solvent hating) and lyophilic (solvent liking) colloids must take place. According to the theory when a repulsive double layer coexists with Van Der Waals forces, then both are combined to generate a global minimum at contact between surfaces. The repulsive forces between particles belonging to the colloidal range, have an entropic origin and this is suggested that should apply to the hydration force [46].

Mizes *et al.* suggested that adhesion forces are composed of the non electrostatic and the electrostatic forces [47]. The calculation of the adhesion forces demands a well defined relation between the adsorbent material and the surface. If this is not the case then a few assumptions must take place in order for the calculation to be correct. Further strict categorization of the adhesion forces to electrostatic and non electrostatic is deficient when the roughness of the surface is changeable.

The adhesion forces have been measured for surfaces with stable roughness. The adhesion force measurements took place with the help of Atomic Force Microscopy (AFM) and revealed that for smooth particles and smooth surfaces the adhesion force distributions were narrow [48,49]. For rough adhesion partners though, these distributions showed a much wider tension. Furthermore the AFM measurements confirmed that the magnitude of the electrostatic interaction force depends strongly on local charges in the vicinity of the contact area.

The same conclusion was supported by a different study where the adhesion between solid bodies with adsorbed layers of surfactant and polymers, was being examined [49]. Polyelectrolytes with different charge density were used and the surface observations revealed that the adsorbed low charge density polyelectrolytes were dragged along the surface during the scanning. Hence polyelectrolytes with

reduced charge density were bonded to the surface in a weak way. As for the polyelectrolytes with increased charge density, they adhered strongly at the surface. For these cases the source of the adhesion phenomenon was the electrostatic surface-polyelectrolyte-surface bridges. The adhesion force measurements revealed that thin polyelectrolyte layers are effective adhesion modifiers.

The strength of adhesion as a phenomenon can be found in the nature of the forces present when the attachment of the barium sulphate scale on the surface occurs. The existing forces during the adhesion are able to prevent the inhibitor action on the formed barite scale. Thus for the inhibition of deposition and adhesion, a balance must occur between chemical interactions with the additive and electrostatic interactions between the surface and additive. Those interactions were confirmed to control the particle and structure formation [48].

2.5.3 Methods for measuring adhesion

The fundamental methods measuring the adhesion between two surfaces are wettability, contact angle [50] and interfacial tension [46]. As wettability of a reservoir rock can be defined as the ability of one fluid to spread over the solid substrate in the presence of another immiscible fluid such as crude oil and water [51]. In addition the contact angle measures the wettability of a specific surface.

Wettability and contact angle are major parameters affecting the heterogeneous nucleation stage during precipitation. As it has been determined for adhesion phenomena, increase of the contact angle corresponds to reduced wettability. Subsequently the induction period is increased as the nucleation rate is lower. According to the above increase of contact angle results in reduce of scale formation. However measuring the contact angle as a method, seems weak when actual crude oils and core samples are used. The contact angle measurements do not consider the effects of roughness and heterogeneity [50].

Further interfacial tension is used for measuring the work of the adhesion between two similar materials in a medium [52]. The work of the adhesion is defined as the work done on the system when two condensed phases 1 and 2, forming an interface of a unit area are separated reversibly to form unit areas of each of the interfaces.

According to Dupré equation (Equation 2.6) the work of the adhesion in a microscopic model is equal to interaction energy at contact between the two half-planes of material when the same quantity for the medium is added and the interaction energy material-medium is twice subtracted. In order to obtain the free energy the changes in entropy should be included.

$W_{121} = W_{11} + W_{22} - 2W_{12}$ **Equation 2.6**

Direct calculation of all the adhesion energies that are present when the two surfaces of the material are contacting directly can take place through the equation:

$$W_{121}(\text{contact}) = -1/A \int_{\delta_c}^{\delta_m} F(z)dz + 2\gamma_{12}$$ **Equation 2.7**

Where F(z)/A: integral of the force per unit area between the surfaces in the medium

γ_{12}: interfacial tension

At contact the interaction free energy is dominated by the electrostatic and dispersion interactions across the interface. For both cases the interfacial tension is related to the work of adhesion as:

$2\gamma_{12} = W_{121}$ **Equation 2.8**

2.6 Barium Sulphate

2.6.1 Chemical properties of $BaSO_4$

Barium sulphate is formed after formation water and seawater are mixed. The reaction between Ba^{2+} and SO_4^{2-} is spontaneous and is described with the Equation 2.9.

$$BaCl_2 + Na_2SO_4 \rightarrow BaSO_4\downarrow + 2NaCl \qquad \textbf{Equation 2.9}$$

The produced inorganic salt is white crystalline solid [53] (Figure 2.6) with low porosity and its basic chemical properties are summarized in the Table 2.2.

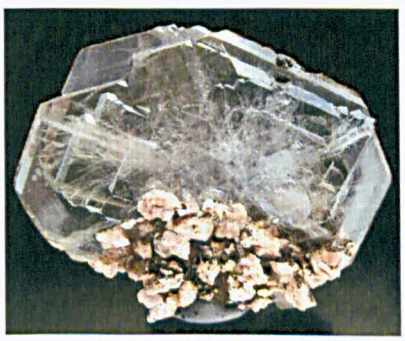

Figure 2.6: Barium sulphate mineral [54]

Table 2.2: Chemical properties of $BaSO_4$ [55]

Chemical Formula	$BaSO_4$
Molecular Weight	233.43
Density	4.5 g/cm^3
Solubility	2.33 mg/l
Melting Point	1580 °C

The solubility of barium sulphate is influenced by the biological activity in aquatic deposition processes [11]. Studies of aquatic sediments and terrestrial subsurface sediments suggested that the biological activity plays important role in modulating the solubility of barium sulphate. Due to the insolubility of the formed barite, several mechanical and chemical approaches for preventing or to removing scale seem useless during the recovery of the facilities and surface treatments. Even chemical treatment of the adherent barite with acid seems ineffective.

The extreme low solubility of barium sulphate is due to the high energy bonds which are found between the Ba^{2+} ions and SO_4^{2-} ions belonging to the first coordination sphere [56]. There are no Coulombic interactions in the sulphate ion itself [57]. None of the reactant species Ba^{2+} and SO_4^{2-} undergo any direct oxidation in water environment or when other elements are present [58]. Since the bonds between the barium and sulphate ions are very strong their formation is difficult to be retarded.

The mass composition of $BaSO_4$ is 58.84 % barium, 13.74 % sulphur and 27.42 % oxygen. The infrared spectra (IR) of barium sulphate in powder state (Figure 2.7) provides a better element analysis of $BaSO_4$ [59]. The main adsorption band of barium sulphate is in the range of 1000 cm^{-1}.

Regarding the hazardous aspects of barium sulfate scale, it has shown potential to contain co-precipitated and enriched radium, which results in the occurrence of naturally formed radioactive materials [34]. The radioactivity of the barium sulphate scale in combination with the extreme insolubility makes the barite one of the most hazardous inorganic salts. Concerning barite toxicity levels the guidelines for drinking water give maximum limitation at 2 mg/l [60].

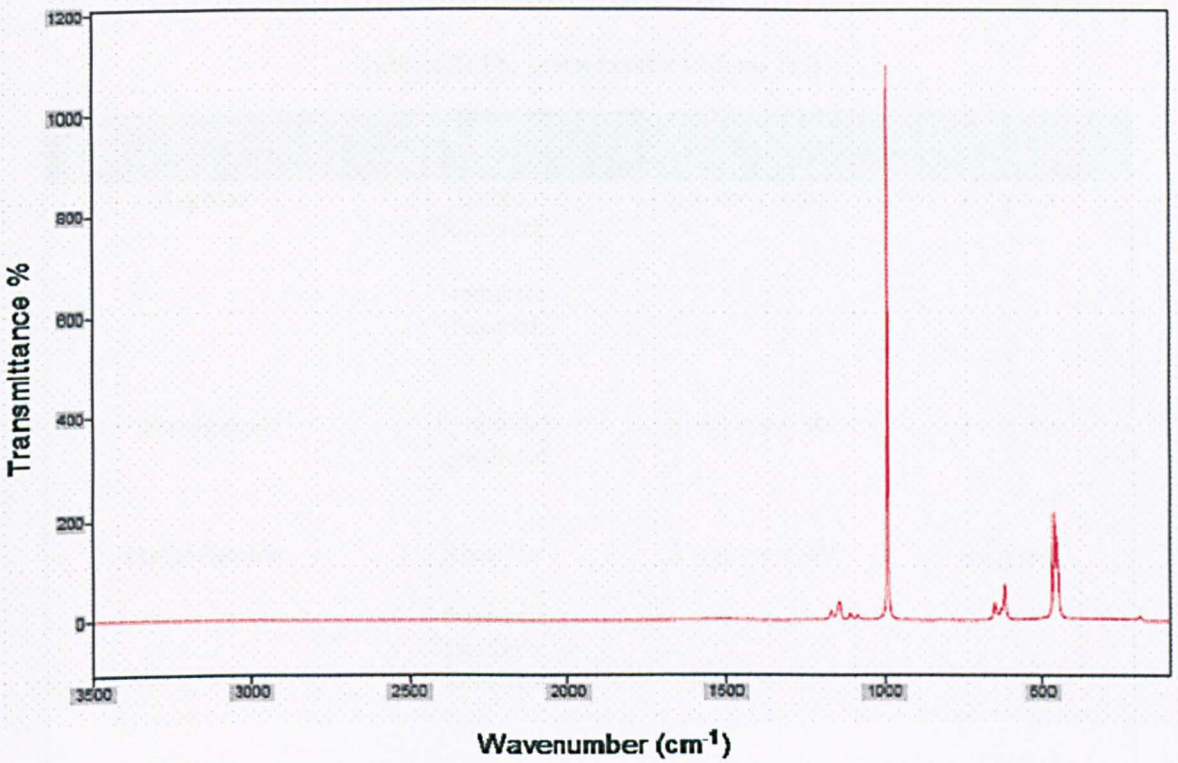

Figure 2.7: IR spectra of $BaSO_4$ [61]

2.6.2 Crystallography of $BaSO_4$

2.6.2.1 Introduction

Barium sulphate morphologies are found in nature as chemical compounds in the shape of solid polyhedrons bounded by definite planes. Hence $BaSO_4$ formations are crystals with shape and symmetry based on an internal atomic arrangement extending in three dimensions in an orderly way. Deeper analysis of the barium sulphate crystals reveals the formation of orthorhombic structures [22]. This is the only crystallization phase of barium sulphate than can be found in nature. On the contrary other types of inorganic scale like calcium carbonate exhibit polymorphism during crystallization [62]. All the existing crystal systems are presented in Table 2.3.

Table 2.3: The seven crystal systems [37]

System	*Other names*	*Angles between axes*	*Length of axes*
Regular	Cubic Octahedral Isometric Tesseral	$\alpha = \beta = \gamma = 90°$	$x = y = z$
Tetragonal	Pyramidal Quadratic	$\alpha = \beta = \gamma = 90°$	$x = y \neq z$
Orthorombic	Rhombic Prismatic Isoclinic Trimetric	$\alpha = \beta = \gamma = 90°$	$x \neq y \neq z$
Monoclinic	Monosymmetric Clinorhombic Oblique	$\alpha = \beta = 90° \neq \gamma$	$x \neq y \neq z$
Triclinic	Anorthic Assymetric	$\alpha \neq \beta \neq \gamma \neq 90°$	$x \neq y \neq z$
Trigonal	Rhombohedral	$\alpha = \beta = \gamma \neq 90°$	$x = y = z$
Hexagonal (four axes are necessary for description of the system)	None	z axis is perpendicular to the x, y and u axes, which are inclined at 60 °	$x = y = u \neq z$

Barite crystallizes in the orthorhombic system (system Pnma) with a typical unit cell as shown in Figure 2.9. Generally the distances between the unit cells in a crystal lattice are constant and they are known as lattice parameters. For barium sulphate the lattice parameters are a= 8.88 Å, b= 5.46 Å and c= 7.15 Å [63].

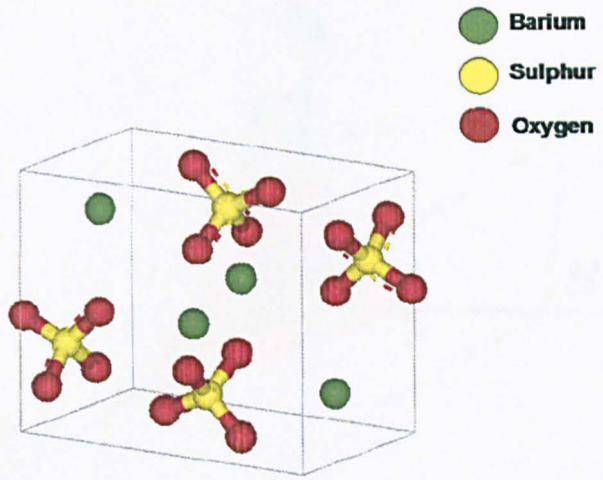

Figure 2.8: Unit cell of barite

In the barite structure the sulphur and two oxygen atoms of each SO_4 tetrahedron lie on mirror plane. The other two oxygen atoms are placed in an equal distance above and below the plane. Ba^{2+} ions are characterized by ionic radius equal to 1.35 Angstroms and they lie on the same mirror plane. Ba^{2+} ions are also in 12-fold coordination with oxygen atoms belonging to 7 different sulphate groups.

2.6.2.2 Miller Indices

The faces of a crystal are described in terms of their axial intercepts. The axes used are the crystallographic axes which are chosen to fit the symmetry of the crystal. In 1839 Miller contributed significantly in the crystallographic characterizations as he suggested that each face and direction of a crystal could be represented by the h, k and l indices [37]. These indices are defined as shown in Equation 2.10 and the interception of the planes on the crystallographic axes is illustrated in Figure 2.9.

$$h = \frac{a}{X}, \; k = \frac{b}{Y} \text{ and } l = \frac{c}{Z} \qquad \textbf{Equation 2.10}$$

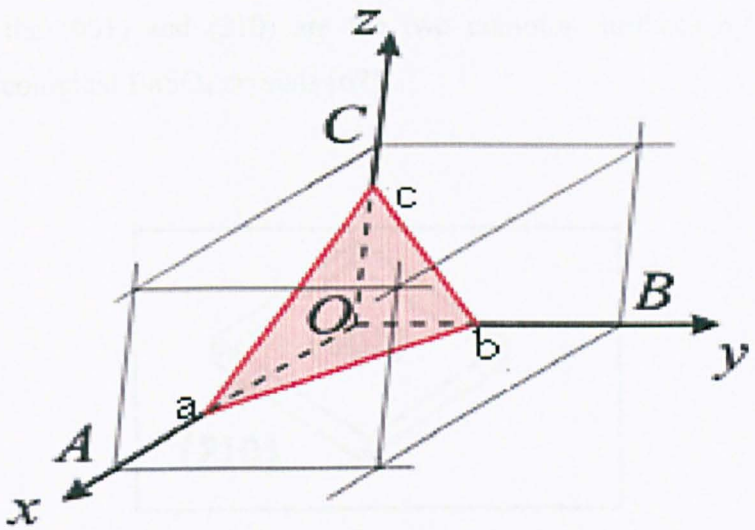

Figure 2.9: Intercept of planes on the crystallographic axes

By defining the h, k and l of each plane using the Miller indices, the (hkl) crystal face and [hkl] direction of the crystal is being determined. The crystal faces which are found to be closest packed in a crystal, are the faces with the lowest Miller indices.

The determination of the Miller indices is quite important when examining the development of crystal systems in atomic level. In a wider range the Miller indices of lattice planes and directions of the crystals is crucial as many material properties and processes vary with direction in the crystal.

Concerning the crystal faces of barium sulphate they have been determined under different conditions of supersaturation ratio after precipitating from brines containing $BaCl_2$ and Na_2SO_4. Among the growth planes of barite the (001) and (210) have proved to be the most morphologically important surfaces [64,65]. These crystal faces of barium sulphate (Figure 2.10) are dominant since they have the

lowest surface energy and thus they consist the most stable surfaces of barite [66]. Furthermore the (001) and (210) are the two common surfaces by far that are observed in geological $BaSO_4$ crystals [67].

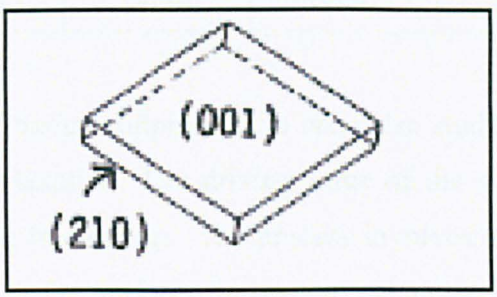

Figure 2.10: The (210) and (001) lattice plane of $BaSO_4$

As the growth of the barite particles continues, the morphology of the $BaSO_4$ crystals is being modified and new crystal faces start to grow (Figure 2.11).

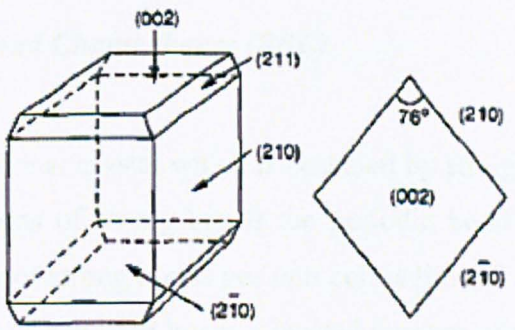

Figure 2.11: The appearance of the (002) and (211) lattice planes of barite [68]

The $BaSO_4$ crystal faces which have been identified from minerals and have been determined by statistical analysis for their dominance [69] are presented in Table 2.4.

Table 2.4: Crystal faces found in barite minerals

Barite crystal faces					
(011)	(210)	(101)	(002)	(211)	(200)
(020)	(111)	(102)	(220)	(212)	(410)
(201)	(213)	(230)	(620)	(112)	

The crystal faces of barium sulphate have been also studied and simulated under the effect of surface relaxation. The driving force of the surface relaxation is the reduction in the surface free energy. The process involves adjustments in the layer spacing perpendicular to the surface, however no changes in the symmetry of the surface neither in the periodicity parallel to the surface occur [70]. Surface relaxation studies of barite have also confirmed that the (001) and (210) lattice planes of barite consist the dominant surfaces [57]. The surface relaxation of the (001) surface is thought to be slight [67] as the energetic changes of the (001) and of the (210) due to surface relaxation, were found to be small [71].

2.6.2.3 Periodic Bond Chains theory (PBC)

For a two-dimensional crystal which is bounded by straight edges that are parallel to uninterrupted chains of strong bonds the periodic bond chains theory (PBC) is applied. The number of strong bonds per unit cell is limited thus there is a maximum length for the period of PBC and hence a limited number of PBCs [37].

Based on the PBC theory the formed faces are divided in to three categories. The minimum thickness of the elementary growth layer is named slice d_{hkl}. The faces that grow slice after slice are called flat or F-faces. The condition for the F-faces to grow is that two neighboring parallel periodic bond chains are bonded together with strong bonds. If this condition is not satisfied then no layer growth occurs hence the faces formed are the stepped ones or else S-faces. The F and S faces are presented in Figure 2.12.

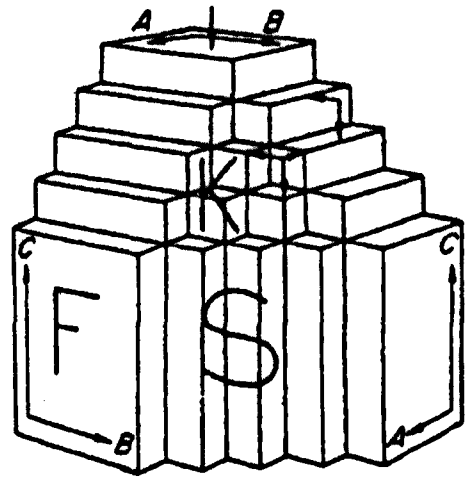

Figure 2.12: Diagram of F, S & K crystal faces [37]

The third group of formed faces is called kinked or K-faces and they grow when no PBC exists within the layer d_{hkl}. The K-faces need no nucleation for growth and they represent a generalized type of repeatable steps.

2.7 Factors affecting nucleation and crystal growth of $BaSO_4$

The crystal growth and nucleation rate depend on important factors, which highly affect the stages of precipitation. The factors are related with the characteristics of the mixing brines, the nature of the formed scale, the conditions present in the examined system and the type of the inhibitor if added during the injection of the seawater. Consideration of all the factors is necessary, in order for the study of the nucleation and growth to be complete.

2.7.1 Supersaturation Ratio

Essential condition for reactive crystallization to occur is high supersaturation ratio of the solution [72]. So far it has been determined that an increase in

supersaturation ratio leads to increasing reaction rate. The saturation ratio (SR) of the solution with respect to a crystal of barite is related to the supersaturation index (SI) according to the following equation:

$$SI=\log (SR) \text{ or } SI=\log \frac{a_{Ba^{2+}} a_{SO_4^{2-}}}{K_{sp}} \qquad \textbf{Equation 2.11}$$

Where $a_{Ba^{2+}}, a_{SO_4^{2-}}$ are the activities for Ba^{2+} and SO_4^{2-} respectively and K_{sp} the thermodynamic solubility product of the barite crystal. For $BaSO_4$ the solubility product K_{sp} is equal to 1.08×10^{-10} M^2 at 25°C [8].

For a given brine composition, the ions tend to precipitate when $\frac{a_{Ba^{2+}} a_{SO_4^{2-}}}{K_{sp}} > 1$. When the solution is not supersaturated then SI<1 and precipitation does not occur. In the case of ions equilibrium the saturation index value is equal to one [15].

The effect of temperature and concentration of the Ba^{2+} and SO_4^{2-} on the supersaturation ratio is illustrated in Figure 2.13. The diagram shows three potential zones occurring after the mixing of formation water and seawater [8]. The first zone is the stable or soluble one where the supersaturation ratio is maintained below 1, thus crystallization is impossible. There is also the metastable zone which is supersaturated and is placed between the solubility and supersolubility curves. The metastable zone is characterized by low nucleation rate thus spontaneous crystallization is improbable. However if a crystal seed is present growth will occur on it. The upper zone is the unstable-supersaturated one and it is where crystallization occurs. The supersaturation level is the driving force for the ions to bond and form inorganic particles.

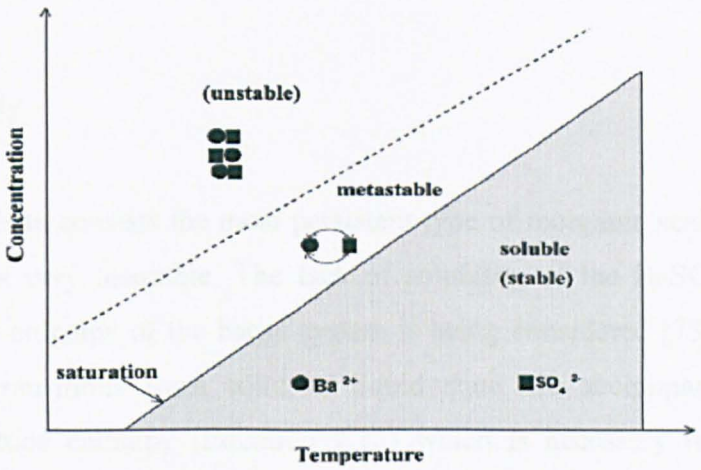

Figure 2.13: Solubility supersaturation zones for $BaSO_4$ [8]

Generally the supersaturation ratio of a solution participating in precipitation processes can be modified many times due to the changes in the thermodynamic conditions, which characterize the precipitating system. However the initial supersaturation ratio guides significantly the particle morphology of barium sulphate [27]. Additionally intense mixing rates in combination with high supersaturation ratio in a given solution results in distribution of smaller particles in the nanometer range [31]. The formation of the smaller size particles is due to the increase of the nucleation rate.

There are a number of methods for calculation the supersaturation ratio of a precipitating system. In this study ScaleSoft Pitzer software version 4.0 was used for the calculating the supersaturation ratio of barium sulphate. The specific software consists one of the most accurate methodologies for supersaturation ratio determinations [72]. ScaleSoft Pitzer is used for calculating the initial supersaturation ratio of barium sulphate at the time point where the mixing of the brines has just taken place.

2.7.2 Solubility

Barium sulphate consists the most persistent type of inorganic scale formed in the oil field as it is very insoluble. The lack of solubility of the $BaSO_4$ can be better explained if the enthalpy of the barite system is being considered [73]. The reactions of the barite transitions from solid to liquid state are accompanied by (i) the endothermic lattice enthalpy (Equation 2.12) which is necessary for the lattice to break into ions and (ii) the exothermic enthalpy of hydration of the ions (Equation 2.13).

$$BaSO_{4(s)} \longrightarrow Ba^{2+}_{(g)} + SO_4^{2-}_{(g)} \qquad \Delta H^{-}_{lat} = +2374 \text{ kJ/mol} \qquad \textbf{Equation 2.12}$$

$$Ba^{2+}_{(g)} + SO_4^{2-}_{(g)} \longrightarrow Ba^{2+}_{(aq)} + SO_4^{2-}_{(aq)} \qquad \Delta H^{-}_{hyd} = -2355 \text{ kJ/mol} \qquad \textbf{Equation 2.13}$$

The lattice enthalpies of the sulphate for all the physical states are approximately the same since the sulphate ion is quite large and the change in the size of the metal has very little effect. On the contrary the hydration enthalpies decrease significantly, as the metal ion size increases during the change from the solid state into the aqueous one. The total enthalpy becomes correspondingly more endothermic and in this way the dissolution of barite is not favoured.

2.7.3 Temperature & Pressure

The temperature of the examined brine is an important factor during the scale formation stages since temperature is tightly related with the supersaturation ratio conditions of the system. For barium sulphate which is a normal solubility inorganic salt, a decrease in temperature results in increase in supersaturation ratio due to the reduced solubility of the formed inorganic scale [74]. When the temperature increases

from 25°C to 100°C, the solubility of $BaSO_4$ increases by a factor of two [75]. Furthermore the temperature plays a key role when it comes to evaluation of the inhibition efficiency during the scaling processes [76]. Most of the inhibitors show significant variations in their performance when the temperature changes.

Also any variations in the pressure influence the scaling tendency of barium sulphate but less compared to the effect that changes in temperature can cause [74]. Individual changes in the pressure do not affect the supersaturation ratio significantly [77]. However changes in the pressure affect the scaling trend of barite when the temperature is increased.

2.7.4 pH

In the different parts of the oil plant the range of pH is found to be between 4 to 7 [19]. At this range extremely acidic or alkalic conditions are avoided. Although the solubility of barium compounds increases with decreasing pH, barium sulphate shows no difference in its properties under any pH changes [78]. However the effect of pH on barium sulphate formation kinetics becomes more important on the supersaturation ratio and in the presence of inhibitors.

2.7.5 Divalent Cations

Divalent cations like Ca^{2+}, Sr^{2+} and Mg^{2+} are usually present during the mixing of the formation water and the synthetic seawater although their concentrations varies depending on their origin source. The presence of these cations affects the nucleation and growth process of $BaSO_4$ [79]. It has been shown that when calcium is present it co-precipitates with $BaSO_4$ as $CaSO_4$ and at room temperature the co-precipitation level can reach the 6% [79]. The emergence of calcium within the barite lattice follows the Vegard's law [80]. According to the law the unit cell parameters of the main forming scale should change in a linear way with the degree of foreign ion

substitution. Hence a substitution or an interstitial mechanism by foreign ions results in a linear increase of the crystallographic axes.

Concerning the Sr^{2+} ions they are present in lower concentrations compared to the concentration of barium cations, in most of the formation water types. When the Sr cations are mixed with the sulphate in the presence of Ba^{2+}, the formation of $SrSO_4$ is difficult as $BaSO_4$ forms rapidly and remains insoluble. Also strontium sulphate is more soluble than barite as the hydration energy for Sr^{2+} is about 0.5 eV higher than for Ba^{2+} [81]. Since most of the injected water compositions contain Sr^{2+} but no $SrSO_4$ is formed it is believed that strontium cations co-precipitate within the barium sulphate lattice. What is actually happening is that the Ca^{2+} and Sr^{2+} ions perform substitution in greater concentrations towards the non-centered planes [79].

2.7.6 Stoichiometry of lattice ions in solutions

Generally the ratio of the lattice ions in the solution contributes in the precipitation kinetics that dominates an examined system. The precipitation of barium sulphate in the oil fields takes place mostly under non stoichiometric conditions. Good evidence for the effect of the ratio of the lattice ions on the barite nucleation and growth kinetics is provided through the observed morphologies of the precipitated inorganic scale particles.

From previous studies it has been shown that deviations from the stoichiometric ratio lead to decrease in the perfection of the barite morphology particles [82] and in variety of precipitated growth forms. Reversely this is an effective way to achieve particle size control is by modifying the lattice ion ratio [83]. Kucher *et al.* showed that at high supersaturation ratio excess of barium ions in the precipitating system results in inhibition of barium sulphate aggregations due to the increased number of electrostatic interactions between the forming particles [82]. On the contrary excess of sulphate ions influences the aggregation process in a very low level.

Moreover under inhibition conditions the ratio of the lattice ions $[Ba^{2+}] / [SO_4^{2-}]$ influences the induction time [84]. It was suggested that the degree of the inhibition of barite nucleation increases when increasing lattice cation/anion ratios. Also anion additives have been proved more effective inhibitors when $[Ba^{2+}] / [SO_4^{2-}] > 1$.

2.7.7 Inhibitors structure and concentration

The structure of the additives used as inhibitors influences the scale formation kinetics. Threshold inhibitors interact chemically with crystal nucleation and growth sites. In this way the tendency for crystallisation is reduced as well as the amount of the formed scale [6]. The inhibitors are requested to own functional groups which are able to form coordinative bonds with cations at the crystal surface [10]. The active groups of the inhibitors participate in the precipitation processes and that is revealed by determination of the deposited formations of barite at the surface. It has been established from previous research that ionic additives with high molecular weight as polyelectrolytes manage to reduce the barite precipitation rate. Further application of these additives resulted in formation of round shaped crystals of barium sulphate [85].

The inhibitors are used in molar concentrations below those of the crystallising material. When an inhibitor is being tested it is important to examine and define the range of concentrations where it remains effective. The performance of the inhibitors, is satisfactory, when the minimum inhibitors concentration (MIC) is low [6]. The MIC is defined as the good efficiency (above 90 %) of the inhibitor in a time range of 2 to 22 h under scale build up conditions.

As mentioned above for the inhibitors structure effect on the barite formations, the same can be supported again for the inhibitors concentration effect. The morphologies of $BaSO_4$ that have been observed after changes in the inhibitors

concentration, are variable and reveal different crystallization and growth processes of barium sulphate every time [86].

The choice of a potential inhibitor as well as the effective dosage is complicated and so far has lead often to applications of inactive inhibitors. In addition when factors that influence the scale formation processes are ignored or considered as negligible, then the precipitation kinetics are not calculated correctly. More information for the nucleation, growth and adhesion of inorganic scale at surfaces is required. In this way correct approach and determination of the scale precipitation kinetics can take place under conditions of inhibition and non inhibition.

2.8 Applied techniques for scale surface studies

The number of applied techniques for probing into barium sulphate formation on surfaces is limited. Most of the studies so far have focused on barium sulphate precipitation processes in the bulk phase as it was believed that the mechanisms dominate the precipitation and the deposition on the surface were the same. However the better understanding of the barite formation process contributed to the division of the bulk and surface mechanisms. Initially barium sulphate bulk jar tests combined with surface growth tests took place [6]. Through these experiments the bulk and the surface precipitation stages were both examined in an effort of understanding barite precipitation kinetics. The surface growth study was based on the use of the metal coupons tested under different temperature and supersaturation ratio conditions. The effect of PPCA as inhibitor and the effect of the minimum inhibition concentration (MIC) were investigated.

2.8.1 Stopped flow technique

In time the focus was turned on more delicate techniques which were able to provide information about the scale formation mechanisms. Carosso and Pelizzetti

showed in the 1980s with the help of a Stopped Flow Technique, that for a range of supersaturation values the scale growth on the surface is controlled by diffusion [36]. This was in good agreement with the conclusions drawn by other studies as well [6]. Concerning the inhibition conditions, it was determined that at concentrations of inhibitor below the MIC the surface deposition rate is mediated by diffusion and hydrodynamic forces and is faster compared to the bulk precipitation rate of barium sulphate. Above the MIC the surface deposition is effectively reduced as the inhibitor surface adsorption is increased.

2.8.2 Rotating cylinder electrode

Another beneficial surface technique used for $BaSO_4$ scale studies was the Rotating Cylinder Electrode Apparatus [87]. The experimental aim of the project was the determination of the effects of fluid hydrodynamics on $BaSO_4$ deposition. It was shown that deposition rate of $BaSO_4$ increased when the value of Reynolds number was also increased. Remarkably the same trend was recorded for polished as well as pre-scaled samples. The turbulence generated due to the artificial agitation of the solution was identified as major hydrodynamic factor, which enhances the scale formation as more active scale forming species are adsorbed on the substrate surface. Subsequently extended adhesion takes place.

2.8.3 Thickness Shear Mode Resonator

Another method applied for measuring the scale potential of a given brine on the surface is based on the Thickness Shear Mode Resonator (TSMR) [88]. The functionality of the Thickness Shear Mode Resonator is based on the use of piezoelectric wafer, which consists of material already known for applications with the Quartz Crystal Microbalance. The frequency changes are being recorded when mass changes on the surface of the piezoelectric crystal occur. The frequency response of the TSM device is a complex function of the properties of the quartz and

the surrounding environment [89]. The technique provides direct measurements of the formed scale on a surface with high accuracy. TSMR yields information about the stability of the produced waters relative to scale deposition under variable tested conditions like in the presence or absence of inhibitors.

2.8.4 Quartz Crystal Microbalance

So far Quartz Crystal Microbalance has been used in many scientific fields. In chemistry and biochemistry QCM applications are dealing mostly with proteins and organic chemicals investigations [90,91]. In addition QCM has been used for environmental monitoring and detection of environmental pollutant characterized by low molecular weight and extremely high toxicity for fishes and all the aquatic life species [92,93]. The results from the QCM measurements showed a good agreement when compared to the ones received from other methods like Enzyme - Linked Immunosorbent Assay (ELISA) and Gas Chromatography - Mass Spectrometry (GC/MS).

QCM applications are also found in developing biosensors. Study of immobilization of proteins on the crystal took place where the QCM was combined with electrochemical impedance (EQCM) [94] and hence one side of the EQCM behaved as the working electrode. Other applications of the sensor as EQCM were based on investigations of the behavior of metals. More specific the deposition and dissolution of Ag and Cu on polycrystalline Au was examined [95]. From this study information was extracted regarding the nature of the formed film on the quartz electrode.

Regarding the application of Quartz Crystal Microbalance for scale studies, the adhesion mechanism of calcium carbonate has been determined with QCM [96]. For the specific study QCM was used in combination with ion concentration measurements. The recorded data resulted in interpretation of the mechanism of the adhesion reaction and precipitation reaction. Additionally QCM was used for

investigating the calcium sulfate kinetics [97]. Measurements of the gypsum precipitating from supersaturated brines resulted in determination of the gypsum kinetics. Moreover based on the QCM measurements the induction time of the calcium sulfate was précised which further contributed to calculations of the activation energy. The observations of the adhered gypsum on the quartz electrode showed that calcium sulfate dehydrate, was the only precipitating phase independently of the supersaturation ratio conditions.

2.8.5 Atomic force applications

The ability of the Atomic Force Microscopy to provide high resolution topography images of a scanned surface, made the use of the AFM very popular in a wide range of scientific fields. Significant applications of the Atomic Force Microscopy have been reported in the tribology, corrosion electrochemistry and biomedical sectors. Referring to a few characteristic studies, AFM has been used for observations of metal surfaces under corrosion conditions [98]. Silver and copper surfaces have been observed with the AFM during their degradation in the presence and absence of acidifying gases. Further the electrodeposition of silver (Ag) on a platinum (Pt) film has been recorded *in-situ* with the AFM [99]. It was revealed that the electrodeposition of Ag was only a surface reaction and oxides of platinum were not involved in the procedure. Another use of the Atomic Force Microscopy was for observation of proteins binding on thin polymer films [100]. The scanning of the proteins on the biosensors clarified the immobilization of the proteins on the polymer.

The applications just described above show the variety of the scientific areas that Atomic Force Microscopy is being used as an observation tool. What is worth noting is that for these studies the Quartz Crystal Microbalance has also been used. QCM was applied for the record of frequency changes or for quantification of the deposited mass. Comparison of the AFM images with the QCM measurements

showed a very good agreement [99]. Therefore it is clear that the combination of these two sensitive techniques is able to lead to undoubted measurements.

Recently Atomic Force Microscopy was used for scaling studies. AFM was used in *in-situ* mode for studying the crystal formation and the growth process of calcium carbonate [101]. The record of data *in-situ* resulted in deeper understanding of the nucleation and growth of the calcareous scale. Also AFM application was found in observations of barite and calcite crystals formed in the bulk phase [102]. The focus of the specific study was turned to the step dynamics of the formed minerals and to further use of the data for modeling. Again AFM was used for application in the crystallization medium [103]. The effect of CO_3^{2-} on the crystallographic forms {210} and {001} of barium sulphate in the presence and absence of inhibitors was investigated.

Moreover Pina *et al.* has used *in-situ* AFM for following the kinetics of the two most important barite crystal faces the (001) and (210) [104]. Additionally he used the atomic force microscopy *in-situ* for observations of the formed barium sulphate after being treated with inhibitors [105]. From both studies the conclusions drawn enlightened the growth mechanism of $BaSO_4$ and the way the inhibitors act on the formed barite.

2.8.6 X-ray diffraction applications

Although *in-situ* SXRD has been established during the last decades, it has been already used for a high number of applications. Quite significant has been proved the contribution of the *in-situ* X-ray diffraction for the determination of the crystallographic nature of proteins during crystallization [106,107].

In-situ SXRD was been proved useful for characterization of different thin films [108] and materials such as carbonaceous materials [109]. In addition *in-situ* X-ray

has been used for observation of transformation phases of compounds such as boron nitride [110]. The main focus of that study was the transformation of boron nitride under static high temperature and pressure.

With *in-situ* synchrotron X-ray technology the monitoring of scale processes can be achieved. In this way the kinetics and furthermore the mechanisms, of inhibitors can be studied. X-Ray synchrotron diffraction measurements have proved to be very useful and accurate in probing the precipitation and growth kinetics of $CaCO_3$ scale and Mg^{2+} containing scales, on a surface [111].

Synchrotron radiation XRD has been used to follow the real - time evolution of calcareous scale formed on silicon and polymethyl methacrylate (PMMA) substrates at different temperatures and in the presence of conventional inhibitors (DETPMP and PPCA) [112]. The specific capillary cells were chosen for the applications of the *in-situ* technique for studying scale, although they are not imitating realistic industrial materials. However these substrates are quite useful at the initial point of committing the technique, since they offer weak X-ray diffraction patterns thus the substrate background in the received patterns is low. The formation of calcareous scale on industrial substrate such stainless steel was studied later on by Martinod *et al.*, again in the presence and absence of inhibitors, where the effect of inhibitors on the different polymorphs and the crystal faces of calcium carbonate was clearly determined [113]. The data provided from the SXRD tests, pointed out the effect of temperature on the growth of the different planes of $CaCO_3$ on different substrates. The role of inhibitors (e.g PPCA) in changing the polymorphic form of $CaCO_3$ was discussed and the effect of Mg^{2+} on the scale morphology was shown.

In terms of measuring the barium sulphate kinetics by SXRD only a few efforts have been made so far. Barium sulphate precipitation has been monitored using angle dispersive XRD [114]. The tested cell for that study was silicon one with diameter 1 mm and wall thickness 2.6 mm and it was used under conditions of high pressure (1.38×10^7 Pa). The use of silicon cell capillary was based on the fact that

silicon has a low atomic number and therefore it is relatively transparent to X-rays. Furthermore since it is a single crystal, it does not generate diffraction rings, which would interfere with the experiment.

The X-ray synchrotron diffraction measurements of barium sulphate precipitation made by other researchers, have lead to determination of the main faces of barite [69,114]. Jones *et al.* studied the effect of inhibitors such as nitrilotriacetic acid (NTA) and nitrilomethylenephosphonic acid (NTMP) on barite precipitation at 80°C with *in-situ* X-ray diffraction [115]. The two inhibitors were investigated for their effect on the barite formation on stainless steel at high pH. As concluded, NTA resulted in a rounded morphology of barite particles, which allows more planes to be accessed by the X-ray beam. This was the reason for receiving X-ray patterns with more barite peaks, compared to the spectra received for the uninhibited system. As far as NTMP it managed to inhibit the precipitation of barium sulphate completely, when the pH was adjusted at 7. This was supported from the X-ray diffraction patterns, where all the peaks were smaller and broader when NTMP was present. Even the detected peak for the (200) plane of barite, belonging to one of the dominant planes, was very weak.

2.9 Dissolution

The method of dissolution is based on the removal of the already formed barite scale. The process can be placed in time after a potential inhibition approach. Crystal growth and dissolution are not reciprocal processes. $BaSO_4$ precipitation reveals different rate constants for growth and dissolution [116]. The suggested dissolution mechanism supports dissolving crystal surfaces, which are partly unhydrated [117]. According to this, the rate of dissolution is controlled by the rate at which unexposed units of the crystal lattice enter the hydrated monolayer. The dissolution is controlled by a surface reaction than diffusion [118].

The dissolution kinetics of $BaSO_4$ in water is second order process and the dissolution rate is not influenced by the stirring rate. Dissolution of deposited barium sulphate so far has not been successful as the chosen dissolvers haven't been the appropriate ones.

Diethylenetriaminepentaacetic acid (DTPA) is believed to be the most effective scale dissolver in the petroleum industry since the early studies by Morris and Paul [119]. The structure of DTPA is presented in Figure 2.14.

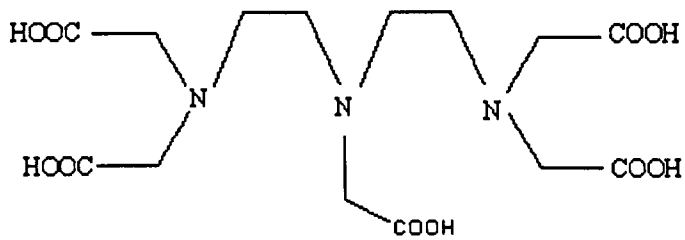

Figure 2.14: DTPA structure structure

DTPA is an octodentate ligand which forms a 1:1 chelate in solutions with high pH. Only at high pH range the ligand is able to complex metal ions that are free in the solution and not to form a strongly bound site on an ionic solid like a mineral. Wang *et al.* [67] used DTPA as dissolver of barite at pH>12 in order to investigate the chemical reactions underlying the effective dissolution of barium sulphate. It was determined that the dissolution in pure waters proceeds via attack of sites such as steps, kinks and other defects on the (001) surface of $BaSO_4$.

Another tested additive is the EDTA (ethylenediaminetetraacetic acid) which is suggested to be effective dissolver of barium sulphate. The specific chemical reagent contains 4 carboxylic groups as shown in Figure 2.15 and it dissolves the precipitated barium sulphate scale in high percentage.

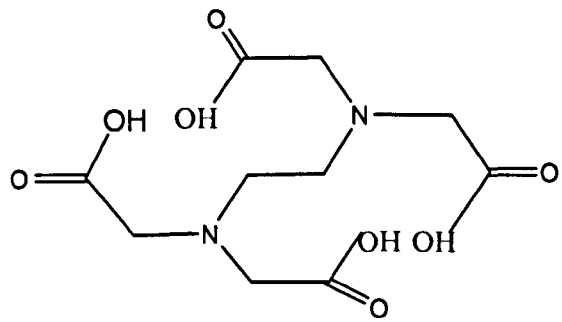

Figure 2.15: EDTA (ethylenediaminetetraacetic acid) structure

The main disadvantage of the scale dissolvers is the large amounts of the additive needed in order the stoichiometry of one chelator molecule for each dissolved cation to be satisfied [81]. Additionally the chelates are effective dissolvers only at high pH and they usually contain hazard elements. Hence treatment of the formed scale with dissolvers is quite expensive and not benign for the environment.

2.10 Inhibition

2.10.1 Introduction

Scale inhibition technology deals with reservoirs and other oil facilities parts that have potential for inorganic scale formation. The technology is based upon the ability of specific molecules to inhibit or delay the nucleation and/or the crystal growth of inorganic scale particles. Potentially the application of chemical additives results in inhibition of the growth rates of the forming scale in all the developed directions of the lattice planes and lost of the anisotropy of the growth [120].

For downhole applications the inhibitors are injected into the near wellbore formation in a squeeze process. The treatments are carried out by squeezing an aqueous solution of the inhibitor [121]. The injection takes place several meters into the formation where the inhibitor is retained within the rock. The release of the used

additive into the produced water provides the desirable protection against scaling. When the concentration of the inhibitor falls below the threshold level for effective inhibition, then the treatments are repeated.

The inhibitors must have a sufficient interaction with the formation, they should be compatible with the field brines and stable to thermal degradation at reservoir conditions [76]. Thus before the application of an inhibitor, the additive should be tested for its (i) inhibition efficiency, (ii) retention properties in the formation, (iii) compatibility with the field brines and (iv) stability under reservoir conditions. Nevertheless in all field applications the inhibition efficiency is the primary criterion for the inhibitor selection.

2.10.2 Inhibition efficiency

In the last two decades the interpretation of the inhibitors design and structural functionality resulted in a number of criteria that an inhibitor should satisfy in order to be effective. It has been shown that the inhibitor is being highly attracted and further effectively bonded on the particles of the formed scale when it is provides flat configuration upon the crystal surface [10]. When the configuration of the inhibitor is not flat then the attachment with inorganic formed crystals is not strong enough.

Furthermore the inhibitor should contain the least hydrophobic groups as possible. The presence of hydrophobic groups in the structure of a chemical additive do not favour the inhibition neither structurally nor energetically [10,74]. The hydrophobic groups have the trend to extend from the surface resulting in a loopy configuration of the inhibitor. Respectively the presence of high number of hydrophobic groups of the additive results in increase of the molecular weight of the inhibitor without offering higher bonding possibilities with the formed particles of scale. Also the existence of the hydrophobic groups in the structure of the inhibitor

might block the inhibiting action of other functional groups of the additive causing steric hindrance.

In addition to the above the efficiency of the inhibitor on the forming scale strongly depends on the temperature, pressure and pH conditions present in the precipitating system. High temperature and pressure affects the stability of the inhibition and hence its efficiency [122]. Depending on the structure of the chemical additive, degradation of the inhibitor under the applied conditions in the system is inevitable or oppositely the inhibitor species remain thermally stable maintaining in this way high inhibition levels.

Furthermore the pH of the system always affects the efficiency of the inhibitors. At pH above 5.5 the dissociated inhibitors molecules are negatively charged and also the barite surface bears a net negative charge [74]. Since the present forces in the pH range above 5 are repulsive, excess of energy is requested in order the inhibitor to be adsorbed on the barite surface. The adsorption reaction is endothermic and demands ionization conditions in order for the adsorption process to start [68]. However total ionization is not desirable as under conditions of total ionization all the species are ionized and their energy needs for creation of new bonds are high. Furthermore the consumed energy for the approach of the inhibitor to the negative net of barite and the attendant entropy loss can not be compensated by the energy gain obtained by bondage with the surface [10]. Subsequently in order an inhibitor to act efficiently on the barite particles under these pH conditions, firstly it must ionized in order to be adsorbed on the formed barium sulphate.

2.10.3 Inhibitor families

Crystal growth inhibitors are used to prevent scale precipitation. Attachment of these molecules to the active growth sites disrupts the nucleation process and hinders

the continuation of growth [123]. The inhibitors usually are active in the bulk phase of the system or on the surface.

The inhibition of scale on the surface is more challenging. Inhibition of the kinetics on the surface is believed to be more complex and source of many following problems, as the bulk inhibitors at some point are removed by water flow and finally disposed. However the deposition of the surface inhibitors within the inorganic scale leads to subsequent adhesion and moreover is directly connected with corrosion behaviour of the metal and fouling conditions [10,124]. The performance of specific additives as scale – corrosion inhibitors is already concern of progressed studies [125].

The main families of inhibitors used so far are the:

- Polyphosphinoacrylates
- Polyphosphonates
- Polyelectrolytes
- Polycarboxylates

The group of polyphosphonates is widely applied for the inhibition of barium sulphate during both the nucleation and growth stages of the precipitation. The effectiveness of the polyphosphonates is based on the simultaneous formation of covalent bonds with the cations and hydrogen bonds with the anions present in the crystal surface [126].

Generally the inhibition mechanism of the polyphosphates is assumed to be a combination of stereochemistry and presence of two fully deprotonated phosphate groups [127]. For achieving maximum inhibition the surface interactions must be balanced between the chemical interactions with the additive and electrostatic interactions between the surface and the additive.

The polyelectrolyte – type inhibitors have been designed and applied during scale formation as they have the ability to form a relatively large number of coordinative bonds with the cations of the pronounced scale [10]. In a relative way the polycarboxylates are able to perform as inhibitors by attaching their carboxylic groups after being deprotonated on the crystal surfaces of the formed barium sulphate.

2.10.4 Barium sulphate inhibitor performance in bulk solutions

The inhibitors effectiveness on barite formed in the bulk phase has been investigated, after the precipitation of barium sulphate from mixing simple brines. Most of the barium sulphate inhibitors were tested for their performance in the bulk phase during static barite precipitation tests [128,129].

The polyphoshinacrylates (PPAA) with general structure presented in Figure 2.16 consist one of the initial groups of $BaSO_4$ inhibitors [130]. Seeded suspension growth experiments that took place in the past under the influence of PPAA with different molecular weights, lead to useful confirmations. A comparison of the performances of three PPAA indicated that higher molecular weight resulted in higher adsorption level and more effective inhibition.

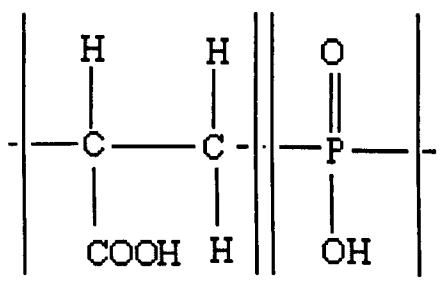

Figure 2.16: PPAA structure

From the same group polyphosphinocarboxylic acid (PPCA) has been proved effective inhibitor due to the high number of –COOH groups (Figure 2.17). Static

inhibition efficiency tests showed an increase in the effectiveness of PPCA as the pH was increased [74].

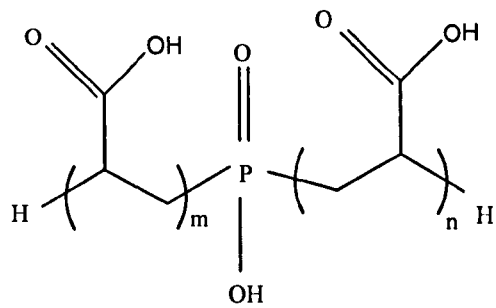

Figure 2.17: Poly-phoshinocarboxylix acid (PPCA) structure

Van Der Leeden and Van Rosmalen have further focused on inhibition of barium sulphate precipitation using polycarboxylates [131] as well as polyelectrolytes [68,74]. The performance of the additives was tested under different pH values. Polycarboxylates proved effective growth retarders as the increased number of –COOH groups influence positively the inhibition processes. The same conclusion was supported by Leung and Nancollas [118].

Concerning the polyelectrolytes the treatment of barium sulphate supersaturated solutions with high concentration (1000 ppm) of polyacrylic acid (PAA) resulted in formation of round shaped barite morphologies at pH= 5. The transformation of the barite crystals into round particles indicated the effectiveness of the polyelecrolyte which was further confirmed by X-ray diffraction [85].

Another polyelectrolyte PMA-PVS (copolymer of maleic acid and vinyl sulfonic acid) (Figure 2.18) resulted in total growth blockage of $BaSO_4$. PMA-PVS revealed high performance as it owns a high number of carboxylic groups (characteristic –COOH groups of maleic acid). The strong inhibition that PMA-PVS offers, is based on the potential of sulphonic acid group to form strong bonds with Ba^{2+} at the surface [131]. In this way further replacement of the sulphate ions that belong to the initial lattice takes place. Occupation of SO_4 lattice sites by SO_3 ions can easily

occur, when the lattice sulphate ions in the (011) and (101) faces are orientated perpendicular to the crystal surface. This type of orientation declares that one S-O bond has direction out of the surface.

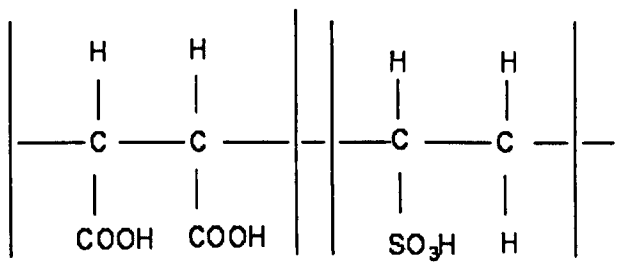

Figure 2.18: PMA-PVS structure

Additionally vinyl sulphonic acid (PAA-PVS) presented in Figure 2.19 has also performed in a satisfying way as an inhibitor and it is suggested that it acts in the same way as PMA-PVS.

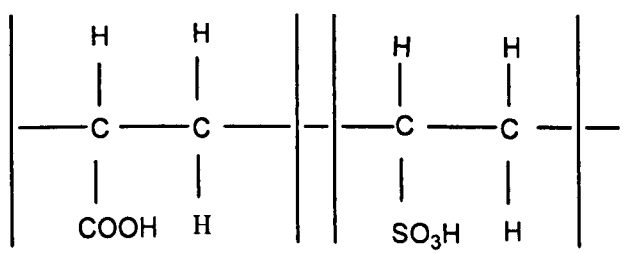

Figure 2.19: PAA-PVS structure

Other additives tested for their inhibition performance on barium sulphate originating from the sulphonates family were the poly vinyl sulphonate (PVS) and sulphonated copolymer (VS-Co). Both inhibitors have been used for their efficiency in dynamic tube blocking tests [77]. From the results of the tube blocking tests it was concluded that PVS performs more efficient as scale inhibitor compared to VS-Co.

Phosphonates containing different number of phosphonic groups like the ones illustrated in Figure 2.20 and Figure 2.21 have been used in wide range for barite growth retardation [86,105,127,132].

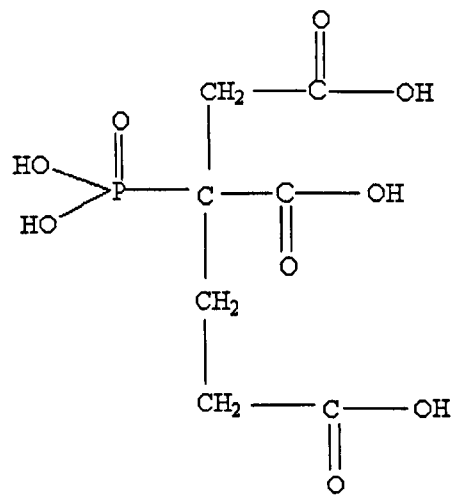

Figure 2.20: PBTC -2-Phosphonobutane-1, 2, 4-tricarboxylic acid structure

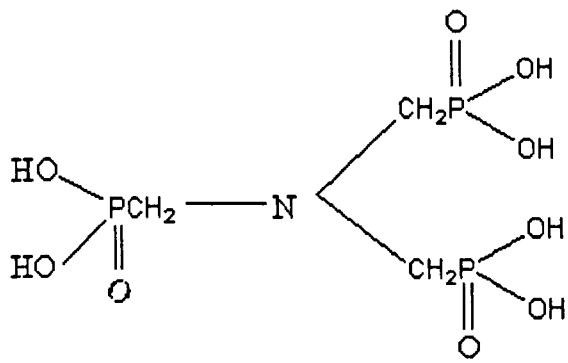

Figure 2.21: ATMP -Amino tri (methylene-phosphonic) acid structure

It has been clearly determined that the increase in the number of the phosphonic groups does not coincide with an increase in the inhibition efficiency. Factors like the pH, the structural matching of the phosphonic groups within the barite lattice and also the degree of dissociation complexation with ions in solution, dominate the inhibition process when phosphonates are present [64,133]. However essential

condition for the phosphonate groups to be active for barite inhibition is that phosphonic groups must be in a double unprotonated state.

One of the well known phosphonate additives applied for barium sulphate inhibition is DETPMP (Figure 2.22) [19]. DETPMP has been tested for its inhibition effect on barite illustrating an effective performance.

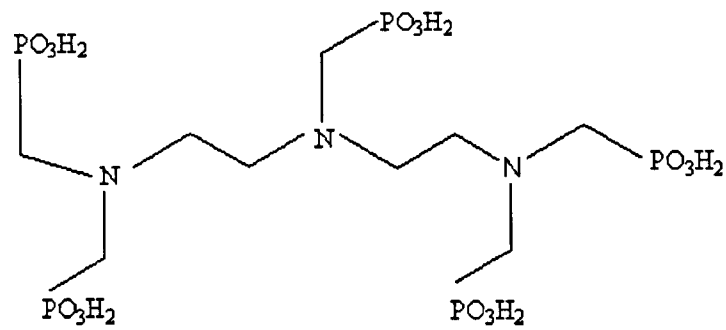

Figure 2.22: DETPMP-Diethylenetriamine penta methylenephosphonic acid structure

When brines containing barium and sulphate cations were mixed at room temperature and pH=4, the precipitated morphologies of barium sulphate were smaller revealing the effect of DETPMP on the crystallization and growth of barite particles [86]. Since the effect of DETPMP had already been tested in different pH ranges, it was determined that the improvement in its performance was a matter of more $-PO_3H_2$ groups deprotonating to form $-PO_3^{2-}$groups when the pH was increased. Under Coulombic static interactions these $-PO_3^{2-}$ groups interact better with the crystallizing surface and manage to block the barite crystal planes. Hence the formed inhibited barite particles are round shaped and smaller as determined with XRD analysis, illustrating a lost in their geometrical perfection as the pH increases.

Furthermore when DETPMP was added as inhibitor, during the mixing of supersaturated brines with respect to barite in the presence of Ca^{2+} and Mg^{2+}, inhibition also occurred [134]. It was shown that at low concentrations of calcium,

the inhibition efficiency of DETPMP was poisoned by the presence of magnesium ions. On the other hand at high concentration of calcium, DETPMP reveals high inhibition efficiency as it creates more bindings with the calcium ions rather with the magnesium ions.

It is also worth noting that DETPMP has been proved a more effective inhibitor at high temperatures as 95°C. At this temperature level DETPMP approached the adsorption level of 80% on barite crystals when compared to the adsorption occurred at 5°C. Yet the adsorption was noted so high at pH equal to 6 [74].

The group of organic additives has been chosen many times for tracking a potential inhibitor. In general the organic compounds consist of a good source for scale inhibitors nevertheless most of them hint high level of hazardness. Yet there are non – phosphorous organic compound such as mellitic acid [118], polyepoxysuccinic acid [10] and poly (styrene – alt – maleic acid) [135] which have been used in the past as barite crystal modifiers.

Mellitic acid is characterized by six carboxylate groups [Figure 2.23] and in previous studies has been proved more effective inhibitor compared to other additives with lower number of carboxylic groups. The number and the placement of the –COOH groups in the structure of the compound is strongly supported that enhances the inhibition.

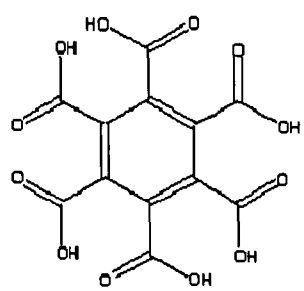

Figure 2.23: Mellitic acid structure

Polyepoxysuccinic acid [Figure 2.24] in combination with agaric acid has been tested for its inhibition action on barium sulphate [136]. The effectiveness of this benign blending on the barium sulphate formations was remarkable compared to the common used inhibitors and seemed independent of pH changes. However the mixture of polyepoxysuccininc acid and agaric acid does not consist an ideal treatment for the barite scale formation problems as the concentrations of the mixture needed in order an effective treatment to take place are usually approaching the level of 500 ppm.

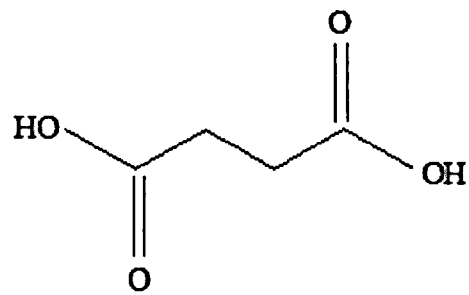

Figure 2.24: Polyepoxysuccinic acid structure

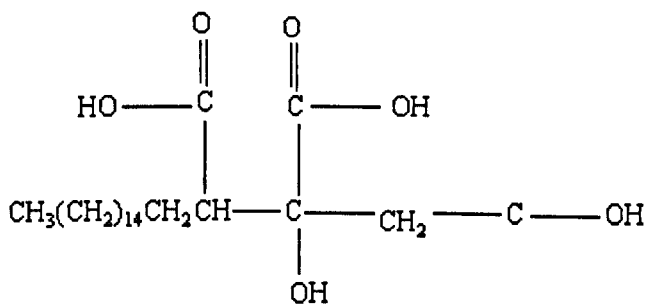

Figure 2.25: Agaric acid structure

Further for the inhibition of barium sulphate homo and copolymers of maleic acid [Figure 2.26] and acrylamide have been used [79]. The static tests that took place provided well observable barite crystals. Crystals that formed after the solution was treated with inhibitor were characterized as needle - like crystals.

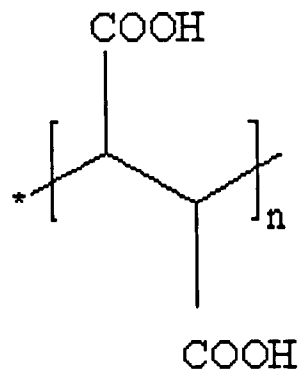

Figure 2.26: Polymaleic acid structure

As positive approach for using benign additives for barite inhibition [137] was proposed the application of poly a, β aspartic acid. The origin of the poly a, β aspartic acid is the a – form of polyaspartic acid, which is the existent form found in nature, subsequently this family of additives is considered environmental friendly. The surface electrical properties of barium sulphate modified by adsorption of poly a, β aspartic acid (Figure 2.27) were studied.

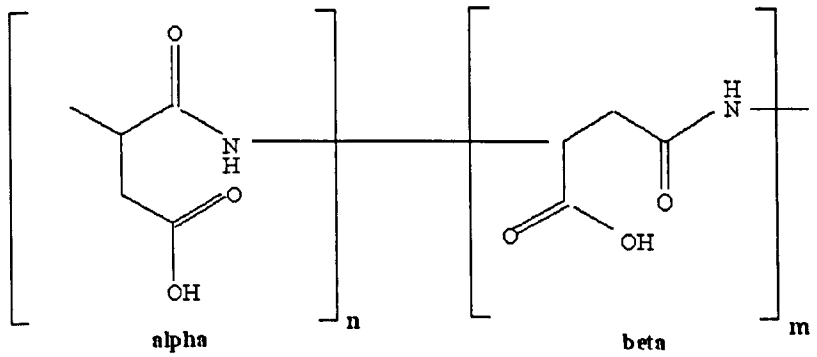

Figure 2.27: a, β aspartic acid structure

During the adsorption experiments the equilibrium concentration of polyaspartate was determined by hyamine technique. IR studies showed that the additive is bound to the barite via the backbone nitrogen atoms. However the performance of polyaspartic acid was low during the $BaSO_4$ precipitation kinetics. The performance of polyaspartic acid was improved when calcium cations were present. The Ca^{2+} complexes with the polyaspartic acid resulted in decrease of the molecules electrical charge thus the adsorption of the inhibitor on the negatively charged surfaces of barite was easier.

Finally another barite inhibition treatment is based on reduction of sulphate by adding organic carbon [22]. The inorganic and biologically mediated reduction of sulphate takes place at intermediate pH through the following reactions:

$$BaSO_4 \rightarrow Ba^{2+}_{(aq)} + SO_4^{2-}_{(aq)} \qquad \textbf{Equation 2.14}$$

$$SO_4^{2-}_{(aq)} + H^+ \rightarrow HS^- + 2O_{2(aq\ or\ g)} \qquad \textbf{Equation 2.15}$$

$$SO_4^{2-}_{(aq)} + CH_2O_{(s)} \rightarrow HCO_3^-{}_{(aq)} + HS^-_{(aq)} + O_{2(aq\ or\ g)} \qquad \textbf{Equation 2.16}$$

The reduction of barite is thus favoured by low fO_2 and low pH conditions.

2.11 Inhibition Mechanisms

The inhibition mechanisms are significant since their determination is able to reveal the functionality of the active groups and further to explain the performance of different inhibitors. The three main inhibition mechanisms as presented in Figure 2.28 are the; (a) threshold effect, (b) crystal distortion and (c) dispersancy and stabilization.

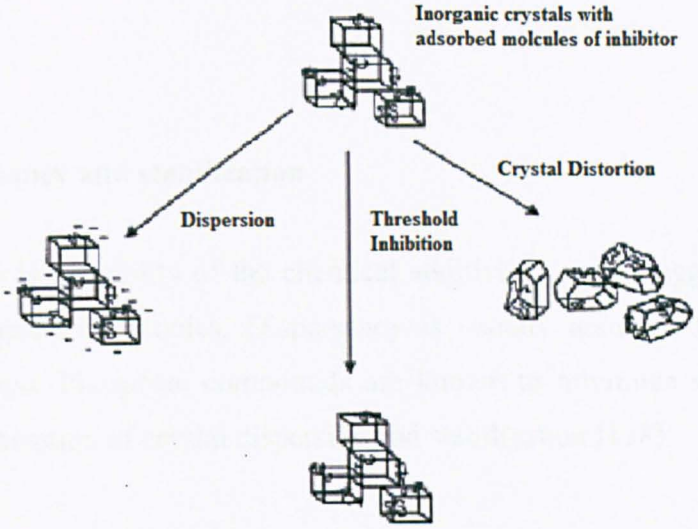

Figure 2.28: Three main inhibition mechanisms [111]

2.11.1 Threshold effect

This mechanism is based on treatment of the inorganic particles with sub-stroichiometric concentrations of the inhibitor. The main action during this mechanism is the disruption of the thermodynamic stability of the growing nucleus during the homogeneous crystallization nucleation. The threshold effect is related with endothermic adsorption of the inhibitor species causing dissolution of the $BaSO_4$ embryo crystals. Generally the aim is the enhancement of the solubility of the inorganic particles.

2.11.2 Crystal distortion

This mechanism is based on the distortion of the growing crystals due to the adsorption of the inhibitor. The distorted crystals reveal smaller tension to be adherent on the surface and further they are more easily dispersed. Then the

distorted crystals are maintained in suspension by the normal water flow of the system.

2.11.3 Dispersancy and stabilization

Dispersancy is the ability of the chemical additive to reduce agglomeration and settling of suspended particles. Dispersancy is usually assumed to be a charge repulsion process. Phosphate compounds are known to minimize scale deposition through a combination of crystal dispersion and stabilization [138].

2.12 Synopsis of the literature review

Many interrelated processes generate precipitation of scaling mineral. In oil and gas production this is particularly the case due to the wide range of conditions and complex environment (e.g. brines). Although scale is generally only problematic if it adheres and grows on surfaces, this has only recently (last two decades) been considered in any detail. This work will build on a range of modern surface and *in-situ* techniques to improve the understanding of surface growth phenomena that occur during the initial stage of barite formation, in the presence and absence of inhibitors.

CHAPTER 3 Development of the experimental techniques

3.1 Introduction

The preference in the techniques used in this study is based on the accuracy and sensitivity that the aims of this project demand. So far most of the methods, which have been applied elsewhere for probing the barite formation on a surface lack of reproducibility, hence studies of barium sulphate formation on surfaces have therefore rarely been reported. The choice of the methodology was made after considering that the main emphasis should be the early stages of barium sulphate formation at surfaces. The three main techniques used are the Quartz Crystal Microbalance, the Atomic Force Microscopy and the X-ray diffraction, which are described in detail in this chapter.

3.2 Chemical Reagents

Generally two aqueous, supersaturated brines are essential for the precipitation and deposition of $BaSO_4$ to occur. The formation water is the source of Ba^{2+} and the synthetic seawater is the source of SO_4^{2-}. The brines tested in this study are imitating realistic compositions of formation and synthetic seawater. Hence besides the essential ions for the $BaSO_4$ formation, other cations were also included. The examined compositions are described in the next chapter. An overview of the inorganic salts used for the selected brine compositions is presented in Table 3.1.

Table 3.1: Inorganic salts of the brines

Formation Water	$BaCl_2.2H_2O$, KCl, $CaCl_2.6H_2O$, $MgCl_2.H_2O$, $SrCl_2.6H_2O$, NaCl
Synthetic Seawater	Na_2SO_4, KCl, $CaCl_2.6H_2O$, $MgCl_2.H_2O$, $SrCl_2.6H_2O$, NaCl

3.3 Scale Inhibitors

The chemical additives tested in this study for their inhibition effect on the barium sulphate formation are two commercial inhibitors already used in the oil and gas sector. The first additive applied was the polyphosphinocarboxylic acid (PPCA) provided by Biolab. PPCA has a molecular weight 3600 g/mole and activity 42%. The second additive tested was the Diethylenetriamine penta (methylenephosphonic acid) (DETPMP) provided by Rhodia. DETPMP has molecular weight equal to 573 g/mol and activity 45%. The structures of the two inhibitors are presented in Figure 2.16 and Figure 2.21 respectively.

The specific inhibitors were selected to be examined for their inhibition performance on the barium sulphate formed on the surface, as the differences in their structures are able to show which functional groups are responsible for their effective or failing performance on the deposited scale. More specific the presence of carboxylic groups (-COOH) in the structure of PPCA is expected to have a different effect on the formed barite compared to the effect of DETPMP which is characterized by 5 phosphonic groups.

PPCA and DETPMP have been the main chemicals of interest for a high number of publications investigating their inhibition performance during the precipitation of $BaSO_4$ [6,74,79,86,139]. These previous efforts made on the effect of the specific inhibitors on the formation of barite in the bulk phase can be used as a useful basis for the current study. Consequently a more complete image of the kinetics occurring in both bulk phase and surface during the barite formation system can be built up leading to further understanding of the effect of the inhibitors.

3.4 Quartz Crystal Microbalance

3.4.1 Introduction

Quartz Crystal Microbalance (QCM) is a very sensitive and accurate apparatus. The functionality of the Quartz Crystal Microbalance is based on the changes in frequency of a piezoelectric quartz crystal when it is disturbed by the addition of a small mass [140].

QCM has roots back in 1880's when Curies first observed piezoelectricity as a potential generated across two surfaces of a quartz crystal under strain [141]. Until the late 1950's the quartz crystals have already been used as mass sensors following the Sauerbrey theory. Sauerbrey coined the term Quartz Crystal Microbalance and an extended reference to his pioneering work follows later in this chapter.

Initially QCM was used only for gas applications. In the mid 1980's QCM measurements in liquid environment were accomplished as the effects due to the density of the reaction solution and the viscosity of the loaded layer on the quartz crystal were treated.

3.4.2 Quartz Crystal Microbalance apparatus

The QCM has been modified many times through years in order to be improved and hence all the potential errors during the measurements to be minimized. Generally the number of commercial models, that can provide the accuracy in the tests independently of the measuring environment and easy handling of the equipment, is small.

In this study the QCM200 model used is provided by Stanford Systems. In Figure 3.1 the different parts of the Quartz Crystal Microbalance are illustrated. The main

parts of the QCM are the digital controller, the crystal oscillator, the crystal holder and the crystal sensors. The crystal holder is the part of the QCM where the crystal sensor is placed. The crystal holder components are presented in Figure 3.2.

Figure 3.1: Complete QCM set up (QCM200 Digital Controller, QCM25 Crystal Oscillator, Crystal Holder and Quartz Crystal sensors)

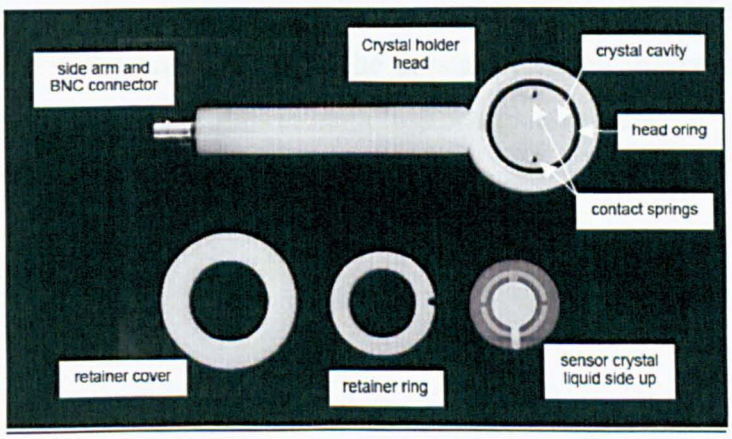

Figure 3.2: Crystal holder components

3.4.3 Quartz Crystal Microbalance principles

Initially there is a time-dependent inertial field developed at the surface of the QCM, which permits the use of the Quartz Crystal Microbalance as mass sensor [142]. The piezoelectric quartz crystals generate a voltage in response to applied mechanical stress originating from the inertial field. Since each site of the QCM

crystal forms an electric dipole, the crystal is overall electrically neutral. When mechanical stress is applied the symmetry of the crystal is disturbed and a voltage across the material is generated. The changes in the frequency are being recorded.

The Quartz Crystal Microbalance as an extremely sensitive sensor is capable of measuring mass changes in the ng/cm^2 range with a wide dynamic range extending into the 100 μg/cm^2. The mass changes during the QCM measurements are given in a function of time.

The Quartz Crystal Microbalance principle is based on the Sauerbrey equation (Equation 3.1). According to Sauerbrey, when small amounts of mass are deposited and adsorbed on the quartz electrode surface, the frequency of the quartz is changed. The change in oscillating frequency of the quartz crystal (Δf) is directly proportional to the change of the mass of adhesion (Δm). Thus the physical quantity which determines the mass measuring sensitivity in every point on the surface of a quartz crystal resonator is the acceleration of the crystal vibration in that point [142]. It should be noted that Δm represents either a loss or a gain in mass.

$$\Delta f = \frac{-2 f_o^2 \Delta m}{A(\mu_q p_q)^{1/2}} \qquad \textbf{Equation 3.1}$$

Where:

Δf = measured frequency shift

f_o = resonance frequency

Δm = the mass change

A = effective area of the electrode

μ_q = shear modulus of the quartz

p_q = quartz density

For the appropriate application of Sauerbrey model, the following assumptions must be made concerning the quartz crystal and the nature of the deposited mass:

- The quartz is composed of two parallel plane faces. The model is in one dimension and the loss of amplitude of vibration of quartz is negligible.
- The mass of the electrode is negligible and totally conductive.
- The mass of deposit is uniform on the surface.
- The contact between quartz and covered film is perfect: continuity of particle moving and equally stress of the surface.
- The mass of deposit is very small compared to the mass of crystal.

It is important when the Sauerbrey equation is applied to keep the density of the reaction solution and the viscosity of the loaded layer constant. Viscosity changes can produce frequency shift and signal attenuation that require appropriate algorithm to separate the effects [143]. Nevertheless the density of the liquid and the viscosity of the loaded layer change during the measurements with the QCM [144]. Thus it is essential these factors to be treated in order correct measurements to take place.

3.4.4 Quartz crystal microbalance measurements in liquid environment

The problems of the frequency decrease due to the viscosity and the density of the solution were first treated by Glassford [145] and later by Kanazawa and Gordon [144]. The Kanazawa's consideration of the influence of the solution properties on the crystal permits the prediction of the change in resonance frequency, which accompanies the immersion of the crystal into a viscous medium. The improved Equation 3.2 originating from the Sauerbrey equation includes the viscosity and density of the solution and is applied for liquid environment.

$$\Delta f = -f_v^{3/2}\left(\frac{\rho_L \eta_L}{\pi \rho_q \mu_q}\right)^{1/2}$$ **Equation 3.2**

Where:

f_v= frequency of oscillation of unloaded crystal

ρ_q= density of quartz

μ_q= shear modulus of quartz

ρ_L= density of liquid in contact with the electrode assess

η_L = viscosity of the liquid in contact with the electrode

When the QCM is used in liquid environment, the vibration amplitude and the acceleration decays exponentially from the crystal surface into the liquid as presented in Figure 3.3.

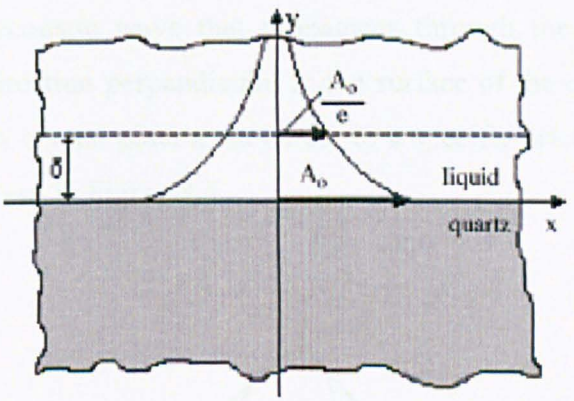

Figure 3.3: Amplitude and acceleration decay at the quartz – liquid interface [142]

The vibration amplitude at given distance y is calculated from the Equation 3.3.

$$A(y) = A_0 \exp\left(\frac{-y}{\delta}\right)$$ **Equation 3.3**

Where A_0 is the maximum vibration amplitude at the centre of the crystal resonator and δ is the penetration depth equal to $(n_L/\pi f_0 \rho_L)^{1/2}$. The definition of the penetration depth is the distance into the liquid layer when the vibration amplitude has diminished *e* times [142].

As the parameter y of Equation 3.3 becomes bigger showing that the distance from the liquid-quartz interface becomes larger, the vibration amplitude and the acceleration decrease. The intensity of the inertial field developed at the quartz crystal surface changes in the same way. The decaying profile of the amplitude and of the field intensity is determined from the liquid viscosity.

3.4.5 Quartz Crystals

As QCM crystals are piezoelectric an oscillating electric field applied across the device induces an acoustic wave that propagates through the crystal [140]. The acoustic wave has direction perpendicular to the surface of the crystal. In order this to happen, the quartz crystal plate must be cut to a specific orientation with respect to crystal axes as shown in Figure 3.4.

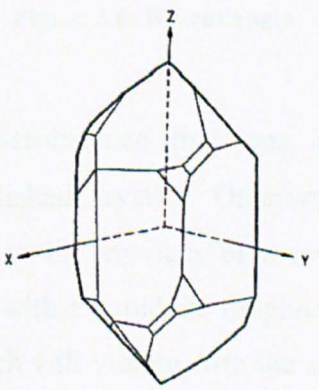

Figure 3.4: Assignment of axes to a quartz crystal [140]

The AT-cut and BT-cut are the two common types of cut of the quartz crystals. Considering z as the vertical axis, then the angle between the z and the crystal is 35°

and 15′ for the AT-cut crystals and 49° for the BT-cut crystals respectively as presented in Figure 3.5 and Figure 3.6. The type of quartz crystals commonly used including in this study as well, is the AT-cut type as their smaller cut minimizes the f_0 temperature dependence.

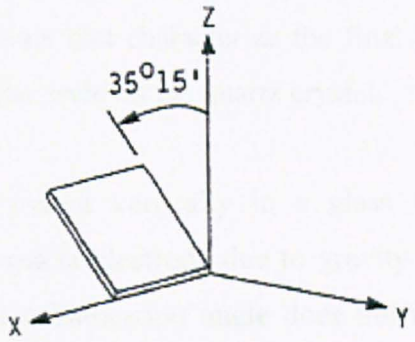

Figure 3.5: AT-cut angle

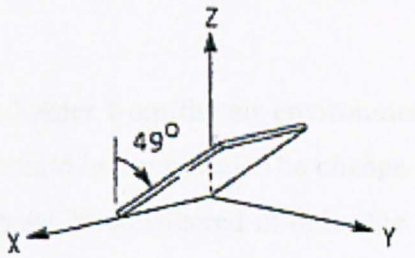

Figure 3.6: BT-cut angle

When Quartz Crystal Microbalance functions in liquid environment, it is essential to use optically polished crystals. Otherwise it is more likely for the reaction liquid to get caught in the crevices of a rough crystal [140]. When the resonating quartz is in contact with a liquid, its roughness or the presence of crevices can trap liquid molecules which will vibrate with the same amplitude and accelerate as the quartz resonator surface. These trapped molecules will exhibit a solid film behavior, producing an additional frequency change [142].

3.4.6 Static Tests with Quartz Crystal Microbalance for $BaSO_4$ Deposition

In this study QCM was used to follow in detail the initial kinetics of the barium sulphate formation on the surface, when precipitating from complicated brines. The total amount of mass deposited on the quartz crystal was recorded during each test. The supersaturated conditions that characterize the final brine consists the driving force for the formation of the scale on the quartz crystal.

The QCM holder is placed vertically in a glass vessel in order to avoid deposition effects on the quartz electrode due to gravity forces although based on previous reports, a different immersion angle does not result in variations in the recorded frequency changes [146]. However if the quartz crystal must be placed horizontally for measurements needs, then it's necessary the flow rate to be considered.

Transfer of the crystal holder from the air environment to the liquid one occurs every time the brines are mixed in the vessel. The change in the environment around the crystal is crucial and must be considered in order the recorded frequency values to be correct.

In this study the QCM200 model considers the change in the environment which surrounds the crystal by nulling the capacitance of the crystal. QCM incorporates a method of adjusting the C_o capacitance of the crystal equal to zero, insuring that the frequency values correspond to the true series resonant parameters of the quartz oscillator [147]. The capacitance cancellation always occurs when the crystal holder and the crystal are in the real measuring environment.

3.5 Atomic Force Microscope

3.5.1 Introduction

The observations of materials and surfaces is a key stage in most of scientific fields. The observations, as a method of defending the suggested hypothesis, were given the appropriate respect since sciences were born. However the development of the appropriate techniques did not follow the same progress as the sciences themselves.

The first step in the world of the observations was made in the 16^{th} century with the establishment of the microscopes [148]. In the following decades the light microscope was improved by far. In 1938 the transmission electron microscope (TEM) was developed bringing revolutionary progress in the world of observations. With the transmission electron microscopy, images of the specimen were accomplished from the interaction as the electrons beam passed through the examined sample. The electron microscopes were further improved to scanning electron microscopes, which use even higher energy beams and are capable of scanning specimens in high resolution.

The latest development in the field of observations was made with the invention of the scanning tunneling microscope in 1986. Since the inventors Binnig and Rohner made the scanning of surfaces at atomic level real, they were awarded the Nobel price in physics. The Atomic Force Microscope (AFM) belongs to this generation of microscopes and consist high accuracy scanning equipment for providing 3-D images of the topography of the scanned specimen. AFM consist an essential tool in this study for the observations of the adhered nature of the barite morphologies on the quartz electrode.

The force microscopy can be used in different extensions considering the needs of a project and the nature of the specimen. The Magnetic Force Microscopy (MFM) is based on the spatial variations of the magnetic forces on a sample surface [149].

Another type is the Lateral Force Microscopy (LFM) which measures lateral deflections of the cantilever that arise from forces on the cantilever parallel to the plane of the sample surface. This type of microscopy is useful for imagining variations in surface friction. Furthermore the Force Modulation Microscopy (FMM) is quite known as it is used for characterization of the sample's mechanical properties. Also the Phase Detection Microscopy (PDM) is used for mapping the variations in surface properties as elasticity. For measuring the charge of the surface, the Electrostatic Force Microscopy (EFM) is being used as voltage is being applied between the tip and the sample while the cantilever hovers above the surface.

3.5.2 AFM instrumentation

The extremely high quality of the AFM images is based on the scanning method but also on the analysis of the recorded topographies of the scanned samples. Instrumentation like the one presented in Figure 3.7 is needed in order for the scanning topographies to be recorded and further analyzed.

The equipment consists of the sample translator base, the AFM explorer, a scanner connected to an electronic control unit and a 3D scanning graphics software. The software used in this study is called Thermomicroscopes and is provided by Thermomicroscopes Corporation [150]. The examined sample is placed on the AFM base as shown in Figure 3.8.

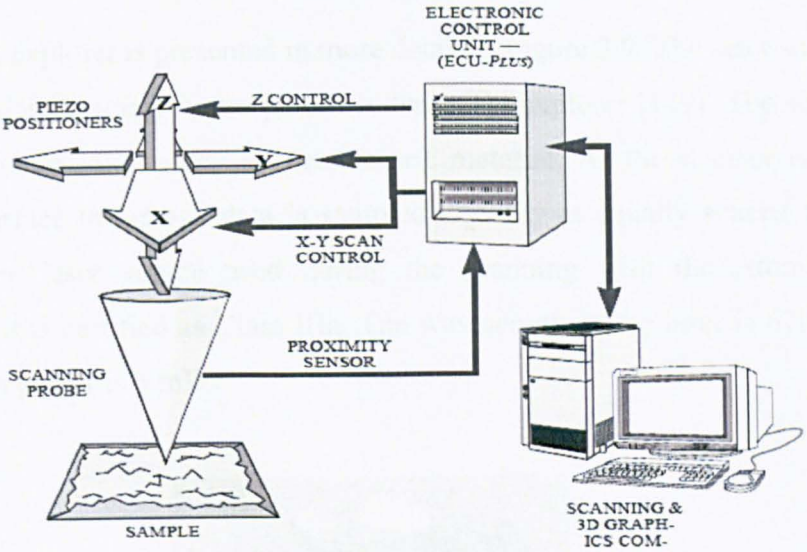

Figure 3.7: Diagram of the AFM equipment [150]

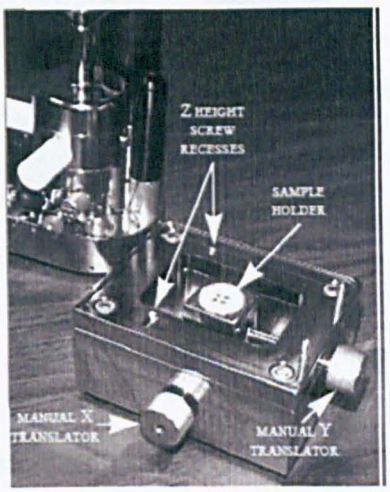

Figure 3.8: Sample translator [150]

The scanning takes place along the X and Y directions and the scanning range varies with the maximum approaching the 100 x 100 μm. The Z range approaches a few microns. All the X, Y and Z parameters are adjusted before the scanning of the sample. The X and Y parameters are adjusted according to the specific area of the specimen that is going to be scanned. The Z parameter is adjusted considering the nature and the thickness of the examined sample, as the Z factor is the responsible for the position of the cantilever and consequently of the tip.

The AFM explorer is presented in more detail in Figure 3.9. The laser source, the detector and the scanning tip are placed in the AFM explorer [149]. The scanner of the Atomic Force Microscopy is piezoelectric material. As the scanner is moving across the surface the image data is sampled digitally at equally spaced intervals. Regarding the laser source used during the scanning with the Atomic Force Microscopy, it is certified as Class IIIa. The wavelength of the laser is 670 nm and the maximum power is 3 mW.

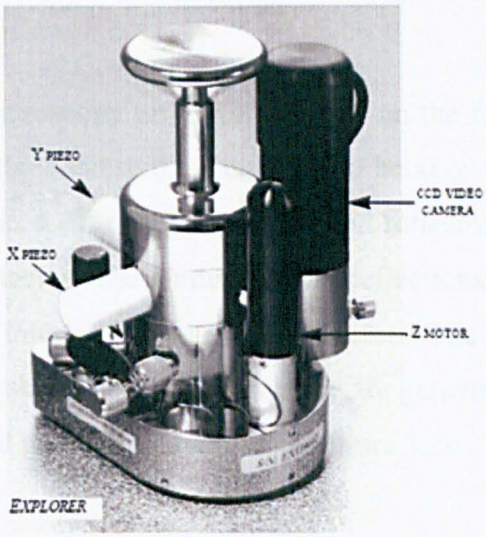

Figure 3.9: AFM explorer [150]

The tip used for scanning the surface is a couple of microns long, often less than 100 Angstrom in diameter and is located at the free end of a cantilever (100 - 200 μm long). The cantilever is V shaped providing low mechanical resistance to vertical deflection and high resistance to lateral torsion. The type of tips used in this study is Silicon Boride.

The tip consists the most fragile part of the atomic force microscope. Keeping the scanning tip in good conditions is crucial for an accurate scanning. The proper caution should be given to the treatment of the scanned specimen in order to prevent recording images with artifacts or even a damaging the tip. Still even if the samples

are properly pretreated, a scanning might result in images with artifacts due to the sharp surface of the sample. Specimen with steep sides, result in tip imaging. During the scanning of a sample characterized by high features, the tip can be imaged when it touches the bottom between the features. The recorded topography at that case is accurate but the height measurement of the features in the received image is not the real one. When tip imagining occurs according to the recorded data, then the tip must be replaced by a new one.

3.5.3 AFM principle

The Atomic Force Microscopy principle is based on the forces between the tip and the sample surface which cause the cantilever to bend or deflect [150]. A light beam from the laser bounced off of the cantilever and reflected through a mirror on to a four section photodetector. The amount of the deflections can be calculated by the difference in the light intensity in the different sectors. The detector measures the cantilever deflections, which allow the computer to generate a map of surface topography. The described procedure is shown in Figure 3.10.

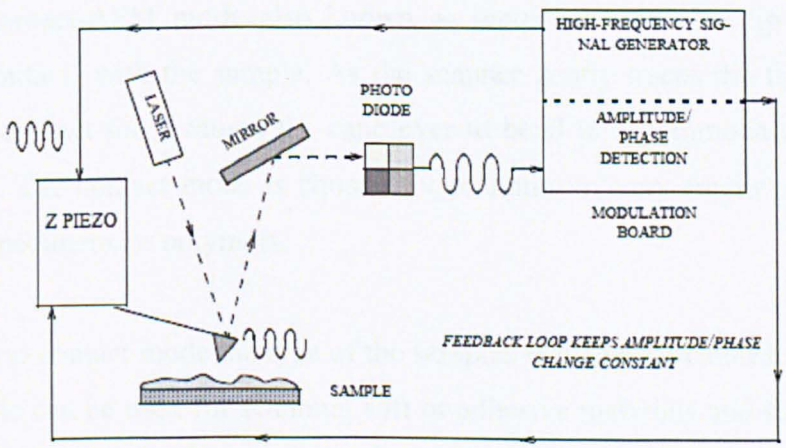

Figure 3.10: Diagram of the scanning process in non-contact operation [150]

The most commonly forces which contribute to the deflection of an AFM cantilever are Van Der Waals forces. The dependence of the Van Der Waals forces

upon the distance between the tip and the sample is shown in Figure 3.11. When the distance between the tip and the sample becomes bigger the attractive forces are in charge and the scanning takes place under non - contact mode.

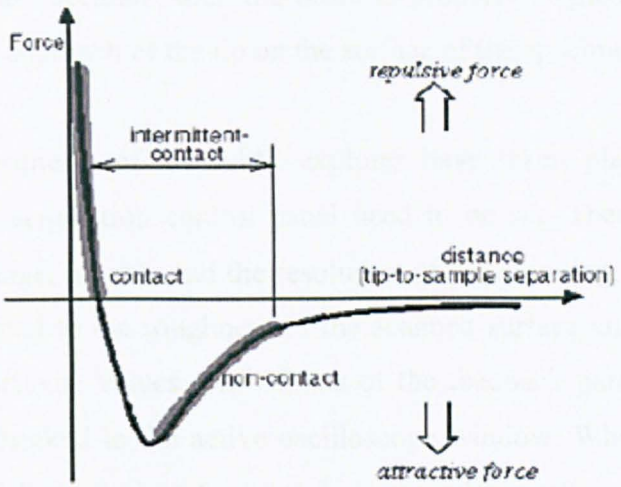

Figure 3.11: Diagram of the Van Der Vaals forces distance between the tip and the sample

Generally the Atomic Force Microscopy can be used in contact or non - contact mode. In contact-AFM mode also known as repulsive mode the tip makes soft 'physical contact' with the sample. As the scanner gently traces the tip across the sample the contact force causes the cantilever to bend to accommodate changes in topography. The contact mode is chosen for scanning of very fragile samples like biological specimens or polymers.

In the non-contact mode the type of the samples that can be scanned varies. Non-contact mode can be used for scanning soft or adhesive materials and further can be used for probation of hard materials which their scanning under contact conditions would blunt the tip and finally break it. As far as the total force between the tip and the sample mode is about 10^{-12} N [149]. In this study non-contact mode was chosen considering the nature of the examined samples.

3.5.4 AFM adjustments and analysis of the AFM topography maps

The proper treatment of the examined specimen and its correct placement on the sample base are followed by a number of adjustments of the AFM explorer. Initially the adjustment of the laser, the photodetector and the mirror are taking place. When these adjustments are accurate, then the beam is properly aligned on the scanning tip. Afterwards the approach of the tip on the surface of the specimen occurs.

Once the adjustments of the AFM explorer have taken place, a number of parameters on the acquisition control panel need to be set. These parameters are dealing with the range, the rate and the resolution of the scanning, as well as the set point which is related to the roughness of the scanned surface and finally with the integral and proportional values. The effects of the feedback parameter settings in real time can be checked in the active oscilloscope window. When the parameters are correct then a fully optimized feedback loop is obvious in the oscillation window showing the Z response. The Z response should be fast enough to keep the cantilever deflection to a minimum, while giving a sharp and clean representation of the surface topography [150].

After the scanning of the sample, a further analysis of the recorded data takes place in order for the received topography images to be as good as possible. The analysis is based on different functionalities of the Thermomicroscopes software which initially contribute to a decrease in the noise level. The most important features of the software during this part are the left or right shading of the recorded image. After the shading option has been applied it can be seen the improvement or even perfection in the calculated histogram. In overall there are many options that the software provides for further analysis of the data like calculation of the roughness of the surface and of the Z height for every data point of the scanning range.

3.6 Synchrotron X - ray diffraction

3.6.1 Introduction

X-rays are electromagnetic radiation with wavelengths between about 0.02 Å and 100 Å. They respond in the electromagnetic spectrum range between gamma-rays and the ultraviolet. X-rays have wavelengths similar to the size of atoms thus they are the correct order of magnitude for diffraction of atoms or crystalline solids. Since X-rays have a smaller wavelength than visible light, they are characterized by higher energies; hence they can penetrate matter more easily than visible light. The density of matter affects in high degree the penetration ability of X-rays [151].

3.6.2 Principles of X-ray diffraction

X-ray diffraction is based on the transfer of X-rays through the matter. When the crystalline solids are exposed to the X-rays, interference occurs among the waves scattered by the atoms. For the case where the waves are moving in phase with each other, then constructive interference takes place. On the other hand when the waves are out of phase, then destructive interference occurs. A better understanding of the interference and how it is related to Bragg's Law is possible through Figure 3.12. Ray 1 reflects off the upper atomic plane at an angle θ equal to its angle of incidence. Similarly, Ray 2 reflects off the lower atomic plane at the same angle θ.

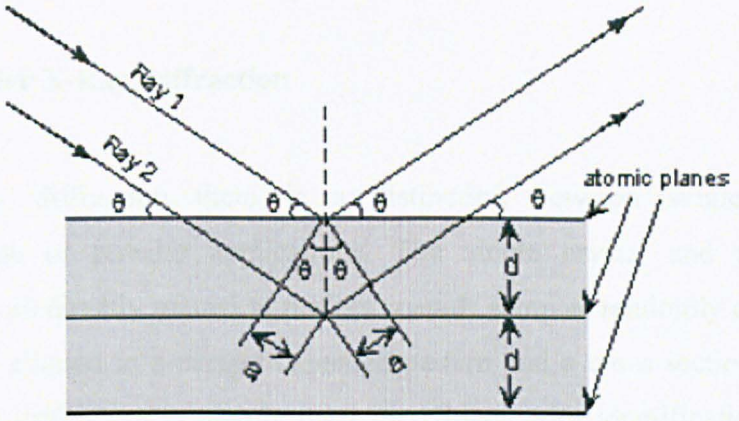

Figure 3.12: Diffraction of X-rays by a crystal [152]

When the distance 2a is not an integral number of wavelengths, then destructive interference will occur and the waves will not be as strong as when they entered the crystal. Thus, the condition for constructive interference to occur is given by Equation 3.4.

$$n\lambda = 2a \qquad \textbf{Equation 3.4}$$

The spacing d, between the atomic planes is given from the Equation 3.5.

$$2a = 2d\sin\theta \qquad \textbf{Equation 3.5}$$

$$\text{Thus } n\lambda = 2d\sin\theta \qquad \textbf{Equation 3.6}$$

Equation 3.6 responses to Bragg's Law for X-ray diffraction and when the equation is converted, the d-spacing between the atomic planes can be calculated [153].

3.6.3 Powder X-Ray Diffraction

In X-ray diffraction there is a distinction between single crystal and polycrystalline or powder applications. The single crystal and polycrystalline applications are directly related to perfect crystals samples randomly orientated with all unit cells aligned in a perfect extended pattern and a cross section of about 0.3 mm. Powder diffraction is mainly used for "finger print identification" of various solid materials, e.g. asbestos, quartz. Ideally in these cases a random distribution of all possible h, k, l planes takes place. The formation of the planes is initially indicated through the development of the Debye rings as shown in Figure 3.13.

Crystallites having reflecting planes (h, k, l) parallel to the specimen surface will contribute to the reflected intensities. Subsequently for a random sample, each possible reflection from a given set of h, k, l planes will have an equal number of crystallites contributing to it. All possible reflections can be revealed when the examined sample is in powder state.

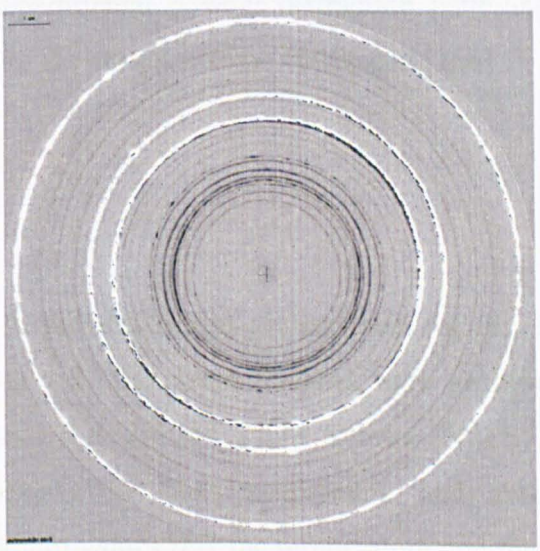

Figure 3.13: Debye Rings of barite formed at 95°C

The process of crystal structure determination for both cases (single crystal or powder) starts from collecting the diffraction data [154]. The diffraction data are recorded from the detector after the beam has penetrated the examined crystalline material as shown in Figure 3.14.

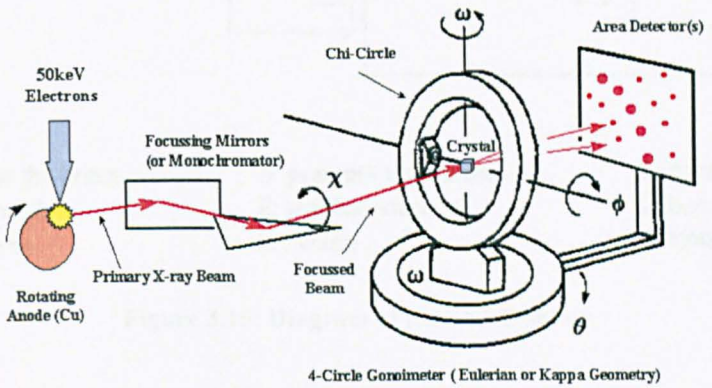

Figure 3.14: Schematic representation of powder X-Ray Diffraction

A series of structures can be generated from the powder diffraction data under a Monte Carlo algorithm [155]. A Rietveld refinement follows next, in order for the calculated and the experimental powder diffraction patterns to be compared and hence the correctness of the structure to be vindicated [156].

3.6.4 SXRD set up

The synchrotron X-ray diffraction set up used for this study is presented in Figure 3.15. The *in-situ* SXRD measurements were accomplished in the station X17B1 at the National Synchrotron Light Source (NSLS) in Brookhaven. The equipment is appropriate for high temperature and absolute pressure tested conditions. The maximum values that the temperature and the absolute pressure can reach are 200°C and 4000 psi respectively.

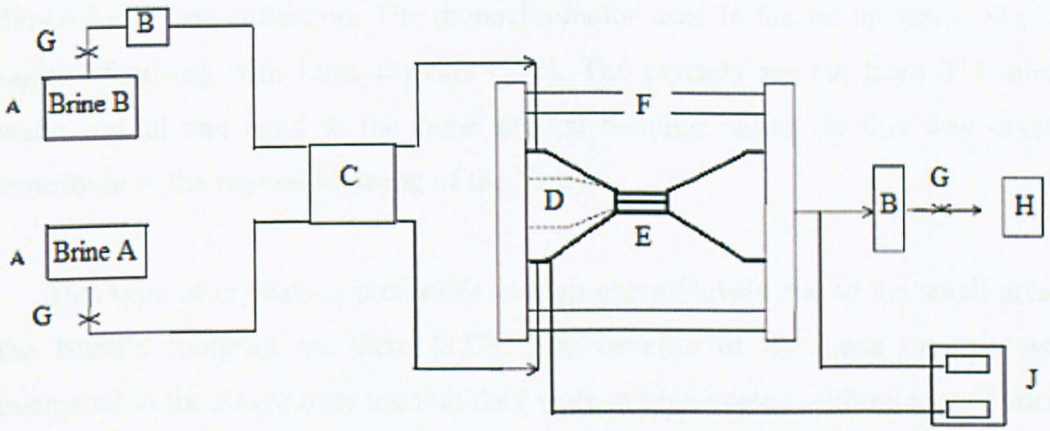

A: pumps for the brines
B: pressure transducers
C: oven unit with heating coils
D: mixing chamber
E: stainless steel cell
F: bolts
G: relief valves
H : waste
J: temperature reading panel

Figure 3.15: Diagram of the SXRD set up

In Figure 3.15 the different parts of the SXRD set up are illustrated. The capillary cell of the equipment is a key part as this is where the scale forms and the X-ray beam is focused. The first cell used in a set up like the one presented in Figure 3.15 was designed by Hennessy *et al.* [114]. During the *in-situ* measurements the precipitation and further the adhesion of inorganic scale in the tested cell results in increase of the differential pressure (ΔP) through time. The higher the differential pressure measured in the cell the higher is the blockage that occurs in the capillary. Potentially an intense increase in the recorded differential pressure due to the preferred orientation of single formed crystals in the capillary can result in further limitation in the flow of the solution.

The capillary cell used for the scaling study can have material, surface roughness and diameter characteristics adjustable to the purpose of the test. These features are the criterion for the choice of the beam line used in order to penetrate the cell and the forming material inside.

The type of radiation used was Cu Ka X-rays (λ= 0.17712 Å) with energy equal to 70 keV. The diffractometer was a siemens D500 model which offers two -

dimensional data collection. The monochromator used in the set up was a Si (311) sagittal focusing with Laue crystals [157]. The crystals are cut from 311 silicon wafer crystal and bend to the same sagittal bending radius. In this way crystals contribute to the sagittal focusing of the X-rays.

This type of crystals is preferable at high energy levels due to the small area of the beam's footprint on them [157]. The benefits of the Laue crystals when compared to the Bragg ones are that they work at high energy without loss of energy resolution and also they can increase the flux of the focused monochromatic beam by an order of magnitude [158]. In this study the flux rate was 10^{11} photons/s.

The data that are collected during the *in-situ* measurements are integrated and converted to appropriate file formats by the beam manager. The data were calibrated with NIST standard Al_2O_3 powder. The package of data is next analyzed by the use of FullProf Suite program. The specific program is the main tool for the basic analysis of the data as through this program the raw data are converted to data reflecting the relationships of the intensity with the θ angle or d space of the recorded diffraction peaks.

Since every diffraction peak detected at a specific θ angle represents a different crystal plane of the examined material the determination of the crystallography can be accomplished. A representative SXRD plot received from the process of the raw data recorded during the formation of barite on surface is shown in Figure 3.16.

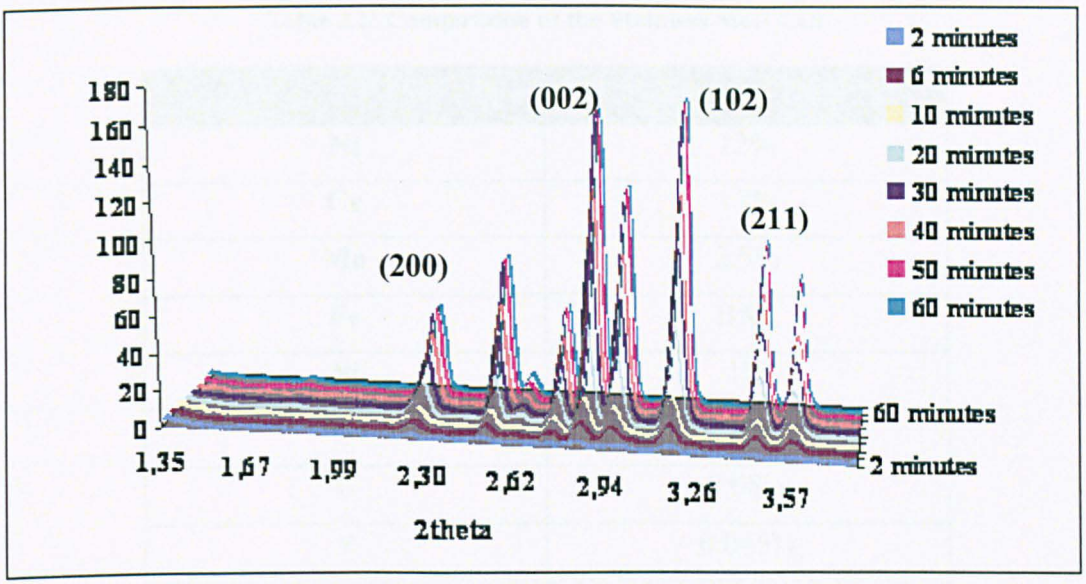

Figure 3.16: SXRD pattern of dominant barite surfaces formed at 95°C

3.7 Metal Substrates

The substrate was chosen considering (i) the compatibility with the selected techniques of this study and (ii) the type of surfaces used in the real systems of the oil sector. For the tests with the QCM, the substrate was a blending of titanium and gold (Ti/Au). This type of QCM electrodes consists a noble substrate, thus the deposition kinetics of barium sulphate are not influenced by the nature of the surface. The QCM electrode has 1 inch diameter and 331 μm thickness. The roughness of the quartz crystals is equal to 0.014 μm as calculated by the Taylor – Hobson precision.

The substrate used for the Synchrotron X-Ray Diffraction Measurements was a stainless steel (UNS 31603) cell. The composition of the stainless steel cell as presented in Table 3.2 is referring to surface composition used in the oil industry equipment, as it has an extreme durability and corrosion resistance in the pH range from 1.6 to 13. The cell is characterized by 2 mm bore diameter and surface finishes less than 1.6 μm Ra.

Table 3.2: Composition of the Stainless Steel Cell

UNS 31603 Stainless Steel	
Ni	12%
Cr	17%
Mo	2.5%
Fe	BAL
Si	1%
Mn	2%
C	0.08%
P	0.045%
S	0.03%

3.8 Techniques for bulk scale measurements

3.8.1 Inductive coupled plasma atomic emission spectroscopy for barium ions detection

One of the most commonly used analytical techniques is the Inductive Coupled Plasma Atomic Emission Spectroscopy (ICP-AES). The ICP-AES is appropriate for tracking metal elements in any kind of sample. The principle of the ICP-AES is based on the use of the inductive coupled plasma by the emission spectroscopy. The atoms and ions of the sample are excited in a higher energy level and emit electromagnetic radiation at wavelengths characteristics for every element. The monochromator separates the different wavelengths of interest. The intensity of the emissions is measured by a detector. The concentration of the element within the sample is indicatively given by the intensity values of the emissions.

When the analysis with the ICP-AES takes place, high importance is given to the preparation of the samples. The correct dilution of the matrix samples is crucial in order the analysis to be accurate. The diluted samples need to have the ion concentrations of the elements that are for tracking, in the range of the detection limits of the instrument.

In this project the JY 138 Ultrace model ICP-AES was used. Main focus was the tracking of the $[Ba^{2+}]$ in the bulk phase, when the formation of the barite on the tested metallic surface had already occurred. The expected variations in the received ICP-AES data would be due to the different supersaturation ratio conditions tested and the effect of the inhibitor if present.

The guideline for the preparation of the samples is dilution of 1 ml of the sample in 19 ml of quencher solution. The examined solutions are prepared after mixing the formation water and seawater, with compositions as they will be presented in chapters 4. For the inhibited tests the inhibitor is added during the mixing of the brines. The final solutions are left in static conditions and after 1 hour of precipitation, samples of 1 ml are taken from the bulk phase with the use of syringe.

The quencher solution consists of KCl in a concentration of 3000 ppm in K^+ and PPCA in concentration 1000 ppm. Analysis of the diluted samples within 48 hours is recommended as after this period the quencher solution can be less active.

3.8.2 Measuring the turbidity

When measuring the turbidity of a solution, the investigation of the bulk phase takes place. During the turbidity measurements a beam focuses on the particles being in the bulk state. The particles scatter the beam and a detector collects the scattered light [159]. Before measuring the turbidity of supersaturated solutions, a

good shake of the solution is necessary prior to the measurement since the amount of particles in the bulk is high.

The turbidity measurements have been proved quite useful in many research fields of water treatment. For example determination of the silica dissolution mechanisms and the effect of inhibitors and dissolvers on silica precipitating from high supersaturated ratio brines under static conditions has taken place through turbidity measurements [160].

The turbidity meter used in this study was a HACH/DR 890 model. Turbidity measurements were done in order to determine the kinetics of the bulk phase during the initial stage of precipitation of barium sulphate in the absence and presence of the tested inhibitors. Measuring the kinetics in the bulk state and determining the kinetics on the surface as the $BaSO_4$ forms, results in a complete description of the barium sulphate precipitation and deposition processes.

CHAPTER 4 Initial stages of barium sulphate formation kinetics on a metallic surface in the presence and absence of inhibitors

4.1 Introduction

In this chapter the results recorded during the initial stages of barium sulphate formation on a metallic surface are presented. The precipitation of barite occurred after mixing brines containing divalent cations (Ca^{2+}, Mg^{2+} and Sr^{2+}). This is one of the few reports of the kinetics of barium sulphate precipitating from complicated brines for surface scaling studies. The presence of divalent cations in the formation and synthetic seawater imitates the real nature of the brines used during oil recovery. Moreover in order to investigate the effect of the supersaturation index on the formation kinetics of barium sulphate on a surface three supersaturation indices were tested.

The kinetics of the barite formation on the surface during the first hour of precipitation was followed with the Quartz Crystal Microbalance. The deposited $BaSO_4$ was observed with the Atomic Force Microscope at different scanning ranges allowing the complete investigation of the adhered layers of barite on the surface. Regarding the barium sulphate kinetics in the bulk phase, it was determined using turbidity measurements and inductive coupled plasma (ICP) analysis.

4.2 Experimental details

The brines tested in this section were characterized by three different compositions. The brines after being prepared were filtered with 0.2 μm cellulose nitrate membrane filters. The pH was measured in the range of 5.5 - 6.5. The

examined mixing ratio of formation water and seawater was 1:1 for all the tests. For the inhibited tests the chemical reagent was added in the seawater just before the mixing of the brines. All the tests took place at room temperature. A summary of the experiments described in this chapter is given in Table 4.1.

Table 4.1: Summary of the experimental session

Type of mixture	Supersaturation index	Supersaturation ratio	Inhibitor	Concentration of inhibitor (ppm)
A	1.45	28	none	none
B	2.64	436	none	none
			PPCA	1
				4
				10
			DETPMP	1
				4
				10
C	4.32	20,892	none	none
			PPCA	1
				2
				4
				10

The quartz crystals used were AT – cut crystals and they are characterized by 5 MHz resonance frequency. The density of the quartz p_q is 2.648 g cm $^{-3}$ and the shear modulus of the quartz μ_q is 2.947 x 10^{11} g cm^{-1} s^{-2}.

The measurements with Quartz Crystal Microbalance (QCM) were of 1 hour duration and the sample interval was adjusted to 0.01 seconds. After mixing the formation water and the synthetic seawater in order to produce the final

supersaturated solution, the adjustment of the capacitance equal to zero took place. After the adjustment of the C_o, the recording of the instantaneous deposited mass of barium sulphate on the quartz crystal started.

4.3 Barium sulphate measurements on the surface

4.3.1 Technique's challenges

Both of the techniques used for the experimental work presented in this chapter, were committed according to the needs of this study. The QCM200, used for the first time for studying the deposition of barite, was able to provide accurate and reproducible results after a month's period. Within this time period the experimental protocol and the effect of the capacitance cancellation were under probation. The previous choice of a different Quartz Crystal Microbalance model was false, since operation of the crystal in liquid environment could not be achieved. Regarding the Atomic Force Microscope, the committing period approached four months. This was due to the skillful operation that the equipment requires and also due to the insoluble nature of the barite samples, which results quickly in damaging the scanning tip.

During the barium sulphate formation kinetics measurements on the surface it was crucial to achieve reproducibility in the recorded data. Reproducible results show that the techniques used, are suitable for the specific experimental goal and most important the investigated scaling system can be followed with high accuracy. In the following sections where the $BaSO_4$ surface measurements with the Quartz Crystal Microbalance are presented, 2 reproduced tests for each examined case are given. However the number of tests that took place for each examined case was equal or higher than 4. The standard deviations of the recorded data for all the measurements are presented later on showing that the reproducibility was maintained even for a high number of tests.

4.3.2 $BaSO_4$ formation kinetics from mixture A

The first set of brines tested named as mixture A and presented in Table 4.2, was the one characterized by the lower supersaturation index. The calculations with the ScaleSoft Pitzer software have given the value of 1.45 for the supersaturation index for mixture A. This brines mixture was composed and tested in order to follow the kinetics of barium sulphate formation at very low supersaturation index. The composition of mixture A is based on the brine composition found in a sponsor's reservoir.

Table 4.2: Composition of mixture A

Type of ions	Formation Water (ppm)	Synthetic Seawater (ppm)
K^+	400	350
Ca^{2+}	200	700
Mg^{2+}	700	200
Ba^{2+}	100	0
Sr^{2+}	200	350
SO_4^{2-}	0	101
Na^+	13570	17940

The formation kinetics of the barium sulphate precipitating from mixture A on the surface is presented in Figure 4.1, as recorded with the Quartz Crystal Microbalance. Figure 4.1 shows that during the first two minutes of barium sulphate precipitation the formation of the barite on the surface is not linear and the amount of scale deposited on the quartz crystal is less than 0.5 $\mu g/cm^2$ Afterwards the formation of barite reveals a linear growth trend, as at this low supersaturation index conditions $BaSO_4$ grows steadily on the surface. The deposited mass on the gold

electrode after the first hour of precipitation was less than 4 μg/cm^2. The barite formed on the electrode of the Quartz Crystal Microbalance has been observed with the Atomic Force Microscope at different ranges as presented in Figure 4.2-Figure 4.4.

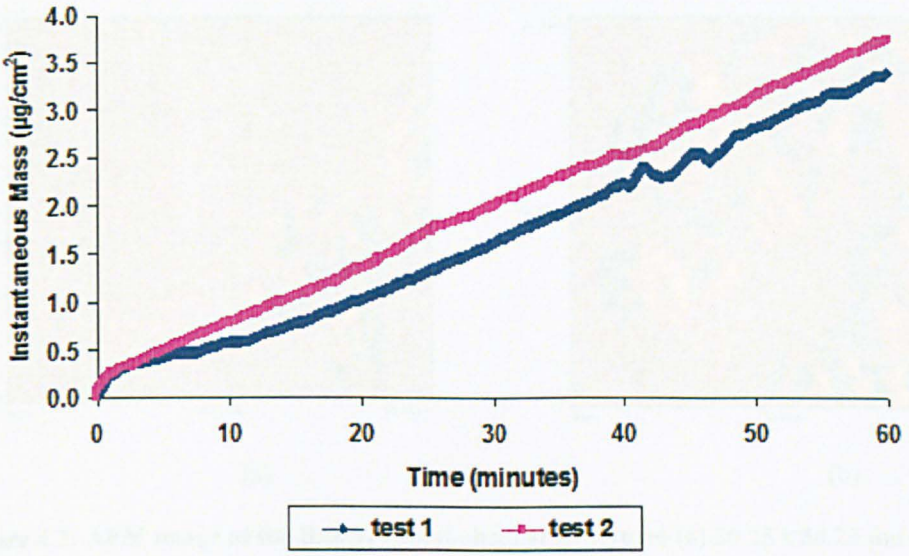

Figure 4.1: QCM measurements for mixture A

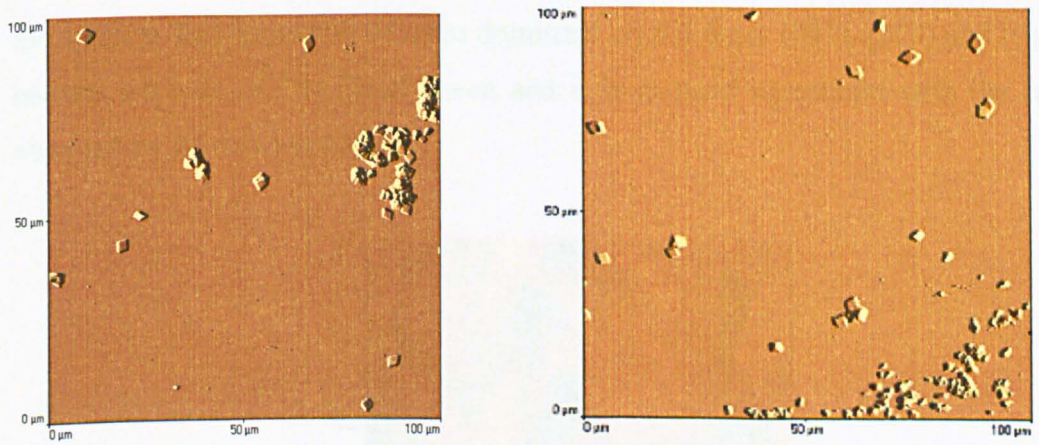

(a) (b)

Figure 4.2: (a) Adhered $BaSO_4$ on quartz crystal & (b) different scanned area of the crystal

Figure 4.2 shows that the amount of the barium sulphate formed on the surface is small and most of the active area of the surface has no scale on it. A closer

observation to the barite crystals formed when precipitating from mixture A is possible through Figure 4.3. Barium sulphate has deposited as single crystals and also as agglomerations of crystals. Under these low supersaturation index conditions the observed morphology of the barite is strictly rhombohedral

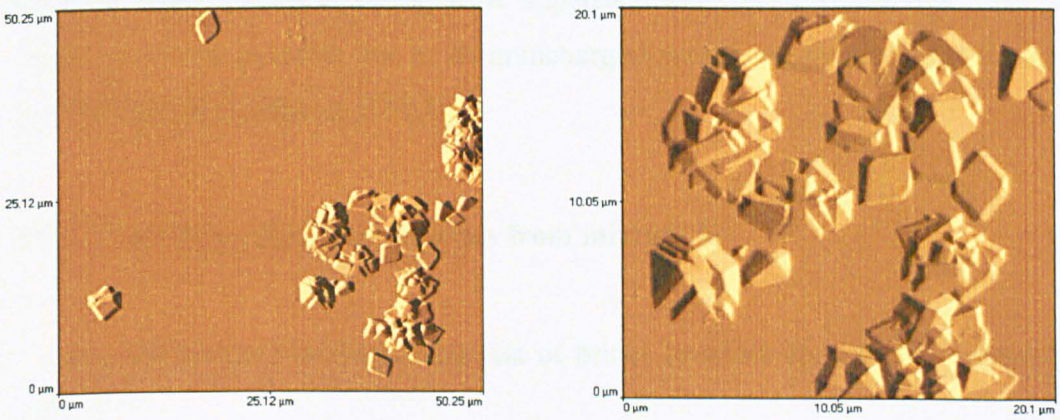

(a) (b)

Figure 4.3: AFM image of the $BaSO_4$ rhombohedral structures (a) 50.25 x 50.25 µm scanning range (b) 20.1 x 20.1 µm scanning range

Figure 4.4 shows clearly the rhombohedral structure of the deposited barite on the surface. The formation of three dominant crystal faces (001), (210) and (011) of barium sulphate can be clearly seen and it is in good agreement with the results obtained by Bromley *et al.* [65].

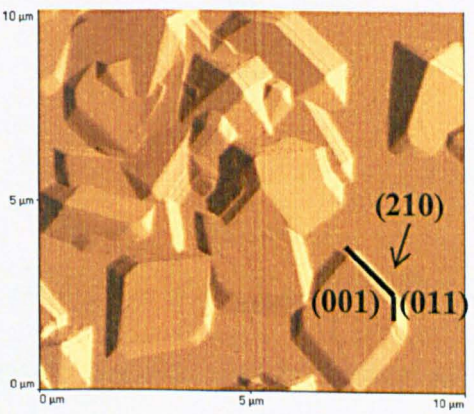

Figure 4.4: The (210), (001) and (011) crystal faces of the formed barite

Regarding the (001) crystal surface of $BaSO_4$ is a flat surface growing parallel to the monolayer. Both the (001) and (210) crystal surfaces of barium sulphate manage to dominate the equilibrium morphology of the formed barite since they are the crystal faces with the lowest energy [57]. The presence of the (011) crystal face of barite is important under the specific supersaturation index conditions, since it is considered to be unstable due to its unincharged nature and the very fast formation thus its capture is difficult [161,162].

4.3.3 $BaSO_4$ precipitation kinetics from mixture B

The composition of the second test of brines (mixture B) tested is presented in Table 4.3.

Table 4.3: Composition of mixture B

Type of ions	Formation Water (ppm)	Synthetic Seawater (ppm)
K^+	1906	380
Ca^{2+}	2033	405
Mg^{2+}	547	1215
Ba^{2+}	80	0
Sr^{2+}	417	0
SO_4^{2-}	0	2780
Na^+	26535	10900

The specific composition has been used by Boak *et al.* for seeded and unseeded tests of barium sulphate as it imitates an off-shore composition found in North Sea [129]. The supersaturation index for mixture B is equal to 2.64 revealing that the

concentrations of the divalent cations are high. Only the concentration of barium is kept at a low level (80 ppm) in order to achieve the specific supersaturation index with respect to barite.

4.3.3.1 Uninhibited formation of barite

The QCM measurements for the formed barite precipitating from mixture B are presented in Figure 4.5. The plots recorded during the reproduced tests are characterized by two parts. The first part reveals a quick formation of barite on the surface which lasts until the 10th minute followed by a steady growth until the end of the test.

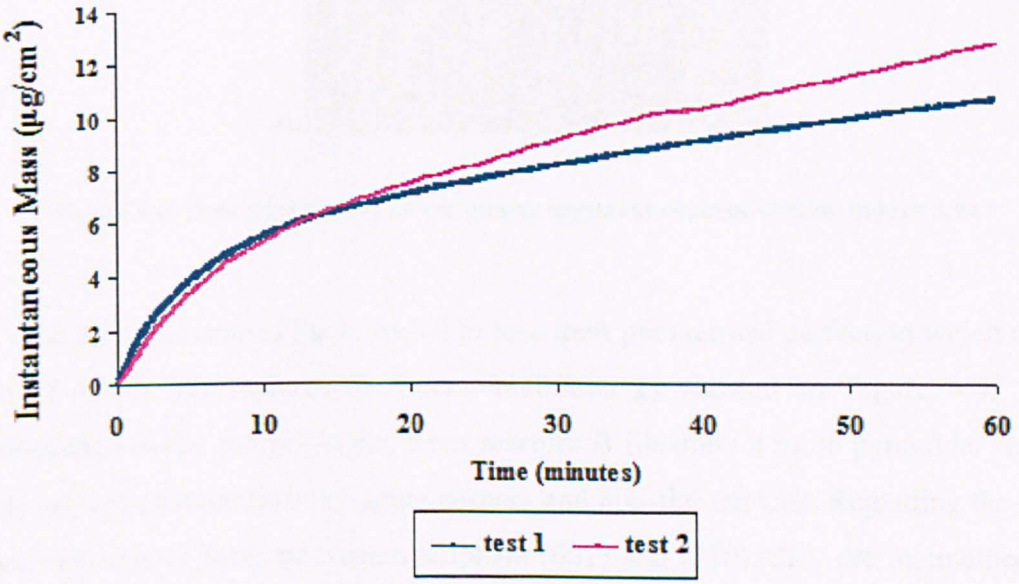

Figure 4.5: QCM measurements for mixture B

The deposited mass on the gold electrode after the first hour of precipitation was between 10 and 14 µg/cm^2. The formation of barite when precipitating from mixture B results in a larger amount of barium sulphate deposited on the surface compared to the amount formed when mixture A was tested. This is due to the increased

supersaturation index tested with mixture B, which results in faster kinetics of the system and higher amount of formed barite.

The observations of the deposited barite crystals on the surface are in good agreement with the QCM measurements. Figure 4.6 shows the high number of $BaSO_4$ crystals formed on the surface. The barite crystals are distributed all over the surface. The structure of the barium sulphate formed under these tested conditions can be seen clearly in Figure 4.7 and Figure 4.8.

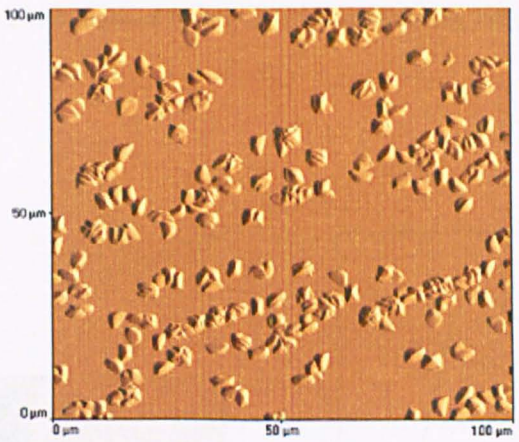

Figure 4.6: Deposited $BaSO_4$ on the quartz crystal at supersaturation index= 2.64

The barite structures have started to lose their geometrical perfection which they had at lower supersaturation index conditions as showed in Figure 4.4. The precipitated barite morphologies from mixture B illustrate a more pyramidal shape and they are characterized by acute corners and non-flat terraces. Regarding the two dominant crystal faces of barium sulphate (001) and (210), they are maintained in the formed barite (Figure 4.8 (a)). However at this supersaturation index the (011) is not present anymore but new crystal faces start becoming dominant for the deposited barium sulphate like the (110). The growth of the (110) lattice plane of barite on the b axis is presented in Figure 4.8 (b).

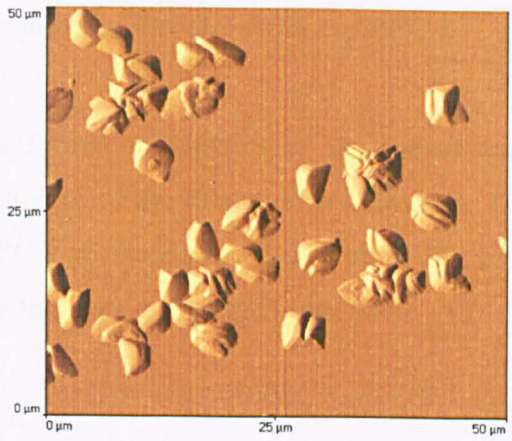

Figure 4.7: AFM images of barite crystals at scanning range 50 x 50 µm

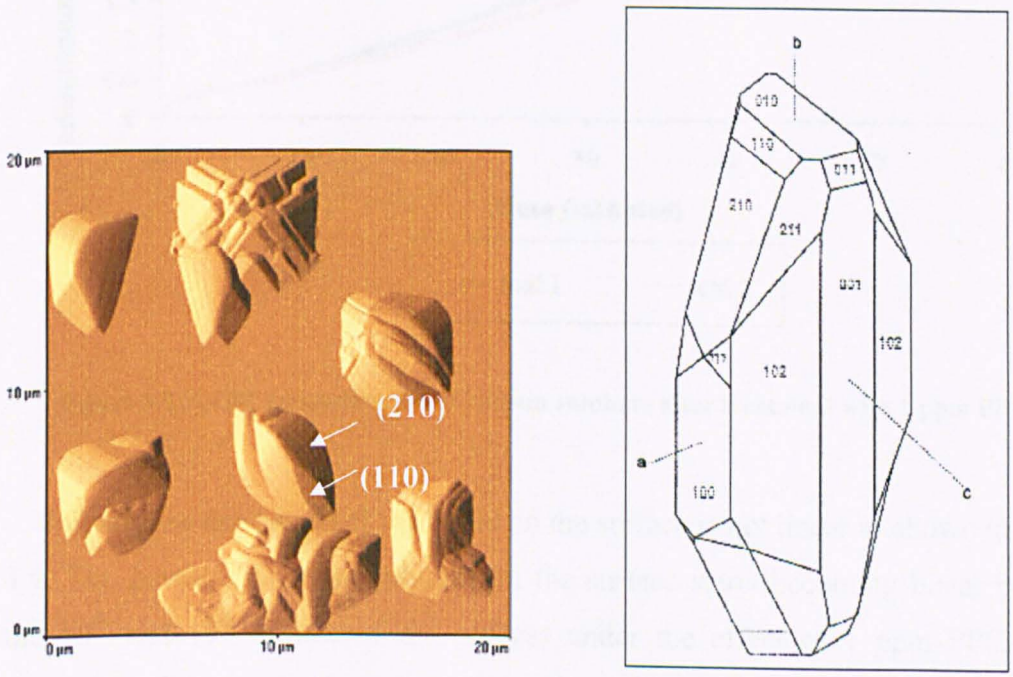

(a) **(b)**

Figure 4.8: (a) AFM image of barite and (b) Diagram of typical barite crystal [163]

4.3.3.2 Inhibited formation of $BaSO_4$ - Effect of PPCA

In this section the formation kinetics of the barite scale on the surface are presented after the treatment of the brines with inhibitors. The first inhibitor tested with mixture B was PPCA at concentration of 1 ppm. The plots recorded during the QCM measurement are the ones shown in Figure 4.9.

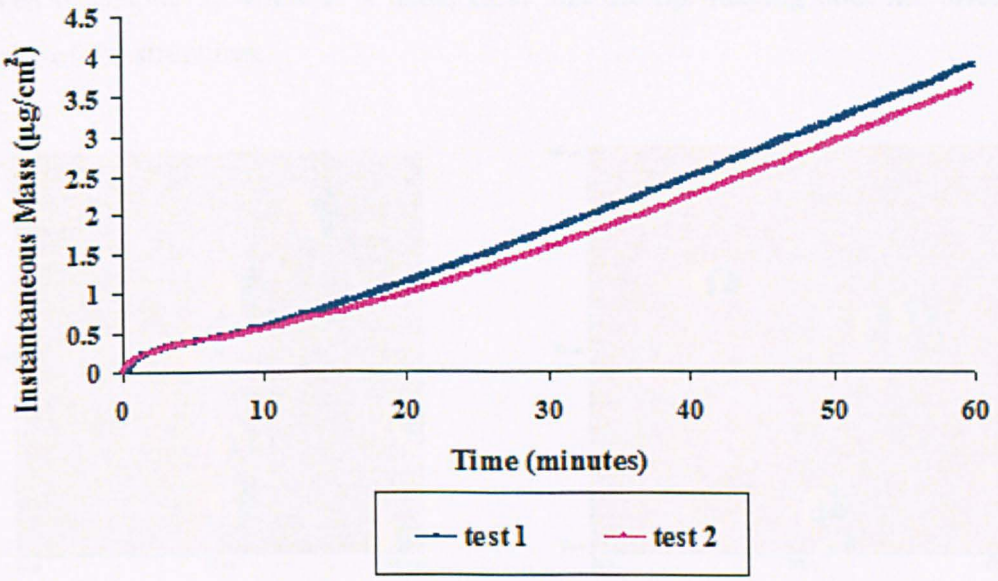

Figure 4.9: QCM measurements of barium sulphate after treatment with 1 ppm PPCA

Initially the deposition of the barite on the surface is not linear as shown in Figure 4.9. The growth of barium sulphate on the surface starts becoming linear between the 10^{th} and 18^{th} minute of the process under the effect of 1 ppm PPCA. The formation of the inorganic scale continues to follow the linear trend until the end of the test where the recorded mass is equal to 4.5 $\mu g/cm^2$. Although the growth of the barite crystals formed on the surface continues in time as shown by the QCM measurements, the final amount of the deposited barium sulphate after 1 hour of precipitation is quite small. This is also confirmed by the observations with the Atomic Force Microscope.

Figure 4.10 presents two different areas of the scanned surface. The number of the deposited barite crystals is small thus most of the surface remains uncovered. In Figure 4.11 the barium sulphate structures formed, after 1 ppm of PPCA was applied to the system, are presented. It is obvious that the presence of the inhibitor affected the geometry of the crystals resulting in more round shaped barite morphologies. Further no flat terraces are observed. It is worth noting that in Figure 4.10 and Figure 4.11 the tip imaging has been recorded. Details for the tip imaging were given in chapter 3, where it is made clear that the tip imaging does not affect the shape of the structures.

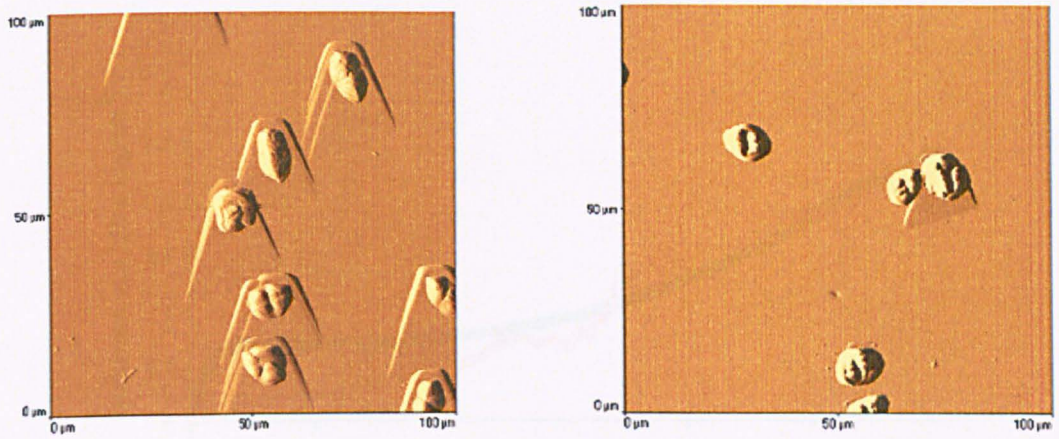

(a) (b)

Figure 4.10: Barite crystals after treatment with 1 ppm PPCA (a) first scanned area of the surface & (b) second scanned area of the surface

Figure 4.11: Barite morphologies under the treatment of 1 ppm PPCA

The kinetics of the barium sulphate formation on the surface was followed after the addition of 4 ppm PPCA. The plots presented in Figure 4.12 show that the growth of $BaSO_4$ on the surface does not follow a linear trend. Moreover the plots seem to vary between them. It is suggested that the reproducibility is difficult to be achieved at this low level of precipitation with 4 ppm PPCA present. However the amount of barite deposited on the surface after one hour of precipitation is in the same range for both tests approaching the value of 2.5 $\mu g/cm^2$. The decrease in the barite mass on the quartz crystal indicates the effectiveness of PPCA on the formed barite crystals.

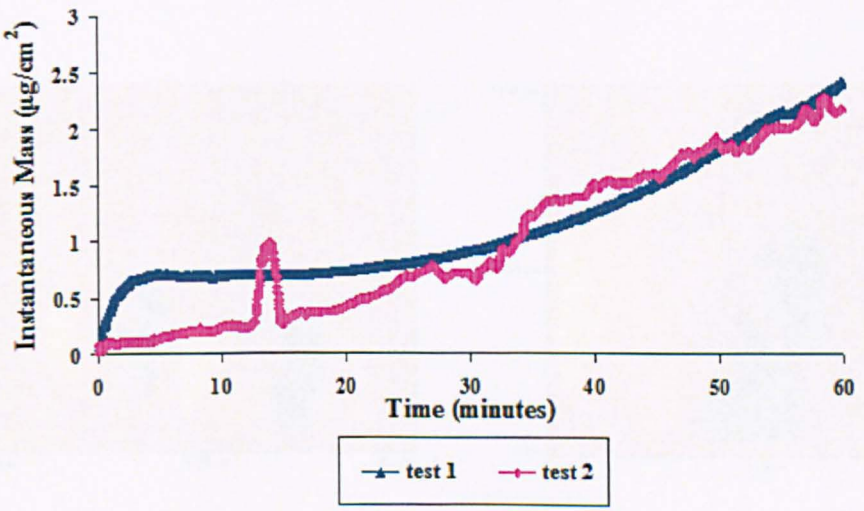

Figure 4.12: QCM measurements of barium sulphate after treatment with 4 ppm PPCA

The observations with the Atomic Force Microscope presented in Figure 4.13 show the decreased amount of barite formed on the gold electrode. A closer investigation of the topography recorded indicates the different size of crystals present on the surface (Figure 4.14 (a)).

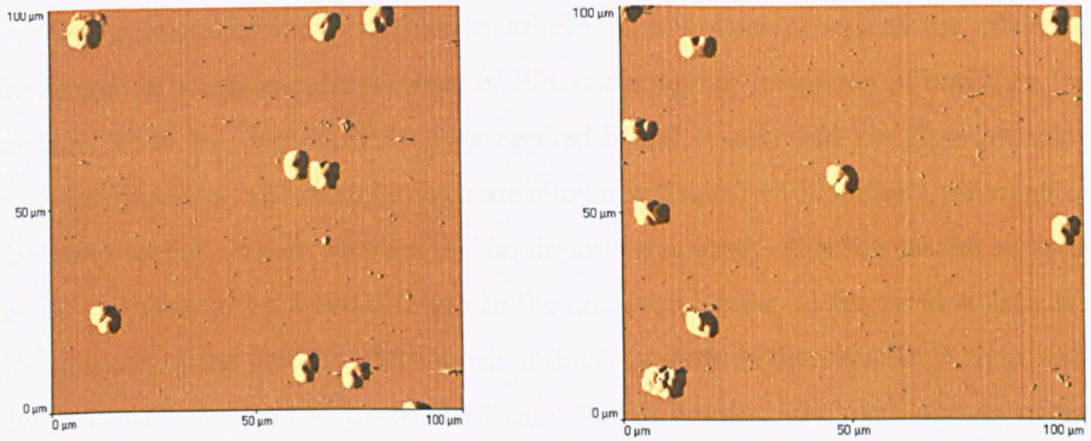

(a) (b)

Figure 4.13: Barite morphologies after treatment with 4 ppm PPCA (a) first scanned area of the surface & (b) second scanned area

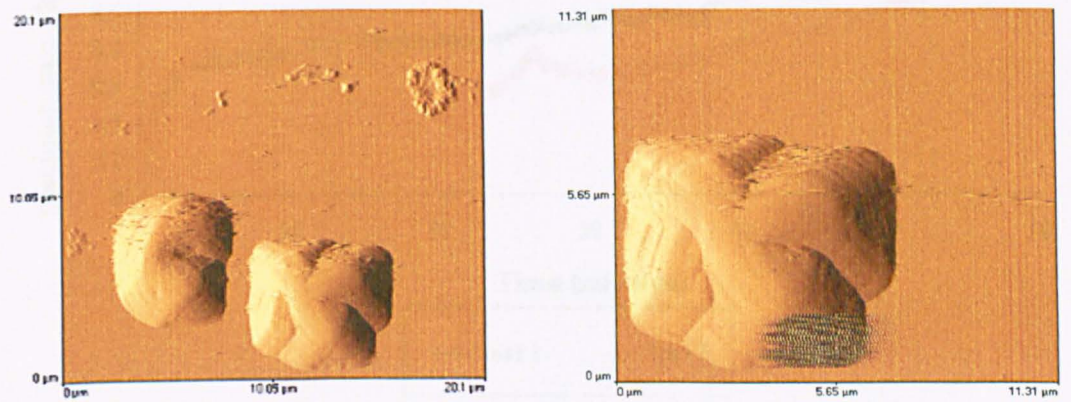

(a) (b)

Figure 4.14: AFM images of the inhibited barite crystals at (a) 20.1 x 20.1µm & (b) 11.31 x 11.31 µm

The formation of barite on the surface was inhibited by the presence of 4 ppm PPCA thus the growth of the early deposited barite crystals was retarded. The grown $BaSO_4$ crystals are affected by the presence of PPCA in the precipitating system since they reveal a more square shaped structure as shown in Figure 4.13 and the corners of the morphologies are obtuse (Figure 4.14).

The good inhibition performance of PPCA at 4 ppm promoted the effort of investigating a higher concentration of PPCA during the formation of barite on the surface. Thus 10 ppm of PPCA was applied in the system and the plots recorded with the quartz crystal microbalance are shown in Figure 4.15. Initially the trend of the plots reveal a quick increase in the deposited amount of barite on the surface, which is followed by a stabilization in the amount of mass on the surface until the 15th minute of the process. Afterwards a linear growth of the crystals in time until the end of the test can be determined from the QCM plot. The total amount of the deposited barite under the influence of the 10 ppm PPCA was less than 0.9 μg/cm^2.

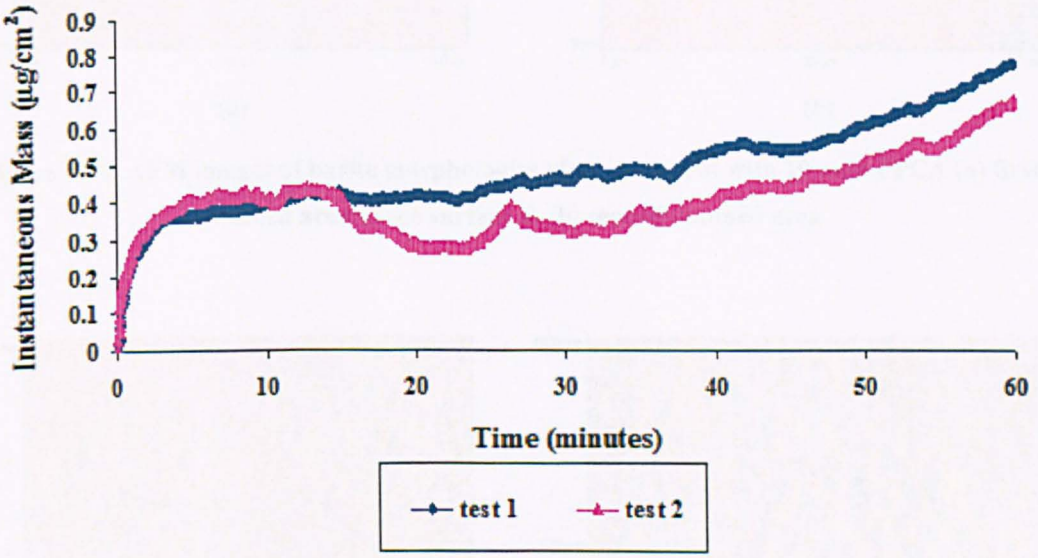

Figure 4.15: QCM measurements of barium sulphate after treatment with 10 ppm PPCA

The significant inhibition effect of PPCA on the barite crystals at this concentration was also confirmed by the observations of the deposited morphologies on the surface. Figure 4.16 presents the formation of barium sulphate on the quartz crystal. It is obvious that barite crystals are considered in different sizes. The exact structure of the $BaSO_4$ morphologies adhered on the surface is difficult to characterize. The scanning of the topography at higher magnification (Figure 4.17) indicates the formation of round barite particles. The morphology of the particles suggests that the aggregation mechanism is dominant under these supersaturation

ratio conditions and in the presence of 10 ppm PPCA, since no preference to the surface or to any direction is shown [27].

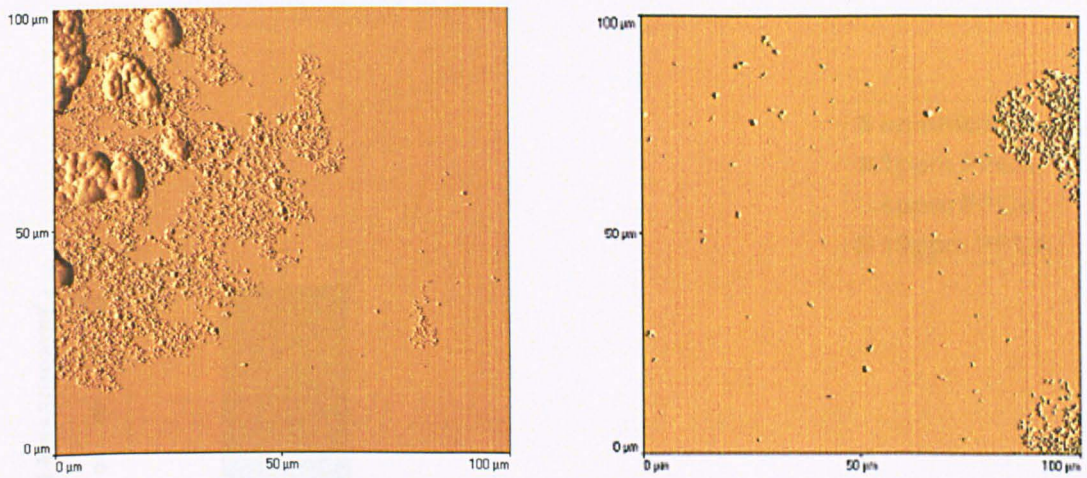

(a) (b)

Figure 4.16: AFM images of barite morphologies after treatment with 10 ppm PPCA (a) first scanned area of the surface & (b) second scanned area

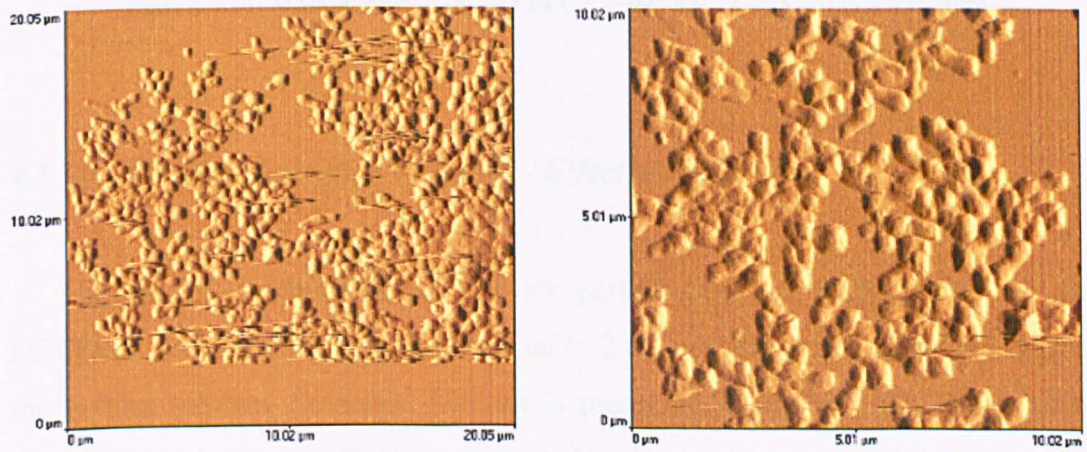

(a) (b)

Figure 4.17: AFM images of inhibited barium sulphate crystals at (a) 20.05 x 20.05 µm & (b) 10.02 x 10.02 µm

The total effect of PPCA on the formed barite precipitating from mixture B, including the standard deviations for all the measurements that took place with the

QCM are presented in Figure 4.18. The improvement of the performance of PPCA as inhibitor, when its concentration was increased, is confirmed for a high number of tests that took place for every examined case.

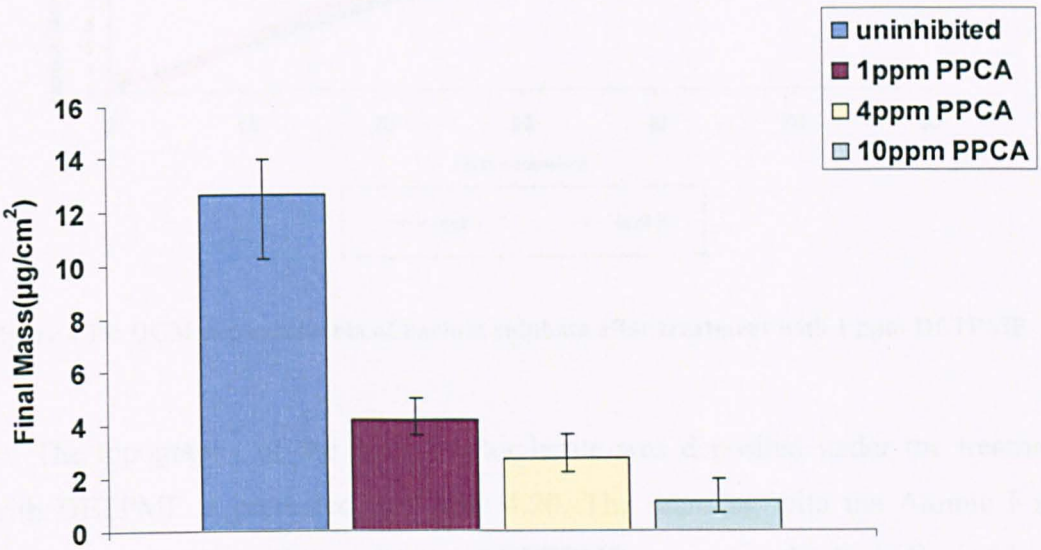

Figure 4.18: Standard deviation of PPCA effect on formed barium sulphate

4.3.3.3 Inhibited formation of $BaSO_4$ - Effect of DETPMP

The second inhibitor tested for its performance on barite formation was DETPMP. At supersaturation index equal to 2.64, the effect of 1 ppm DETPMP on the barium sulphate formation kinetics is presented in Figure 4.19. The recorded plots show a steady growth of the deposited scale on the surface. After the first hour of precipitation, the amount of mass deposited on the quartz crystal approached the value of 12 μg/cm^2. DETPMP, at least at this specific concentration, does not inhibit the presence of $BaSO_4$ on the surface.

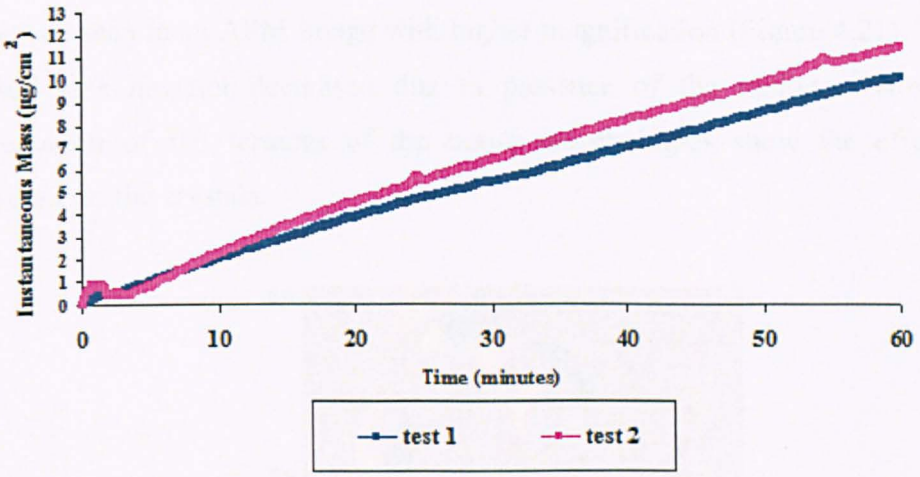

Figure 4.19: QCM measurements of barium sulphate after treatment with 1 ppm DETPMP

The topography of the surface after barite was deposited under the treatment with DETPMP is presented in Figure 4.20. The scanning with the Atomic Force Microscope confirms the weakness of DETPMP to prevent the formation of barite thus the amount observed on the quartz crystal is high.

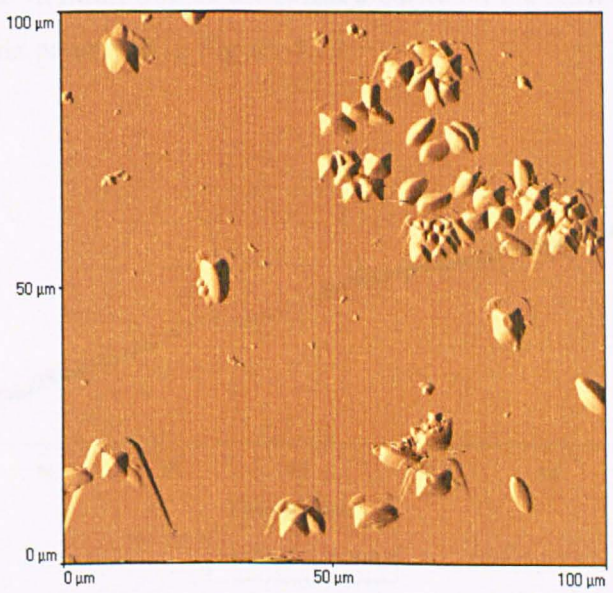

Figure 4.20: Formed barite scale after treatment with 1 ppm DETPMP

The $BaSO_4$ particles formed after the addition of 1 ppm DETPMP can be better observed seen in an AFM image with higher magnification (Figure 4.21). The barite crystal size has not decreased due to presence of the inhibitor. However the observation of flat terraces of the barite morphologies show the effect of the inhibitor on the crystals.

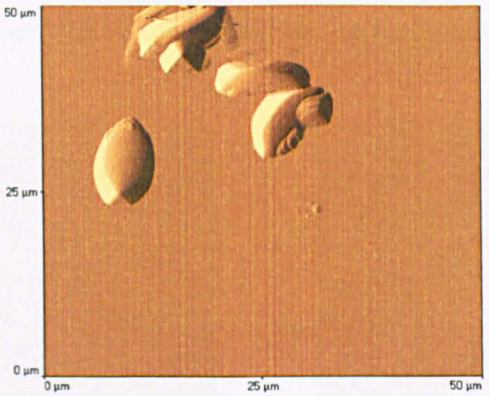

Figure 4.21: AFM image of barite morphology (50x50 µm)

An increase in the concentration of the examined inhibitor up to 4 ppm was still not enough to result in inhibition of the formed barite on the surface as shown by the QCM measurements presented in Figure 4.22.

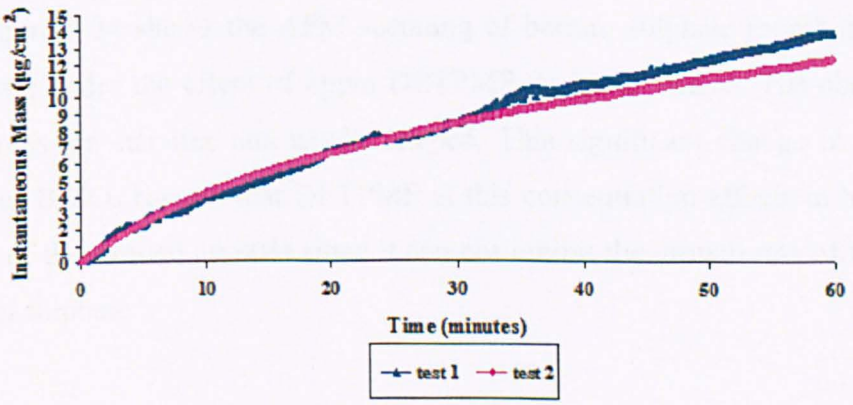

Figure 4.22: QCM measurements of barium sulphate after treatment with 4 ppm DETPMP

Again the recorded growth of barium sulphate seems steady in time resulting in deposition of 14 μg/cm^2 of formed scale on the surface similar to the amount recorded with the 1 ppm of DETPMP as presented above. The AFM images from the quartz crystals scanning show the presence of different barite morphologies grown on the surface compared to the ones observed previously. Figure 4.23 presents the observed structures of barite at different parts of the surface, where a variation in the size of the crystals developed on the surface is noticeable.

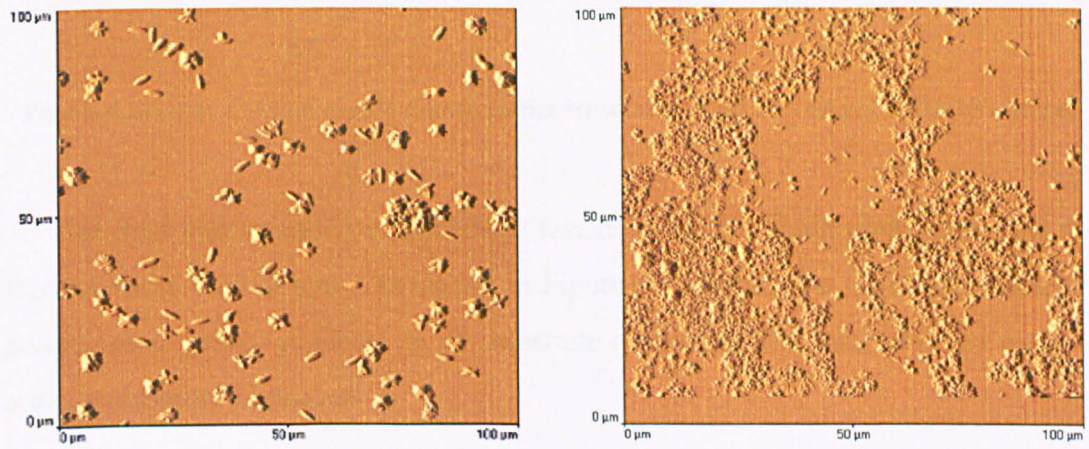

(a) (b)

Figure 4.23: The effect of 4 ppm DETPMP on barite structures (a) big size barite crystals & (b) small size crystals

Figure 4.24 shows the AFM scanning of barium sulphate morphologies on the substrate under the effect of 4ppm DETPMP, at lower ranges. The observed barite structures are star like and needle shaped. This significant change in the adherent scale of $BaSO_4$ reveals that DETPMP at this concentration affects in high level the shape of the formed crystals since it can not inhibit the growth rate of the deposited barium sulphate.

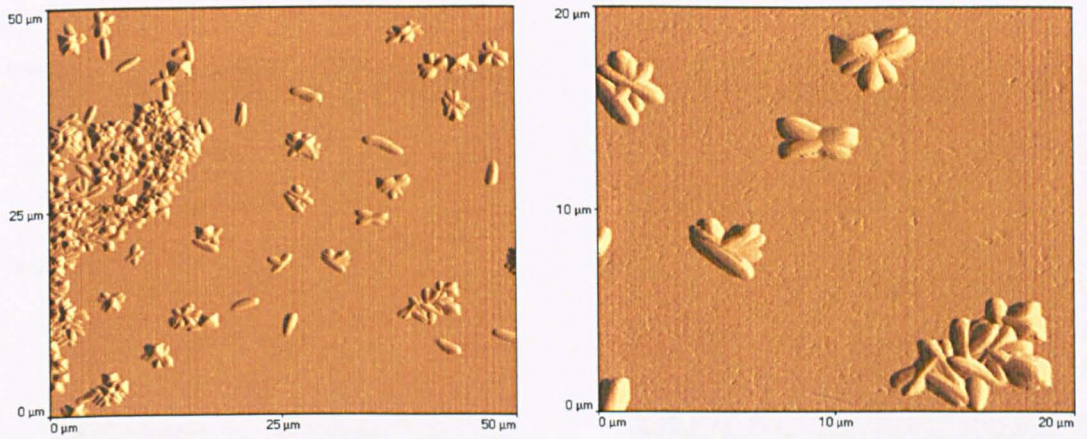

(a) (b)

Figure 4.24: Star like and needle shaped barite structures at (a) 50 x 50 µm & (b) 20 x 20 µm

The final concentration of DETPMP tested for its inhibition performance on the formed barite was 10 ppm. As shown in Figure 4.25 during the first hour of $BaSO_4$ precipitation growth of barite on the substrate occurs and the final recorded mass of scale was almost 11 µg/cm^2.

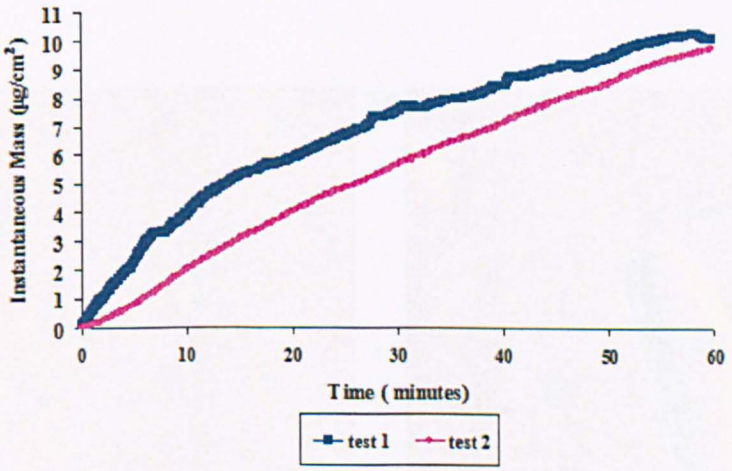

Figure 4.25: QCM measurements of barium sulphate after treatment with 10 ppm DETPMP

Figure 4.26 and Figure 4.27 confirm that 10 ppm of DETPMP act on the barite morphologies in the same way as the concentration of 4 ppm DETPMP.

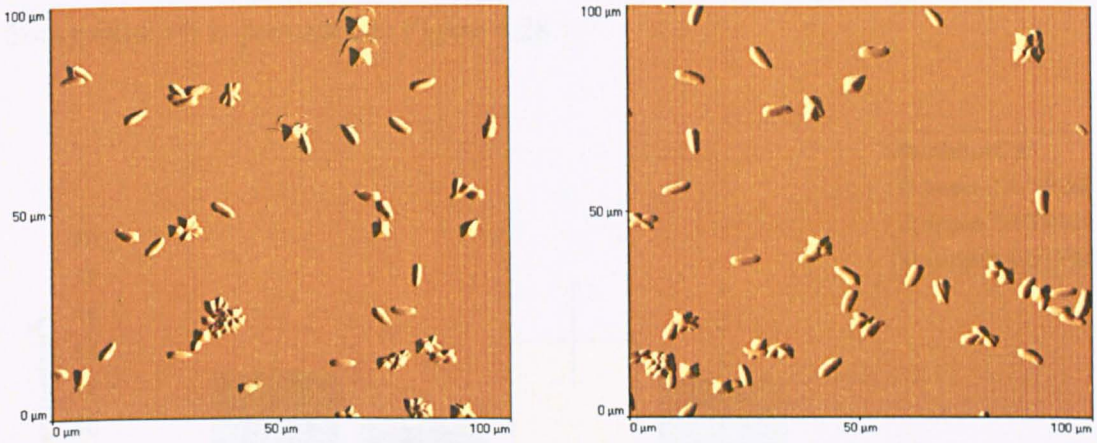

(a) (b)

Figure 4.26: Barite morphologies under treatment of 10 ppm DETPMP (a) first scanned area of the substrate & (b) second scanned area

The observed morphologies under the effect of 10 ppm DETPMP are again star and needle like. When needle like morphologies were developed, the crystals faces of barite grown were the (001), (210) and the (011). The rough (011) surface of barite was progressively developed when 4 ppm and 10 ppm of DETPMP were applied.

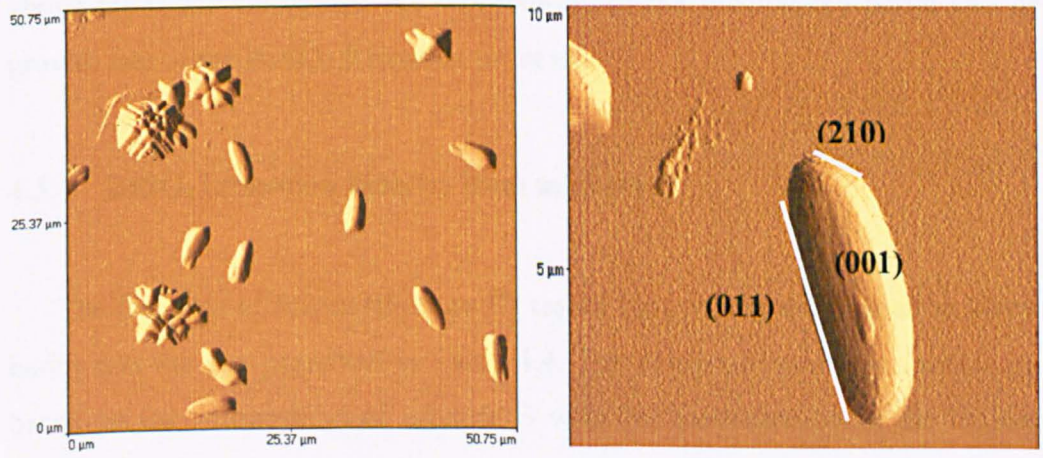

(a) (b)

Figure 4.27: AFM scanning (a) 50.75 x 50.75 µm and (b) 10 x 10 µm

An overview of the DETPMP effect on the formed barium sulphate precipitating from mixture B is presented in Figure 4.28.

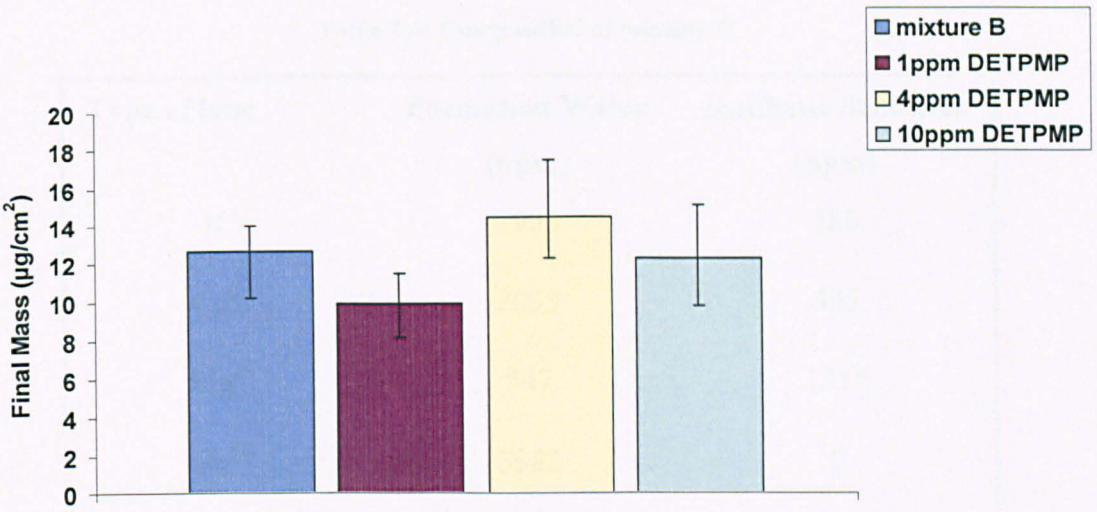

Figure 4.28: Standard deviations for DETPMP effect on the deposited $BaSO_4$

The diagram shows that DETPMP acted as inhibitor of barite only at concentration of 1 ppm as higher concentrations of DETPMP did not manage to decrease the amount of the deposited barium sulphate on the surface. As presented above DETPMP influenced the morphology of the precipitated barite and not the growth rate of the $BaSO_4$ formation process.

4.3.4 $BaSO_4$ formation kinetics from mixture C

The third set of brines (mixture C) tested for probing the formation kinetics of barite was the one presented in Table 4.4. The composition of the specific brine is based on the composition of mixture B with the concentration of the barium ions being modified. The supersaturation index of the final brine, after mixing the formation and the synthetic seawater, was equal to 4.32. The extreme high concentration of Ba^{2+} in the brine was applied in order to follow the kinetics of the

barium sulphate forming on the surface under scale favorable conditions. This type of composition imitates systems which are supersaturated in barium.

Table 4.4: Composition of mixture C

Type of ions	Formation Water (ppm)	Synthetic Seawater (ppm)
K^+	1906	380
Ca^{2+}	2033	405
Mg^{2+}	547	1215
Ba^{2+}	3982	0
Sr^{2+}	417	0
SO_4^{2-}	0	2780
Na^+	26535	10900

4.3.4.1 Uninhibited formation of barite

The QCM measurements for mixture C were useful to record characteristic plots of the barite formation kinetics like the ones presented in Figure 4.29. Under the high supersaturation index conditions tested with mixture C, the formation of barite is sharp during the first three minutes of precipitation. The rapid increase during the first minutes of precipitation resulted already in deposition of 34 $\mu g/cm^2$ of barite on the electrode. A steady growth of barite crystals follows until the end of the first hour of precipitation, where 50 $\mu g/cm^2$ is the deposited mass on the surface as recorded with the mass sensor.

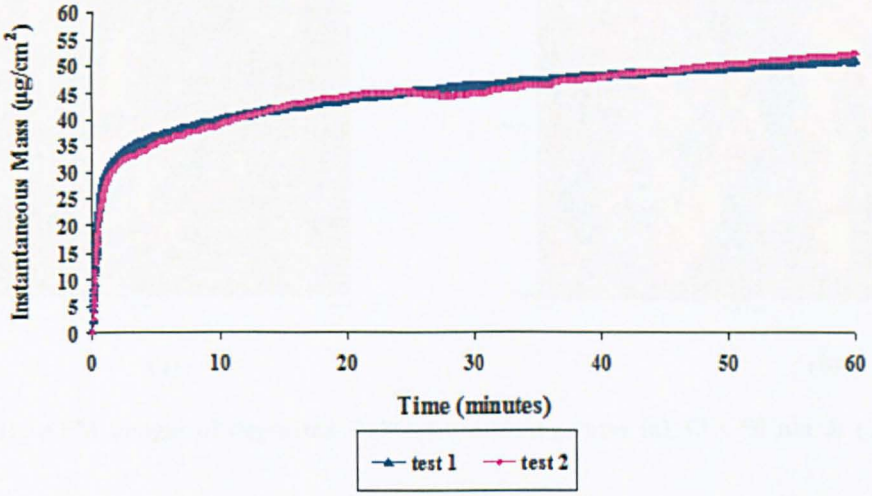

Figure 4.29: QCM measurements for mixture C

The barite morphologies observed on the substrate can be seen in Figure 4.30 and Figure 4.31. The most significant barite morphological changes are the size of the barite crystals deposited on the surface and also the shape of the crystals. The topography images show that the formed crystals are characterized by bigger size compared to the crystals deposited when mixture A and mixture B were tested at uninhibited conditions. The growth of the crystals was promoted under these supersaturation index conditions. The complexes formed can be clearly seen in Figure 4.31.

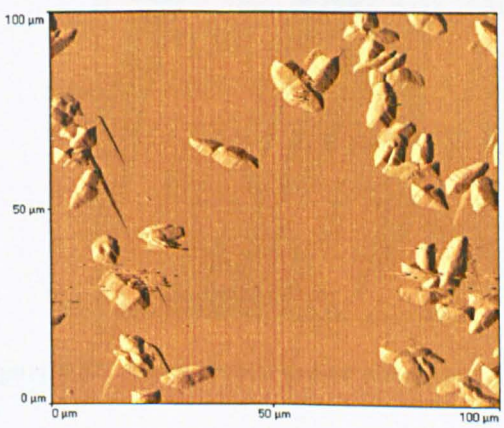

Figure 4.30: Barite morphologies at high supersaturation index (SI=4.32)

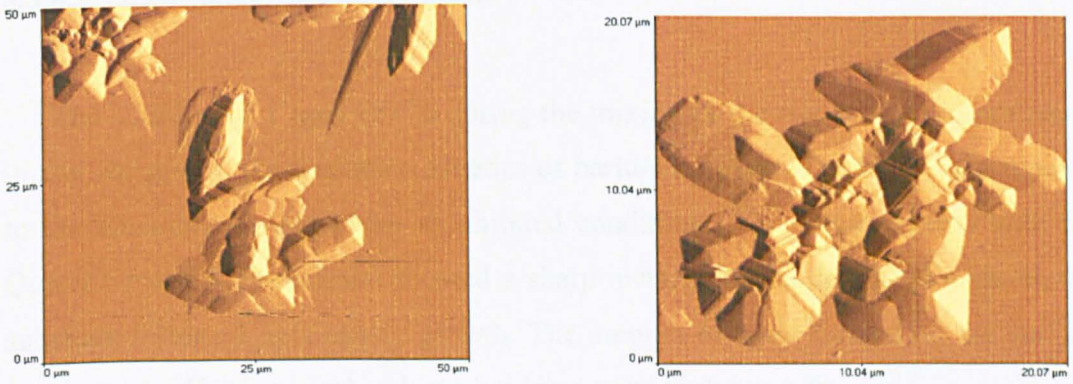

(a) (b)

Figure 4.31: AFM images of deposited $BaSO_4$ at scanning rates (a) 50 x 50 µm & (b) 20.07 x 20.07 µm

$BaSO_4$ crystals they seem to have grown faster along one specific direction compared to the rest directions (Figure 4.32). The barite crystal is orientated along the b crystallographic axis. The dominant direction for barium sulphate growth according to the observations is the $[1\bar{2}0]$ direction, where the growth rate is approximately ten times faster compared to the opposite direction and is characterized by high anisotropy [104].

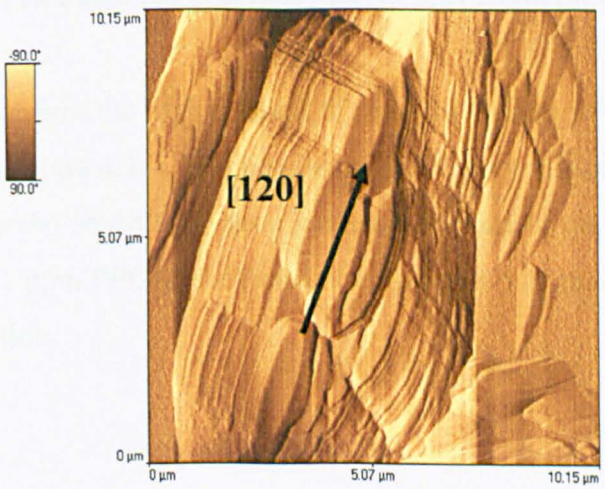

Figure 4.32: Barite crystal grown along the [120]

4.3.4.2 Inhibited formation of barite

The addition of 1 ppm PPCA during the mixing of the two brines did not result in any changes in the formation kinetics of barium sulphate (Figure 4.33) compared to the kinetics recorded under uninhibited conditions. The measurements with the Quartz Crystal Microbalance showed a sharp increase in the deposited mass on the substrate followed by a steady growth. The amount of mass formed on the surface was between 40-45 $\mu g/cm^2$ and is considered to be high enough.

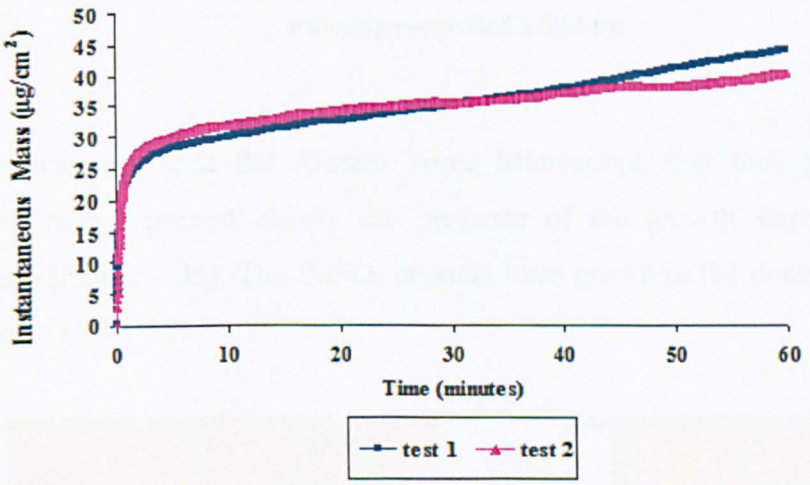

Figure 4.33: QCM measurements of barium sulphate after treatment with 1 ppm PPCA

AFM images confirm the high amount of mass of barium sulphate deposited on the gold electrode (Figure 4.34). The number of $BaSO_4$ crystals on the surface seems bigger compared to the uninhibited tests however the size of the crystals is smaller. This suggests that 1 ppm PPCA is affecting the formation of barite but not in a way of providing inhibition.

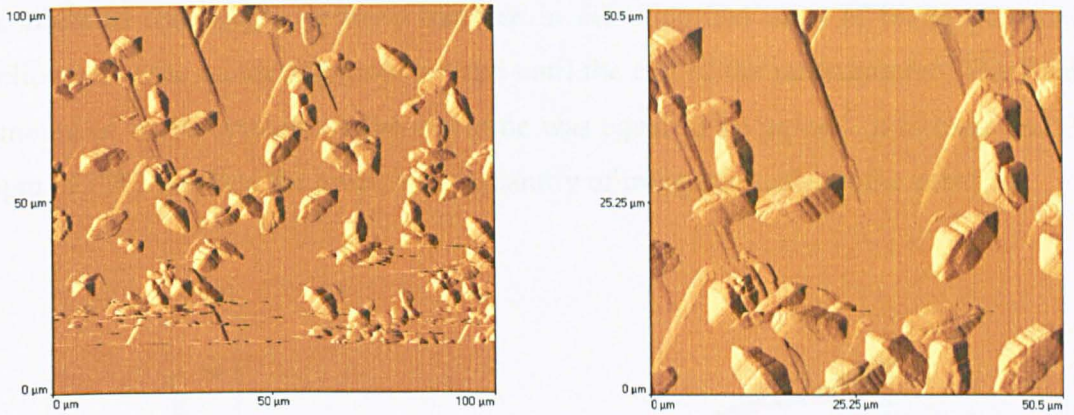

(a) (b)

Figure 4.34: Formed barite under 1ppm PPCA treatment (a) scanning range 100 x 100 µm (b) scanning range 50.5 x 50.5 µm

The scanning with the Atomic Force Microscope that took place in lower scanning ranges present clearly the presence of the growth steps in the barite structures (Figure 4.35). The $BaSO_4$ crystals have grown in the dominant directions [010] and [120].

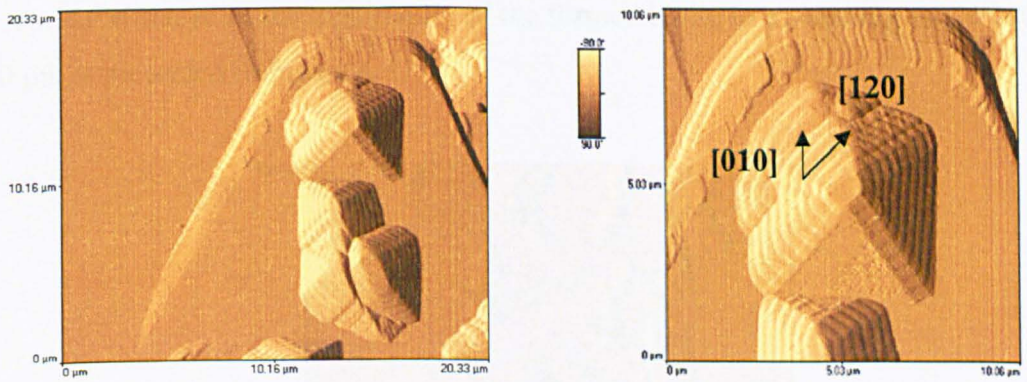

(a) (b)

Figure 4.35: (a) Formation of barite growth steps (b) [010] and [120] growth directions of barite morphologies

The next concentration of PPCA tested for its inhibition effect on barite deposition on surface was 2 ppm (Figure 4.36). The formation kinetics of barium sulphate on the surface is characterized by two parts as it was recorded in the

uninhibited tests. Again a sharp increase in the deposited mass of barite occurred followed by the increasing growth trend until the end of the measurement. The final amount of barite crystals on the electrode was equal to 20 μg/cm^2. It is clear that 2 ppm of PPCA reduce the precipitated quantity of inorganic scale on the substrate.

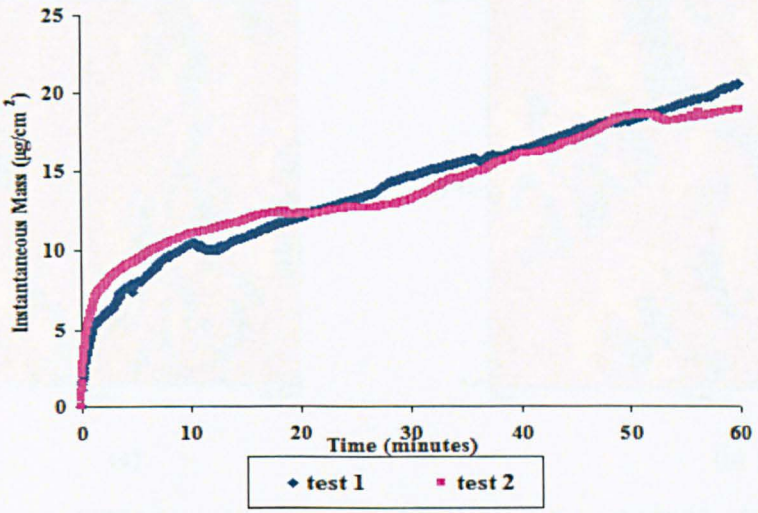

Figure 4.36: QCM measurements of barium sulphate after treatment with 2 ppm PPCA

An AFM image of the topography of the formed barite in a scanning range 100 x 100 μm is presented in Figure 4.37.

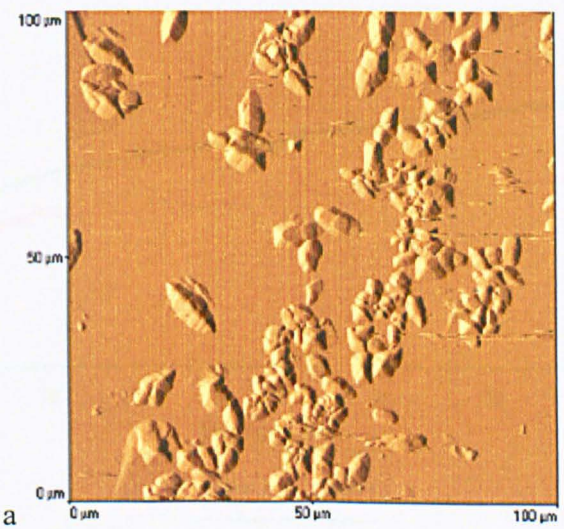

a

Figure 4.37: Barite morphologies after treatment with 2 ppm PPCA

The AFM images received at lower scanning ranges (Figure 4.38) show the formed barite crystals after the treatment with 2 ppm PPCA in more detail. The formation of barite structures with undistracted by the presence of inhibitor growth steps, is illustrated in Figure 4.38 (b).

(a) (b)

Figure 4.38: AFM images (a) scanning range 49.8 x 49.8 µm (b) 20.17 x 20.17 µm

When mixture C was treated with 4 ppm PPCA of inhibitor, the recorded measurements with the QCM showed significant change in the amount of the deposited barite as illustrated in Figure 4.39.

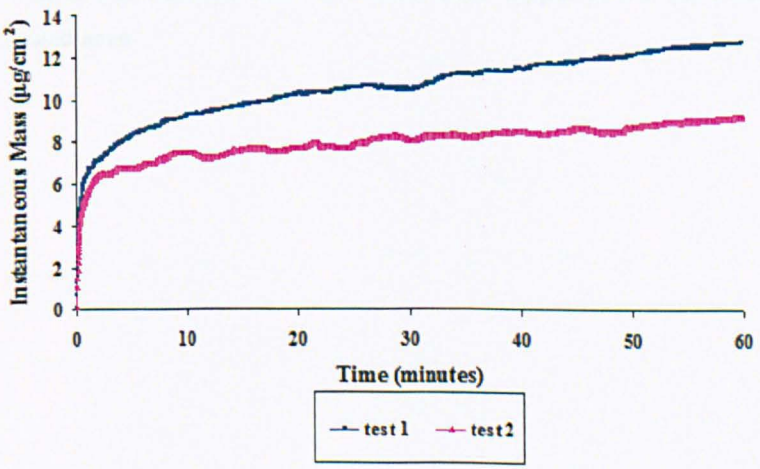

Figure 4.39: QCM measurements of barium sulphate after treatment with 4 ppm PPCA

The trend of the formation kinetics was the same as recorded in the previous tests with mixture C but the deposited amount of formed barium sulphate approached a smaller value than 14 $\mu g/cm^2$. Figure 4.40 shows the scale formed on the quartz crystal. It is obvious that the size of the barite crystals has decreased after the addition of 4 ppm PPCA. The shape of the crystals has remained prolonged in one direction but also pyramidal shaped morphologies of barite are observed on the surface (Figure 4.41). Important feature in Figure 4.41 (b) is the absence of the growth steps of the barite crystals. This can justify the strong effect of PPCA on the forming scale.

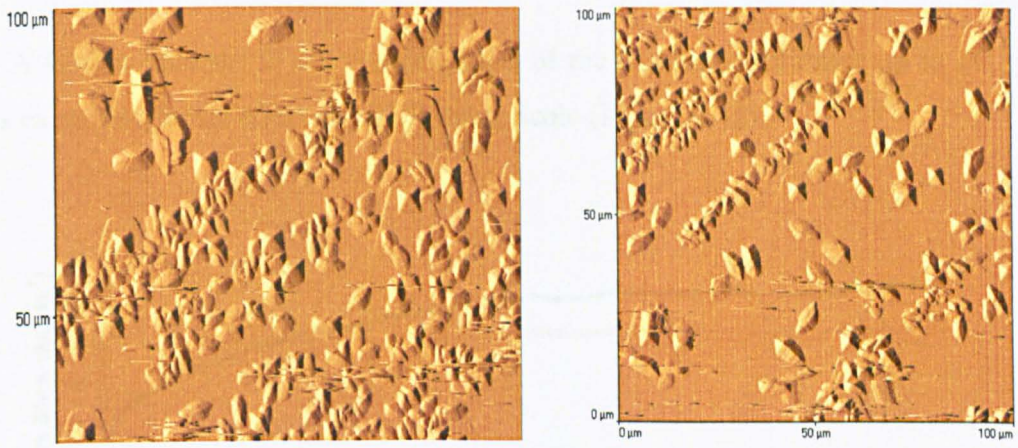

(a) (b)

Figure 4.40: $BaSO_4$ formations after treatment with 4 ppm PPCA (a) First scanned area (b) different scanned area

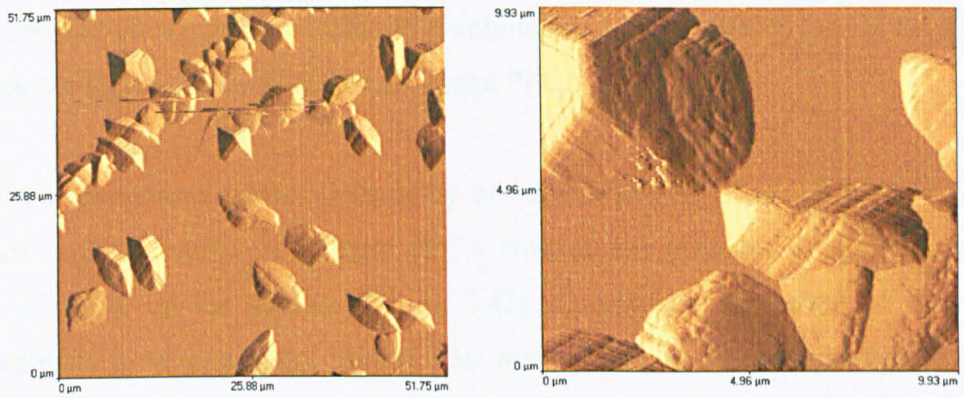

(a) (b)

Figure 4.41: (a) Barite structures (b) Pyramidal structure of barium sulphate with absent growth steps

A further increase in the concentration of the examined inhibitor up to 10 ppm was examined for its effect on the forming scale (Figure 4.42).

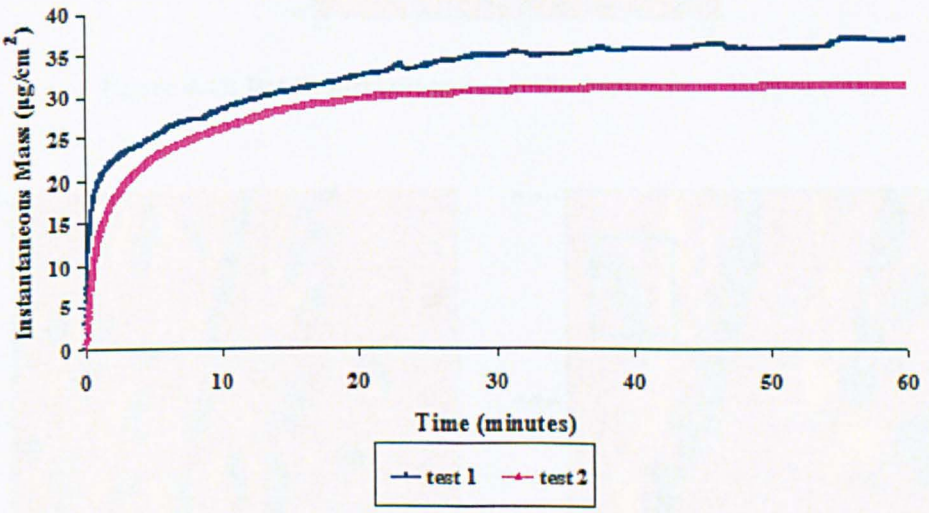

Figure 4.42: QCM measurements of barium sulphate after treatment with 10 ppm PPCA

The addition of 10 ppm PPCA resulted in recording the same formation kinetics trend like the one presented in Figure 4.39. The amount of the deposited amount was equal to 35 µg/cm^2, which is less than the values recorded in the uninhibited case but higher compared to the mass recorded after treatment with 4 ppm PPCA. This

suggests that after one hour of barite precipitation 10 ppm PPCA inhibit the $BaSO_4$ growth but not in the same degree as 4 ppm PPCA.

The observations of the topography of barium sulphate formed crystals on the surface in the presence of 10 ppm PPCA confirm the presence of high amount of mass of barite on the surface (Figure 4.43). Considering the shape of the barite structures is more pyramidal shaped like with acute corners present (Figure 4.44). The indicated area in Figure 4.44 (b) shows the presence of growth steps on barite crystal.

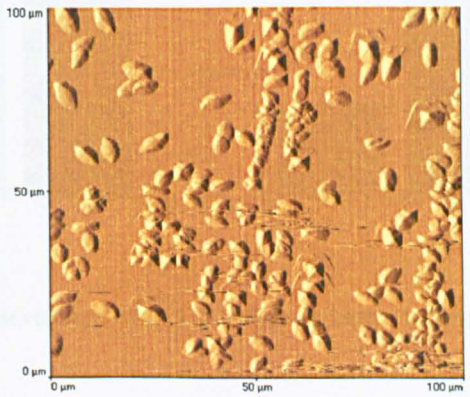

Figure 4.43: $BaSO_4$ formations under the treatment of 10 ppm PPCA

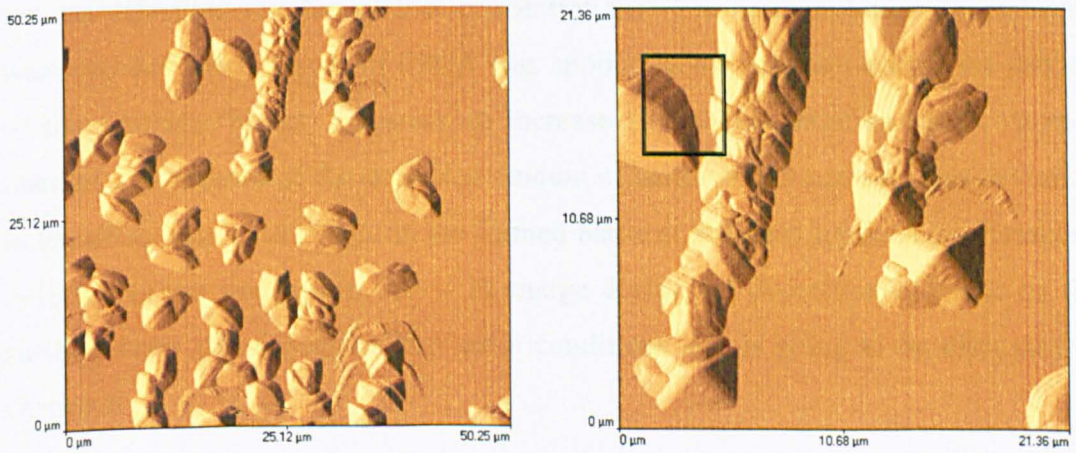

(a) **(b)**

Figure 4.44: AFM image of formed scale type (a) 50.25 x 50.25 µm (b) 21.36 x 21.36 µm

A summary of the effect of PPCA on the barium sulphate precipitating from mixture C is shown in Figure 4.45.

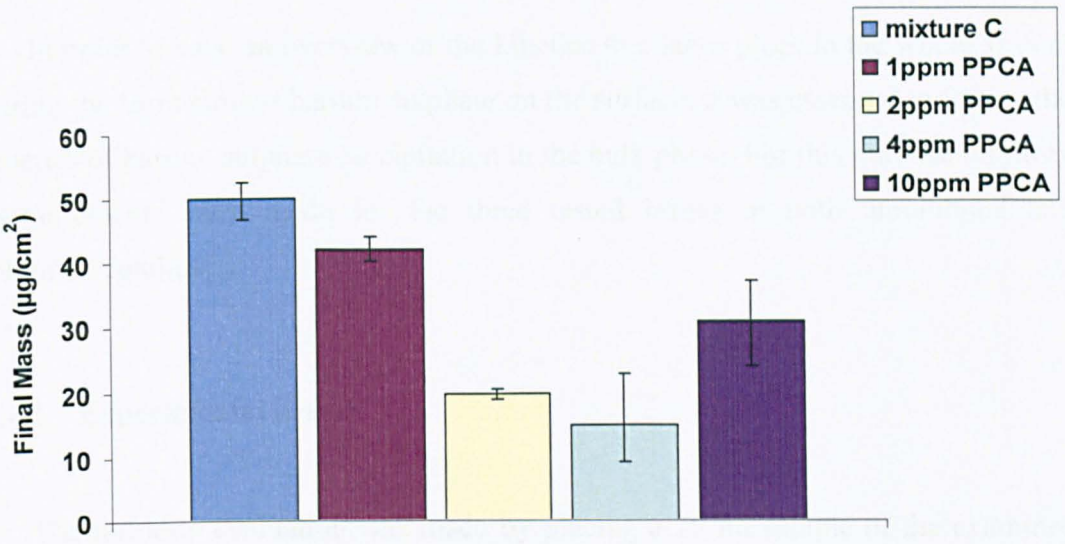

Figure 4.45: Standard deviations of PPCA effect on barite precipitating from mixture C

When the deposited amount of barite mass during the uninhibited tests is compared to the one recorded under the effect of PPCA, it is determined that PPC A was an effective inhibitor at low concentrations. The best inhibition performance was recorded when 4 ppm of PPCA was applied to the seawater during the mixing of the synthetic brines. However an increase in the concentration up to 10 ppm resulted in increased of the deposited amount of barite on the surface. This deviation in the effectiveness of PPCA on the formed barite at different applied concentrations is linked to the mechanism that is in charge during the deposition of barite on the surface under this supersaturation ratio conditions and is going to be discussed in chapter 6.

4.4 Barium sulphate measurements in the bulk phase

In order to have an overview of the kinetics that takes place in the whole system during the formation of barium sulphate on the surface, it was essential to follow the kinetics of barium sulphate precipitation in the bulk phase. For this purpose turbidity measurements were made for the three tested brines in both uninhibited and inhibited conditions.

4.4.1 Experimental details

The turbidity evaluation was made by placing a 10 ml sample of the examined brine in a appropriate glass cell. The glass cell is placed in the turbidity meter and is being covered in order to avoid any light effect as the measurement occurs. The turbidity measuring units are the F.A.U - Formazin Attenuation Units and the wavelength of the beam during the measurements is automatically adjusted after choosing the right program for the measurement. It is worth to note that the turbidity meter has specific detection limits. When the examined solution is not supersaturated or respectively extremely supersaturated, then the measurement can not take place.

A summary of the turbidity measurements that took place is presented in Table 4.5.

Table 4.5: Overview of the turbidity measurements

Mixture	Duration (hours)	Inhibitor	Inhibitors concentration (ppm)
A	1	none	none
B	1	none	none
		PPCA	1
			4
			10
	1	DETPMP	1
			4
			10
C	1	none	none
		PPCA	1
			4
			10

4.4.2 Uninhibited $BaSO_4$ precipitation measurements

The recorded values during the turbidity measurement of the brine with the low supersaturation index (mixture A) are presented in Figure 4.46. The plot shows that the barium sulphate precipitation from mixture A has a prolonged induction time. The turbidity measurements show that there is almost no activity in the bulk phase until the 15th minute of the precipitation. After the 15th minute the turbidity starts to increase showing that barite particles of detectable size are being formed.

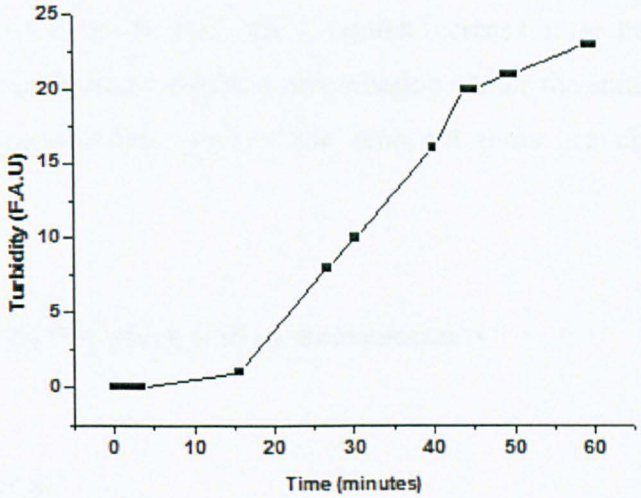

Figure 4.46: Turbidity measurements for mixture A

The turbidity values measured for the three examined supersaturated brines are compared in Figure 4.47.

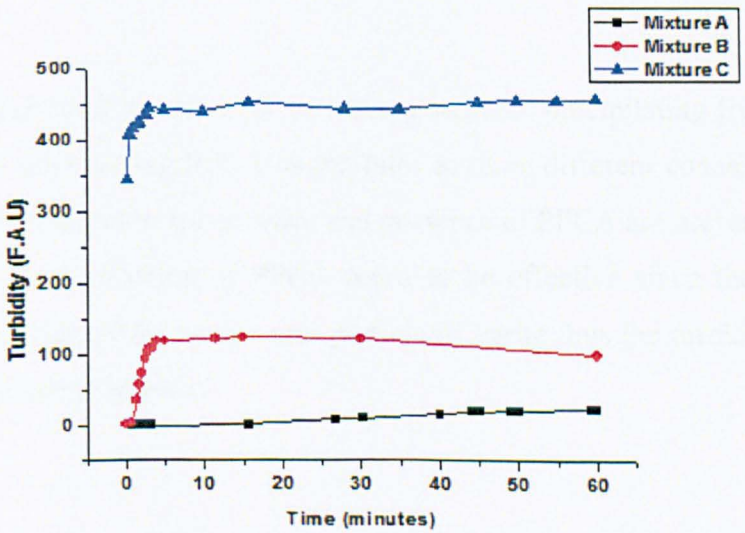

Figure 4.47: Comparison of the turbidity for the three mixtures

As expected the increase in the supersaturation index results in increase of the turbidity with the mixture C giving highest turbidity values above 400 (F.A.U). The recorded plots for mixtures B and C show a quick increase in the turbidity during the first 5 minutes of the barium sulphate precipitation. After the initial increase in the turbidity of the precipitation process the received plots are characterized by a plateau.

4.4.3 Inhibited $BaSO_4$ precipitation measurements

4.4.3.1 PPCA effect

For mixture A where the supersaturation index was the lowest, no turbidity measurements after treatment of the brine with inhibitors took place. Measuring the turbidity of mixture A in the presence of inhibitors is not necessary, since the turbidity measurements under uninhibited conditions have already confirmed that at this supersaturation index the scaling activity in the bulk phase is maintained at low level.

On the other hand the turbidity of barium sulphate precipitating from mixture B was measured after adding PPCA as inhibitor at three different concentrations. The turbidity measurements in the absence and presence of PPCA are presented in Figure 4.48. All the concentrations of PPCA seem to be effective since they manage to block the formation of detectable size particle of barite thus the turbidity values are recorded in the range of zero.

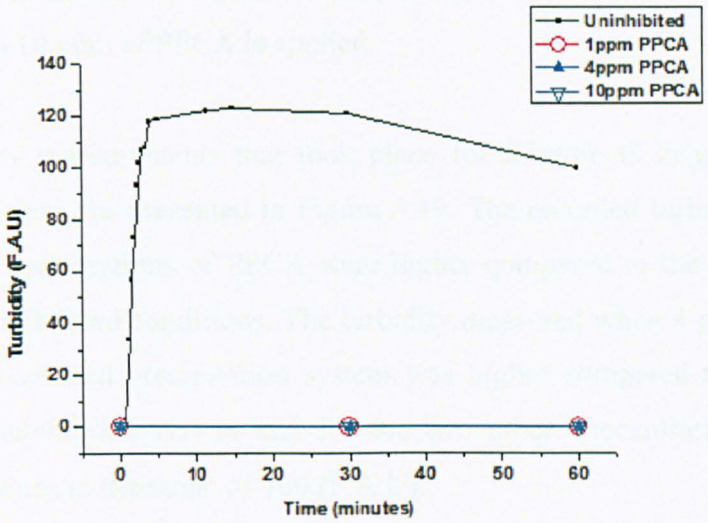

Figure 4.48 : Turbidity measurements of mixture B for 1 hour – treatment with PPCA

Table 4.6 : ICP measurements

Tested Brine	Concentration of inhibitor	Hours of precipitation	Initial Concentration of Ba^{2+}(ppm)	Final Concentration of Ba^{2+}(ppm)
Mixture A	None	1	100	47
Mixture B	None	1	80	36
Mixture C	None	1	3982	193
Mixture B	1ppm PPCA	1	80	7
Mixture B	10ppm PPCA	1	80	34

The final concentrations of barium cations in the bulk phase for the uninhibited tests are lower compared to initial ones as expected due to the formation of barite scale hence there is a decrease in the activity of Ba^{2+} in the bulk state. In addition the ICP analysis for the inhibition tests as presented in Table 4.6, showed that by the end of 1 hour of precipitation 10 ppm PPCA manage to keep the Ba^{2+} concentration in the bulk higher compared to the 1 ppm of PPCA. The further meaning of the results

received with the inductive coupled plasma, is that the mass of the deposited barite is smaller when 10 ppm of PPCA is applied.

The turbidity measurements that took place for mixture C in uninhibited and inhibited conditions are presented in Figure 4.49. The recorded turbidity values for all the tested concentrations of PPCA were higher compared to the turbidity value measured in uninhibited conditions. The turbidity measured when 4 ppm PPCA was added in the examined precipitation system was higher compared to the turbidity recorded for uninhibited system and for the two other concentrations examined, approaching values in the range of 700 (F.A.U).

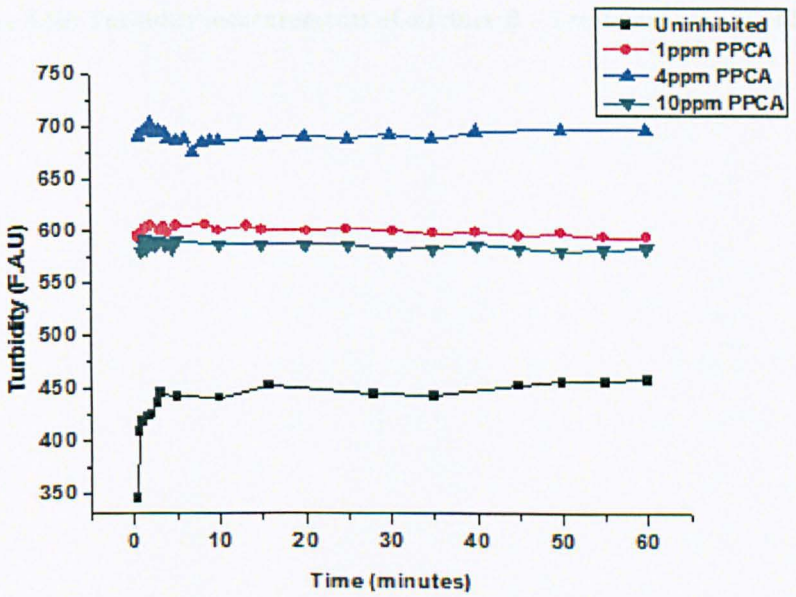

Figure 4.49: Turbidity measurements of mixture C- Treatment with PPCA

4.4.3.2 DETPMP effect

Regarding the effect of DETPMP as inhibitor on the precipitated $BaSO_4$ is shown in Figure 4.50. It is clear from the received plots that DETPMP resulted in decrease in the amount of precipitated barium sulphate.

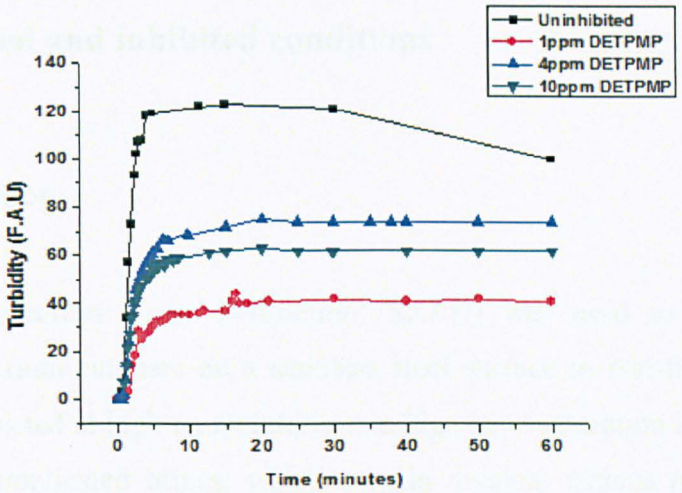

Figure 4.50: Turbidity measurements of mixture B – Treatment with DETPMP

CHAPTER 5 *In-situ* X-ray diffraction for $BaSO_4$ formation in uninhibited and inhibited conditions

5.1 Introduction

In-situ Synchrotron X-ray Diffraction (SXRD) was used to investigate the formation of barium sulphate on a stainless steel surface in real-time. The *in-situ* study was conducted at high temperatures and high supersaturation index conditions after mixing complicated brines, which contain divalent cations (Ca^{2+}, Mg^{2+} and Sr^{2+}). The choice of quite high supersaturated brines was a matter of making the precipitation and deposition of barite crystals feasible on the surface in the shortest time. The application of the specific technique for barium sulphate scale studies is new and the technique is being refined to look at a range of brines.

Through the *in-situ* X-ray diffraction measurements the barite crystal faces present on the surface were detected. The progress of these recorded crystal faces of barium sulphate on the substrate through time was followed. Furthermore the *in-situ* X-Ray diffraction tests took place in the presence of inhibitors (PPCA and DETPMP) at different concentrations. The effect of the inhibitors on the recorded crystal faces of barium sulphate was investigated. Hence probing the kinetics of the barite formation and its crystallography were accomplished for both uninhibited and inhibited conditions.

In this chapter the results presented from the *in-situ* X-ray diffraction measurements of the $BaSO_4$ formation on the substrate compile a new direction in investigating the scaling kinetics of barite. Although the synchrotron X-ray diffraction technique has been used by a few research groups previously for barium sulphate scaling purposes, this is the first time that the formation of barite is being followed *in-situ* after mixing complicated brines imitating the off-shore

environment. Moreover the deposition of the scale on a stainless steel surface brings this experimental study closer to the industrial applications.

5.2 Experimental details

5.2.1 *In-situ* SXRD set up

The *in-situ* SXRD measurements for this study were accomplished in the station X17B1 at the National Synchrotron Light Source (NSLS) in Brookhaven. The equipment provided is appropriate for high temperature and pressure applications reaching final values 250 °C and 34 MPa respectively. During the barium sulphate experiments the temperatures were 95°C and 57°C and as far the pressure, it was equal to 1 atmosphere.

The type of radiation used was Cu Ka X-rays with energy equal to 70 keV in wavelength 0.17712 Å. The specific type of high energy radiation was chosen as the level of the energy needed to penetrate the substrate and the polycrystalline material formed on the surface is high. The specific beam successfully penetrates both substrate and formed scale as in the meantime no energy lost in the resolution is recorded.

The duration of the experiments was set up to 60 minutes and 30 frames were collected during this time. The time gap between each frame was 2 minutes.

5.2.2 Experimental Overview

Two sets of supersaturated brines were used for the *in-situ* X-ray diffraction measurements. The preparation of the tested brines and their compositions (Table 4.3 and Table 4.4) are already known from the previous chapter, where the tested

sets of brines were characterized as mixture B and mixture C. The only main difference in the compositions of the examined brines was the concentration in Ba^{2+}, which in mixture B and C the concentration was 80 ppm and 3982 ppm respectively.

The final pH of the brines was equal to 5.5. A quantity of 500 ml of each brine (formation water and synthetic seawater) was placed in each reservoir. The total flow rate of the brines in the system was 10 ml/min (5 ml/min for each brine). For the inhibition tests the chemical additive was initially mixed in the reservoir containing the synthetic seawater. A summary of the experimental details including the concentrations of the inhibitors added during the *in-situ* tests is presented in Table 5.1.

Table 5.1: Experimental overview of the *in-situ* X-ray diffraction measurements

Initial Concentration of Ba^{2+} in the formation water (ppm)	**Supersaturation Index**	**Temperature (°C)**	**Inhibitor**	**Concentration of inhibitor (ppm)**
3982	3.65	95	none	none
			PPCA	1
				4
				10
			DETPMP	10
				20
	3.89	57	PPCA	1
				4
				10
			DETPMP	10
				20
80	1.96	95	none	none

5.3 *In-situ* SXRD measurements

5.3.1 *In-situ* SXRD analysis remarks

The raw data was collected during the *in-situ* measurements and then it has been processed in order to remove any noise originating from the stainless steel background. This is a crucial stage during the treatment of the raw data since any mistake will result in incomplete or even false analysis of the data. The initial conversion to appropriate file formats takes place through an in-house program used by the beam-manager in the X17B1 at the NSLS. Afterwards the data is converted properly following a number of steps within a routine program (FullProof software) so that as a final stage the relationship of the recorded intensities versus the d space of the diffraction peaks are plotted. The d space was chosen as its independence of the wavelength (λ) reduces the errors during the analysis of the data.

Next the correlation of the recorded diffraction peaks with the formed crystal faces of barite follows, which is based on the established crystallographic database for $BaSO_4$ (Pnma system) as it was given by Sawada *et al.* [164]. The correlation shows a good agreement of the experimental d space values of the diffraction peaks with the d space values provided for the barite lattice planes by the database. What is worth to note is that some of the experimental d space values recorded are slightly shifted when compared to the theoretical ones. This was pointed out in the SXRD patterns received from the tests where the brine with the high supersaturation index was used resulting in formation of big size $BaSO_4$ crystals.

As the mixed brines contain other divalent cations besides barium, it is necessary to use all the respective databases in order to determine any diffraction peaks present due to other deposited scale type than barium sulphate. Thus the SXRD patterns were investigated for any potential crystal faces present due to $SrSO_4$ or $CaSO_4$ formation and/or any possible known mixtures containing Ba^{2+}, S, O, Sr^{2+}, Ca^{2+}, Mg^{2+} and K^{+} [165,166]. None of the d space values for strontium sulphate or calcium

sulphate were in agreement with the d space values received in this session. This was expected as according to other researchers $SrSO_4$ is quite soluble at the tested temperatures [81] and also concerning the calcium ions they reveal a trend to precipitate within the barite lattice instead of depositing as $CaSO_4$ formations [79]. The only case where the recorded diffraction peaks were matching with non barite d space values was for the case of formed celestine barian on the substrate. This indicated that strontium ions incorporation into the barite lattice occurred on the stainless steel surface.

Further scanning of the received in-situ SXRD patterns revealed the presence of three intense peaks recorded for every scale test that took place, as shown in Figure 5.1. Two of these peaks were present in the patterns due to the strong background of the stainless steel that was used as substrate. The two stainless steel peaks were detected at d space= 1.875 and 2.165 Å respectively.

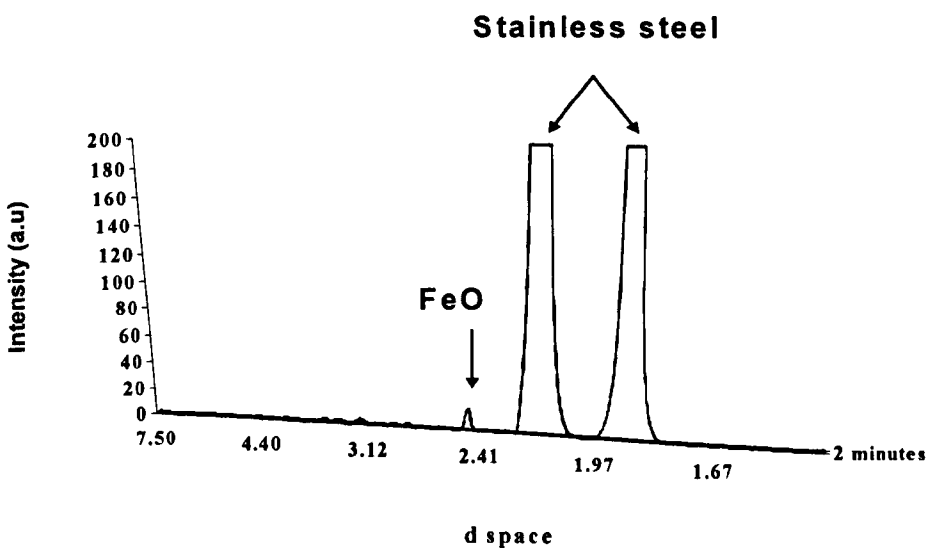

Figure 5.1: SXRD pattern showing the stable peaks

Regarding the third peak which showed stable intensity and it always present in every SXRD pattern, was due to the formation of maghemite (Fe21.34O26.27)

during the barite scaling tests [167]. The source of the Fe^{2+} in the system was the stainless steel substrate. The peak representing maghemite was marked at d space= 2.47 Å.

It is quite likely that in the same d-space where the stable peaks appear, peaks due to the formed scale are hidden. Subsequently peaks representing crystal faces of $BaSO_4$, $CaSO_4$ or any other formed scale type might be missed during the analysis of the SXRD patterns. Nevertheless the number of potentially hidden peaks is expected to be small, allowing the analysis to be complete.

Further refinement of the crystallographic data can lead to determination of the formed structures. However the refinement of a structure based on the diffraction data is quite a challenging process as the received SXRD patterns are compared to standard patterns which are being recorded under ideal conditions. This justifies the problems arising in this study during the effort to refine the formed barite structures with Rietveld refinement. The main difficulty was the complicated nature of the received SXRD patterns as the examined brines contained a high number of divalent cations. Thus the SXRD patterns could not be compared with the standard patterns provided by the Accelrys software [55].

Considering all the above, the conversion of the raw data into the appropriate formats and the interpretation of every frame for each of the SXRD patterns, needs extended treatment. The analysis of the raw data is challenging and needs months of processing, in order to be complete. Nevertheless the prolonged analysis reassures that the determination of the peaks is accurate and the correlation with the crystal planes of the formed scale is correct. Subsequently a complete characterization of the crystallographic nature of the formed scale is feasible.

The data collected from the *in-situ* SXRD measurements are presented below as functions of integrated intensity versus time for every crystal plane of barite present on the stainless steel cell. The integrated intensity is proportional to the crystal

volume formed in the capillary cell [153]. Thus plotting the relationships of the intensity in a function of time provides a good way to point out the proportion of mass formed in the tested cell and the formation kinetics of the barium sulphate surfaces under the different examined conditions. Moreover the determined crystallographic nature of the deposited scale can be clearly illustrated. For a few cases the SXRD patterns are also presented in order some details of the $BaSO_4$ crystallography to be highlighted.

5.3.2 Uninhibited $BaSO_4$ formation precipitating from mixture C

The SXRD data received during the deposition of the barium sulphate after precipitating from the mixture C at 95°C is presented in Figure 5.2.

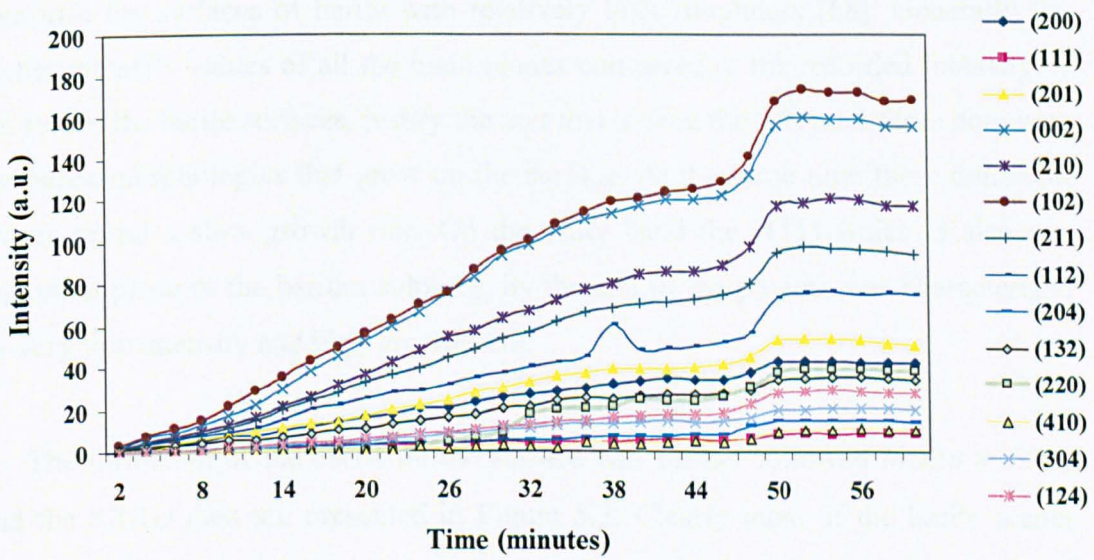

Figure 5.2: SXRD plot of uninhibited $BaSO_4$ formation at 95°C

During the *in-situ* X-ray diffraction measurement of the $BaSO_4$ formation on the cell, 14 crystal planes of barite were present. Among the formed barite crystal faces the most dominant surfaces (210), (002), (200), (111) and (102) as published by

Hartman and Strom can be identified [69]. The (002) and (210) crystal planes are important as they consist the bounding faces for the equilibrium form of the barite.

The formation kinetics of the different planes is shown in Figure 5.2. An important feature is the simultaneous way that all the crystal planes of barite grow in time. The recorded intensities reveal the slow growth of the barite planes until the 8^{th} minute of the deposition. Then the intensity values are increased until the 50^{th} minute. The last stage of the plots is characterized by a plateau for all the recorded surfaces of barium sulphate. The stability in the received intensity values during the last minutes of the process shows that no further growth takes place on the surface.

The barite surfaces that illustrate higher intensity values by the end of 1 hour precipitation are the (102), (002), (210), (211) and (112). The highest intensity values were received by the growth of the (102) and (002) planes of barite, which comprise the surfaces of barite with relatively high roughness [68]. Generally the higher intensity values of all the main planes compared to the recorded intensity of the rest of the barite surfaces, justify the fact that indeed these crystal faces dominate the barite morphologies that grow on the surface. At the same time these dominant planes reveal a slow growth rate. On the other hand the (111) which is also one important plane of the barium sulphate, by the end of the process was characterized by very low intensity and high growth rate.

The formation of the barite on the surface was further followed *in-situ* at 57°C and the SXRD data are presented in Figure 5.3. Clearly most of the barite planes recorded at 57°C were present during the tests at 95°C as well. However there are changes in the crystallography of the formed barite as the number of the formed surfaces is smaller. In addition the appearance of the (011) has been recorded. Generally the presence of the (011) crystal plane of $BaSO_4$ identifies the slower kinetics of the barium sulphate precipitation process. This is in agreement with the fact that the temperature is decreased thus the slower rate of the kinetics was something expected.

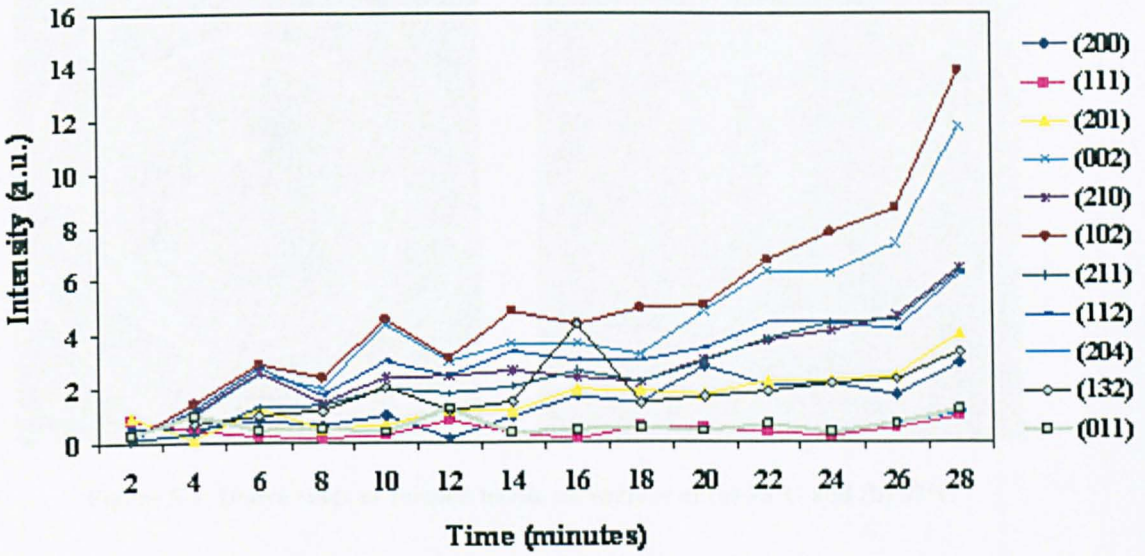

Figure 5.3: SXRD plot of uninhibited $BaSO_4$ formation at 57°C

As far as the kinetics of the crystal faces again they seem to follow a general increasing trend as time evolves, however the kinetics was recorded only until the 28th minute. By the end of the test the intensity values do not approach any plateau in contrast to the one at 95°C. This suggests that the growth under the specific tested conditions continues after the recorded time of precipitation. The intensity values of the dominant planes increase in time with the (102) and (002) again showing the maximum intensity recorded by the end of the test. However all the intensity values recorded for the tests at 57°C are lower than at 95°C.

This sharp decrease in the intensity values of the barite crystal faces in combination with the decrease in the experimental duration suggests that the crystals are orientated in a preferred way within the capillary cell. A comparison of the Debye rings images formed during the *in-situ* measurement at the two different temperatures (Figure 5.4) is actually a good way to prove if preferred orientation of the developing material in the capillary cell occurs or not, under the specific examined conditions [168].

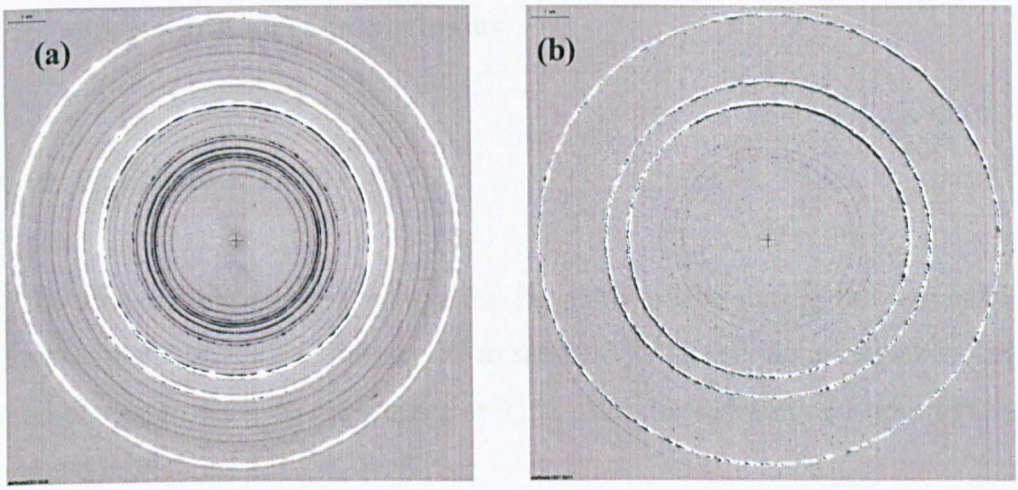

Figure 5.4: Debye rings of formed barite on surface at (a) 95°C and (b) 57°C

The white coloured rings as shown in both images of Figure 5.4 are due to the presence of the three stable peaks as described earlier in this chapter. In Figure 5.4 key point for observation is the Debye rings formed in the areas surrounded by the white coloured rings. It is clear that the intensity level of the Debye rings of $BaSO_4$ formed during the *in-situ* measurement at the two different temperatures changes. At 95°C the diffraction rings are quite dark coloured and they seem homogeneous. No variations in the intensity of the Debye rings are observed. On the other hand the diffraction rings formed during the in-situ test at 57°C are not intense at all and they can hardly be noticed. Only the Debye rings in the centre of the image can be seen and still not all the points of the formed circles area revealed. This difference in the intensity of the rings developed at both temperatures and also the variation in the density of the rings (Figure 5.4) (b) confirms that the barite deposited on the surface at 57°C is more textured compared to the one formed at 95°C [168].

5.3.3 The effect of PPCA on the formed barite precipitated at high supersaturation ratio conditions

5.3.3.1 Inhibition at 95°C

The first inhibitor tested *in-situ* for its performance during the formation of barium sulphate on the capillary cell was the PPCA. The formation kinetics and the crystal planes growing on the surface at 95°C after the addition of 1 ppm PPCA are presented in Figure 5.5.

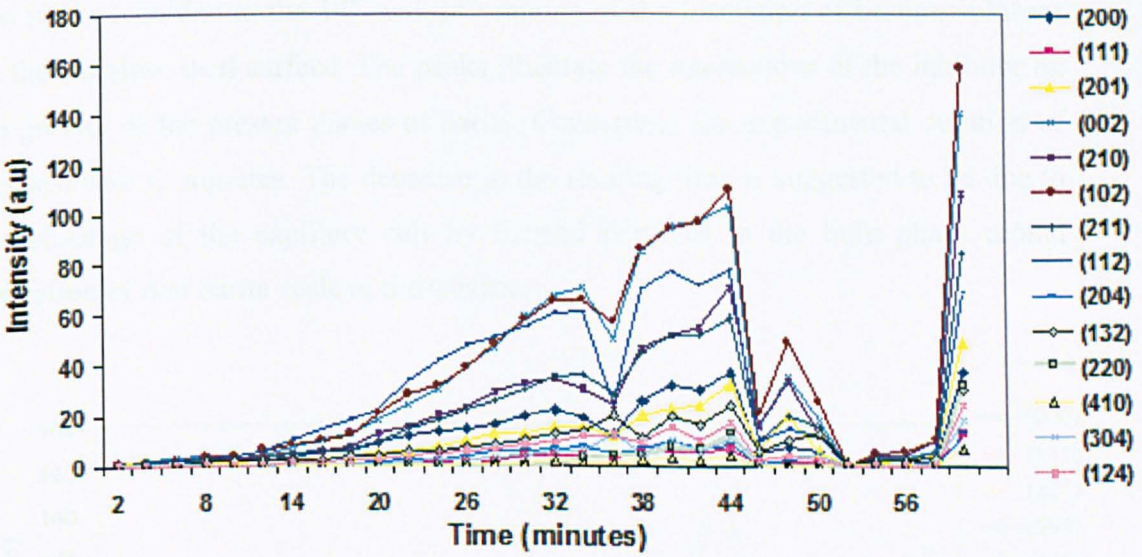

Figure 5.5: Effect of 1ppm PPCA at 95°C

According to the recorded barite crystal planes on the surface the crystallographic nature of the formed barium sulphate did not change when 1 ppm of PPCA was added in the mixing brine at 95°C. The surfaces of barite characterized by the highest intensity are the (102) and (002) just as recorded in the uninhibited systems.

What is being more affected by the presence of the inhibitor in the supersaturated brine is the time that the planes of barite appear on the surface and the way they grow in time. All the crystal planes reveal a prolonged induction time on the surface which approaches the 16th minute after the mixing of the brines in the capillary cell. This lag in the barite formation is then followed by an increase in the intensities of all the crystal faces of barite which show a similar kinetics trend. An important feature in the recorded plots is the decreased intensity between the 52nd and 56th minute, which represents a limited amount of scale formed on the substrate.

The next concentration examined was 4 ppm PPCA. As shown in Figure 5.6 all the dominant planes of barite are present from the start of the precipitation process. The plots reveal a general increasing trend of the intensity. It is worth to note the two peaks recorded at the 14th and 24th minute of the formation of barium sulphate on the stainless steel surface. The peaks illustrate the interactions of the inhibitor on the growth of the present planes of barite. Concerning the experimental duration of this test was 32 minutes. The decrease in the running time is suggested to be due to the blockage of the capillary cell by formed particles in the bulk phase or/and formation of non barite scale at the surface.

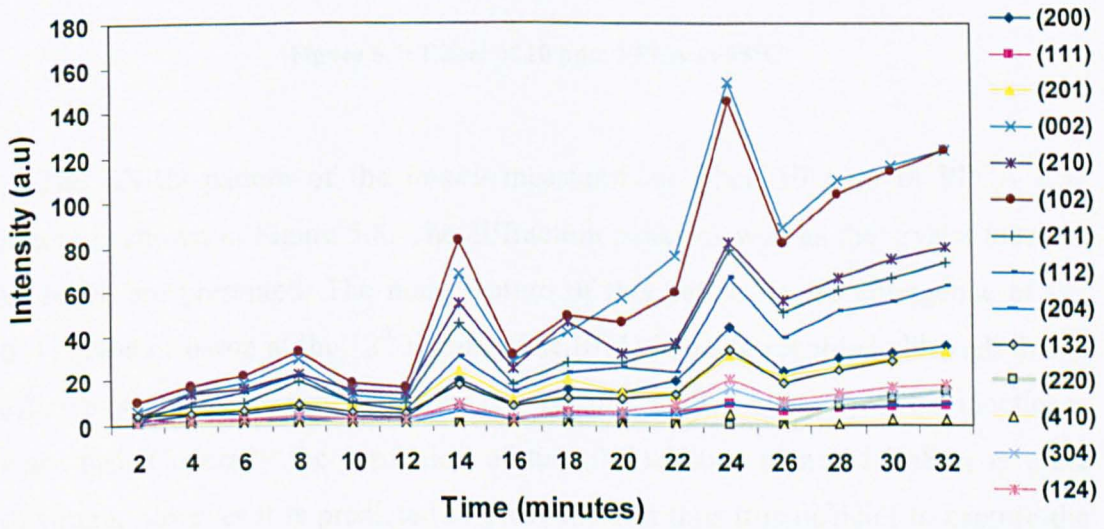

Figure 5.6: Effect of 4 ppm PPCA at 95°C

With further increase in the concentration of the inhibitor up to 10 ppm the barite crystal faces seem to grow in a similar way on the surface (Figure 5.7). The (220) and (410) surfaces of barium sulphate were not detected at all. Although the barite planes emerge from the 2nd minute after mixing the brines with no obvious prolonged induction time on the surface, the intensity values at the end of the process were significantly low. Based on that, 10 ppm of PPCA seems to be effective on the inhibition of the dominant planes of barite.

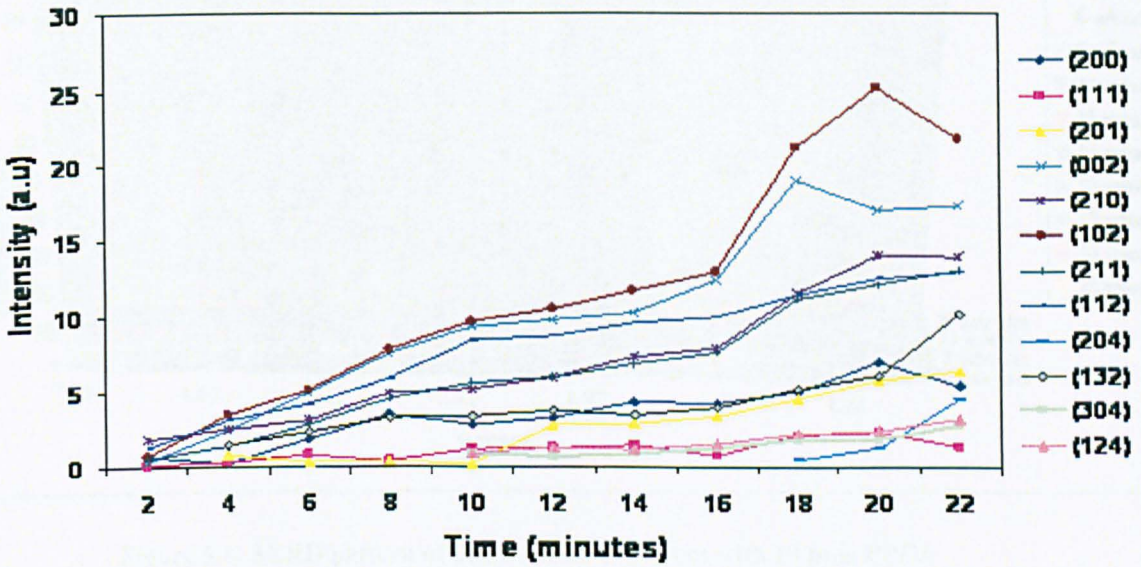

Figure 5.7: Effect of 10 ppm PPCA at 95°C

The SXRD pattern of the *in-situ* measurement when 10 ppm of PPCA was present is shown in Figure 5.8. The diffraction peaks as well as the crystal faces of the barite are presented. The main feature of this pattern is the emergence of the (011) plane of barite at the 12th minute. The (011) is being recorded although this is difficult especially for tested systems like the one studied here, where the kinetics is really fast. Generally the formation of the (011) lattice plane of $BaSO_4$ is quite important, however it is predicted to grow too fast thus it is difficult to capture the appearance of the (011) in the system [64]. Yet the presence of the (011) at the 12th minute and its disappearance after that time point highlights the performance of

PPCA. The inhibitor at the concentration of 10 ppm managed to reduce the growth rate of the specific plane thus the (011) is detected revealing a high intensity value. After the 12th minute the diffraction peak responding to the (011) barite plane can not be identified as probably the (011) could not further being retarded by the presence of the inhibitor.

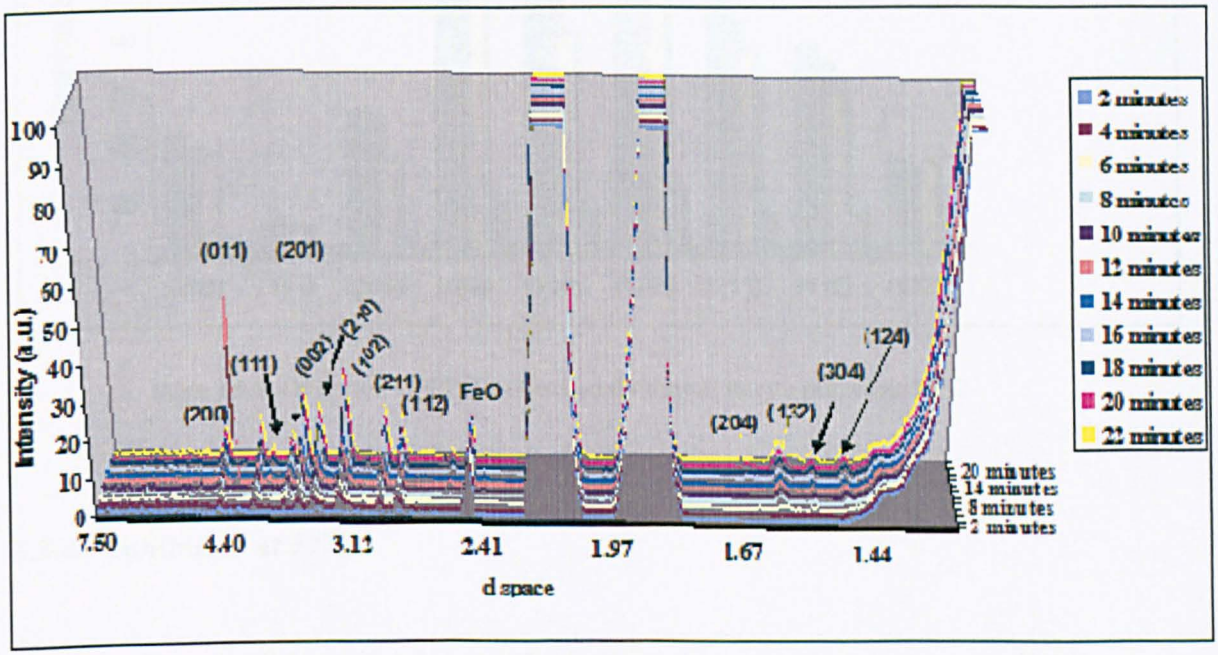

Figure 5.8: SXRD pattern of $BaSO_4$ after treatment with 10 ppm PPCA

An overview of the effect of PPCA on the constant barite planes at 95°C is presented in Figure 5.9. The intensity values in this graph correspond to the value recorded at the end of every experimental run.

It is clear that the increase in the concentration of the applied inhibitor resulted in retardation of all the barite planes. The concentration of 10 ppm PPCA inhibits the formation of the dominant barite planes at high degree. It is important the inhibition of the (111) plane of barite when 10 ppm of PPCA is present. The growth of the (111) seems to be strongly blocked despite the known fast growth rate that characterizes the specific plane.

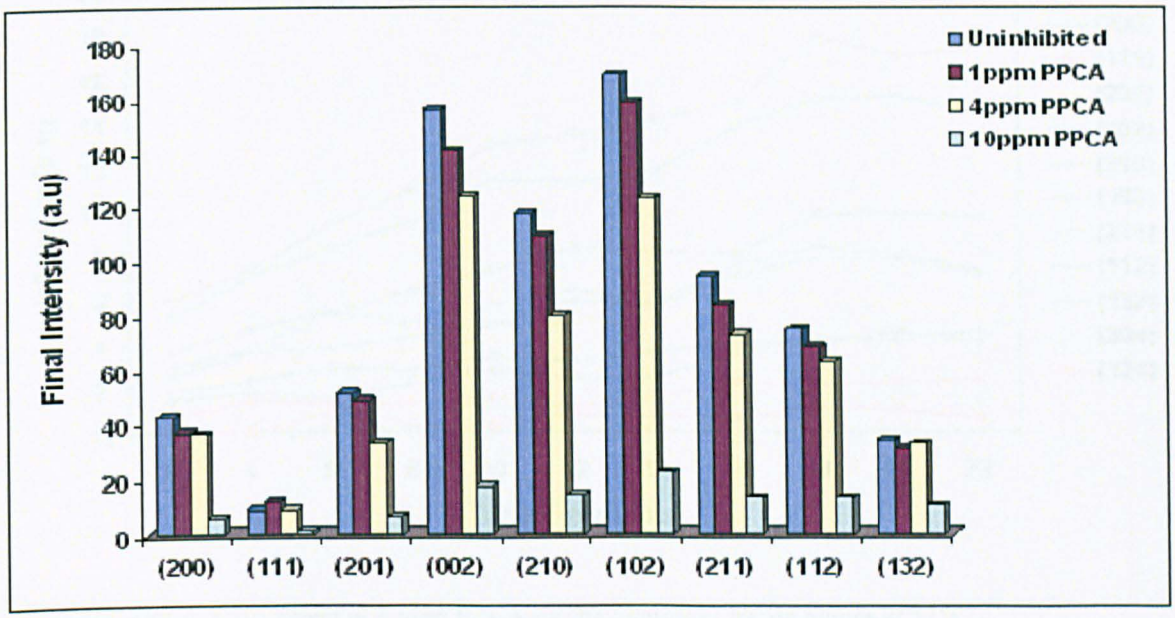

Figure 5.9: Overview of PPCA effect on dominant barite planes at 95°C

5.3.4 Inhibition at 57°C

The effect of PPCA as inhibitor of barium sulphate was further examined at the temperature of 57°C. The decrease in the applied temperature leads to extended increase in the supersaturation index compared to the one at the temperature of 95°C. Thus it is interesting to probe any changes in the formation kinetics and in the crystal planes of the formed barite on the surface under extreme high supersaturation index conditions.

Initially 4 ppm of PPCA was tested for its effect and the *in-situ* SXRD data received is presented in Figure 5.10.

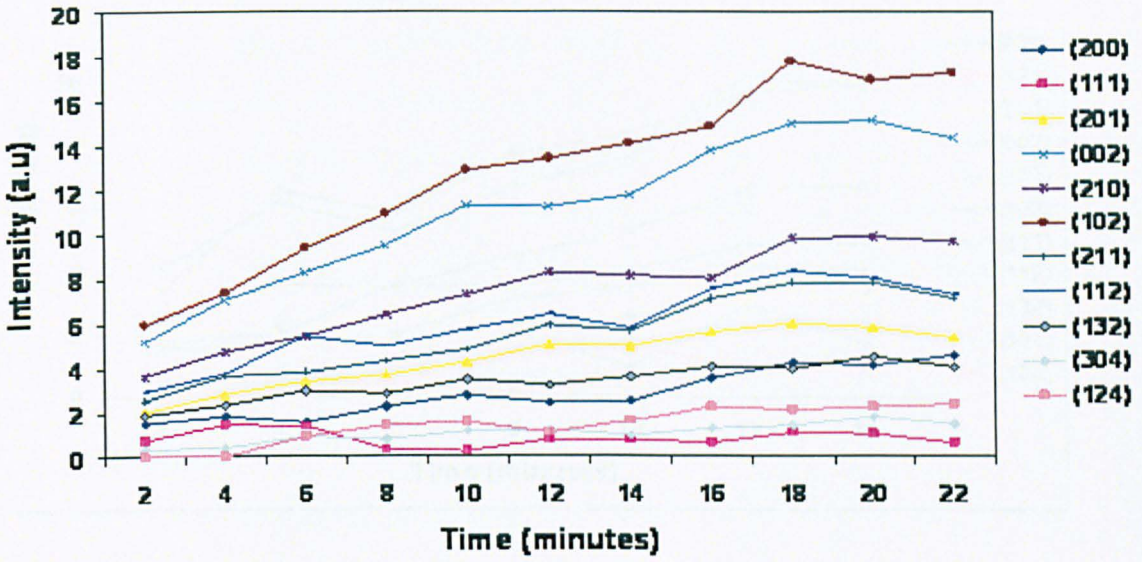

Figure 5.10: Effect of 4 ppm PPCA on the dominant barite planes at 57°C

The formation kinetics is shown to be the same for all the planes of barite recorded on the surface. Concerning the planes which dominate the growth of the barite on the surface are the same as previously. The surfaces of barium sulphate that have not been recorded under these examined conditions are the (220), (410) and (204). For this test the running time approached the 22 minutes.

Further increase in the concentration of the inhibitor up to 10 ppm PPCA resulted in recording plots like the ones illustrated in Figure 5.11. At this concentration of the inhibitor the intensity values recorded at the end of the test were lower compared to the previously examined dosage of 4 ppm PPCA.

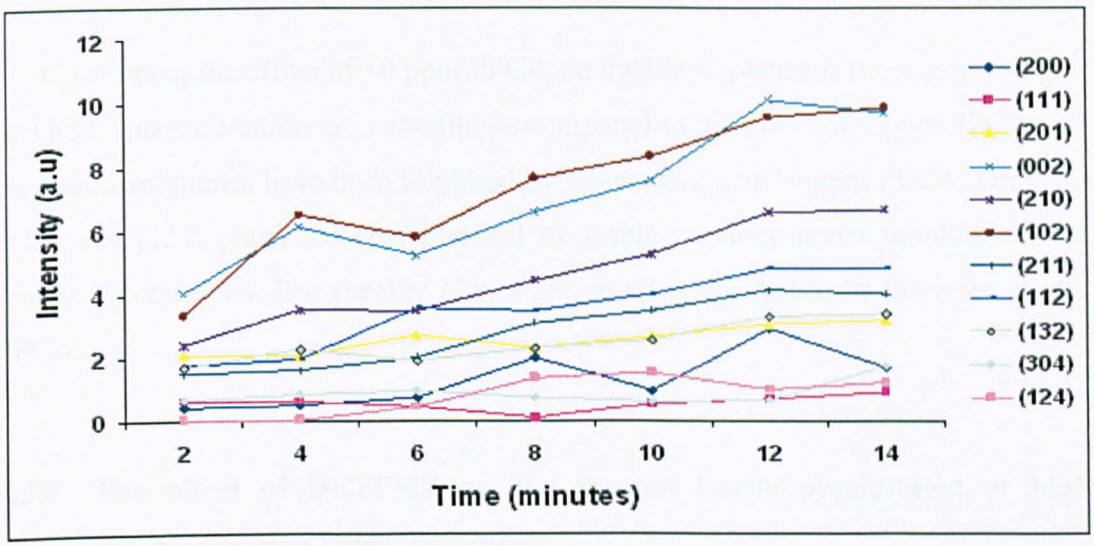

Figure 5.11: Effect of 10ppm PPCA on the dominant barite planes at 57°C

The total effect of PPCA on the $BaSO_4$ surfaces present on the surface is illustrated in Figure 5.12. According to the graph the addition of 4 ppm PPCA in the system resulted in higher intensity values of the dominant barite planes. The enhancement of the growth of the barite surfaces is remarkable for the (002), (210) and (102).

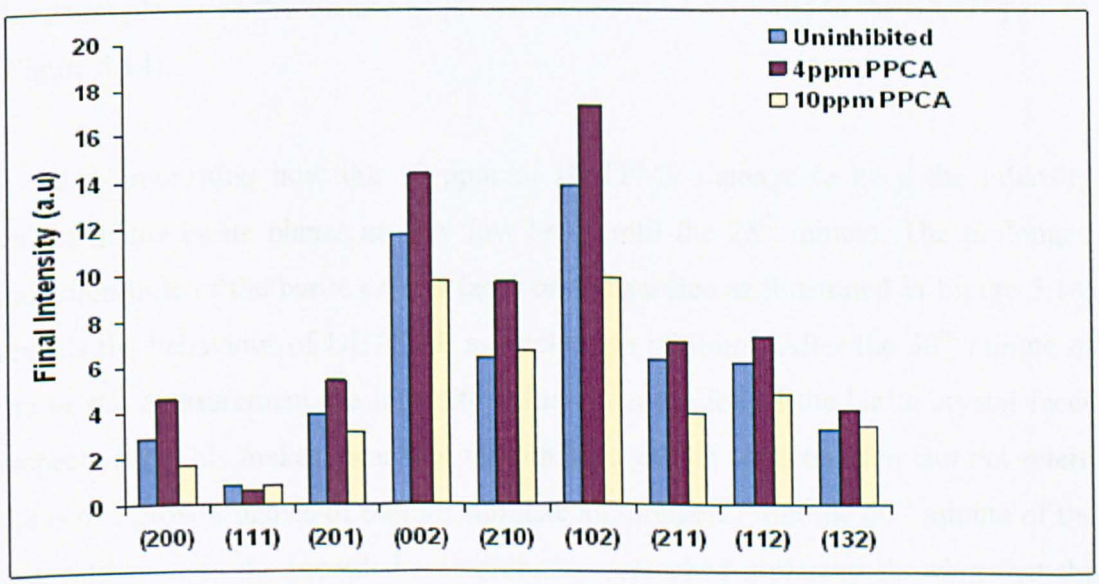

Figure 5.12: Overview of the PPCA effect on dominant barite planes at 57°C

Concerning the effect of 10 ppm PPCA on the barite planes is more promising at this high supersaturation ratio conditions compared to the effect of 4 ppm PPCA. All the dominant planes have been inhibited by the presence of 10 ppm PPCA. Only the (111) and (132) plane are characterized by stable intensity under uninhibited and inhibited conditions. The specific planes are growing too fast to be inhibited by the PPCA.

5.3.5 The effect of DETPMP on the formed barite precipitated at high supersaturation index conditions

5.3.5.1 Inhibition at 95°C

The first concentration of DETMP tested for its performance on the barite formation at 95°C on the surface was 10 ppm. The crystal faces of barite detected under the influence of 10 ppm DETPMP were the same as recorded in the previous measurements. The addition of DETPMP initially inhibited the presence of the dominant planes on the surface as presented in Figure 5.13 and in the SXRD pattern (Figure 5.14).

It is interesting how the 10 ppm of DETPMP manage to keep the intensity values of the barite planes at very low level until the 28th minute. The prolonged induction time of the barite crystal faces on the surface as illustrated in Figure 5.14, reveals the behaviour of DETPMP as nucleation inhibitor. After the 30th minute of the *in-situ* measurement the intensity values increase for all the barite crystal faces respectively. This makes clear that the inhibitor at this concentration can not retard the active growth planes of barium sulphate any longer. From the 40th minute of the test until the end the recorded intensities have reached a plateau showing that the further growth of the barite crystal faces on the surface has stopped.

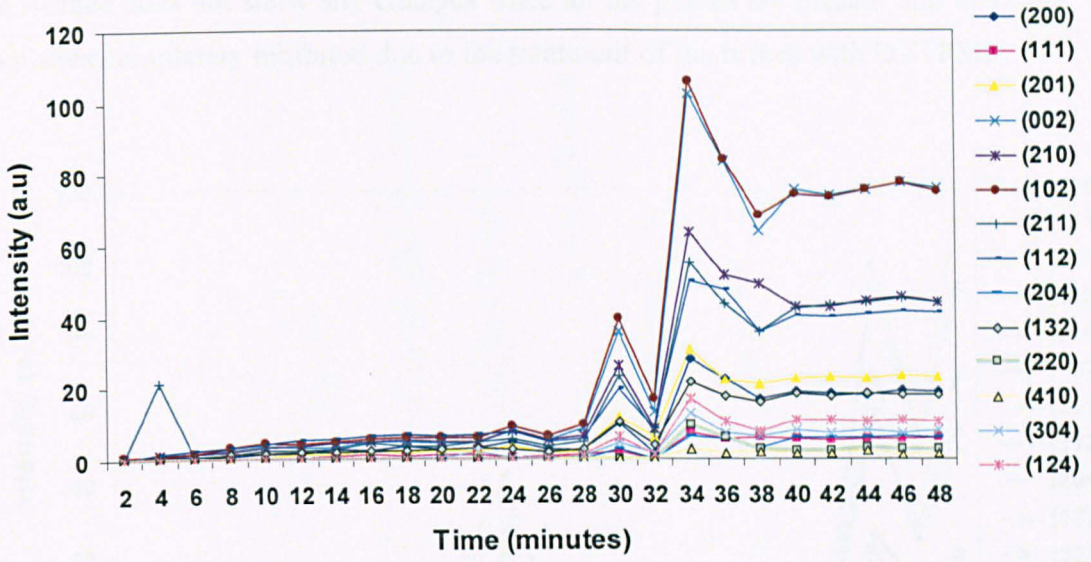

Figure 5.13: Effect of 10ppm DETPMP on dominant barite planes at 95°C

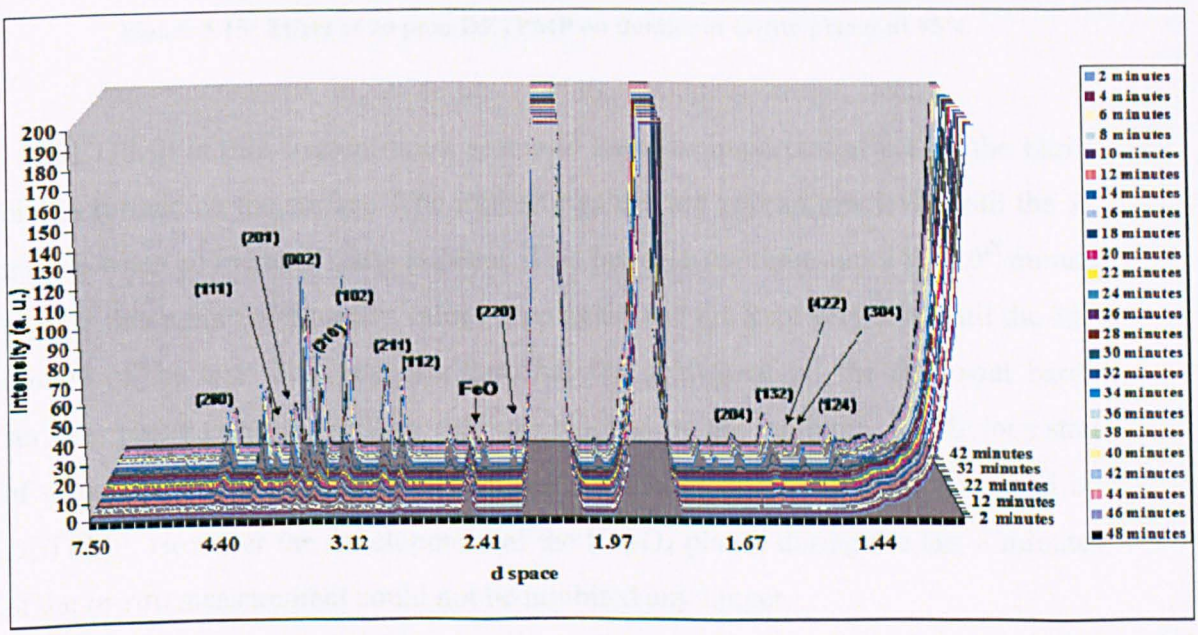

Figure 5.14: SXRD pattern of barite planes after treatment with 10 ppm DETPMP at 95°C

The SXRD data received after an increase in the concentration of DETPMP up to 20 ppm is presented in Figure 5.15. The crystallography of the inhibited barite on

the surface does not show any changes since all the planes are present and there are no planes completely inhibited due to the treatment of the brines with DETPMP.

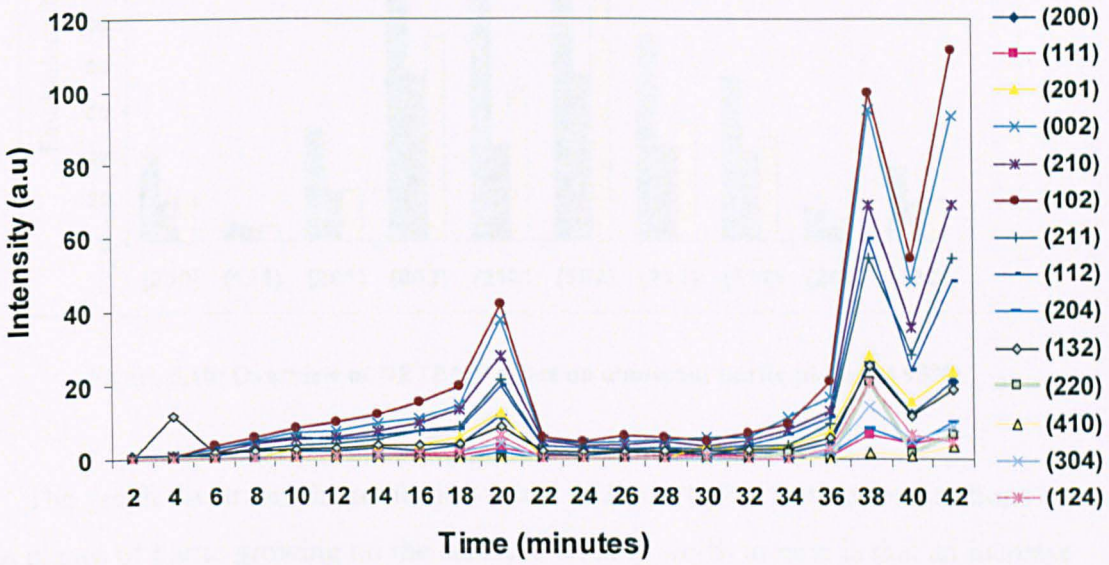

Figure 5.15: Effect of 20 ppm DETPMP on dominant barite planes at 95°C

DETPMP at this concentration seems to have an important effect on the barite planes formed on the surface. The intensity values are kept in low level until the 8th minute when an increase starts to occur. This increase continues until the 20th minute as after this point the intensity values drop again and are kept very low until the 34th minute of the test. This suggests that that the growth of all the dominant barite surfaces present on the capillary cell was blocked by the inhibitor. An obvious start of growth of the active barite sited in the middle of the process was executed by DETPMP. However the development of the $BaSO_4$ planes during the last 8 minutes of the *in-situ* measurement could not be inhibited any longer.

The effect of DETPMP on the stable planes of barium sulphate at 95°C is more obvious in Figure 5.16.

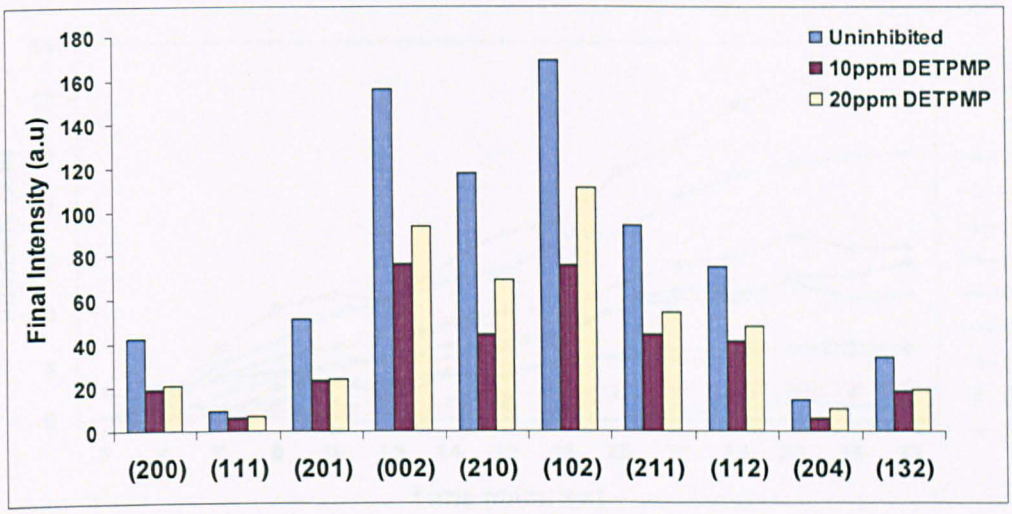

Figure 5.16: Overview of DETPMP effect on dominant barite planes at 95°C

The graph illustrates the inhibition effect of DETPMP at both concentrations on the planes of barite growing on the surface. What is worth to note is that an increase in the concentration of the applied inhibitor does not result in better inhibition conditions. Figure 5.16 reveals that the addition of 20 ppm DETMP did not manage to retard in higher level the morphology of the barium sulphate compared to the 10 ppm. The (200), (201) and (132) crystal faces seem to be uninfluenced by the increase in the concentration of the inhibitor. On the other hand the F faces; (102), (002), (210), (211) and (112) showed enhanced growth due to the presence of 20 ppm DETPMP. Concerning the intensity of the (111) crystal face present on the surface it showed no changes at all under inhibited conditions.

5.3.5.2 Inhibition at 57°C

DETPMP was further tested as inhibitor of forming barite on the surface at 57°C. The concentration of 10 ppm did not result in any changes in the crystallography (Figure 5.17). The formation kinetics shows a constant increasing trend.

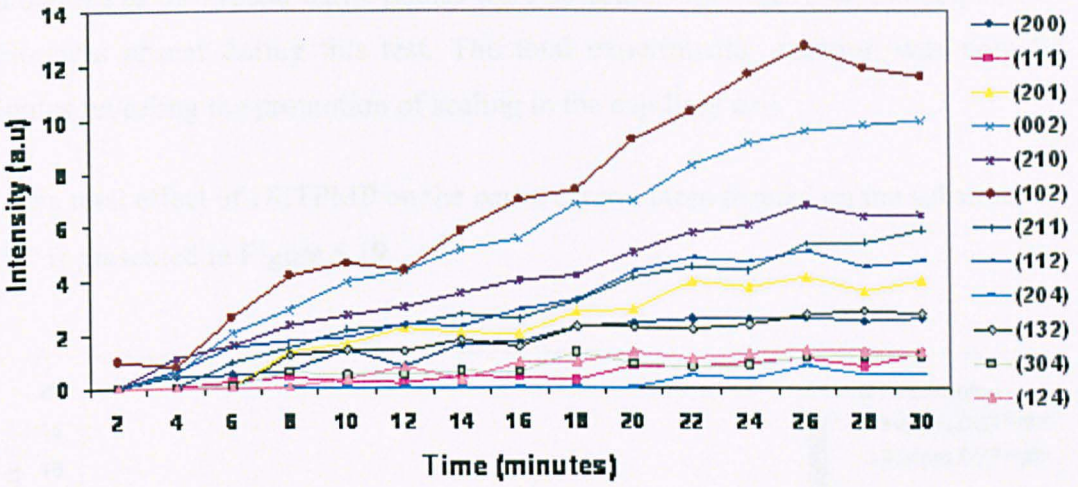

Figure 5.17: Effect of 10 ppm DETPMP on dominant barite planes at 57°C

In a similar way the increase in the concentration of DETPMP to 20 ppm caused no inhibition in the growth of the dominant planes (Figure 5.18).

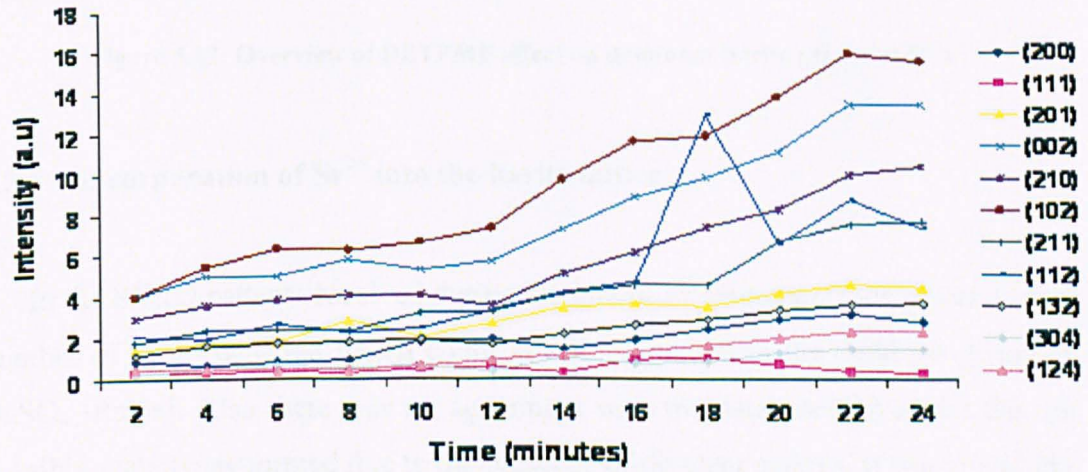

Figure 5.18: Effect of 20 ppm DETPMP on dominant barite planes at 57°C

On the contrary the crystal faces seemed to grow more since the intensity was higher compared to one measured when 10 ppm of DETPMP was added. The crystallographic nature of the formed barite in the presence of 20 ppm DETPMP is

maintained as the typical barite planes were detected. Only the (204) lattice plane of barite was absent during this test. The total experimental duration was only 24 minutes revealing the promotion of scaling in the capillary cell.

The total effect of DETPMP on the barite crystal faces formed on the substrate at 57°C is presented in Figure 5.19.

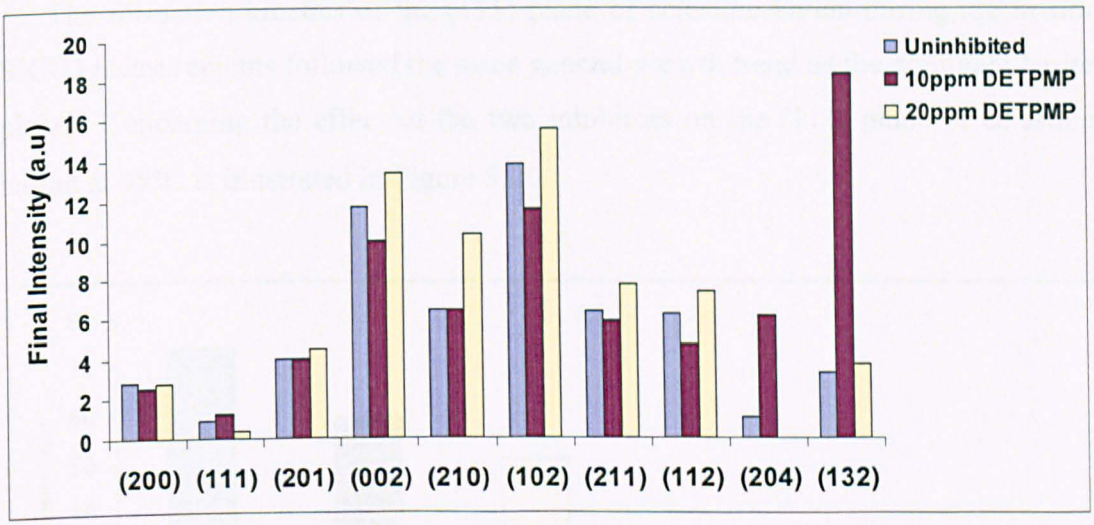

Figure 5.19: Overview of DETPMP effect on dominant barite planes at 57°C

5.3.6 Incorporation of Sr^{2+} into the barite lattice

In the SXRD patterns received during the *in-situ* measurements there was a small number of peaks detected which could not be correlated to the database given for $BaSO_4$ [Pnma]. Also there was no agreement with the databases given for the rest possible scale types formed due to the presence of divalent cations. It was found that most of these peaks were responding to the crystal planes of celestine barian (Sr 0.87 Ba 0.13) (SO_4) formed during the incorporation of strontium ions into the barite lattice. The peaks were detected at d space= 4.04 Å, 2.40 Å and 1.73 Å representing the (111), (212) and (031) crystal planes of celestine barian respectively [169]. For the other peaks in the SXRD pattern which can not be linked to the known databases, it is suggested that their presence is due to formation of non-well

established mixtures of barite with the divalent cations and especially with Ca^{2+}. The presence of these potential mixtures could be favoured by the current examined conditions of temperature and supersaturation index.

5.3.6.2 (111) plane of celestine barian

The formation kinetics of the (111) plane of celestine barian during the *in-situ* SXRD measurements followed the same general growth trend as the dominant barite planes. Concerning the effect of the two inhibitors on the (111) plane of celestine barian at 95°C is illustrated in Figure 5.20.

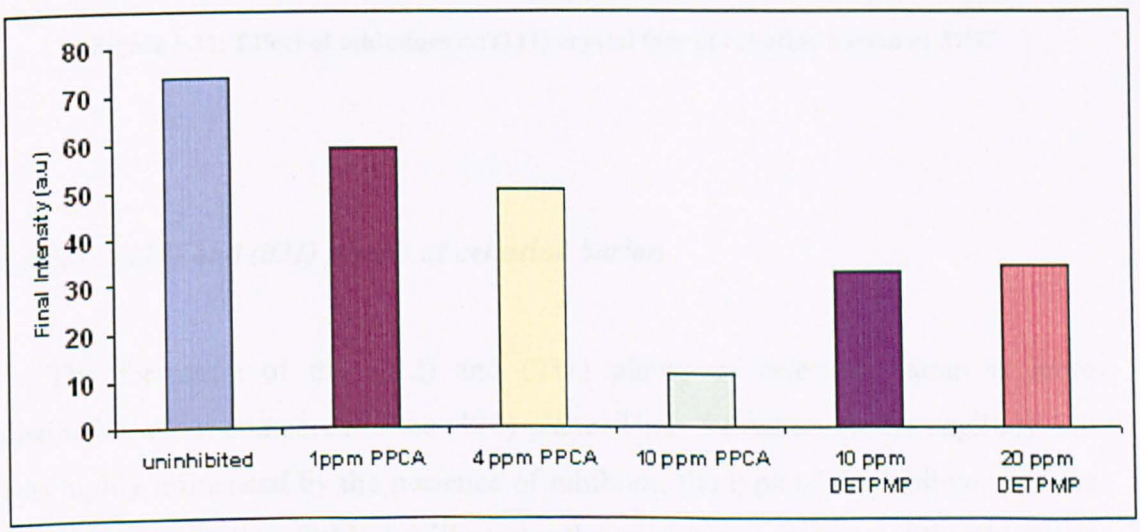

Figure 5.20: Effect of inhibitors on (111) crystal face of celestine barian at 95°C

At 95°C the inhibitors seemed to be effective in inhibiting the formation of (111) plane. The increase in the concentration of PPCA resulted in higher retardation of the specific crystal face. On the other hand the intensity of the (111) plane remained at the same level at 57°C even when inhibitors were present in the system, as shown in Figure 5.21. Furthermore at this temperature level 4 ppm of PPCA and 20 ppm of DETPMP promoted the growth of the (111) surface of celestine barian.

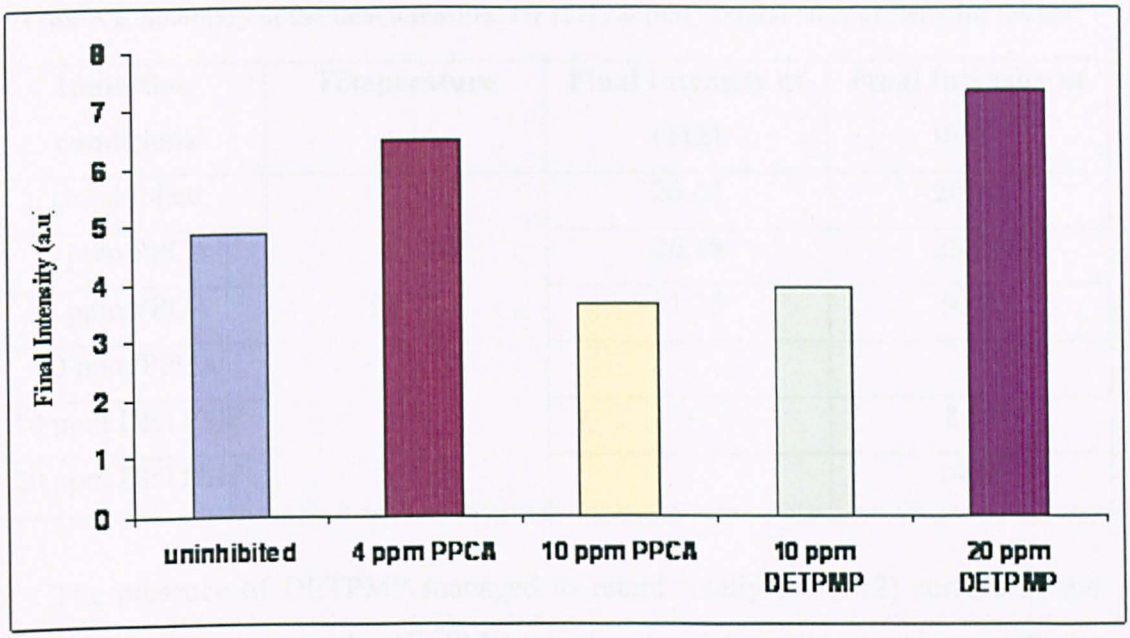

Figure 5.21: Effect of inhibitors on (111) crystal face of celestine barian at 57°C

5.3.6.3 (212) and (031) planes of celestine barian

The formation of the (212) and (031) planes of celestine barian is more distinctive when compared to the (111) plane. Their formation on the capillary cell was highly influenced by the presence of inhibitor, the type of the inhibitor and the applied concentration. Table 5.2 illustrates the presence or absence of the (212) and (031) crystal faces of celestine barian at 95°C only, as at 57°C none of these crystal faces of celestine barian was identified.

According to the Table 5.2 both planes (212) and (031) are inhibited with the increase of the PPCA concentration at 95°C. The highest applied concentration of 10 ppm resulted in complete retardation of the two planes.

Table 5.2: Summary of the final intensities for (212) & (031) crystal faces of Celestine barian

Inhibition conditions	Temperature	Final Intensity of (212)	Final Intensity of (031)
Uninhibited	95°C	26.64	26.30
1 ppm PPCA		26.18	25.33
4 ppm PPCA		11.25	9.44
10 ppm PPCA		-	-
10 ppm DETPMP		-	8.54
20 ppm DETPMP		-	14.51

The presence of DETPMP managed to retard totally the (212) surface of the celestine barian. Apparently DETPMP reveals a trend to inhibit the planes with the highest Miller indices. On the other hand the (031), which is close packed plane was detected even after the addition of DETPMP. It is interesting the variation in the effect of DETPMP on the formed barite according to the applied concentration. The 10 ppm of DETPMP inhibited more the formation of the specific plane compared to the 20 ppm of the additive.

5.3.7 Uninhibited $BaSO_4$ formation precipitating from mixture B

The formation of barium sulphate was assessed *in-situ* with synchrotron X-ray diffraction, after the barite precipitated from mixture B. The supersaturation index of mixture B with respect to barite is quite smaller as shown earlier in the beginning of this chapter. Main reasons for these tests to take place were:

- to determine if the SXRD technique is able to perform even when the formation of barite scale is not favoured at these low supersaturation index conditions

- to assess the original kinetics and the crystallography of barite formed at low supersaturation index

The application of inhibitors was not an objective when the mixture B was tested *in-situ* with SXRD.

For this experimental session the SXRD pattern is presented in Figure 5.22. Plotting the graph of the intensity of the diffraction peaks in a function of time was not feasible due to the extremely high number of peaks with very low recorded intensity values. The SXRD data recorded during the investigation of mixture B at 95°C are different compared to the data received during all the previous assessments described above. At the specific examined conditions of temperature and supersaturation index the constant growth of the dominant planes of barium sulphate on the surface is prolonged.

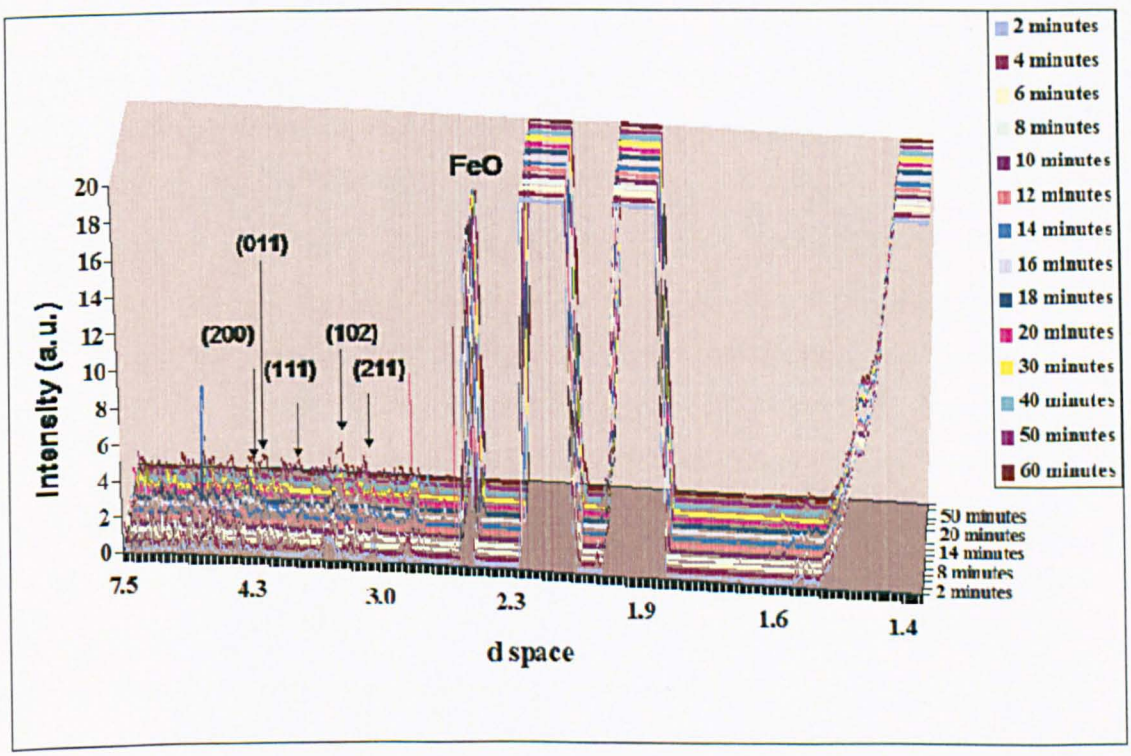

Figure 5.22: SXRD pattern for barite precipitating from mixture B at 95°C

Figure 5.22 illustrates many diffraction peaks of low intensity to be present in the pattern during the 1 hour of precipitation in the capillary cell, representing the formation of small crystallites of scale formed on the surface of the cell. Only at the end of 1 hour precipitation the presence of the dominant planes (200), (111), (102) and (211) of barite on the surface is clear. In addition the (011) lattice plane is being identified confirming the slow kinetics that dominate the formation of barium sulphate at the specific examined conditions.

CHAPTER 6 Discussion

6.1 Introduction

Studying the formation of barium sulphate on surfaces is challenging in terms of understanding kinetics and mechanisms of (i) inorganic scale growth and (ii) retardation of the adhered crystal growth by chemical additives. The two previous chapters of this work have shown the variations in the formation kinetics during the emergence and growth of barite on the surface depend on the examined conditions. In addition the kinetics on the surface are different compared to the kinetics that dominate the bulk phase. Undoubtedly the formation of barium sulphate is complicated; however the complexity of this system can be identified and controlled by investigating the early stages of the barite deposition on a substrate. The initial stage of formation is crucial since it seems to align the further barite growth routes.

The QCM and AFM techniques used for the purposes of this study, were very useful to allow determination of the barium sulphate kinetics and mechanisms in the presence and absence of inhibitors in the early stages of the deposition process. Quartz Crystal Microbalance proved to be sensitive and accurate to give reproducible measurements allowing the barium sulphate deposition kinetics to be controlled. The observations of the barium sulphate morphologies with the Atomic Force Microscope allowed the identification of the main crystallographic growth directions and crystal faces of barite growth in uninhibited and inhibited conditions. The crystallography of the $BaSO_4$ formed on a surface was followed *in-situ* under flowing conditions and high temperatures. The input of the *in-situ* SXRD technique in this study is significant. The *in-situ* SXRD measurements allowed the determination of the crystallographic nature of the formed barite as a function of time, revealing the key crystal faces of barite during the growth and retardation stages.

In this chapter the results presented in chapters 4 and 5 are analysed and discussed. An overall interpretation of the results is being presented through three parts and a discussion on how the current work fits into the literature is given. The first part of this chapter refers to the kinetic aspects of the barite formation on the surface. Further the formation kinetics of the barite on the surface is compared to the bulk kinetics. The second part of the discussion deals with the $BaSO_4$ crystallography and with the retarded nature of the barite crystals in the presence of inhibitors. In the last part the industrial impact of the results presented in this work, is discussed in terms of growth kinetics and inhibitors efficiency.

6.2 Kinetics

6.2.1 Growth rate of $BaSO_4$

6.2.1.1 Uninhibited tests

Quartz Crystal Microbalance was used for determination of the formation kinetics of barium sulphate on the surface under three different supersaturation indices during the first hour of the precipitation. QCM measurements follow all the stages of the barite formation on the surface in uninhibited and inhibited conditions. In Figure 6.1 the plots recorded from the uninhibited tests show how the process of the barium sulphate formation on the surface consists of two parts; an initial non-linear part and a second linear one. The type of plots received with the QCM are in good agreement with the work published by Nancollas *et al.* where the seeded crystal growth of barium sulphate was investigated [118]. Furthermore the work published by Rollheim *et al.* [170], which has as the base the work of Nancollas, refers to the barite precipitation kinetics and is in agreement with the results of this study. In addition Rollheims work can be used in terms of calculating the number of active sites present during the crystal growth as a function of the radius of the tube

where the scale formation occurs. Developing a relationship between the active sites and the tube radius is practically desirable and it can be also applied to the study presented here, since the record of the active sites of barium sulphate during the deposition process consist one main objective. However the active sites calculation of Rollheim based on the precipitation kinetics has a few problematic aspects since distinguishing between the actual adhered crystals and the ones settling from the solution, is not clear. Also the presence of divalent cations although it is necessary in order to imitate the real off-shore environment, was not included in the model.

The non-linear part of the plots represents the nucleation process and the beginning of the growth of $BaSO_4$ that takes place on the surface. The second part illustrates how the growth of barium sulphate continues in a linear way.

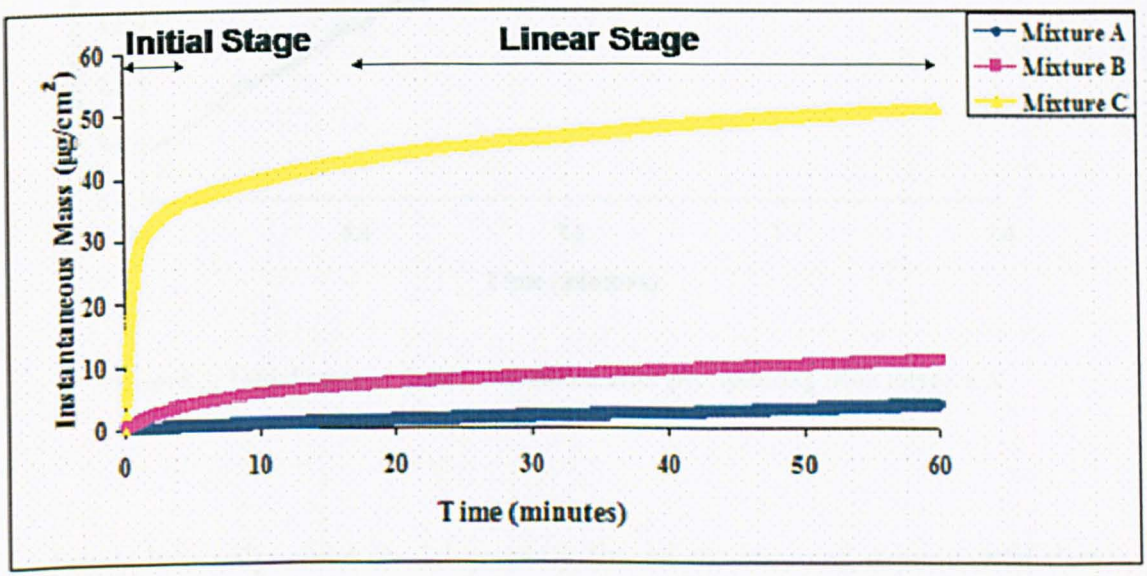

Figure 6.1: Deposition of $BaSO_4$ on quartz crystal at three different supersaturation indices

In order to determine the formation kinetics immediately after the precipitation process of $BaSO_4$ has started, the first two minutes of the mass measurements of barite as recorded with QCM, were plotted.

Figure 6.2 shows the first two minutes of the barite formation on the surface when mixture A was used as initial brine. The model which fits on the experimental data is a polynomial of second order and reveals the tendency by which the barite scale mass increases on the surface even at the low supersaturation index conditions. The polynomial second order equations have been also applied to describe the barite growth in Nancollas *et al.* work [116].

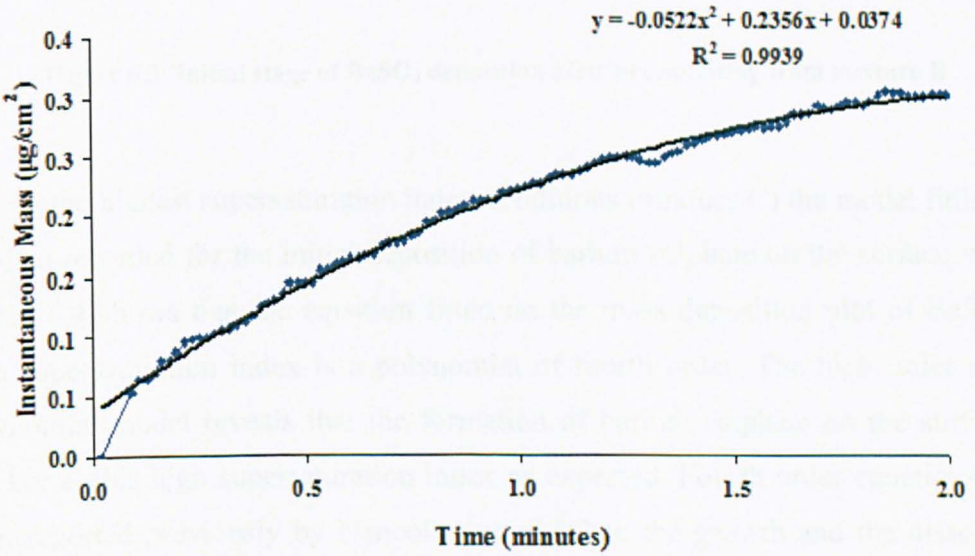

Figure 6.2: Initial stage of $BaSO_4$ deposition after precipitating from mixture A

Similarly a polynomial model properly fits on the received experimental data from the first two minutes of barite deposition from mixture B with supersaturation index equal to 2.64 as shown in Figure 6.3. The equation is again a second order polynomial, as in the lower supersaturation index tests (Figure 6.2).

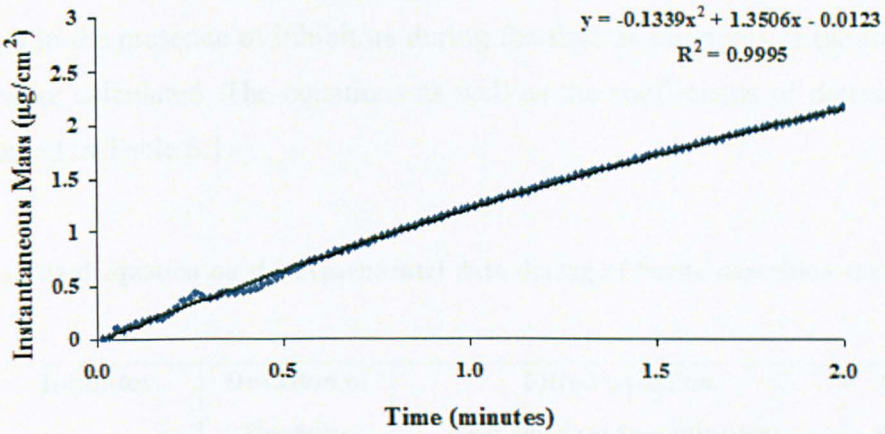

Figure 6.3: Initial stage of $BaSO_4$ deposition after precipitating from mixture B

For the highest supersaturation index conditions (mixture C) the model fitting on the data recorded for the initial deposition of barium sulphate on the surface varies. Figure 6.4 shows that the equation fitted on the mass deposition plot of $BaSO_4$ at high supersaturation index is a polynomial of fourth order. The high order of the polynomial model reveals that the formation of barium sulphate on the surface is quicker at this high supersaturation index as expected. Fourth order equations have been reported previously by Nancollas *et al.* when the growth and the dissolution process of barite formation were examined in seeded growth tests, however no further investigation on these kinetic rates took place [116].

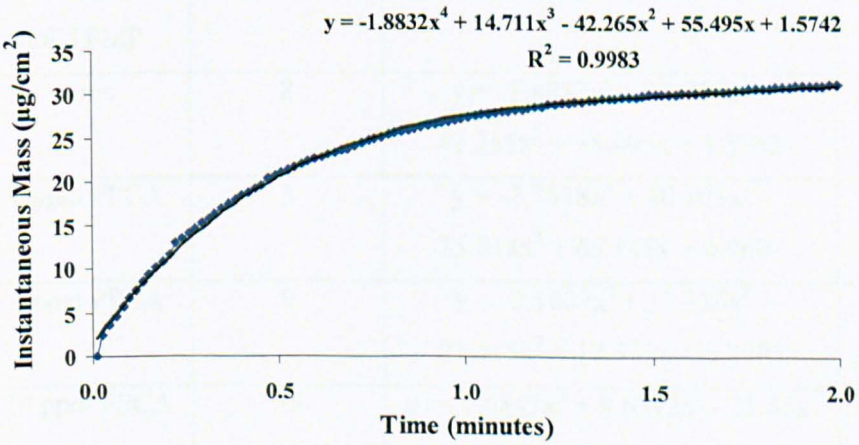

Figure 6.4: Initial stage of $BaSO_4$ deposition after precipitating from mixture C

In a similar way the equations fitted on the data recorded from the barite deposition in the presence of inhibitors during the first two minutes of the formation process were calculated. The equations as well as the coefficients of determination are presented in Table 6.1.

Table 6.1: Fitted equation on the experimental data during of barite deposition the first two minutes

Type of brine	Inhibitor	Duration of the non-linear stage (minutes)	Fitted equation (for the first two minutes)	Coefficient of determination
Mixture A	none	2	$y = -0.0522x^2 + 0.2356x + 0.0374$	0.9939
Mixture B	none	13	$y = -0.1339x^2 + 1.3506x - 0.0123$	0.9995
	1 ppm PPCA	11	$y = -0.0483x^2 + 0.2355x - 0.0166$	0.9838
	4 ppm PPCA	3	$y = 0.1052x^3 - 0.4666x^2 + 0.8496x - 0.0751$	0.9835
	10 ppm PPCA	1.25	$y = 0.0696x^3 - 0.2969x^2 + 0.4713x + 0.0007$	0.9968
	1 ppm DETPMP	1	$y = -0.0618x^2 + 0.3382x + 0.0161$	0.9876
	4 ppm DETPMP	16	$y = -0.0558x^2 + 0.6692x - 0.101$	0.9979
	10 ppm DETPMP	12	$y = 0.0199x^2 + 0.0558x + 0.0098$	0.9814
Mixture C	none	8	$y = -1.8832x^4 + 14.711x^3 - 42.265x^2 + 55.495x + 1.5742$	0.9983
	1 ppm PPCA	5	$y = -7.7538x^4 + 40.103x^3 - 75.848x^2 + 65.348x + 0.9607$	0.9974
	4 ppm PPCA	9	$y = -2.1887x^4 + 11.336x^3 - 21.415x^2 + 18.353x + 0.2903$	0.9962
	10 ppm PPCA	15	$y = -1.6843x^4 + 9.6392x^3 - 21.88x^2 + 27.446x + 0.0187$	0.9997

From the kinetic data presented in Table 6.1 related to the inhibited tests, it is interesting the modification in the model when it comes to the concentrations of 4 ppm and 10 ppm of PPCA tested with mixture B. For these two cases the best fitted model is a polynomial of third order instead of the second order as fitted in the previous tests. The third order polynomials show that at the specific concentrations of the inhibitor the kinetics on the system become faster. Thus PPCA does not act on the nucleation stage of the barite formation on the surface. On the contrary the data from the tests with DETPMP are characterized by second order polynomial models, revealing that DETPMP acts on the nucleation stage and is able to maintain the order of kinetics during the formation of $BaSO_4$ on the surface.

In addition the duration of the non-linear stage of the $BaSO_4$ deposition for every examined case was identified from the QCM plots as shown in Figure 6.5 and is given in Table 6.1. The duration of the non-linear part refers to the induction time of the barium sulphate on the surface.

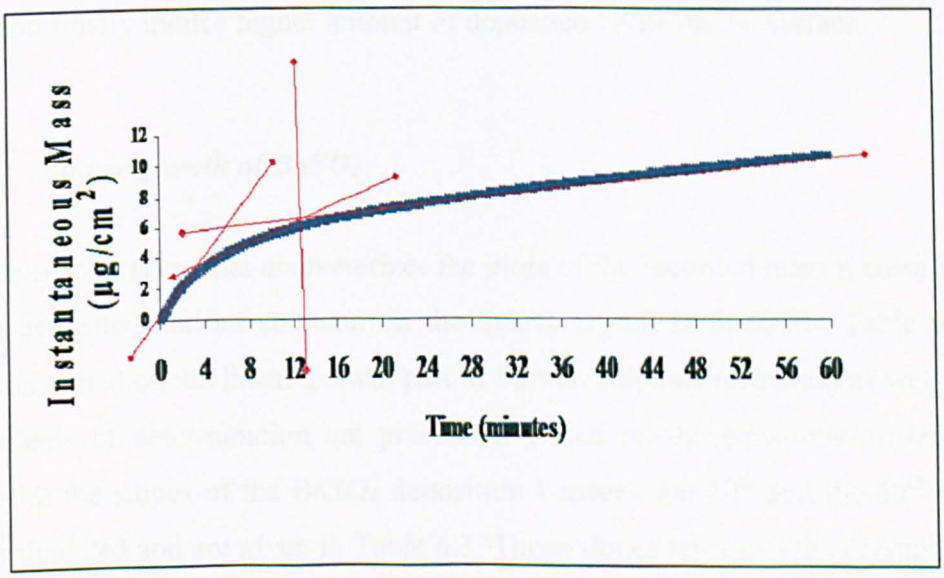

Figure 6.5: Approach of the induction time of barium sulphate on the surface for mixture B

The values of the non-linear part presented in Table 6.1 for the different mass measurements shows how the initial stage period of the barite formation is being modified at different experimental conditions. The increase in the supersaturation

index from 1.45 to 2.64 for the uninhibited tests, leads to a prolonged non-linear stage of barium sulphate formation on surface.

Most important the presence of PPCA as scale inhibitor in the mixture B at concentrations higher than 4 ppm, results in a shorter non-linear formation of barite on surface. This shorter duration of the non-linear stage of the deposition agrees with the transition from second order to third order polynomial equations as mentioned earlier. This is due to the lack of effectiveness of PPCA as inhibitor to act on the nucleation stage of $BaSO_4$ crystals formed on the surface. In this way the induction time of barium sulphate on the surface is shorter and the linear growth of the barite particles starts soon. Similar phenomenon was recorded when mixture C was treated with PPCA as shown from the duration of the non-linear stage.

On the contrary when DETPMP was tested with mixture B at concentrations higher than 4 ppm for its inhibition activity on barium sulphate, the duration of the non linear stage was extended. Hence DETPMP was able to prolong the nucleation stage and finally induce higher amount of deposited barite on the surface.

6.2.1.2 Linear growth of $BaSO_4$

The second stage that characterizes the plots of the recorded mass measurements of the deposited barium sulphate on the quartz crystal is linear. In Table 6.2 the equations fitted on the linear growth part of barium sulphate formation as well as the coefficients of determination are presented. Based on the equations presented in Table 6.2 the slopes of the $BaSO_4$ deposition between the 30^{th} and the 60^{th} minute were calculated and are given in Table 6.3. These slopes represent the crystallization rates of barium sulphate and any variations in the slopes reveal the change in the crystallization rate of barite on the surface, under different experimental conditions and in the presence or absence of inhibitors.

Table 6.2: Fitted equation on the experimental data during linear stage of the barite deposition in the presence of inhibitors

Type of brines	Inhibitor	Equation	Coefficient of determination
Mixture A	None	y = 0.0011x + 1.9439	0.9965
Mixture B	None	y = 0.0015x + 8.2555	0.9989
	1ppm PPCA	y = 0.0013x + 1.7836	0.9999
	4ppm PPCA	y = 0.0009x + 0.7934	0.9894
	10ppm PPCA	y = 0.0002x + 0.2967	0.9692
	1ppm DETPMP	y = 0.0029x + 5.3307	0.9996
	4ppm DETPMP	y = 0.0023x + 8.5246	0.9974
	10ppm DETPMP	y = 0.0025x + 5.7263	0.9982
Mixture C	None	y = 0.1662x + 41.397	0.9887
	1ppm PPCA	y = 0.0054x + 34.869	0.9969
	4ppm PPCA	y = 0.0012x + 10.745	0.9787
	10ppm PPCA	y = 0.0003x + 30.851	0.898

According to Table 6.3 when mixture A and mixture B were tested they gave similar slopes, despite the difference in the supersaturation index. Thus it can be suggested that after the 30th minute of precipitation, the barium sulphate growth occurs in a similar rate in a supersaturation index range between 1.45 and 2.64. However for the supersaturation index equal to 4.32, which is the highest supersaturation index tested in this study, the crystallization rate of barium sulphate was higher by a factor of 10 compared to the one recorded for mixture B.

Table 6.3: Slope of the linear growth of $BaSO_4$

Type of brines	Inhibitor	Slope of the plot between 30th and 60th minute
Mixture A	None	0.0011
Mixture B	None	0.0015
	1ppm PPCA	0.0013
	4ppm PPCA	0.0009
	10ppm PPCA	0.0002
	1ppm DETPMP	0.0029
	4ppm DETPMP	0.0023
	10ppm DETPMP	0.0025
Mixture C	None	0.0155
	1ppm PPCA	0.0054
	4ppm PPCA	0.0012
	10ppm PPCA	Coefficient of determination of the trend line < 0.9

The slopes of the plots recorded with the Quartz Crystal Microbalance for the inhibited tests as presented in Table 6.3, illustrate the effect of (i) inhibitor type and (ii) concentration of the inhibitor on the formation of $BaSO_4$ on the surface. The key point is the decrease in the slopes of the plots in the presence of PPCA compared to the slopes for the uninhibited cases. The smaller slope during the linear growth of barium sulphate on the surface after treatment with PPCA reveals the performance of the additive as growth retarder.

On the other hand the slopes of the barite growth in the presence of DETPMP seem to be higher compared to the one recorded for the uninhibited test. This confirms that DETPMP has not inhibition effect on the growth rate of the barium sulphate formed on the surface, at the specific examined conditions. The lack of effectiveness of DETPMP on the formed barite on the surface during the first hour of precipitation was initially determined with the QCM mass measurements, where

the recorded amount of barite mass was similar in the presence and absence of DETPMP.

The poor performance of DETPMP on the barite formed at surfaces is in agreement with the work of other researchers, where they have concluded that the specific inhibitor of barite is less effective in the bulk phase at low temperatures [74,76]. Furthermore the low concentrations of calcium cations in the examined brines suggests that both inhibitors would perform less effective since high concentrations of calcium promote the inhibition activity as shown by Graham *et al* [134].

A comparison of the crystallization rate of $BaSO_4$ formed on surface as determined in this study, with the ones published elsewhere is difficult since most of the previous research has focused on the rates during the precipitation of barite in bulk phase. In addition comparison of the crystallization rate of barium sulphate formed on surface with crystallization rates of other inorganic types of scale which their presence is crucial for the oil extraction process is not straightforward. Most of the crystallization rates of these inorganic types of scale known so far are referring again to the bulk phase. Even for the few cases where calculations have taken place for crystallization rates of the inorganic salts on surface, the experimental conditions and supersaturation indices vary a lot. This makes the comparison among the crystallization rates difficult.

6.2.2 Quantification of barite scale formed at different growth rates

The results presented from the QCM measurements have indicated that there is an early stage (<2 minutes) process followed by a steady linear process. However the polynomial models of the initial stages of formation presented in Table 6.1 apply for a specific time period; zero until second minute of deposition. In order to predict the deposited mass on the surface as a function of time after a period of 1 year (365

days) based on each of the different growth rates, it was necessary to determine the equations fitted on the data during the first 0.5 minute of the barite deposition process. These equations are referring to the mass of barite deposited right after the mixing of the brines and describe conditions where the initial supersaturation index is almost equal to the initial value. Hence in an analogous way to measurements in corrosion, the scale amount in mm/year was evaluated with the Quartz Crystal Microbalance under static conditions.

The equations fitted on the data recorded during the 0.5 minutes of the barium sulphate formation are given in Table 6.4 and the evaluated masses of the $BaSO_4$ expected to deposit in one years time are presented in Table 6.5.

Table 6.4: Equations fitted on data recorded during the first 0.5 minutes of barite deposition

Type of brines	Inhibitor	Equation (for the 0.5 minutes of barite deposition)
Mixture A	None	y = 0.1864x + 0.0458
Mixture B	None	y = 1.2099x + 0.0103
	1ppm PPCA	y = 0.1924x - 0.0108
	4ppm PPCA	y = 0.1215x - 0.0188
	10ppm PPCA	y = 0.2316x + 0.0388
	1ppm DETPMP	y = 0.2572x + 0.0336
	4ppm DETPMP	y = 0.6122x - 0.0904
	10ppm DETPMP	y = 0.0756x + 0.0063
Mixture C	None	y = 38.784x + 3.2096
	1ppm PPCA	y = 34.886x + 3.4277
	4ppm PPCA	y = 9.5889x + 1.0416
	10ppm PPCA	y = 18.007x + 0.854

Table 6.5: Evaluation of the $BaSO_4$ mass formed at different growth rates

Type of brines	Inhibitor	Quantification based on initial growth rate (mm/year)	Quantification based on linear growth rate (mm/year)
Mixture A	None	0.22	0.04
Mixture B	None	1.41	0.16
	1ppm PPCA	0.22	0.04
	4ppm PPCA	0.14	0.02
	10ppm PPCA	0.27	0.01
	1ppm DETPMP	0.30	0.11
	4ppm DETPMP	0.71	0.17
	10ppm DETPMP	0.09	0.11
Mixture C	None	45.36	1.0
	1ppm PPCA	40.81	0.69
	4ppm PPCA	11.22	0.21
	10ppm PPCA	21.05	0.60

The values in Table 6.5 reveal that the predicted amount of barite formed on the surface is significantly higher when it follows the initial non-linear growth rate. In real terms the quantification made on the growth rate of the initial stage of the barite formation, represents a precipitation system where the supersaturation index is kept

sustained. This can be linked to the real oil field activities when the seawater injections are constant hence the supersaturation index is maintained at high level.

On the contrary the quantification of the barium sulphate mass based on the linear growth rates shows smaller values. The linear growth rate represents a precipitation system where the supersaturation index is decreased within time until it approaches the equilibrium. For this case it is expected the deposited mass amount to be smaller when compared to one formed under sustained supersaturation index conditions.

6.2.3 Comparison of the bulk and surface kinetics

6.2.3.1 Uninhibited case

The study of the formation kinetics of barium sulphate is approached in a complete way when both the bulk phase and the surface are investigated during the precipitation and deposition of barite. The formation kinetics of the $BaSO_4$ that took place both in the bulk phase and on the surface for the three brines are illustrated and compared in Figure 6.6 (a).

The mass and the turbidity measurements of the $BaSO_4$ confirm that an increase in the supersaturation index is followed by (i) increase in the bulk activity and (ii) increase in the amount of deposited barite on the surface. Most important Figure 6.6 (a) reveals that when the mixtures B and C are tested, the plots of the bulk kinetics in the bulk phase seem to have reached a plateau although at the same time the scaling activity on the surface continues. The difference in the kinetics that dominate the bulk and the surface of the system, clarifies that the formation of barium sulphate on a surface is a process which needs to be considered as two simultaneous phases: precipitation in the bulk phase and deposition on the surface.

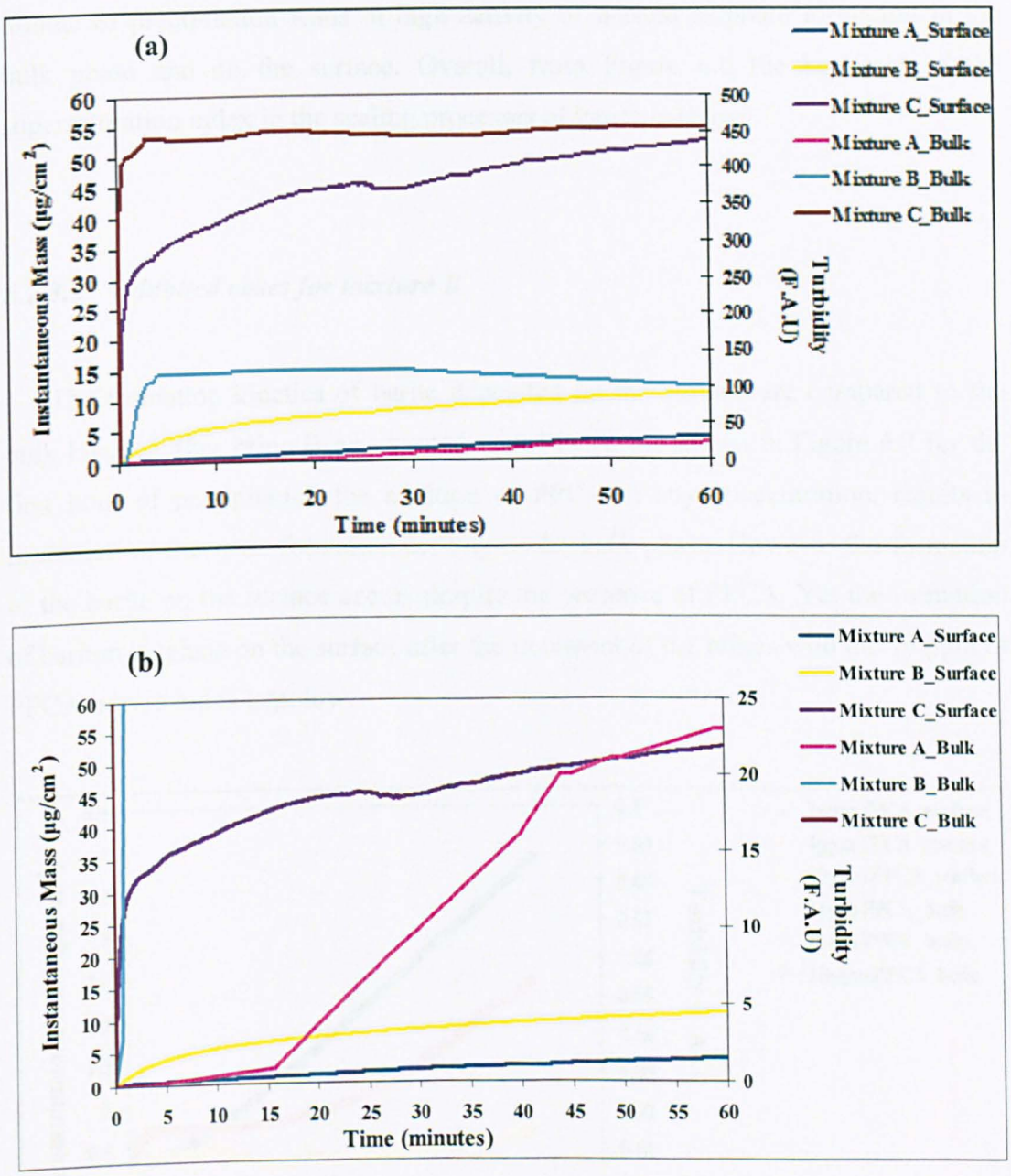

Figure 6.6: Surface and Bulk measurements for the three different brines (a) overview of all the kinetics and (b) focusing on the lower scale measurements

Figure 6.6 (b) presents in more detail the initial part of the plots. It is obvious that the formation processes of barite when mixture A was tested, are prolonged during the first 15 minutes. At the same time period, mixture B is able to promote the precipitation in the bulk phase but the deposition on the surface is just starting.

Only mixture C with the highest supersaturation index is the one that during the first minute of precipitation leads in high activity of barium sulphate formation in the bulk phase and on the surface. Overall, from Figure 6.6 the key role of the supersaturation index in the scaling processes of barite is shown.

6.2.3.2 Inhibited cases for mixture B

The formation kinetics of barite deposited on the surface are compared to the bulk kinetics after brine B was treated with PPCA. As shown in Figure 6.7 for the first hour of precipitation the addition of PPCA at any concentration, results in limitation of the scale formation activity in the bulk phase. However the formation of the barite on the surface occurs despite the presence of PPCA. Yet the formation of barium sulphate on the surface after the treatment of the brines with the 10 ppm of PPCA occurs but is kept low.

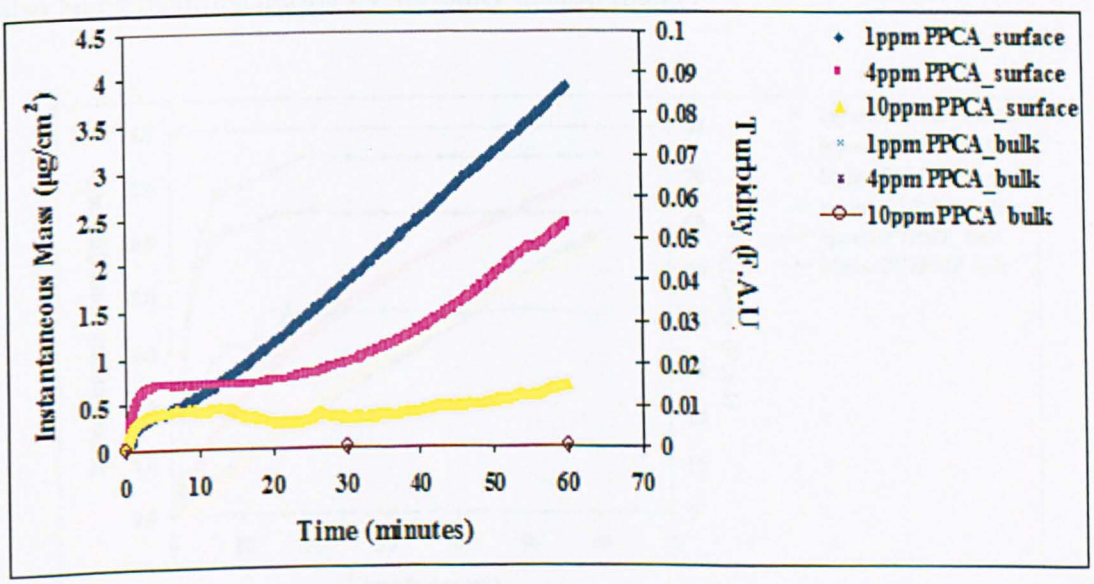

Figure 6.7: Comparison of bulk and surface measurements for mixture B after treatment with PPCA

Regarding the effect of DETPMP on the formation kinetics of barite in both bulk and surface is illustrated in Figure 6.8. The presence of DETPMP at these concentrations does not affect precipitation neither deposition of the barium sulphate. The supersaturation index is quickly approached even in the presence of the specific inhibitor and then reached a plateau at high range of turbidity, as the growth of the deposited scale on the surface occurs almost linearly. The same type of plot presented in Figure 6.8 showing the behavior of DETPMP at the concentration range from 1 ppm up to 10 ppm, has been recorded by Wang *et al.*, where the inhibition performance of DETPMP on barite in the bulk phase was investigated [86].

Its worth noting that when DETPMP was examined for its effect on barite at the concentrations of 4 ppm, gave highest turbidity and surface deposition measurements compared to the other two examined concentrations as presented in Figure 6.8. Potentially at this concentration, DETPMP interacts with the divalent cations present in the system resulting in formation of non-barite particles, which are also being recorded during the turbidity measurements.

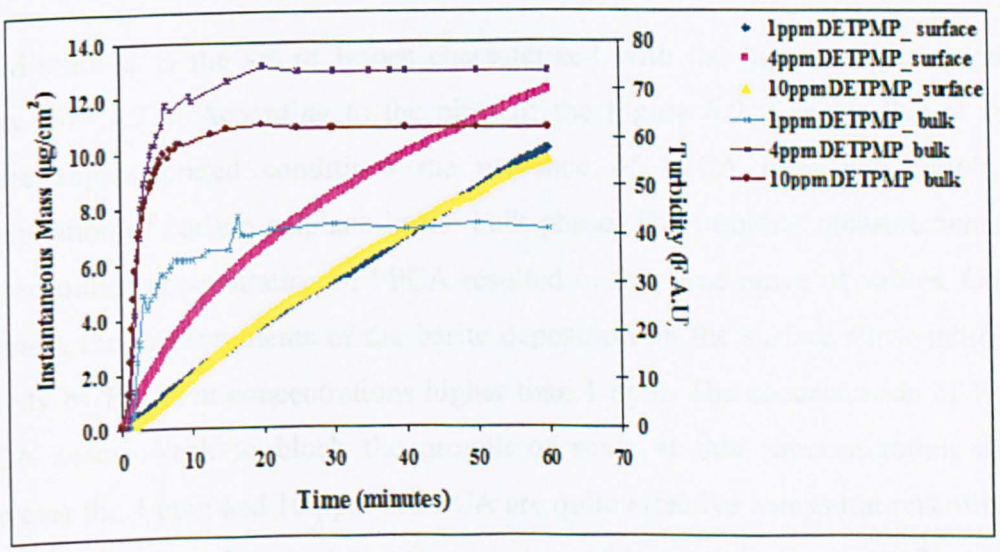

Figure 6.8: Comparison of bulk and surface measurements for mixture B after treatment with DETPMP

6.2.3.3 Inhibited cases for mixture C

The comparison of the formation kinetics of barium sulphate on the surface with the bulk kinetics, when precipitating from mixture C in the presence of PPCA is presented in Figure 6.9.

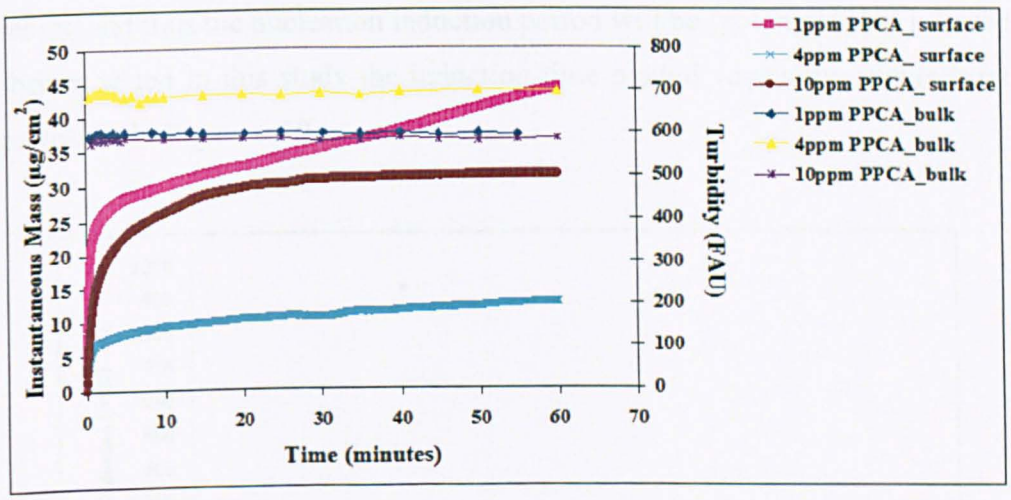

Figure 6.9: Comparison of bulk and surface measurements for mixture C after treatment with PPCA

Mixture C is the set of brines characterized with the highest supersaturation index (SI= 4.32). According to the plots of the Figure 6.9 it seems that at these severe supersaturated conditions the presence of PPCA does not inhibit the precipitation of barium sulphate in the bulk phase. The turbidity measurements for any examined concentration of PPCA resulted in the same range of values. On the contrary, the measurements of the barite deposition on the surface show inhibition activity by PPCA at concentrations higher than 1 ppm. The concentration of 1 ppm PPCA seems weak to block the growth of scale at this supersaturation index. However the 4 ppm and 10 ppm of PPCA are quite effective concentrations of barite inhibition on the surface, with the concentration of 4 ppm to be the most effective.

6.2.4 Supersaturation index

Based on the classical nucleation theory the inhibition of nucleation is mostly depending on the induction period which is controlled by the interfacial tension between the crystal and the aqueous solution, as well as the temperature and the supersaturation index. In the presence of inhibitors the interfacial tension is increased and thus the nucleation induction period will be prolonged [171]. Based on the brines tested in this study the induction time plotted versus the supersaturation index results in Figure 6.10.

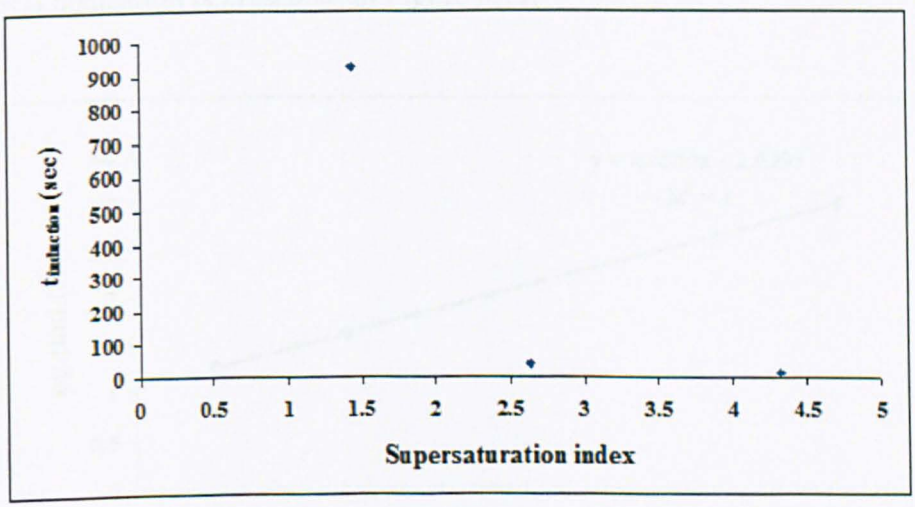

Figure 6.10: Plot of induction time versus supersaturation index

It is obvious that in the range where the supersaturation index is high the induction time gets shorter. This has an effect on the mechanisms that dominate the different supersaturation index ranges. After combining the QCM, AFM and the *in-situ* SXRD measurements it is clear that the formation of barium sulphate on surfaces is governed by different mechanisms depending on the conditions of precipitation.

From the turbidity measurements that took place for the bulk phase of all the three mixtures, the induction time was calculated for every supersaturation index as presented in Table 6.6.

Table 6.6: Induction time of the bulk phase

TYPE OF BRINES	SUPERSATURATION INDEX	$T_{INDUCTION}$ (MINUTES)
Mixture A	1.45	15.5
Mixture B	2.64	0.7
Mixture C	4.32	0.3

The effect of the supersaturation index on the logarithm of the induction periods for $BaSO_4$ nucleation is presented in Figure 6.11.

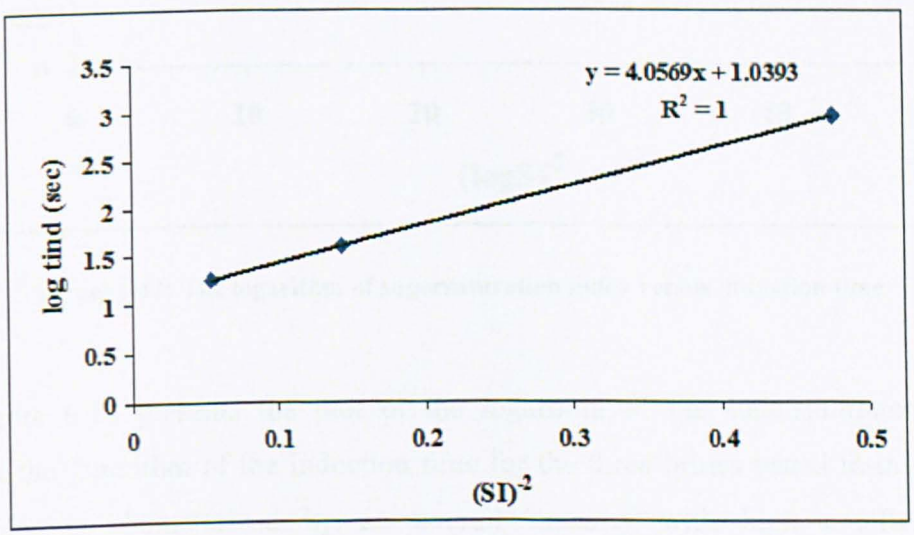

Figure 6.11: Effect of supersaturation index on induction period for $BaSO_4$ nucleation

The plot illustrated in Figure 6.11 reveals an extremely good linearity between the $(SI)^{-2}$ and the $\log_{tind}$. This type of plots has reported by Söhnel *et al.* and actually reveals that at low supersaturation index heterogeneous nucleation dominates the process [25,35].

Furthermore when the logarithm of the supersaturation index is plotted versus the logarithm of the induction time, it can be confirmed if the system is

characterized by diffusion or not. Generally diffusion as a process can not be neglected in any precipitation system. When diffusion is present, then the relationship between the logarithm of supersaturation index and the induction time is linear.

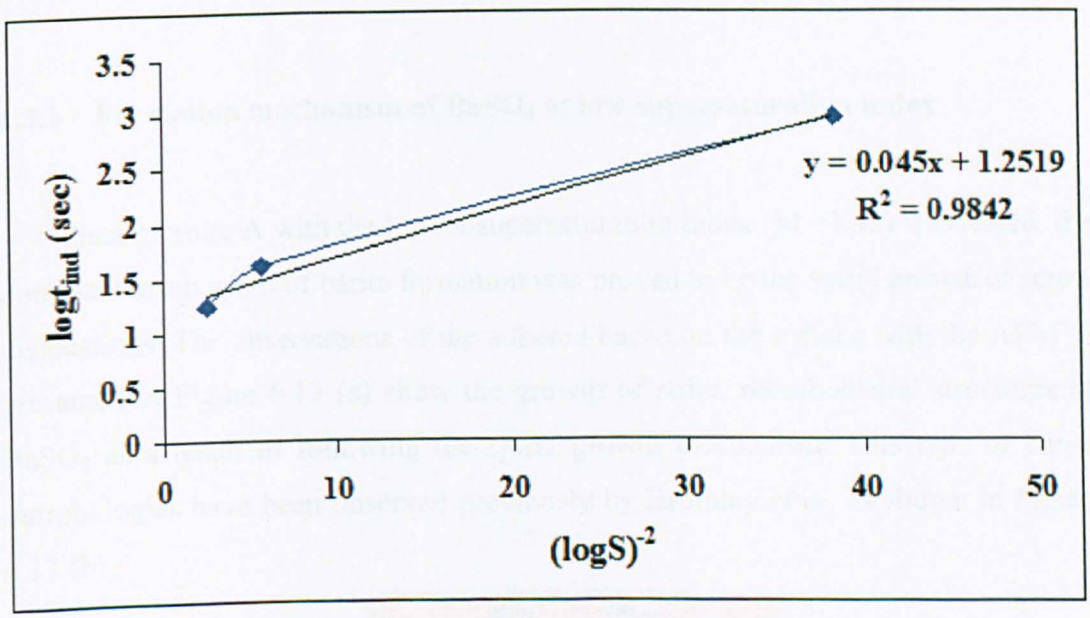

Figure 6.12: The logarithm of supersaturation index versus induction time

Figure 6.12 presents the plot of the logarithm of the supersaturation index against the logarithm of the induction time for the three brines tested in this study. The plot is characterized by an overall linearity with high coefficient of determination. However the presence of diffusion in the barium sulphate formation system needs further investigation.

6.3 Mechanisms

The formation of barium sulphate on the surface follows specific growth mechanisms. The variations among the mechanisms can be found at the examined conditions of the system and key point is the supersaturation index as driving force of the $BaSO_4$ formation. In this study the growth mechanisms of barite were

followed at three different supersaturation indices and the variations in the growth process were highlighted. The observations with the atomic force microscope proved to be significant during the interpretation of the mechanisms. The scanning of the barite topography for every test clearly demonstrates the preferred orientation of the barite morphologies on the surface.

6.3.1 Formation mechanism of $BaSO_4$ at low supersaturation index

When mixture A with the lowest supersaturation index (SI =1.45) was tested, the dominant mechanism of barite formation was proved to be the spiral growth at screw dislocations. The observations of the adhered barite on the surface with the AFM as presented in Figure 6.13 (a) show the growth of strict, rhombohedral structures of $BaSO_4$ as a result of following the spiral growth mechanism. This type of barite morphologies have been observed previously by Bromley *et al.* as shown in Figure 6.13 (b).

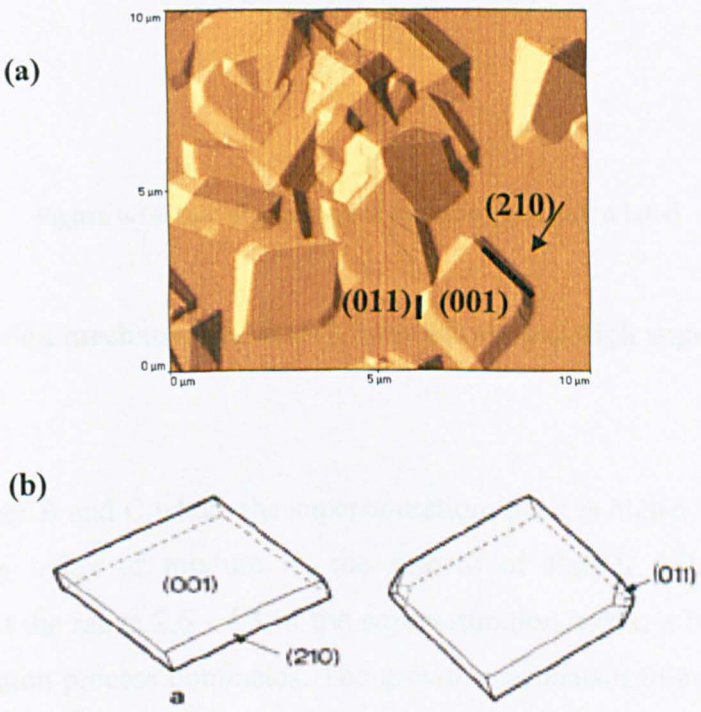

Figure 6.13: $BaSO_4$ formation under spiral growth mechanism (a) experimental morphologies and (b) simulations of rhombohedral structures [64]

Figure 6.13 illustrates the formation of growth steps of barite based on the dominant crystal faces (001) and (210) of $BaSO_4$ as well as the (011) surface. This is in an excellent agreement with the prime work published by Pina *et al.* on barite mechanisms and with the approach made by Dunn *et al.* [104,163]. These steps develop on the screw dislocations and become narrow, as they are limited in time to even tighter spirals. An accurate diagram illustrating the growth of barium sulphate under the spiral growth mechanism is presented in Figure 6.14.

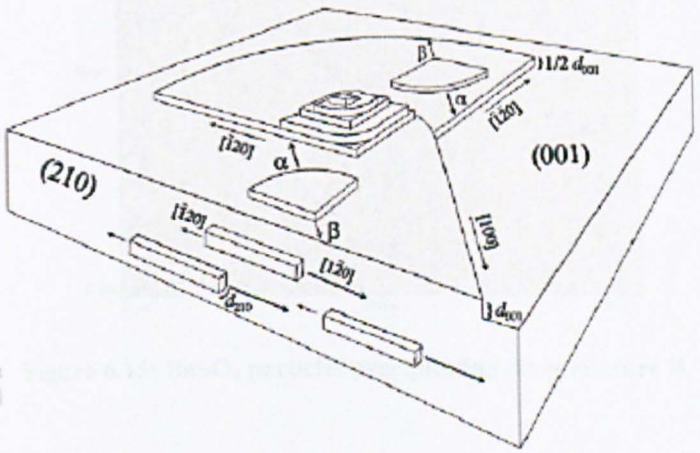

Figure 6.14: Spiral mechanism at screw dislocation [104]

6.3.2 Formation mechanism of $BaSO_4$ at medium and high supersaturation indices

For mixtures B and C where the supersaturation index is higher compared to the supersaturation index of mixture A, the growth of $BaSO_4$ follows a different mechanism. At the range 2.6 - 4.3 of the supersaturation index, a two dimensional-surface nucleation process dominates. The growth mechanism follows the birth and spread model, thus the birth of nuclei occurs anywhere on complete layers as well as islands formed by already developed nuclei [172]. Following this mechanism the

growth develops through time and the crystal faces of barite grow in coincide way as shown in the *in-situ* SXRD patterns in chapter 5.

The AFM observations of barium sulphate precipitating from mixture B as presented in Figure 6.15 show the two dimension nucleation growth of the barite particles on the surface.

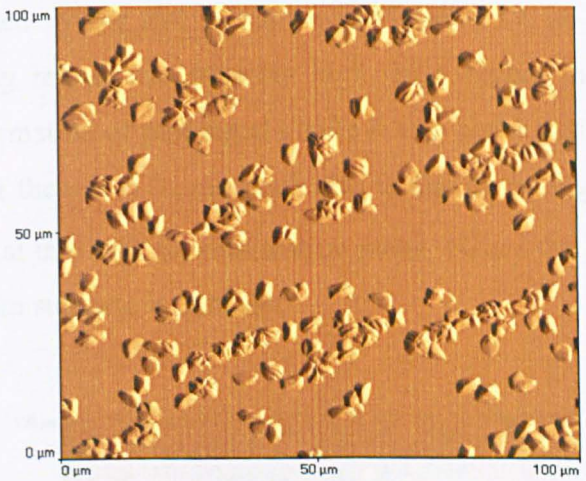

Figure 6.15: $BaSO_4$ particles precipitating from mixture B

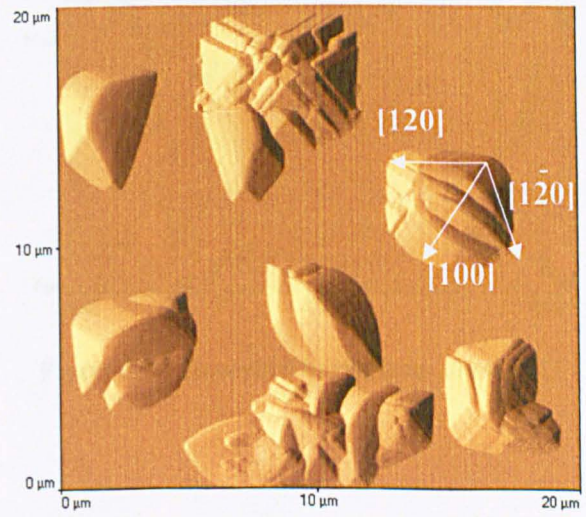

Figure 6.16: Two dimensional nuclei of barium sulphate formed at medium SI

From previous studies by Pina *et al.* it is known that the two dimensional nuclei have a characteristic circular sector shape [105]. This shape of the formed barite was observed with the AFM as illustrated in Figure 6.16. The two dimensional growth of the barite particles on the surface occurs on the (001) crystal face of $BaSO_4$ and follows the main directions of [120] and [100].

Regarding the $BaSO_4$ morphologies formed after precipitating from mixture C, they are characterized by big size as shown in Figure 6.17, as the supersaturation index of the mixing brines was severely high. In a higher magnification image (Figure 6.18) the formation of prolonged on the b axis barite particles can be clearly seen. The growth of these $BaSO_4$ morphologies is due to the high anisotropy along the $[1\,\bar{2}\,0]$ direction at this high supersaturation index. Hence the growth of the (210) crystal face of barium sulphate is extended.

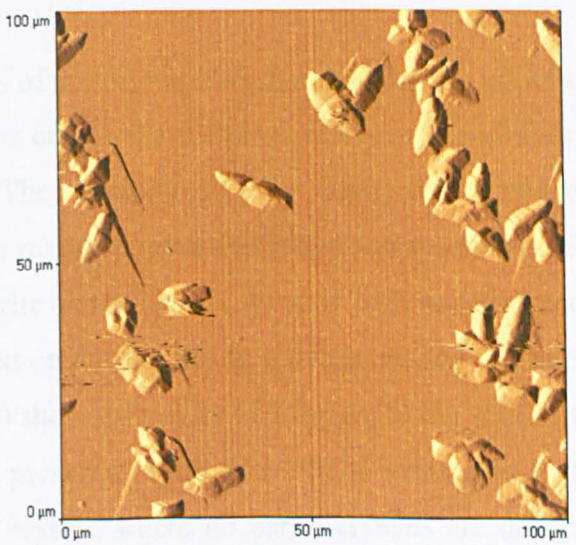

Figure 6.17: Deposited barite from mixture C

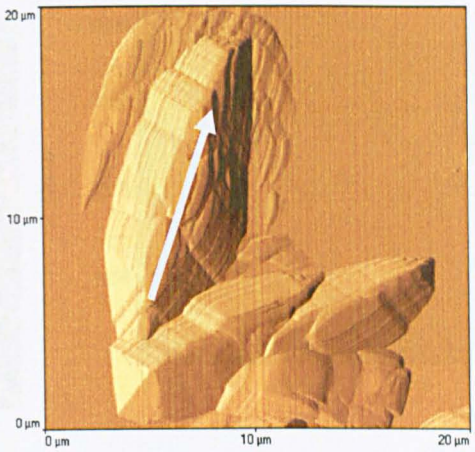

Figure 6.18: Two dimensional nucleation in the [120] direction

6.4 Inhibition

6.4.1 Characteristics of the adherent $BaSO_4$ morphologies

The observations of the formed $BaSO_4$ on the surface allow a deep understanding of the effects caused due to the different examined conditions on the structure of barium sulphate. The analysis of the topographic images of the adhered morphologies on the quartz crystals confirmed the absence of film formation during the deposition of barite on the surface. Even at high supersaturation index (SI= 4.32) no film was detected on the surface in uninhibited and inhibited conditions. Figure 6.19 and Figure 6.20 show the values of Z height of the adherent scale on the surface in the absence and presence of 10 ppm PPCA respectively. It is clear that in the areas of the quartz crystal, where no barite crystals are deposited, the Z height is equal to zero.

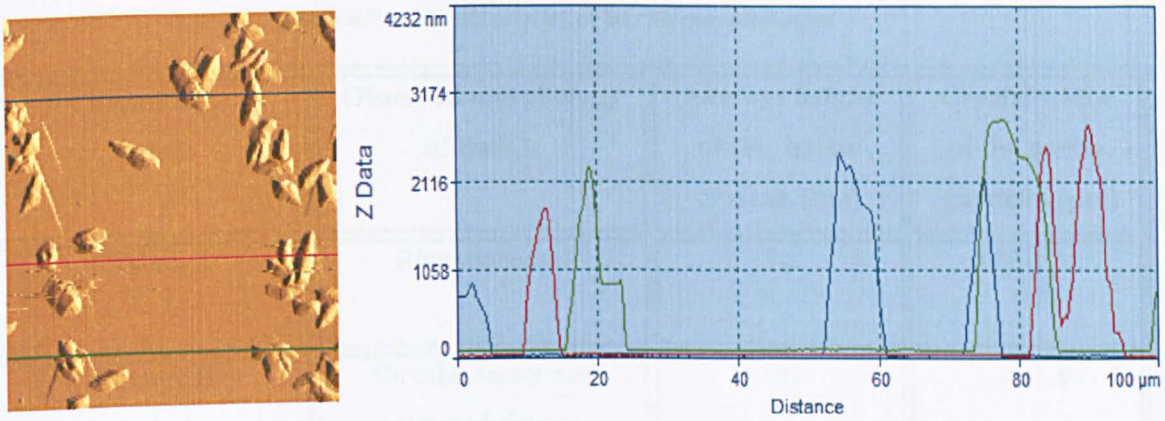

Figure 6.19: Diagram of the Z height of formed barite versus distance in the absence of inhibitor

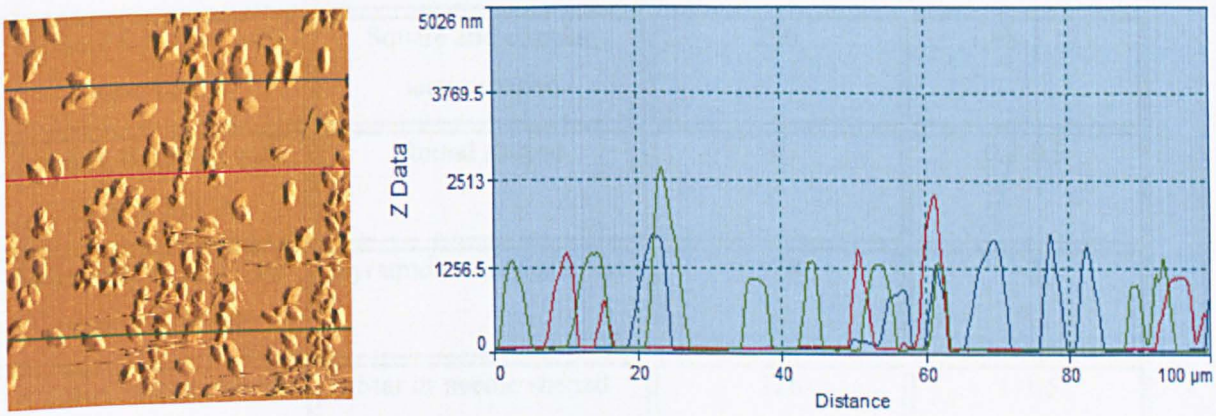

Figure 6.20: Diagram of the Z height of the formed barite versus distance in the presence of 10 ppm PPCA

So far it is illustrated that the barite morphologies deposited on the surface depend on the examined conditions. The morphology of the barite particles formed under uninhibited conditions shows significant changes as the supersaturation index is increased. A summary of morphological characteristics of the adherent barite formed in the presence and absence of inhibitors is presented in Table 6.7 at different supersaturation indices.

Table 6.7: Characteristics of barite morphologies

Examined brine	Observed morphology of $BaSO_4$	Average height of the barite crystals (nm)	Crystal width of the barite particles (μm)
Mixture A	Rhombohedral	74	0.80-1.50
Mixture B	Circular sector and pyramid shapes	307	1.40-1.80
Mixture B treated with 1 ppm PPCA	Circular sector and square shaped	382	2.98-3.08
Mixture B treated with 4 ppm PPCA	Square and circular sector shaped	236	1.68-3.17
Mixture B treated with 10 ppm PPCA	Round shaped	107	0.2-0.3
Mixture B treated with 1 ppm DETPMP	Pyramids and needle like	578	~3
Mixture B treated with 4 ppm DETPMP	Star or needle shaped	126	1-1.5
Mixture B treated with 10 ppm DETPMP	Star or needle shaped	280	0.98-1.5
Mixture C	Elongated on b axis	769	3.7
Mixture C treated with 1 ppm PPCA	Elongated on b axis and pyramids shaped	762	1.78
Mixture C treated with 4 ppm PPCA	Elongated on b axis and pyramids shaped	393	0.8-1.5
Mixture C treated with 10 ppm PPCA	Elongated on b axis and pyramids shaped	414	1.2-1.4

The strict rhombohedral form of the barium sulphate crystals is lost as soon as the supersaturation index is increased reaching a value equal to 2.64 (mixture B). The observed barite crystals at this supersaturation index reveal a characteristic circular sector shape. A further increase in the supersaturation index (mixture C) results in morphologies elongated on the b axis. The results presented in Table 6.7 show that an increase in the supersaturation index results in increase of the average height of the barite crystals and in formation of bigger particles.

In the presence of PPCA at supersaturation index equal to 2.64, the height of the barite particles seems to be considerably affected, resulting in smaller morphologies as illustrated in Figure 6.21. On the other hand the width seems to be less affected. Only when 10 ppm of PPCA was added in mixture B, both the height and the width of the crystals were determined to be much smaller. The shrinking of the barite particles in the presence of 10 ppm PPCA coincides with the good inhibition performance of the additive on the formed $BaSO_4$, as presented in Figure 4.18.

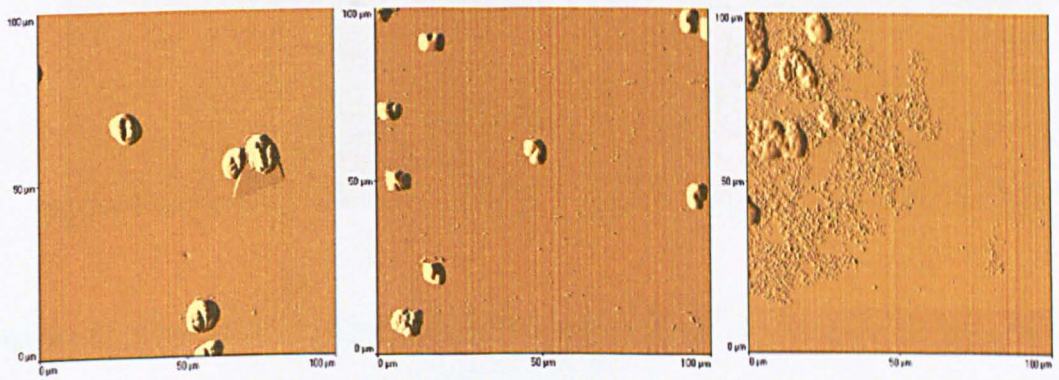

(a) (b) (c)

Figure 6.21: Round shaped barite particles after treatment with (a) 1 ppm PPCA (b) 4 ppm PPCA (c) 10 ppm PPCA

Significantly, at any concentration PPCA acts as growth retarder of the barite formed on the surface. This comes to contradiction with what was known so far for the PPCA which was believed to be a nucleation inhibitor [76, 134]. However now it is quite clear from the scanning topographies with the Atomic Force Microscopy and

from the formation kinetics of barium sulphate as it was recorded *in-situ* with the SXRD in the presence of PPCA, that the performance of the additive on barium sulphate is different in the bulk phase and at the surface.

On the other hand the treatment of mixture B with DETPMP revealed that the inhibitor acts in the nucleation stage of the barite formation. Therefore after the addition of DETPMP the barite morphologies were modified into star like or needle like particles as shown in Figure 6.22. This change in the crystallography of barium sulphate demonstrates the different inhibition action of DETPMP on the barite formed in the bulk phase and on the surface.

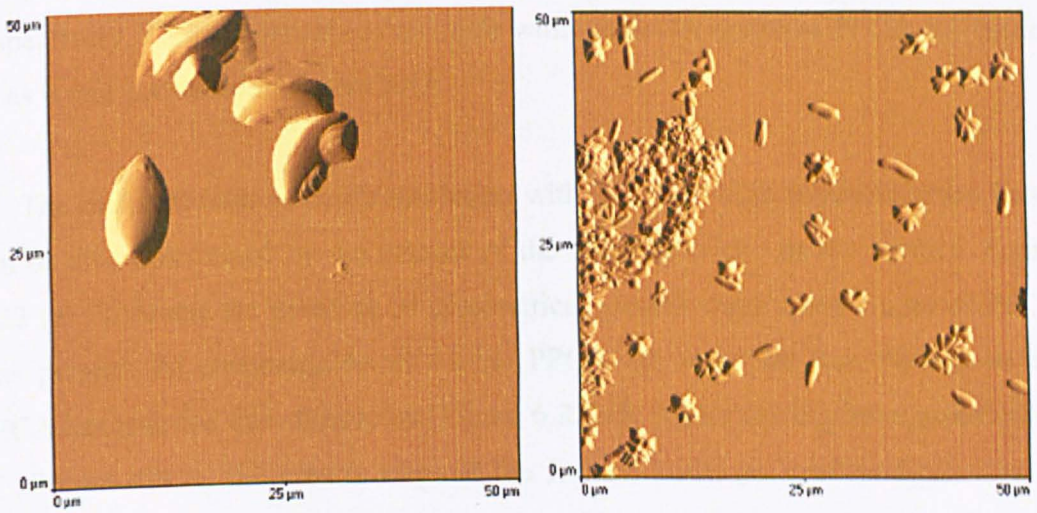

(a) (b)

Figure 6.22: Effect of DETPMP on barium sulphate particles at concentrations (a) 1ppm (b) 4 ppm

The formation of needle shaped particles of barium sulphate can be related to a prolonged growth along the [001] where the (011) crystal face becomes the main surface. Needle shaped morphologies have been published elsewhere as the result of high concentration of Sr^{2+} being present in the system [173]. Actually the high concentration of Sr^{2+} was able to stabilize the (011) crystal face. In the present work, a further analysis is needed in order to determine whether or not strontium cations are responsible for stabilizing the recorded (011) surface of barite. Nevertheless

strontium is expected to be the quencher of the (011) barite surface, since even at high tested temperatures strontium finds no difficulty in interacting with the crystal faces of barite and easily co-precipitating within the barium sulphate lattice, as recorded with the *in-situ* SXRD measurements.

Concerning the characteristics of the particles formed on the surface when tested mixture C with the highest supersaturation index, it was determined that the smallest morphologies were observed when 4 ppm of PPCA was added in the system. According to Table 6.7 under the treatment of 4 ppm PPCA, the barite particles observed on the quartz surface, were characterized by the smallest height and width compared to the ones formed after treatment with 1 ppm or even with 10 ppm PPCA respectively. These observations coincide with the performance of PPCA on mixture C, as it was presented in Figure 4.45.

The different path of barite inhibition with PPCA at high supersaturation index can be also determined by the images of the adherent barite on the surface. Figure 6.22 (a) illustrates the presence of symmetrical growth steps when 1 ppm of PPCA was present. At concentration of 4 ppm PPCA the steps are less obvious as the PPCA has retarded their formation (Figure 6.22(b)). As for the highest concentration of 10 ppm PPCA, the growth steps of the formed barite are present again (Figure 6.22 (c)) and as it can be seen they are less symmetrical compared to the ones recorded with the smallest concentration of PPCA.

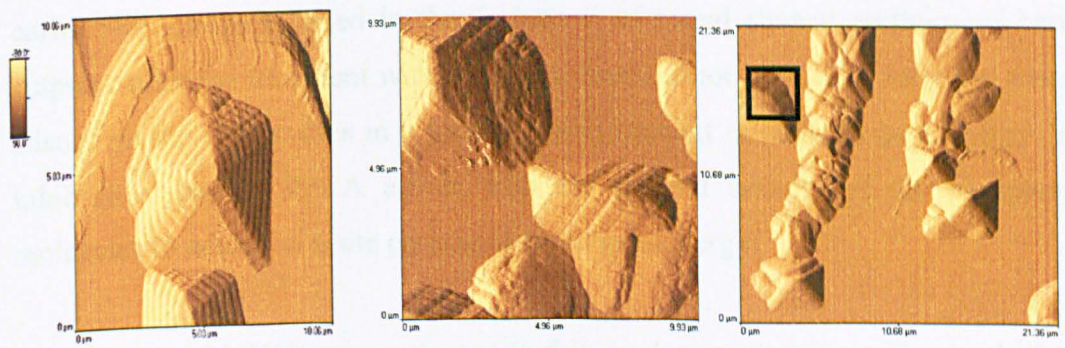

(a) (b) (c)

Figure 6.23: (a) Presence of growth steps, (b) Absence of growth steps and (c) Appearance of less intense steps

It can be suggested that at this severe supersaturation index an increase in the concentration of the inhibitor to 10 ppm, does not contribute to reduction of the growth rate as probably there are no available adsorption sites on the barium sulphate crystals. However this particular performance of PPCA at these examined conditions is related to specific inhibition mechanisms and to MIC concentrations effect, hence further investigation is necessary.

6.4.2 Functional groups of inhibitors

The inhibition of the formed barium sulphate occurs as soon as the forces developed between the $BaSO_4$ and the functional groups of the inhibitors favour the attachment of the inhibitor with the barium cations. The complexation of barium cations with the additive involves van der Waals forces, electrostatic forces and hydrogen bonding.

In this study two types of inhibitors were tested for their inhibition effect on formed barite. Initially investigation of the inhibition performance of PPCA, representing the inhibition family of polyacrylates on barium sulphate occurred. The good inhibition activity of PPCA on the barite particles, refers to the presence of and functionality of the carboxylic groups (-COOH) in the structure of the additive. The carboxylic groups resulted in the formation of round shaped particles of barium sulphate after the treatment with PPCA as the inhibitor molecules have the trend to adsorb on the corner sites in a hydrated environment in order to gain energy. This inhibition trend of PPCA agrees with the general activity of the phosphonate molecules to adsorb to acute parts in order to gain energy.

The second inhibitor investigated in this work for its performance on the barite formations was DETPMP. The specific additive was chosen as a representative of the phosphonate family. From this study it is clear that the performance of DETPMP

depends on the temperature and the supersaturation index of the examined system. Even in the presence of the five phosphonate groups belonging to the DETPMP, inhibition of the formed barite is not certain. In overall an increase in the amount of the phosphonate groups is not related with a more effective inhibition. Pina *et al.* has shown that among a number of phosphonate inhibitors with a different number of functional groups, the sodium phosphonobutane tricarboxylic acid (PBTC) characterized by only one phosphonate, proved to be the most effective inhibitor for barite [105].

6.4.3 Identification of $BaSO_4$ crystal faces with *in-situ* SXRD

The *in-situ* SXRD measurements resulted in an extended identification of the dominant and less important crystal faces of barium sulphate. The lattice planes of barite as recorded for every tested case at 95°C in the presence and absence of inhibitors are presented in Table 6.8.

It is clear that all the dominant planes of barite are maintained on the surface in the presence of PPCA or DETPMP. However the (220) and (410) surfaces of barite are being blocked when 10 ppm of PPCA were added in the initial tested brines. It is worth to note that both of the blocked barite crystal faces are surfaces with big dimensions. Also the formation of the (232) and (422) crystal faces of $BaSO_4$ seem to be promoted when the lowest concentration of PPCA and DETPMP were added respectively.

Table 6.8: $BaSO_4$ crystal faces at 95°C

Barite crystal faces formed at 95°C	Un-inhibited	1 ppm PPCA	4 ppm PPCA	10 ppm PPCA	10 ppm DETPMP	20 ppm DETPMP
(200)	√	√	√	√	√	√
(111)	√	√	√	√	√	√
(201)	√	√	√	√	√	√
(002)	√	√	√	√	√	√
(210)	√	√	√	√	√	√
(102)	√	√	√	√	√	√
(211)	√	√	√	√	√	√
(112)	√	√	√	√	√	√
(204)	√	√	√	√	√	√
(132)	√	√	√	√	√	√
(220)	√	√	√	X	√	√
(410)	√	√	√	X	√	√
(304)	√	√	√	√	√	√
(124)	√	√	√	√	√	√
(232)	X	√	X	X	X	X
(422)	X	√	X	X	√	X

The (001) crystal face has not been detected although it is one of the dominant planes of the formed barite morphologies as shown from the observations with the Atomic Force Microscope. The (001) crystal face of barium sulphate is absent among the recorded lattice planes recorded *in-situ* with the SXRD since the growth of the specific barite crystal face occurs parallel to the substrate. The (001) crystal

face develops as a monolayer in the directions of [100] and [010] hence the beam diffracted by the (001) lattice planes is characterized by zero angle. Subsequently no diffraction peaks can be identified due to the formation of the (001) $BaSO_4$ surface. The absence of the dominant crystal face (001) due to specific orientation on the surface electrode, has been report by Jones *et al.* as well [115]. Moreover the lack in detecting the main (011) crystal face of barite *in-situ*, is due to the fast kinetics of the barite formation process on the surface at this examined temperature.

A representative diagram of barite which illustrates the main crystal faces of barite as placed on the three crystallographic axes a, b and c is presented in Figure 6.24 [163]

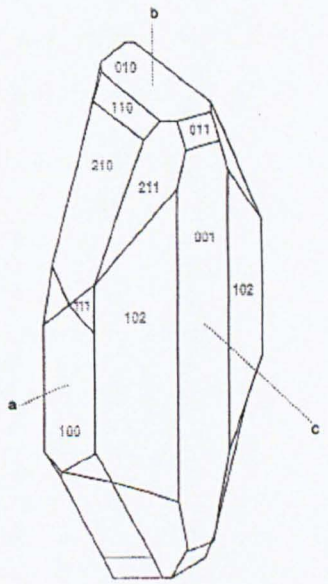

Figure 6.24: Diagram of $BaSO_4$ main crystal faces [163]

In general preferred orientation phenomena are not recorded, at 95°C. Potentially at this temperature the supersaturation index keeps the ionization state of the ions being present in the system prolonged, thus the preferred orientation of the barite crystals is avoided. On the contrary, during the QCM measurements at 23°C and the

in-situ SXRD measurements at 57°C, the formation of the barite crystals occurs on the surface under preferred orientation conditions.

Table 6.9: $BaSO_4$ crystal faces at 57°C

Barite crystal faces formed at 57°C	Uninhibited	4ppm PPCA	10ppm PPCA	10ppm DETPMP	20 ppm DETPMP
(200)	√	√	√	√	√
(111)	√	√	√	√	√
(201)	√	√	√	√	√
(002)	√	√	√	√	√
(210)	√	√	√	√	√
(102)	√	√	√	√	√
(211)	√	√	√	√	√
(112)	√	√	√	√	√
(204)	√	X	X	√	X
(132)	√	√	√	√	√
(011)	√	X	X	X	X
(220)	X	X	X	X	X
(410)	X	X	X	X	X
(304)	X	√	√	√	√
(124)	X	√	√	√	√
(413)	√	√	X	X	X
(223)	X	√	X	X	X

At 57°C all the dominant planes of barium sulphate have been recorded *in-situ* with the SXRD as presented in Table 6.9. Among the dominant lattice planes the (220) and (410) crystal faces of barite are absent due to the preferred alignment of the crystal on the surface. Moreover the growth of the (011) surface of barite is being blocked after the treatment with any of the inhibitors at any concentrations. In

addition at this temperature the (413) and (204) crystal plane of barite are being retarded in the presence of inhibitors. Again the inhibitors reveal a trend to bock the sides of the barite particles characterized by big size. Moreover the (304) and (124) crystal faces of $BaSO_4$ consist lattice planes which their formation is being promoted by the addition of the specific chemical additives.

6.4.4 Characterization of $BaSO_4$ crystal faces based on PBC theory

The *in-situ* SXRD measurements that took place for the purposes of this study revealed in detail the crystallographic nature of barium sulphate formed at different tested conditions on the surface. The crystal faces of barite can be characterized based on the *Periodic Bond Chains* (PBC) theory as F (flat), S (stepped) or K (kinked) surfaces of barium sulphate, as described previously by Hartman *et al.* [69]. The F faces are the ones that grow layer by layer and condition for a face like this to exist is that two neighbouring parallel periodic bond chains are connected together with strong bonds. In absence of these bonds no growth of slides occurs and hence the faces are characterized as S. In addition the K faces are the ones that do not need nucleation to occur and their presence is spontaneous.

Identification of the barium sulphate crystal faces based on the PBC theory, offers a better understanding of the growth process of the barite on the surface and moreover it allows following the inhibition path of the additives on the $BaSO_4$ crystals. The plots of the formation kinetics of barite which were recorded *in-situ* with the SXRD are useful for characterization of the $BaSO_4$ crystal faces as F, S or K faces. With the *in-situ* SXRD measurements it can be confirmed that the (111) and (011) lattice planes of $BaSO_4$ consist K faces. The presence of both (111) and (011) crystal faces of barium sulphate is quick on the surface as soon as the precipitation process starts. The (111) and (011) lattice planes of barium sulphate keep growing through time and manage to reach their final intensity values quickly. As kink sites

the (111) and (011) surfaces of barite are the most important sites for crystal blocking as their appearance establishes the start of the barite formation.

Furthermore the (200) and (102) crystal faces of $BaSO_4$ are characterized as S faces. The growth of both (200) and (102) surfaces of barite enhances the growth of the rest F faces of barite which are present on the surface. When the stepped faces are absent or their growth is stopped then no overall growth of barium sulphate takes place on the surface.

In addition the (201), (002), (210), (211) crystal faces of barite are considered to be F faces, which grow layer by layer through time. The F faces continue to grow until the supersaturation index approaches the equilibrium. Subsequently the F faces are the ones that lead the overall growth process and highlight the end of the barium sulphate growth.

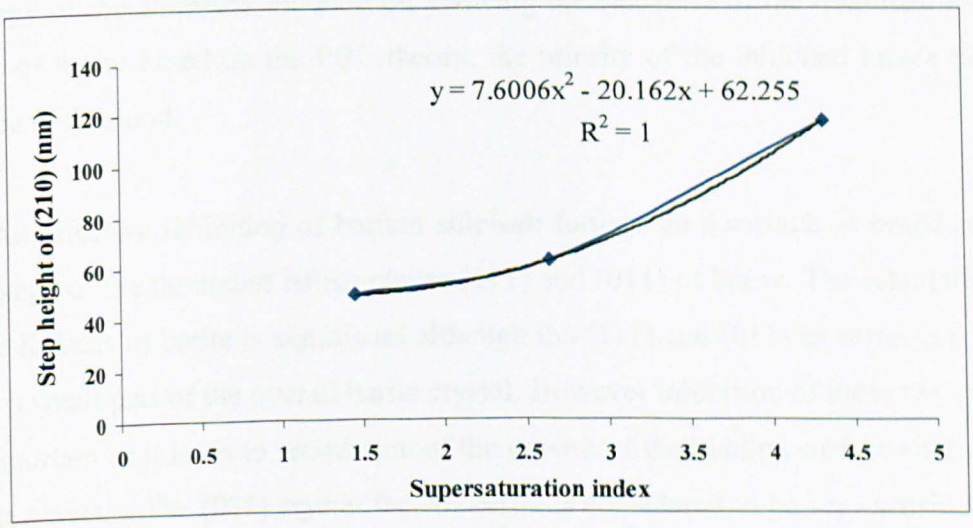

Figure 6.25: Step height of (210) barite crystal face versus SI

The extended growth of one of the dominant F faces of barium sulphate the (210) crystal face of barite can be seen in Figure 6.25, as a function of the step height versus supersaturation index.. The step height of the specific crystal face was identified from the topographic images of barium sulphate on the surface with the

Atomic Force Microscope. It is clear that the growth rate of the specific lattice plane is fast and is described by a polynomial equation second order. The coefficient of determination shows that the polynomial model fits extremely well on the experimental data. In other terms simulating the growth of the (210) crystal face of barite in a function of supersaturation index is significant for predicting the growth trend of one main crystal face S of barium sulphate.

6.4.5 Establishment of an effective inhibition on barium sulphate

The evaluation of an effective inhibition path on barium sulphate crystals formed on a surface consists one of the main objectives of this study. The formation kinetics of $BaSO_4$ on the surface as recorded with the *in-situ* SXRD tests, the determination of the crystal faces of barite that are present in every examined case as well as the valuable observations with the Atomic Force Microscope reveal the inhibition strategy of the additives. In addition knowing the character of the dominant crystal faces of barite based on the PBC theory, the priority of the inhibited lattice planes can be understood.

An effective inhibition of barium sulphate formed on a surface, is based on the blockage of the dominant lattice planes (111) and (011) of barite. The retardation of these K faces of barite is significant although the (111) and (011) as surfaces consist only a small part of the overall barite crystal. However inhibition of these two planes is important as it leads to retardation of the growth of the binding surface sites of the barite crystals. The (011) crystal face of barite is considered to be very sensitive and favours both growth and retardation as the lattice sulphate ions in the (011) are orientated perpendicular to the crystal surface [68].

Next group of planes which must be inhibited is the group of the growing binding crystal faces of $BaSO_4$, meaning the (211) and (200) lattice planes of barium sulphate. Additionally in order the inhibition to be effective, it is necessary that the

(010) lattice plane of barite to be retarded. The blockage of the (010) crystal face of barium sulphate is crucial as it is accompanied by a wider retardation of the growth on the b axis. Generally the b axis is more important compared to the other two axes, as the growth of the [120] direction with the highest anisotropy occurs on the b axis. When the growth of barium sulphate is not favoured any longer in the [120] direction, then the growth of the (210) crystal face of barite is blocked. This is the key point for preventing the formation of one of the dominant F faces of $BaSO_4$. Additionally the inhibition of the (210) crystal face also contributes in limited growth of the (102) and (002) lattice planes of barium sulphate.

6.5 Practical considerations

This study describes the formation kinetics and mechanisms of barium sulphate as one of the most well known problematic inorganic scale types in oil facilities. The experimental work done for the purposes of this study was adjusted as close as possible to the conditions in the off-shore environment. The evaluation of these results regarding their relevance to the oil and gas industry can be seen through (i) the efficiency of the inhibitors, (ii) the formation kinetics of the barium sulphate on the surface and (iii) the crystallography of the barite when inhibitors are present.

In overall the application of two different substrates for the measurements with the Quartz Crystal Microbalance and for the *in-situ* SXRD measurements did not result in any variations in the formation processes of barium sulphate. The crystallography of the barite and the main crystal growth directions remained the same independently of the substrate. Even phenomena like the preferred orientation of the barium sulphate crystals on the surface were irrelevant with the type of substrate since they occurred when specific applied conditions were examined.

6.5.1 Growth trends

The interpretation of the growth kinetics of barium sulphate under complicated conditions, as presented in the first part of this chapter can be proved useful for applications in the oil-industry extraction processes. The models fitted enable the growth rate calculation of the barium sulphate formation at different supersaturation conditions and in the presence of divalent cations. Moreover the equations offer an evaluation of the deposited mass according to the supersaturation condition maintenance at high level or not, during the deposition of barium sulphate on the surface.

6.5.2 Inhibitor efficiency

Through this study the determination of the efficiency of the inhibitors on the $BaSO_4$ deposited on the surface and in the bulk phase, was approached. The efficiency of the two inhibitors PPCA and DETPMP on barite on the surface and in the bulk phase is shown in Table 6.10 and Table 6.11 for mixture B and mixture C respectively. For the calculation of the efficiency, the results from the QCM measurements and the total intensity of the recorded lattices planes with the *in-situ* SXRD measurements for every test were taken under consideration.

Table 6.10: Inhibitors efficiency at medium supersaturation index (SI=2.64)

Inhibitor	Temperature	Concentration of inhibitor (ppm)	Surface efficiency (%)	Bulk efficiency (%)
PPCA	23°C	1	67.2	100
		4	78.5	100
		10	**91.5**	100
	57°C	4	Not tested as low deposition of barite even when inhibitor is absent	
		10		
	95°C	1		
		4		
		10		
DETPMP	23°C	1	21.62	*59*
		4	promotion	*26*
		10	3.2	*38*
	57°C	10	Not tested as low deposition of barite even when inhibitor is absent	
		20		
	95°C	10		
		20		

From the work done at supersaturation index equal to 2.64, is clear that the efficiency of the additive on the barite scale varies according to the concentration of the additive and the conditions present in the system (Table 6.10). PPCA proved to be an effective inhibitor of barite formed in the bulk phase and on the surface at low temperature at concentrations equal or higher than 4 ppm. The performance of DETPMP at the temperature of 23°C is very low and at concentration of 4 ppm the behavior of the inhibitor favors the promotion of the barite on the surface.

Table 6.11: Inhibitors efficiency at high supersaturation index (SI=4.32)

Inhibitor	Temperature	Concentration of Inhibitor (ppm)	Surface Efficiency (%)
PPCA	23°C	1	15.8
		4	70.2
		10	38.6
	57°C	4	Promotion
		10	18.3
	95°C	1	9
		4	26.1
		10	**86.2**
DETPMP	57°C	10	10
		20	Promotion
	95°C	10	56.1
		20	56

At extreme high supersaturation conditions PPCA seems effective at concentration of 4 ppm at low temperature although when the temperature increases up to 95°C, the inhibitor allows blockage of the barite growth at a percentage of 86.2 (Table 6.11). On the other hand DETPMP at the examined concentrations and at high supersaturation index is less effective as an inhibitor of barite. However the efficiency of DETPMP increases with an increase in temperature approaching a 56% of efficiency for any tested concentration.

6.5.3 Presence of foreign ions

The presence of divalent cations in the tested brines resulted in investigation of the parallel formation and growth of other types of scale with the formation of barium sulphate. A potential substitution of divalent cations within the barite lattice during the precipitation of $BaSO_4$ could not be neglected.

During the QCM measurements the formation of other potential scale types like calcium sulphate or magnesium hydroxide is not favoured to occur under the specific temperature and pressure conditions applied. In addition formation of pure celestite growth layers on barite cleavage steps has not been identified. Thus it is suggested that the growth of the (001) crystal face of $BaSO_4$ inhibits the formation of celestite on the barite [174]. Yet the co-precipitation of Ca^{2+} and Sr^{2+} in the barium sulphate lattice can not be neglected during the precipitation and deposition processes. The substitution of divalent cations within the $BaSO_4$ lattice is expected to occur during the linear growth of the barite on the surface following Vegard's law [139]. This is further supported by other researchers who proved that in the presence of foreign ions the centre region near the nucleus of the barite crystal is composed only by Ba ions, as Ca and Sr were found in high concentrations towards the crystal extremities [79]. However the overall observations of the barium sulphate crystals having calcium or strontium cations attached on the surface show no changes as presented by Redfern *et al.* based on attachment energy calculations [175].

During the *in-situ* SXRD measurements at high temperatures the presence and the activity of the divalent cations was easier to be determined. The scanning of the SXRD patterns showed no trace of formed $CaSO_4$. On the contrary the co-precipitation of Sr^{2+} into the barite lattice was identified by detecting main lattice planes of formed celestine barian on the surface. Moreover in every SXRD pattern three diffraction peaks were recorded at d space equal to 4.0, 2.56 and 1.7 Å, that could not be related to the barite crystal faces formed on the surface. An overall investigation of the potential scale types that can form based on the composition of

the examined brine, showed that these unknown peaks can be linked to the formation of polyhalite with molecular type $K_2CaMg(SO_4)_4(H_2O)$ [176].

Another aspect of the divalent cations presence in the initial brines deals with the formation of calcium-phosphonate complexes. The formation of the specific complexes characterized also as pseudo-scale, is strongly suggested to take place, at high supersaturation indices and at high temperature when the additives are present [139]. At high temperature the tendency of calcium to precipitate as calcium sulphate is known from its reverse solubility property. Hence it is very likely a complexation between the cations of calcium and the phosphonate groups of the inhibitors to occur, when they coexist. The *in-situ* SXRD measurements have shown earlier signs of blockage of the cell and this is evidence for a possible formation of calcium-phosphate complexes in the system. The experimental duration of the tests in the presence of the inhibitors was shorter although the SXRD patterns confirmed the inhibition of the dominant crystal faces of the barite scale on the surface. A summary of the experimental testing time for every case is shown in Table 6.12.

Table 6.12: Summary of the *in-situ* SXRD experimental duration

Type of brines	Inhibitor	Duration of the test at 95°C (minutes)	Duration of the test at 57°C (minutes)
Mixture C	None	60	28
	1 ppm PPCA	60	Not tested
	4 ppm PPCA	32	22
	10 ppm PPCA	22	14
	10 ppm DETPMP	48	30
	20 ppm DETPMP	42	24

The decrease in the experimental duration is obvious when inhibitors are present, independent of the applied temperature. Table 6.12 shows that an increase in the

amount of the applied inhibitor leads to decrease in the experimental time. Thus it is suggested that the complexation of calcium ions with the phosphonate groups of the inhibitor and the Ba^{2+} which is maintained in the bulk phase, is responsible for the accelerated blockage of the cell during the measurements. The suggestion that calcium is involved in a complexation process with the phosphonates of the inhibitor needs further evidence in order to be valid.

6.5.4 Crystallography of the adhered $BaSO_4$

The accurate approach of the crystallography of barium sulphate in the absence and presence of inhibitors illustrates the overall behavior of the barite formed crystals during the retardation. The *in-situ* SXRD patters demonstrate the role that each recorded crystal face of barite has, under the effect of a number of parameters. The blockage or promotion of the key-surfaces (011) and (111) of the barite morphologies in the presence of inhibitors reveals the path of an effective inhibition mechanism.

As shown the barite growth on the surface follows specific growth directions driven by the supersaturation conditions, temperature and presence or absence of inhibitors. The consideration of the main growth directions of $BaSO_4$ clarifies the mechanism that a selective inhibitor should follow. In other terms tracking an effective inhibitor of barium sulphate can be successful when main criterion of the inhibitors choice should be the ability of the additive to retard the [120] and [100] growth directions.

CHAPTER 7 CONCLUSIONS

7.1 Introduction

This study has focused on the $BaSO_4$ formation on a surface in the absence and presence of inhibitors. The interpretation of the data received from the measurements offered new knowledge on three main dimensions; (i) barite surface formation kinetics, (ii) inhibition of barite on the surface and (iii) crystallographic nature of $BaSO_4$. The conclusions extracted from this work are divided according to these three dimensions and are presented in this chapter.

7.2 $BaSO_4$ formation kinetics on surface

The investigation of barium sulphate emergence and growth on the surfaces during the initial stages of the deposition revealed the following:

- The deposition of barite on a surface in uninhibited and inhibited conditions is a two stage process. The initial stage is described by a second order polynomial equation when the supersaturation index is less than 2.64. At supersaturation index equal to 4.32 the non-linear part is given by a polynomial model of 4^{th} order as the barite formation kinetics is faster. The second part of the deposition of $BaSO_4$ is characterized by a linear trend.

- In the presence of PPCA the crystallization rate of barium sulphate is decreased independent of the supersaturation index. On the contrary DETPMP results in higher crystallization rate of barium sulphate on the surface under the chosen examined conditions.

- Barite mass evaluation based on the initial slopes results in higher amount of scale representing a system with sustained supersaturation index.

- The formation of barite on the surface is governed by heterogeneous nucleation and the growth continues even when the activity in the bulk phase has stopped.

- The two dominant growth directions of barium sulphate on the surface are the [120] and [100].

- At 23°C, the (210) dominant barite crystal face growth follows a polynomial trend as a function of the supersaturation index.

- Deposition of barite on the surface occurs only in the form of crystals and not as film.

7.3 Inhibition of $BaSO_4$

Studying the formation of barium sulphate after treatment of the initial brines with inhibitors, has pointed out which inhibitors are effective for barium sulphate and in which way they manage to achieve blockage during the emergence of the barite crystals.

- PPCA acts as a growth retarder of the barium sulphate formed on the surface, at medium supersaturation index conditions.

- PPCA decreases the size of the barite particles growing on the surface, resulting in formation of round shaped barite morphologies. The effective action of PPCA is linked to the carboxylic groups of the inhibitor.

- At higher supersaturation index (4.32) the most effective inhibiting dosage of PPCA is 4 ppm.

- DETPMP, at the tested concentrations, is an effective inhibitor of barite only at high temperature (95°C).

- DETPMP acts as a nucleation retarder and strongly modifies the shape of the barite particles on the surface resulting in star and needle like morphologies. Under specific examined conditions DETPMP promotes the formation of barium sulphate on the surface.

- During the formation of barium sulphate in the bulk phase, DETPMP prevents growth and PPCA prevents nucleation.

- During the deposition of barium sulphate on surfaces, DETPMP prevents nucleation and PPCA prevents growth.

7.4 Crystallography of $BaSO_4$

The crystal faces of barium sulphate formed on the surface were determined with the AFM and the *in-situ* SXRD, which are techniques dealing with barium sulphate morphologies in atomic level. The main conclusions from the investigation of the barium sulphate crystallography are:

- The main crystal faces of barium sulphate were identified from the *in-situ* SXRD patterns in the absence and presence of inhibitors. The lattice planes of $BaSO_4$ grow in coincide way on the surface.

- The (111) and (011) crystal faces of barite are K faces and the (200) and (002) are S faces. Concerning the (201), (002), (210) and (211) lattice planes of barium sulphate are F faces.

- The (011) crystal face of barite is present only when the examined conditions favour slow formation kinetics.

- The (011) and (111) consist key crystal faces for an effective inhibition of the barium sulphate deposition.

- The treatment with 10 ppm PPCA resulted in highest inhibition of all the barite crystal faces. The surfaces of barite with the biggest Miller indices were absent in the presence of 10 ppm PPCA.

- The barite forms in a preferred way on the surface, independent of the substrate nature. The deposition of barium sulphate is independent of the preferred orientation phenomena only at high temperature (95°C).

- Strontium co-precipitates within the barite lattice resulting in formation of celestine barian.

CHAPTER 8 FUTURE WORK

8.1 Introduction

The unique nature of barium sulphate as inorganic scale type has been investigated through this study. The work presented here merges the known literature with respect to the barium sulphate nature to new knowledge regarding the formation kinetics of the barite in uninhibited and inhibited conditions. Still in order to achieve complete determination of the barium sulphate deposition in the oil plants facilities, additional experimental approaches can take place based on the path shown from the work accomplished in this study. Hence in this chapter suggestions for potential experimental studies of barium sulphate scale are given.

8.2 Refinement of barite structures in the absence and presence of inhibitors

Understanding the behaviour of the barium sulphate at atomic level is significant since then the formation of the barite is being examined at the very initial stage of the process. The identification of the barite crystal faces that are present and the determination of their retardation mode under different applied conditions make the formation of barite on a surface a controllable process. Hence the modifications caused on the barite crystals formed on the surface as well as the variations on the main crystal growth directions due to external factors as supersaturation index, temperature and pH can be monitored using the Atomic Force Microscope and *in-situ* SXRD techniques. Moreover the *in-situ* SXRD technique can be used to follow the kinetics and the crystallography of barite at low temperature, in order to achieve a comparison with the results received during the tests at higher temperature.

Most important the effect of the different inhibitors on the barite crystallography can be followed. The functionality of different potential inhibitors of barite can be determined by following the variations in the crystal planes and in the growth

directions of barium sulphate. Taking also into account the key crystal faces for an effective inhibition of barite as shown from this study, makes the tracking of an inhibitor successful. Furthermore the design of inhibitors based on appropriate functional groups for inhibiting specific crystal faces and directions of barium sulphate is feasible.

8.3 Inhibitors

Potential inhibitors of barite can be tested with Quartz Crystal Microbalance measurements, in order an initial evaluation of the inhibitors efficiency through the quantification of the deposited mass, to occur. Moreover the effect of the inhibitors can be determined using the SXRD set up under *ex-situ* and *in-situ* experimental conditions.

The work presented here has pointed out when each inhibitor has been consumed during the inhibition process. Hence the techniques used in this study can be also applied for probing the barium sulphate formation kinetics and morphology variations, after treatment of the brines with higher concentrations of inhibitors. Testing higher concentrations of chemical agent, especially for the case of DETPMP, will reassure the performance of the phosphonate groups. Furthermore, repeatable injection of the additive during the scale deposition measurements, could also contribute to a steady inhibition of the formed scale. The reinjection of the same or even a different effective inhibitor at the time when the treatment by the initial dosage of the additive finishes can be proved beneficial for maintaining the scale build up in low level.

In addition a combination of the Quartz Crystal Microbalance with *in-situ* Atomic Force Microscope allows the determination of the nucleation stage during the deposition of barite in the presence and absence of inhibitors.

8.4 Kinetics and modelling

The formation kinetics of barium sulphate deposition has been determined during the early stages of the precipitation process. At this point what actually seems useful is modelling the kinetic equations as functions of the supersaturation index and other crucial for the scale formation factors. Studying the effect of important factors like the hydrodynamics and the applied pressure of the examined system can contribute to completed simulations of the formation kinetics of barite. When the simulations have as base the needs of an oil plant then later on a proper treatment of the oil well can be approached.

8.5 Effect of divalent cations

The brines tested for the needs of this study contained divalent cations in an effort to imitate the aqueous environment in the oil wells. This work has shown the importance of analyzing barite deposition and inhibition on the surface. Certainly the techniques used in this study should also used in order to investigate the kinetics and the morphology of the deposited barite precipitating from simple brines in the absence of divalent cations. Regarding the effect of Ca^{2+} and Sr^{2+}, a further investigation on the formation kinetics of barite and confirmation of the placement of the divalent cations within the barite lattice will result in understanding the stage where these cations start playing a key role during the barite deposition. Moreover the complexation of calcium with the phosphonate groups of the applied inhibitors is a domain of future research. The formation and the complete role of these complexes during the inhibition of barium sulphate need to be completely identified.

REFERENCES

1. http://www.geohelp.net/world.html
2. Ollivier B. and Magot M., 1995, *Petroleum Microbiology,* Ollivier and Magot, Washington DC
3. Demadis K. D., Mavredaki E., Stathoulopoulou A., Neofotistou E. and Mantzaridis C., 2007, *Industrial water systems: problems, challenges and solutions for the process industries*, Desalination, 213, 38-46
4. Shaw B. A. and Kelly R. G., 2006, *What is corrosion?* Electrochemical society interface, 24-26
5. http://www.uni-due.de/imperia/md/content/biofilm-centre/biofouling.pdf
6. Graham A. L., Vieille E., Neville A., Boak L. S. and Sorbie K. S., 2004, *Inhibition of $BaSO_4$ at a Hastelloy metal surface and in solution: The Consequences of falling below the Minimum Inhibitor Concentration (MIC)*, SPE 87444, Aberdeen
7. Raju K. U. and Nasr-El-Din H. A., 2004, *Calcium sulfate scale: Field tests and model predictions*, NACE 04397, New Orleans
8. Boerlage S. F. E., Kennedy M. D., Bremere I., Witkamp G. J., Hoek J. P. V. D. and Schippers J. C., 2002, *The scaling potential of barium sulphate in reverse osmosis systems*, 197, 251-268
9. Bader M. S. H., 2006, *Sulfate removal technologies for oil fields seawater injection operations*, Petroleum Science & Engineering, 55, 93-110
10. Amjad Z., 1995, *Mineral scale Formation and Inhibition,* Plenum Press, New York
11. Senko J. M., Campbell B. S., Henriksen J. R., Elshahed M. S., Dewers T. A. and Krumholz L. R., 2003, *Barite deposition resulting from phototrophic sulfide-oxidizing bacterial activity*, Geochimica et Cosmochimica Acta, 68, 773-780
12. Anastas P. and Warner J., 1998, *Green Chemistry: Theory and Practise,* Oxford University Press, New York
13. Henriquez L. R., 2002, *Chemistry in the oil industry VII,* T. Balson, Royal society of chemistry, Manchester
14. http://en.wikipedia.org/wiki/Barium_sulfate
15. Yuan M., Todd A. C. and Sorbie K. S., 1994, *Sulphate scale precipitation arising from seawater injection: a prediction study*, Marine and Petroleum Geology, 11, 24-30
16. Fernier W. W. and Ziauddin M., 2008, *Formation, removal and inhibition of inorganic scale in the oilfield environment,* Society of Petroleum Engineers, Texas
17. Kalfayan L., 2008, *Production Enhancement with Acid Stimulation,* PennWell Books, Tulsa
18. Leeden M. C. V. D. and Rosmalen G. M. V., 1990, *Effect of the molecular weight of polyphosphinoacrylates on their performance in $BaSO_4$ growth retardation*, Crystal Growth, 100, 109-116

19. Tantayakom V., Sreethawong T., Fogler H. S., Moraes F. F. D. and Chavadej S., 2005, *Scale inhibition study by turbidity measurement*, Journal of Colloid and Interface Science, 284, 57-56
20. Wang Z., Neville A. and Meredith A. W., 2005, *How and why scale stick - Can the surface be engineered to decrease scale formation and adhesion?* SPE 94993,
21. Söhnel O. and Garside J., 1992, *Precipitation, Basic principles and industrial application,* Butterworth-Heinemann Ltd, Oxford
22. Hanor J. S., 2000, *Sulfate Minerals-Crystallography, Geochemistry and Environmental Significance,* Charles N. Alpers, John L. Jambor, D. Kirk Nordstrom, Washington DC
23. Amor M. B., Zgolli D., M.Tlili M. and Manzola A. S., 2004, *Influence of water hardness, substrate nature and temperature on homogeneous calcium carbonate nucleation*, Desalination, 166, 79-84
24. Nielsen A. E., 1967, *Kinetics of precipitation,* New York
25. He S., Oddo J. E. and Tomson M. B., 1995, *The nucleation kinetics of Barium Sulfate in NaCl solutions up to 6 m and 90℃*, Journal of Colloid and Interface Science, 174, 319-326
26. Gunn D. J. and Murthy M. S., 1972, *Kinetics and mechanisms of precipitations*, Chem. Eng. Sci., 27, 1293-1313
27. Judat B. and Kind M., 2004, *Morphology and internal structure of barium sulphate-derivation of a new growth mechanism*, Journal of Colloid and Interface science, 269, 341-353
28. Mason R. E. A. and Strickland-Constable R. F., 1966, *Breeding of crystal nuclei*, Trans. Faraday Soc., 62, 455-461
29. Marsh S. P. and Glicksman M. E., 1997, *Ostwald ripening in non spherical morphologies*, Materials science and engineering, A238, 140-147
30. Madras G. and Mccoy B. J., 2002, *Transition from nucleation and growth to Ostwald ripening*, Chemical engineering science, 57, 3809-3818
31. Schwarzer H. C. and Peukert W., 2005, *Prediction of aggregation kinetics based on surface properties of nanoparticles*, Chemical Engineering Science, 60, 11-25
32. O.Söhnel and Mullin J. W., 1978, *A method for the determination of precipitation induction periods*, Journal of crystal growth, 44, 377
33. Lancia A., Musmarra D. and Prisciandaro M., 1999, *Measuring induction period for calcium sulfate dihydrate precipitation*, AIChE, 45, 390-397
34. He S., Oddo J. E. and Tomson M. B., 1994, *The inhibition of gypsum and barite nucleation in NaCl brines at temperatures from 25 to 90C*, Applied Geochemistry, 9, 561-567
35. Söhnel O. and Mullin J. W., 1988, *Interpretation of crystallization induction periods*, Journal of Colloid and Interface science, 123, 43-50
36. Carosso P. A. and Pelizzetti E., 1984, *A stopped flow technique in fast precipitation kinetics - The case of barium sulphate*, Journal of crystal growth, 68, 532-536
37. Mullin J. W., 2001, *Crystallization,* Elsevier, Reed Educational and Professional Publishing Ltd, Oxford

38. Pina C. M., Becker U., Risthaus P., Bosbach D. and Putnis A., 1998, *Molecular-scale mechanisms of crystal growth in barite*, Letters to nature, 395, 483-486
39. Wulff G., 1901, Zeitschrift fur Krystallographie und Mineralogie, 34, 449-530
40. Nývlt J., 1985, *The kinetics of industrial crystallization,* Elsevier, Prague
41. Burton W. K., Cabrera N. and Frank F. C., 1951, *The growth of crystals and the equilibrium structure of their surfaces*, Philosophical Transactions of the Royal Society of London, 243, 299-358
42. Packham D. E., 1992, *Handbook of adhesion,* Brewis and Briggs, Bath press, Essex
43. Johnson K. L., 1998, *Mechanics of adhesion*, 31, 413-418
44. Cases J.-M., Mielczarski J., Mielczarski E., Michot L. J., Villieras F. and Thomas F., 2002, *Ionic surfactants adsorption on heterogeneous surfaces*, C.R. Geoscience, 334, 675-688
45. Ninham B. W., 1999, *On progress in forces since the DLVO theory*, Advances in Colloid and interface science, 83, 1-17
46. Wennerstöm H., 2000, *Adhesion, entropy and surface forces.*, Colloids and surface A, 167, 209-214
47. Mizes H. A., Ott M., Eklund E. and Hays D. A., 2000, *Small particle adhesion: measurement and control*, Journal of colloids surfaces, 165, 11-23
48. Peukert W., Schwarzer H. C. and Stenger F., 2005, *Control of aggregation in production and handling of nanoparticles*, Chemical Engineering and Processing, 44, 245-252
49. Claesson P. M., Dedinaite A. and Rojas O. J., 2003, *Polyelectrolytes as adhesion modifiers*, Advances in Colloid and Interface Science, 104, 53-74
50. Shedid A. Shedid M. T. G., 2004, *Factors affecting contact-angle measurement of reservoir rocks*, Petroleum Science and Engineering, 44, 193-203
51. Sukka P. O., 2004, *Improving the nuclear tracer imaging centrifuge method for measuring in situ capillary pressures and comparisons with other methods*, Department of physics and Technology, University of Bergen
52. Wennerström H., 2000, *Adhesion, entropy and surface forces.*, Colloids and surface A, 167, 209-214
53. http://webmineral.com/data/Barite
54. http://webmineral.com/specimens/picshow.php?id=3057
55. Inc. A. S. Materials Studio v.4.2.0.0. Computer software, 2007
56. Hartman P. and Perdok W. G., 1955, *On the Relations Between Structure and Morphology on Crystals.III*, Acta Cryst., 8, 525-529
57. Allan N. L., Rohl A. L., Gay D. H., Catlow C. R. A., Davey R. J. and Mackrodt W. C., 1993, *Calculated Bulk and Surface Properties of Sulfates*, Faraday Discussion, 95, 273-280
58. Dinamani M., Kamath P. V. and Seshadri R., 2001, *Electrochemical deposition of BaSO4 coatings on stainless steel substrates*, Chem. Mater, 13, 3981-3985
59. Jackson K. D. O., 1998, *A guide to identifying common inorganic fillers and activators using vibrational spectroscopy*, Journal of vibrational spectroscopy, 2, 1-11
60. Environment A., 2009, *Soil remediation guidelines for barite: Environmental and Human health*,

61. Jackson K. D. O., 1998, *A guide to identifying common inorganic fillers and activators using vibrational spectroscopy*, Journal of vibrational spectroscopy, 2,
62. Sabbides T. G. and Koutsoukos P., 1993, *The crystallization of calcium carbonate in artificial water; role of the substrate*, Crystal growth, 133, 13-22
63. Shindo H., Shitagami K., Kondo S. and Seo A., 1999, *Atomic force microscopic observation of directional layer growth and dissolution on surfaces of sulphate minerals*, Journal of Crystal Growth, 198/199, 253-257
64. Black S. N., Bromley L. A., Cottler D., Davey R. J., Dobbs B. and Rout J. E., 1991, *Interactions at the Organic/Inorganic interface: Binding motifs for phosphonates at the surface of barite crystals*, Chem. Soc. Faraday Trans., 87, 3409-3414
65. Bromley L. A., Cottier D., Davey R. J., Dobbs B. and Smith S., 1993, *Interactions at the Organic/ Inorganic Interface: Molecular Design of crystallization inhibitors for barite*, Langmuir, 9, 3594-3599
66. Hartman P. and Heijnen W. M. M., 1983, *Growth mechanisms of a crystal face for which more than one surface structure is possible*, Journal of crystal growth, 63, 261-264
67. Wang K.-S., Resch R., Dunn K., Shuler P., Tang Y., Koel B. E. and Yen T. F., 1999, *Dissolution of the barite (001) surface by the chelating agent DTPA as studied with non-contact atomic force microscopy*, Colloids and Surfaces A, 160, 217-227
68. Leeden M. C. V. D. and Rosmalen G. M. V., 1995, *Adsorption behavior of polyelectrolytes on barium sulfate crystals*, Colloid and Interface Science, 171, 142-149
69. Hartman P. and Strom C. S., 1989, *Structural morphology of crystals with the barite ($BaSO_4$) structure: A revision and extension*, Journal of Crystal Growth, 97, 502-512
70. http://Www.Chem.Qmul.Ac.Uk/Surfaces/Scc/Scat1_6.Htm
71. Fenter P., Mcbride M. T., Srajer G., Sturchio N. C. and Bosbach D., 2001, *Structure of Barite (001) - and (210) - Water Interfaces*, J. Phys. Chem. B, 105, 8112-8119
72. Oddo J. E. and Tomson M. B., 1999, *The prediction of scale and CO_2 corrosion in oil field systems*, NACE 99041, San Antonio
73. Clugston M. and Flemming R., 2000, *Advanced chemistry*, Oxford University Press, Oxford
74. Laing N., Graham G. M. and Dyer S. J., 2003, *Barium Sulphate inhibition in Subsea systems -The impact of cold seabed temperatures on the performance of generically different scale inhibitor species*, SPE 80229, Houston Texas
75. Aoun M., Plasari E., David R. and Villermaux J., 1999, *A simultaneous determination of nucleation and growth rates from batch spontaneous precipitation*, Chemical Engineering Science, 54, 1161-1180
76. Sorbie K. S., Graham G. M. and Jordan M. M., 2000, *How scale inhibitors work and how this affects test methodology*, 4th Intl. Conference and Exhibition on Chemistry in Industry Manama

77. Dyer S. J. and Graham G. M., 2002, *The effect of temperature and pressure on oilfield scale formation*, Journal of petroleum science and engineering, 35, 95-107
78. Environment B. M. O., 2009, *Requirements for determining barite sites*, Protocol 14
79. Benton W. J., Collins I. R., Grimsey I. M., Parkinson G. M. and Rodger S. A., 1993, *Nucleation, growth and inhibition of barium sulfate-controlled modification with organic and inorganic additives*, Faraday Discuss., 95, 281-297
80. Vegard L., 1921, *Z.Physics 5*, 17,
81. Risthaus P., Bosbach D., Becker U. and Putnis A., 2001, *Barite scale formation and dissolution at high ionic strength studied with atomic force microscopy*, Colloids and Surfaces A: Physicochem. Eng. Aspects, 191, 201-214
82. Kucher M., Babic D. and Kind M., 2006, *Precipitation of barium sulfate: Experimental investigation about the influence of supersaturation and free lattice ion ration on particle formation*, Chemical Engineering and Processing, 45, 900-907
83. Wong D., Jaworski Z. and Nienow A., 2001, *Effect of ion excess on particle size and morphology during barium sulphate precipitation: an experimental study*, Chem. Eng. Sci., 56, 727
84. He S., Oddo J. E. and Tomson M. B., 1994, *Inhibition of calcium and barium sulfate nucleation relationship to scale control*, NACE, 199, 17
85. Yokota M., Oikawa E., Yamanaka J., Sato A. and Kubota N., 2000, *Formation and structure of round - shaped crystals of barium sulfate*, Chemical Engineering Science, 55, 4379-4382
86. Wang F., Xu G., Zhang Z., Song S. and Dong S., 2006, *A systematic morphosynthesis of barium sulfate in the presence of phosphonate inhibitor*, Colloid and Interface Science, 293, 394-400
87. Quddus A. and Allam I. M., 2000, *$BaSO_4$ scale deposition on stainless steel*, Desalination, 127, 217-224
88. Emmons D. H., Graham G. C., Holt S. P., Jordan M. M. and Locardel B., 1999, *On-site, near-real-time monitoring of scale deposition*, SPE 56776, Houston Texas
89. Yang M. and Thompson M., 1993, *Multiple chemical information from the thickness shear mode acoustic wave sensor in the liquid phase*, Anal. Chem., 65, 1158-1168
90. Sun L.-X. and Okada T., 2001, *Studies on interactions between Nafion and organic vapours by quartz crystal microbalance*, Journal of membrane science, 183, 213-221
91. Karpovich D. S. and Blanchard G. J., 1994, *Direct measurement of the adsorption kinetics of alkanethiolate self-assembled monolayers on a microcrystalline gold surface*, Langmuir, 10, 3315-3322
92. Kurosawa S., Park J.-W., Aizawa H., Wakida S.-I., Tao H. and Ishihara K., 2006, *Quartz Crystal Microbalance immunosensors for environmental monitoring*, Biosensors & Bioelectronics, 22, 473-481

93. Mirmohseni A. and Oladegaragoze A., 2004, *Application of the quartz crystal microbalance for determination of phenol in solution*, Sensors and Actuators B, 98, 28-36
94. Zhang Y., Fung Y., Sun H., Zhu D. and Yao S., 2005, *Study of protein adsorption on polymer coatings surface by combining quartz crystal microbalance with electrochemical impedance methods*, Sensors and Actuators B, 108, 933-942
95. Bund A. and Schwitzgebel G., 2000, *Investigations on metal depositions and dissolutions with an improved EQCMB based on quartz crystal impedance measurements*, Electrochemica Acta, 45, 3703-3710
96. Abdel-Aal. N., Satoh K. and Sewada K., 2002, *Study of the adhesion mechanism of $CaCO_3$ using a combined bulk chemistry/ QCM technique*, Journal of crystal growth, 245, 87-100
97. Alimi F. and Gadri A., 2004, *Kinetics and morphology of formed gypsum*, Desalination, 166, 427-434
98. Kleber C., Hilfrich U. and Schreiner M., 2007, *In situ QCM and TM-AFM investigations of the early stages of degradation of silver and copper surfaces*, Applied surface science, 253, 3712-3721
99. Iwata F., Saruta K. and Sasaki A., 1998, *In situ atomic force microscopy combined with a quartz crystal microbalance study of Ag electrodeposition on Pt thin film*, Applied Physics A, 66, S463-S466
100. Atashbar M. Z., Bejcek B., Vijh A. and Singamaneni S., 2005, *QCM biosensor with ultra thin polymer film*, Sensors and Actuators B, 107, 945-951
101. Neville A., Risnes O. and Dastillung R., 2004, *Using in-situ AFM for analysis of scaling processes in carbonate systems*, NACE 04932, Houston
102. Higgins S. R. and Hu X., 2005, *Near molecular-scale growth of natural minerals: Experimental methods and errors in length-dependent step speeds with scanning probe microscopy*, Journal of Electron Spectroscopy and Related Phenomena, 150, 235-247
103. Pastor N. S., Pina C. M., Diaz L. F. and Astilleros J. M., 2006, *The effect of CO_3^{2-} on the growth of barite {001} and {210} surfaces: An AFM study*, Surface Science, 600, 1369-1381
104. Pina C. M., Becker U., Risthaus P., Bosbach D. and Putnis A., 1998, *Molecular-scale mechanisms of crystal growth in barite*, Letters to nature, 395, 483-486
105. Pina C. M., Putnis C. V., Becker U., Biswas S., Caroll E. C., Bosbach D. and Putnis A., 2004, *An atomic force microscopy and molecular simulations study of the inhibition of barite growth by phosphonates*, Surface Science, 553, 61-74
106. Barham A. S., Haque M. D. K., Roos Y. H. and Hodnett B. K., 2006, *Crystallization of spray-dried lactose/ protein mixtures in humid air*, Journal of crystal growth, 295, 231-240
107. Ng J. D., Clark P. J., Stevens R. C. and Kuhl P., 2008, *In situ X - ray analysis of protein crystals in low- birefringent and X - ray transmissive plastic microchannels*, Acta Crystallographica Section D, 64, 189-197
108. Zhao Z. B., Rek Z. U., Yalisove S. M. and Bilello J. C., 2004, *In-situ x-ray diffraction observation of multiple texture turnovers in sputtered Cr films*,

Journal of vacuum science and technology. A. Vacuum, surfaces, and films, 22, 2365-2372

109. Novàk P., Goers D., Hardwick L., Holzapfel M., Scheifele W., Ufheil J. and Würsig A., 2005, *Advanced in situ characterization methods applied to carbonaceous materials*, Journal of power sources, 146, 15-20
110. Taniguchi T., Sato T., Utsumi W., Kikegawa T. and Shimomura O., 1997, *In-situ X-ray observation of phase transformation of rhombohedral boron nitride under static high pressure and high temperature*, Diamond and related materials, 6, 1806-1815
111. Chen T., 2005, *New insights into the mechanisms of calcium carbonate mineral scale formation and inhibition*, PhD Thesis, School of Mechanical Engineering, University of Leeds
112. Chen T., Neville A., Sorbie K. and Zhong Z., 2006, *Using synchrotron radiation wide-angle X-ray scattering (WAXS) to study the inhibiting effect of polyphosphinocarboxylic acid (PPCA) on $CaCO_3$ scale formation*, NACE, 06386, 1-13
113. Martinod A. C., 2008, *An integrated study of $CaCO_3$ formation and inhibition*, PhD Thesis, School of Mechanical Engineering, University of Leeds
114. Hennessy A., Graham G., Hastings J., Siddons D. P. and Zhong Z., 2002, *New pressure flow cell to monitor $BaSO_4$ precipitation using synchrotron in situ angle dispersive X - ray diffraction*, J. Synchrotron Rad., 9, 323-324
115. Jones F., Jones P., Marco R. D., Bobby Pejcic and Rohl A. L., 2008, *Understanding barium sulfate precipitation onto stainless steel*, Applied surface science, 254, 3459-3468
116. Liu S.-T. and Nancollas G. H., 1975, *The crystal growth and dissolution of barium sulfate in the presence of additives*, Journal of Colloid and Interface science, 52, 582-592
117. Bovington C. H. and Jones A. L., 1970, *Tracer study of the kinetics of dissolution of barium sulphate*, Trans. Faraday Soc., 66, 764-768
118. Leung W. H. and Nancollas G. H., 1978, *A kinetic study of the seeded growth of barium sulfate in the presence of additives*, Inorganic Nucl. Chem., 40, 1870-1875
119. Morris R. L. and Paul J. M., 1990, *Method for removing alkaline sulfate scale*, Patent, 4980077
120. Peter V. Coveney R. D., Jonathan L. W. Griffin, Yan He, John D. Hamlin, Stephen Stackhouse and Andrew Whiting, 2000, *A new design strategy for molecular recognition in heterogeneous systems: a universal crystal-face growth inhibitor for barium sulfate*, J. Am. Chem. Soc., 122, 11557-11558
121. Rabaioli M. R. and Lockhart T. P., 1996, *Solubility and phase behavior of polyacrylate scale inhibitors*, Petroleum science and engineering, 15, 115-126
122. Dyer S. J. and Graham G. M., 2003, *Thermal stability of generic barium sulphate scale inhibitor species under static and dynamic conditions*, Petroleum Science & Engineering, 37, 171-181
123. Peter Risthaus D. B., Udo Becker, Andrew Putnis, 2001, *Barite scale formation and dissolution at high ionic strength studied with atomic force microscopy*, Colloids and Surfaces A: Physicochem. Eng. Aspects, 191, 201-214

124. Oliveira R., 1997, *Understanding adhesion: A means for preventing biofouling*, Experimental thermal and fluid science, 14, 316-322
125. Jordan M. M., Archibald I., Donaldson L. and Kemp K. S. S., 2003, *Deployment, Monitoring and Optimisation of a combines scale corrosion inhibitor within a subsea facility in the north sea basin*, SPE 114049, Aberdeen UK
126. Verdaguer S. V., 1996, *Chemical aspects of the effect of impurities in crystal growth*, Prog. Crystal Growth and Charact., 32, 75-109
127. Jones F., Stanley A., Oliveira A., Rohl A. L., Reyhani M. M., Parkinson G. M. and Ogden M. I., 2003, *The role of phosphonate speciation on the inhibition of barium sulfate precipitation*, Crystal Growth, 249, 584-593
128. Hills E., Hase A., Tuerner K., Brice S. and Ross A., 2006, *Hydrate-inhibited scale inhibitor for use on subsea templates*, SPE 100472, Aberdeen
129. Boak L. S. and Sorbie K., 2006, *The kinetics of sulphate deposition in seeded and unseeded tests*, SPE 100513, Aberdeen UK
130. Leeden M. C. V. D. and Rosmalen G. M. V., 1990, *Effect of the molecular weight of polyphosphinoacrylates on their performance in $BaSO_4$ growth retardation*, Crystal Growth, 100, 109-116
131. Leeden M. C. V. D. and Rosmalen G. M. V., 1988, *Inhibition of barium sulphate deposition by polycarboxylates of various molecular structures*, SPE, 5, 70-76
132. Rizkalla E. N., 1983, *Kinetics of the crystallisation barium sulphate*, Chem. Soc., Faraday Trans., 79, 1857- 1867
133. Jones F., Oliveira A., Rohl A. L., Parkinson G. M., Ogden M. I. and Reyhani M. M., 2002, *Investigation into the effect of phosphonate inhibitors on barium sulphate precipitation*, Crystal growth, 237-239, 424-429
134. Graham G. M., Boak L. S. and Sorbie K. S., 2003, *The influence of formation calcium and magnesium on the effectiveness of generically different barium sulphate oilfield scale inhibitors*, SPE 81825, Aberdeen
135. Yu J., Liu S. and Cheng B., 2005, *Effects of PSMA additive on morphology of barite particles*, Journal of Crystal Growth, 275, 572-579
136. Perez L. A., Freese D. T., Rockett J. B. and Carey W. S., 1994, *Methods for controlling scale formation in aqueous systems*, Betz Laboratories, Inc., patent, Patent 5326478
137. Collins I. R., 1999, *Surface electrical properties of barium sulfate modified by adsorption of poly a, b Aspartic acid*, Colloid and Interface science, 212, 535-544
138. Crabtree P. T., Eslinger D., Fletcher P., Johnston A. and King G., 1999, *Fighting Scale-Removal and Prevention, Oilfield Review*, 30-45
139. Hennessy A. J. B. and Graham G. M., 2002, *The effect of additives on the co-crystallisation of calcium with barium sulphate*, Crystal Growth, 237-239, 2153-2159
140. Sullivan C. K. O. and Guilbault G. G., 1999, *Commercial quartz crystal microbalances-theory and applications*, Biosensors and Bioelectronics, 14, 663-670

141. Smith A. L., 2008, *Handbook of thermal analysis and calorimetry,* Gallagher, Elsevier, Ohio
142. Mecea V. M., 2006, *Is quartz crystal microbalance really a mass sensor,* Sensors and Actuators A, 128, 270-277
143. Sauerbrey G., 1959, *The use of quartz crystal oscillators for weighing thin layers and for microweighing,* Z. Physics, 155, 206-222
144. Kanazawa K. K. and Ii J. G. G., 1985, *Frequency of Quartz Microbalance in Contact with liquid,* Analytical Chemistry, 57, 1770-1771
145. Glassford A. P. M., 1978, *Response of a quartz crystal microbalance to a liquid deposit,* J. Vac. Sci. Technol., 15, 1836-1843
146. Lamas-Ardisana P. J. and Costa-Garcia A., 2006, *Behaviour of the series resonant frequency in electrolyte solutions,* Sensors and Actuators B, 115, 567-574
147. Systems S. R., 2005, *QCM200 Quartz Crystal Microbalance,* Operation and Service Manual, Sunnyvale, California
148. http://En.Wikipedia.Org/Wiki/Microscope
149. Digital Instruments V. M. G., 2002, *SPM Lab 6.0, Release Notes,* California
150. Thermomicroscopes, 1996-2001, *Explorer Instrument Operation Manual,* California
151. Cullity B. D. and Stock S. R., 1978, *Elements of X-ray diffraction,* Addison-Wesley Publishing Company Inc., Massachusetts
152. Tareen J. and Kutty T. R. N., 2001, *A basic course in crystallography,* Universities Press, Hyderabad
153. Coppens P., 1992, *Synchrotron Radiation Crystallography,* Academic Press, London
154. Harris K. D. M., 2002, *Structure determination of molecular materials from powder diffraction data,* Current opinion in Solid State & Materials Science, 6, 125-130
155. Harris K. D. M., Tremayne M., Lightfoot P. and Bruce P. G., 1994, *Crystal structure determination from Powder Diffraction Data by Monte Carlo Methods,* J. Am. Chem. Soc., 116, 3543-3547
156. Guo F. and Harris K. D. M., 2005, *Structural understanding of a molecular material that is accessed only by a solid-state desolvation process: The scope of modern powder X - ray diffraction techniques,* J. Am. Chem. Soc., 127, 7314-7315
157. Zhong Z., Kao C. C., Siddons D. P. and Hastings J. B., 2001, *Sagittal focusing of high-energy synchrotron X-rays with assymentric Laue crystals II Experimental studies,* Journal of Applied Crystallography, 34, 646-653
158. Zhong Z., Kao C. C., Siddons D. P. and Hastings J. B., 2001, *Sagittal focusing of high-energy synchrotron X-rays with assymetric Laue crystals. I. Theoretical considerations,* Journal of Applied Crystallography, 34, 504-509
159. Sun Z. and Skold R. O., 2001, *Characterization of barite suspensions during synthesis by light scattering,* Journal of Colloid and Interface science, 242, 67-74
160. Mavredaki E., Neofotistou E. and Demadis K. D., 2004, *Inhibition and dissolution as dual mitigation approaches for colloidal silica (SiO_2) fouling and*

deposition in process water systems: Functional synergies, Industrial and engineering chemistry research, 44, 7019-7026

161. Heywood B. R. and Mann S., 1994, *Template - Directed Nucleation and Growth of Inorganic Materials*, Advanced Materials, 6, 9-20
162. Morris R. L. and Paul J. M., 1990, Patent, 4980077
163. Dunn K., Daniel E., Schuler P. J., Chen H. J., Tang Y. and Yen T. F., 1999, *Mechanisms of Surface Precipitation and dissolution of barite: A morphology approach*, Journal of Colloid and Interface science, 214, 427-437
164. Sawada H T. Y., 1990, *Barite - $BaSO_4$-[PNMA]*
165. Brigatti M. F., Galli E. and Medici L., 1997, *Ba -rich celestite: new data and crystal structure refinement*, Mineralogical Magazine, 61, 447-451
166. Boeyens J. C. A. and Ichharam V. V. H., 2002, *Redetermination of the crystal structure of calcium sulphate dihydrate, $CaSO_4$ x $2H_2O$*, Zeitschrift für Kristallographie, 217, 9-10
167. Cvejic Z. and Rakic S., 2006, *Maghemite C - Fe21.34O26.67-[P4332]*
168. Jawad M. A., Steuwer A., Kilcoyne S. H., Shore R. C., Cywinski R. and Wood D. J., 2007, *2D mapping of texture and lattice parameters of dental enamel*, Biomaterials, 28, 2908-2914
169. Brigatti M., 1997, *Celestine barian - (Sr0.87Ba0.13) (SO_4) - [PNMA]*
170. Rollheim M., Shamsili R. G., Østvold T. and Siamos A., 1993, *Scale formation in reservoir and production equipment during oil recovery IV. Experimental study of $BaSO_4$ and $SrSO_4$*, Acta Chemica Scandinavica, 47, 358-367
171. Shiliang He J. E. O., Mason B. Tomson, 1994, *The inhibition of gypsum and barite nucleation in NaCl brines at temperatures from 25 to 90℃*, Applied Geochemistry, 9, 561-567
172. Rosmalen G. M. V., Leeden M. C. V. D. and Gouman J., 1980, *The Growth Kinetics of Barium Sulphate Crystals in Suspension: Scale Prevention (I)*, Kristall und Technik, 15, 1213-1222
173. Pastor N. S.-. Pina C. M. and -Diaz L. F., 2006, *Relationships between crystal morphology and composition in the (Ba, Sr)SO_4 -H_2O solution-aqueous solution system*, Chemical Geology, 225, 266-277
174. Pastor N. S., Pina C. M., Astilleros J. M., Fernandez-Diaz L. and Putnis A., 2005, *Epitaxial growth of celestite on barite (001) face at molecular scale*, Surface Science, 581, 225-235
175. Redfern S. E. and Parker S. C., 1998, *Atomistic simulation of the effects of calcium and strontium defects on the surface structure and stability of $BaSO_4$*, Faraday Transactions, 94, 1947-1952
176. Schlatti M., Sahl K., Zemann A. and Zemann J., 1970, *Die Kristallstruktur des Polyhalits, K2 Ca2 Mg (SO4)4 (H2O)2*